Magnetic heat transport in low-dimensional quantum magnets

Otter, Marian

Magnetic heat transport in low-dimensional quantum magnets

Marian Otter

university of groningen / faculty of mathematics and natural sciences / zernike institute for advanced materials

Magnetic heat transport in low-dimensional quantum magnets

Marian Otter

PhD Thesis
University of Groningen, the Netherlands

Zernike Institute PhD Thesis Series 2012-05
ISSN: 1570-1530
ISBN: 978-90-367-5337-1 (print)
ISBN: 978-90-367-5338-8 (digital)

This work was supported by
the European Commission through the NOVMAG project (FP6-032980)

The digital version contains all pictures in color. The printed version contains a selection of the pictures in color.

Cover illustration: anisotropic heat transport along the surface in the spin ladder $Ca_9La_5Cu_{24}O_{41}$ as seen through a microscope.

RIJKSUNIVERSITEIT GRONINGEN

Magnetic heat transport in low-dimensional quantum magnets

Proefschrift

ter verkrijging van het doctoraat in de
Wiskunde en Natuurwetenschappen
aan de Rijksuniversiteit Groningen
op gezag van de
Rector Magnificus, dr. E. Sterken,
in het openbaar te verdedigen op
vrijdag 18 mei 2012
om 16.15 uur

door

Marian Otter

geboren op 6 oktober 1983

te Emmen

Promotor:	Prof. dr. ir. P.H.M. van Loosdrecht
Beoordelingscommissie:	Prof. dr. B. Noheda
	Prof. dr. X. Zotos
	Prof. dr. B. Büchner

dedicated to my parents

Contents

1. Introduction

1.1 Motivation

It is well known that efficient heat removal is crucial to the performance of many electronic devices; overheating often leads to overall system failures. For example, in typical silicon semiconductor devices, the relationship between the reliability and the operating temperature shows that a reduction in the temperature corresponds to an exponential increase in the reliability and life expectancy of the device [1]. Another example is given by magnetic sensors in recording heads. They consist of multilayers of nanoscale thin films and are very susceptible to failures caused by thermally activated processes, including interdiffusion and disruption of magnetic coupling among the constituent layers. At higher temperatures they can even melt. Furthermore, the spin valve sensors are based on the giant magnetoresistance effect, which decreases in magnitude with rising temperature. Finally, thermal expansion of the layers can cause mechanical damage. Self-heating is therefore a key factor which limits the maximum permissible bias current and hence the amplitude of the sensor signal output [2].

What makes the problem even more severe is the current trend to miniturize electronics further and further; by doing so, the power density is increased accordingly. Currently the energy density increases up to 28 % per year, as is shown in figure 1.1. This trend shows that self-heating will become more important, as well as heating of neighbouring components, putting high pressure on research and industry to come up with advanced cooling mechanisms and/or materials.

An example of such an advanced cooling device is shown in figure 1.2. A hot spot in a microelectronic structure is generating unwanted heat. This heat could on one hand hamper the performance of the heat releasing structure. On the other hand, heat sensitive structures in its proximity could be damaged. A possible strategy for dissipating the excess heat, while at the same time protecting sensitive structures closeby, is to use a layer with high thermal conduction perpendicular to the surface to guide the heat to a heat sink, as is shown in figure 1.2 right. Then the sensitive structures on the surface could be placed much closer, thereby allowing for further miniturization. Another design, with the heat channel along the surface, could be a suitable choice for linear devices. In order to realize such a device, one needs a material with three necessary properties:

- the thermal conductivity should be high, i.e. ≥ 100 W m^{-1} K^{-1}
- the thermal conductivity should be one-dimensional
- the compound should be electrically insulating.

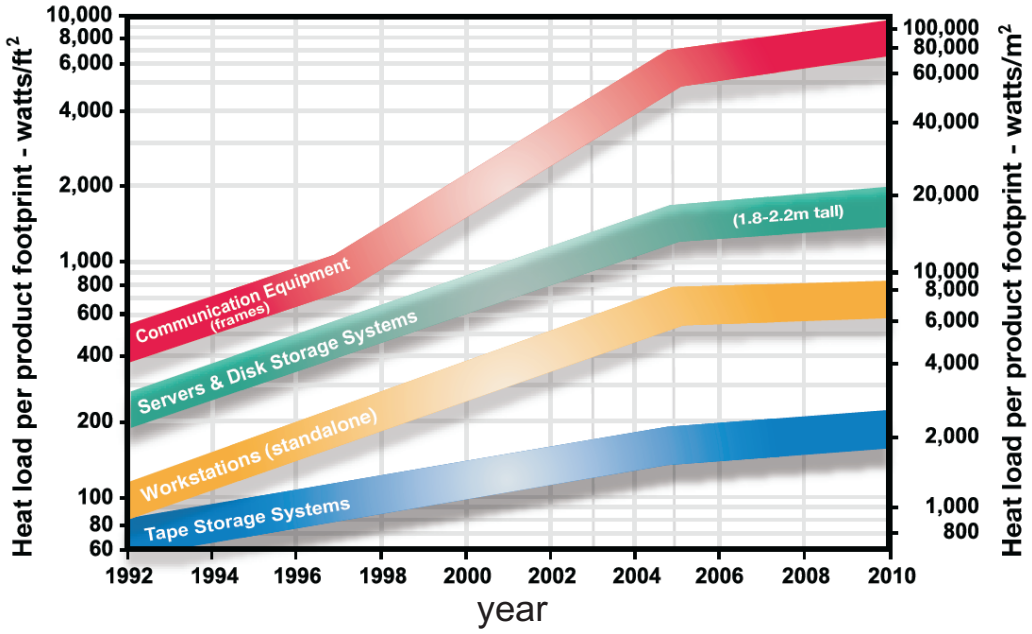

Figure 1.1: Energy density for different types of systems as a function of time. The energy density increases by 7 to 28 % per year, depending on the type of system. Picture taken from [3].

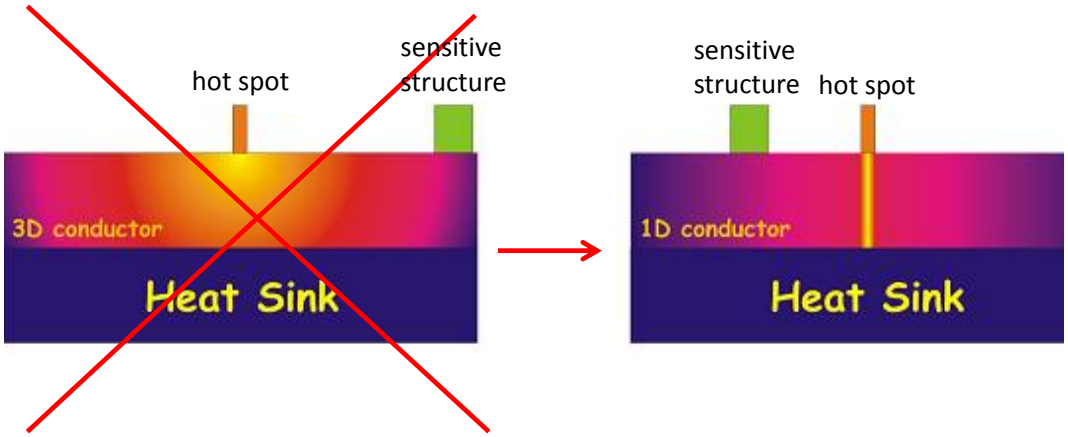

Figure 1.2: Schematic illustration of a thermal management strategy. Left: A conventional heat conductor is normally roughly isotropic (3D heat conductor). The heat spreads in the horizontal direction as well as in the vertical direction, and sensitive structures have to be placed relatively far away. Right: In the case of a quasi one-dimensional heat conductor, heat is channelled away in the vertical direction only, and sensitive structures can be placed much closer without being damaged by overheating.

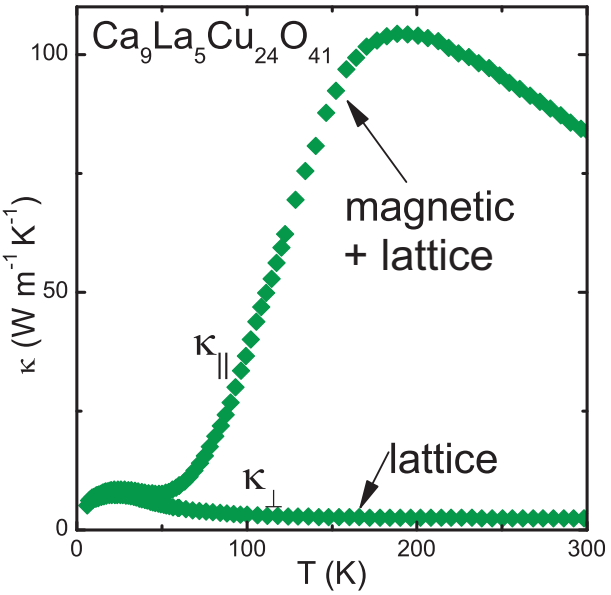

Figure 1.3: Thermal conductivity of the spin ladder compound $Ca_9La_5Cu_{24}O_{41}$ as a function of temperature. The direction parallel to the ladder has a contribution from both phonons and magnons. The directions perpendicular to the ladder only have a phonon contribution. Data taken from [9].

Furthermore, it would be advantageous to have a controllable thermal conductivity, so that the heat transport can be adjusted as desired.

In 1997 it was established that prototype theoretical models for one-dimensional magnetic compounds show unconventional, dissipationless, thermal transport [4]. Experimentally, an unusually large magnetic contribution to the total thermal conductivity has been observed in prototype materials ($SrCuO_2$, Sr_2CuO_3 and $(Sr,Ca,La)_{14}Cu_{24}O_{41}$) with quasi one-dimensional spin arrangements in chains or ladders [5, 6, 7, 8]. In particular, an exceptionally high magnetic thermal conductivity has been found at room temperature in high quality single crystals [6, 9, 10, 11]. The magnetic heat conduction of these electrically insulating oxide materials is highly anisotropic, dwarfing the usual lattice contribution. Since its discovery this new mode of thermal transport has been extensively investigated both theoretically and experimentally. Some selected references give a good impression of the work done so far [4,6-9,12-49].

These materials are promising candidates for advanced cooling solutions. They fulfill all the criteria mentioned above. i) Heat is conducted primarily along one crystal axis, hence the material can thermally insulate in one direction and carry away heat along another. ii) The thermal conductivity along the one-dimensional structure is as high as $\kappa_{mag} \approx 100$ W m^{-1} K^{-1} at room temperature for the spin ladder $Ca_9La_5Cu_{24}O_{41}$, i.e. comparable to a metal, as is shown in figure 1.3. For comparison, for copper $\kappa \approx 350$ m^{-1} K^{-1} and for the widely used material silicon $\kappa \approx 140$ m^{-1} K^{-1}. The anisotropy ratio between different directions is about 40. iii) These compounds are electrically insulating and can therefore be used to simultaneously electrically insulate electronic circuits and transport heat. iv) Heat is carried by localised spins which might be manipulated with magnetic fields or light. This opens the possibility of having a controllable thermal conductivity at room temperature. For example, doping

with switchable magnetic defects potentially makes tuning of the thermal conductivity achievable [50].

As a proof of concept for the spin chain $SrCuO_2$, the thermal conductivity was switched by heating the sample locally. The experiment was performed at the Rijksuniversiteit Groningen in collaboration with IFW Dresden. The sample was placed in an optical cryostat. First the thermal conductivity along the chain was measured at different temperatures to verify that it was in agreement with results obtained in earlier experiments. As a next step, the sample was heated locally between the arms of the thermocouple by a CW laser with a wavelength of 740 nm from time t=0, thereby changing the temperature and thus the thermal conductivity. As is seen in figure 1.4, the change in thermal conductivity is clearly visible and is as large as 45 % for an energy density of about 10 $\mu W/cm^2$. It is difficult to estimate from the energy density which temperature increase would be expected, since the heat is continuously flowing through the sample to the cryostat rod, and the exact equilibrium temperature distribution for the whole system is not known. From the decrease in thermal conductivity an increase in temperature of $\approx$ 70 K is estimated. The oscillations in the signal are due to poor shielding of the connector plug of the cryostat and may be reduced to a large extend by using a better connector. This experiment highlights the possibility of using a heating source to influence the thermal conductivity. However, at room temperature the spin chain compound $SrCuO_2$ is not very suitable due to the small dependence of κ on temperature. The spin ladder $Ca_9La_5Cu_{24}O_{41}$ would be a better candidate at this temperature. The ideal situation for regulating heat flow would be a material in which κ increases when the temperature increases, such that, when used as a cooling substrate, the efficiency increases with increased heat flux, thereby acting as a negative feedback loop. At room temperature this is the case in, for example, the spin chain material $CaCu_2O_3$ [51].

Apart from the possible useful applications, one-dimensional quantum magnets have intriguing fundamental properties. In contrast to the well known ordered three-dimensional magnetism, these systems show only short range order or no order at all. This occurs because there are two competing processes in the material. On the one hand, the system strives for the lowest energy, and therefore most ordered ground state. On the other hand, quantum fluctuations prevent long range ordering in two or one dimensions [52], leading to the intermediate situation of short range order below the ordering temperature and short range correlations above it. Therefore, this magnetic system behaves as a low-dimensional liquid, the so-called Luttinger liquid [53]. In such a state, unusual physics is observed, for example high temperature superconductivity when the material is lightly hole-doped [54] and Bose-Einstein condensation in the presence of a magnetic field [55]. Furthermore, in these materials the interaction between the magnetic excitations and the three-dimensional electronic or lattice excitations can be studied relatively easily by comparing results for different directions, since the magnetic excitations are only present in the direction along the low-dimensional structure. This interaction can give information about the coupling between the one-dimensional magnetic system and the three-dimensional lattice, and how this prevents the material from behaving like an ideal low-dimensional system.

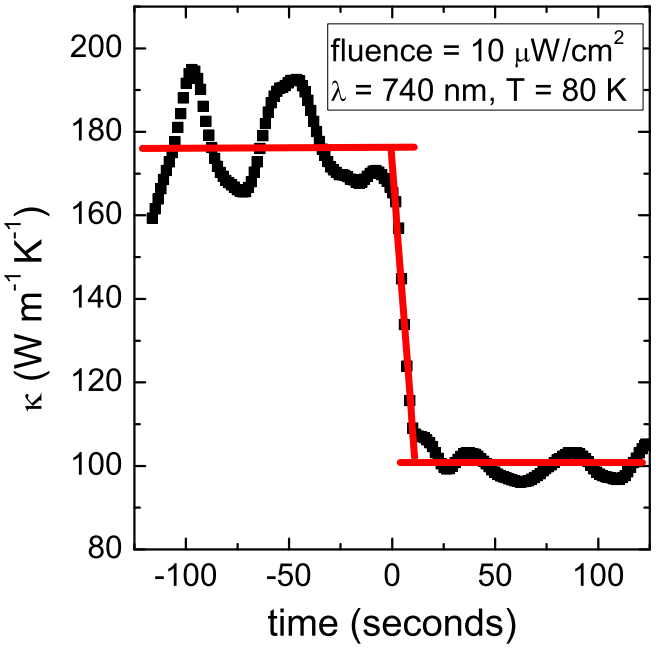

Figure 1.4: Squares: thermal conductivity κ along the chain of the spin chain compound $SrCuO_2$ as a function of time obtained using a steady state method in an optical cryostat at 80 K. Line: guide to the eye. At t=0 a heating laser is switched on, heating the area between the two arms of the thermocouple continuously. It is clearly seen that κ goes down strongly when the laser is heating the sample.

1.2 Thesis overview

In 2007 a 4-year European project called NOVMAG (NOVel MAGnetic-mode heat transport for thermal management in microelectronics) started, with the goal to exploit low-dimensional quantum magnetic oxides for advanced and innovative thermal management. The project is a collaboration between different research groups in Europe:

Experimental

- Leibniz Institute for Solid State and Materials Research (IFW), Dresden, Germany
- Laboratoire de Physico-chimie de l'Etat Solide, Université Paris Sud, France
- Department of Mechanical and Manufacturing Engineering - Nanotechnology Research, University of Cyprus, Greece
- Optical Condensed Matter Physics, Zernike Institute for Advanced Materials, Rijksuniversiteit Groningen, The Netherlands

Theoretical

- Institute of Electronic Structure and Laser, Foundation of Research and Technology, Hellas, Greece
- Theory Division, Jozef Stefan Institute, Slovenia

Industry

- ASCOMP GmbH, Switzerland

The work described in this thesis is performed in the framework of the NOVMAG project. There have been many collaborations with people from different groups within the project. Materials have been obtained from the Université Paris Sud. At the IFW Dresden, similar measurements were done and results were compared. At the University of Cyprus prototype devices were prepared, which were measured at the Rijksuniversiteit Groningen. ASCOMP has been doing simulations of the experiments performed in Groningen. Although all experiments are centered around the feasibility for thermal management applications, the fundamental understanding of phonons, magnons and electrons, and the interaction between those is equally important.

Chapter 2 gives a theoretical description of magnetic materials, focussing on the spin ladder and spin chain materials, on which the experiments described in this work are performed. Both materials are one-dimensional quantum magnets. Important interactions in these materials are discussed, together with the structure, excitations and dispersion relation.

Chapter 3 describes thermal transport in such materials. Two theoretical descriptions of heat transport are treated. The first one is a well known macroscopic diffusion model, which can be used for every diffusive process [56]. The second one is a macroscopic diffusion model starting from two different fluids which travel at a different

speed and equilibrate at a certain rate. After explaining the models, the temperature dependent thermal conductivity of the spin chain and spin ladder is discussed, together with the excitations that are responsible for heat transport.

In chapter 4 the different experiments performed are described in detail. The experimental setup is shown, together with a description of how the experiment is done. Some techniques are adaptions from or combinations of other techniques. Therefore, for these new methods, one has to start with test measurements. Those are described in the chapter as well. Furthermore, advantages and difficulties and/or limitations of several techniques are discussed.

In chapter 5 the steady state bulk thermal conductivity in nickel and a spin ladder is measured using a newly-devised optical steady state method. The method allows to measure the surface temperature locally with a resolution which is only determined by the diffraction limit. The first results obtained with this method are compared to a conventional steady state method.

Chapter 6 focusses on dynamic bulk measurements of the thermal conductivity. Since in the materials under investigation heat is transported by both lattice excitations and magnetic excitations, whereas only the phonon temperatures are measured, the interaction between those is important for how well the heat is transported. In this chapter it is discussed how the thermal conductivity measured in a dynamic bulk measurement could be different from the thermal conductivity in a static bulk measurement. This difference is only observed in the spin ladder compound and not in the spin chain compound, because of differences in spin-phonon coupling.

Chapter 7 describes thermal conductivity measurements along the surface of the spin ladder and spin chain compound. Heat spread is imaged as a function of time, after creating a hot spot with a laser. The thermal conductivity is extracted and surface effects are discussed. Furthermore, a first prototype device was prepared, which consists of two perpendicular gold strips on a well-polished spin ladder crystal surface. One strip is parallel to the fast heat transport axis, while the other one is perpendicular to it. This strip is heated electrically, as would be the case in a real device. The time-resolved spread of heat is monitored for both strips, and the results are analyzed and discussed, focussing on the usage in cooling applications.

Finally, in chapter 8 the ultra-fast (picoseconds) dynamics of the spin ladder are investigated, using different pump-probe techniques. These fast dynamics have not been measured before for the spin ladder compound. Especially the magnon dynamics are of interest, since the magnons provide the fast pathway for the heat transport. Therefore, in one of the experiments, probing is done at the magnon absorption bands in the infrared. These are determined by static infrared transmission measurements. Furthermore, for comparison probing is done at two frequencies close to the magnon bands, which are mainly sensitive to electrons or phonons. From these data some first conclusions can be drawn about magnon, phonon and electron dynamics at the short timescale.

2. Spin chains and spin ladders

This chapter and the next describe the theoretical background which is needed to get a better understanding of the materials used and experimental results obtained. In this chapter, useful theoretical concepts about spin chains and spin ladders will be explained. The next chapter focusses on heat transport properties in these materials. For a general introduction to spin chain and spin ladder materials a vast amount of literature is available, like review papers [8, 57] and special books [58, 59].

The essential difference between three-dimensional, conventional, magnetism and ideal two- or one-dimensional magnetism is that three-dimensional magetism deals with ordered domains, while in low-dimensional magnetism only short-range order can exist at finite temperature. This is due to an interplay between quantum and thermal fluctuations which drive the system to a disordered state, and the tendency for the system to be in the lowest energy state, which is ordered [52]. For two-dimensional systems, thermal fluctuations diverge but quantum fluctuations do not, leading to short-range order at all but zero temperature. For one-dimensional systems, both quantum and thermal fluctuations diverge, so even at zero temperature there is no long-range order. Because of the short-range order the behaviour of the magnetic system is closer to a liquid than to a solid, therefore they are called quantum spin-liquids [60]. In real antiferromagnetic materials there is always an interaction with the three-dimensional lattice, leading to a finite Néel ordering temperature T_N. Another difference between three-dimensional and low-dimensional magnetism is that the low-dimensionality leads to an anisotropic contribution of energy transport from the magnetic system. This is, as was explained in the introduction, one of the key aspects making these materials promising for heat management applications.

2.1 Quantum spin chains

Quantum spin 1/2 systems can be described by the anisotropic antiferromagnetic (AFM) S=1/2 Heisenberg model [23]. The Hamiltonian is given by

$$\widehat{H} = J_x \sum_{<i,j>_x} \vec{S}_i \cdot \vec{S}_j + J_y \sum_{<i,j>_y} \vec{S}_i \cdot \vec{S}_j + J_z \sum_{<i,j>_z} \vec{S}_i \cdot \vec{S}_j \tag{2.1}$$

where i labels the lattice site where the spin 1/2 operator $\vec{S}_i$ is located. The summation is restricted to nearest neighbor sites $< i, j >$, since these give the largest contribution. The constants $J_{i=x,y,z}$ (> 0) are the AF exchange couplings that provide the energy scale in the problem. In the anisotropic Heisenberg model $J_x = J_y \neq J_z$. Here J_z is the exchange coupling along the low-dimensional structure. The model can

be solved analytically for the fully one-dimensional case (i.e. only considering the z-direction, $J_x = J_y = 0$), as was first done by Bethe [61]. Formula 2.1 is a special case of the general three-dimensional Heisenberg model in which J depends on i and j. This model is explained in standard textbooks, see for example [62].

Low-dimensional quantum spin models are interesting from a fundamental point of view since they give rise to very peculiar ground state properties and elementary excitations. These vary strongly from system to system. The elementary excitations, so-called spinons, are gapless (i.e. it costs no energy to flip a spin) and carry a spin S = 1/2 [63]. The interaction of spinons with structural defects and other quasiparticles, such as phonons, is predicted to be low or even absent. This is deduced from theoretical calculations taking into account higher orders in the Hamiltonian [64] and from computer simulations [65]. Theoretically, in the ideal case of non-interacting spinons, ballistic heat transport would be present in the system [4]. This has recently been claimed experimentally for the spin chain $SrCuO_2$ [34].

2.2 The spin chain $SrCuO_2$

One of the materials investigated in this thesis is the spin chain cuprate $SrCuO_2$. It is the simplest compound from which high-T_c superconductors with a T_c up to 90 K can be prepared by high temperature and high pressure treatment. However, the structure element responsible for the superconductivity is a CuO_2 sheet, which is not present in $SrCuO_2$ but is induced by high pressure treatment from the double CuO chains [66]. The structure of $SrCuO_2$ is shown in figure 2.1. The lattice parameters are a=3.56 Å, b=16.27 Å, and c =3.90 Å[67]. The compound is centered orthorhombic and has space group $CMCM$. The right part of the figure shows the structure relevant for the magnetic heat transport, consisting of two stacked Cu-O-Cu chains. Between the copper ions within the chains there are 180 degrees bonds, which leads to strong antiferromagnetic interactions. Between copper ions in parallel chains there are 90 degrees bonds, which leads to weak ferromagnetic interactions. These interactions can be derived from the electron orbital overlap for different configurations, using the Goodenough-Kanamori rule [68]. For $T > T_N = 5$K there is no long range 3D magnetic ordering, due to quantum fluctuations [69]. Therefore the chains are an almost ideal example of the one-dimensional AFM Heisenberg chain. Characteristic for the cuprate systems is a [Cu]$3d^9$ configuration, which gives rise to S = 1/2. Because of superexchange interaction between the Cu^{2+}-ions a large exchange coupling $J_z \approx 180$ meV along the Cu-O-Cu structure is found [70, 69], while J_x, between the chains, is approximately 10 times weaker [44].

When one considers an AFM spin chain, flipping one spin creates exchange interactions with its two nearest neighbors (domain walls). Therefore, by flipping one spin, two counter-propagating spinons are created, as is shown in figure 2.2. This is the lowest lying excitation, corresponding to a pair of triplet spinons with $S_{total} = 1$ which move independently. The two-spinon excitation spectrum is therefore a continuum embracing all pairs of excitations, with momentum along the chain $q^{chain} = q_1^{chain} + q_2^{chain}$ and energy $E = E(q_1^{chain}) + E(q_2^{chain})$ [71, 72]. The continuum is bounded from below

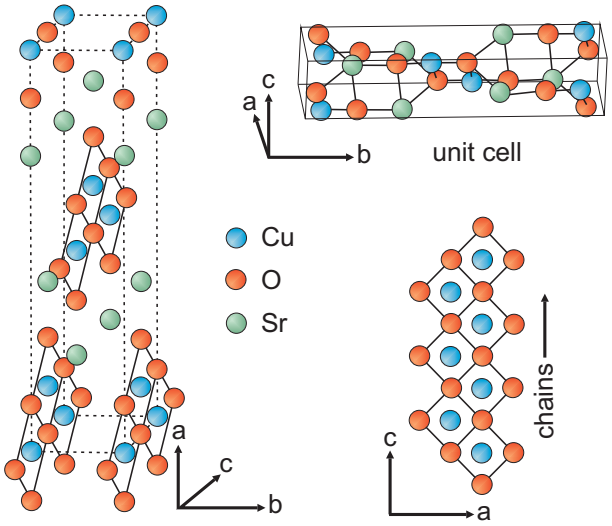

Figure 2.1: Structure of the spin chain compound $SrCuO_2$. The left part of the figure shows the full crystal structure. The top right of the figure shows the unit cell and the bottom right shows the part the structure forming blocks of two parallel spin chains.

by the dispersion relation (The Cloiseaux-Pearson relations),

$$\epsilon_{lower} = \frac{\pi}{2} J \left|\sin(2\pi q^{chain})\right| \tag{2.2}$$

and from above by

$$\epsilon_{upper} = \pi J \left|\sin(\pi q^{chain})\right| \tag{2.3}$$

where q^{chain} is measured in units of $2\pi/c$, with c the lattice parameter along the chain direction. The theoretical dispersion relation is plotted in figure 2.3. One can see from the picture that spinons are gapless. The shaded region between the upper and lower boundaries can be populated. On the right, the dispersion relation of $SrCuO_2$ as measured by inelastic neutron scattering is plotted for comparison.

2.3 Even-legged spin ladders

Low-dimensional quantum magnets have been investigated extensively since the unexpected discovery of high-temperature superconductivity in lightly doped antiferromagnets [73]. Both the 2D AFM square lattice and the 1D AFM spin chain are theoretically well understood and described with exactly solvable models. However, the in-between situation of semi-1D spin ladder systems cannot be explained by making a smooth interpolation between the two models. Furthermore, it turns out that when there is an odd number of legs, the systems behaviour is close to that of a single chain, while for an even number of legs, the behaviour is very different. Since this thesis deals with two-leg ladder materials, only this type of ladder systems will be explained in more detail.

An exact theoretical model for spin ladders does not yet exist. However, to get some insight in their properties, two different limits of the Heisenberg model, equation 2.1, can be used, by adjusting the requirements for the J's [23]. In the first limit,

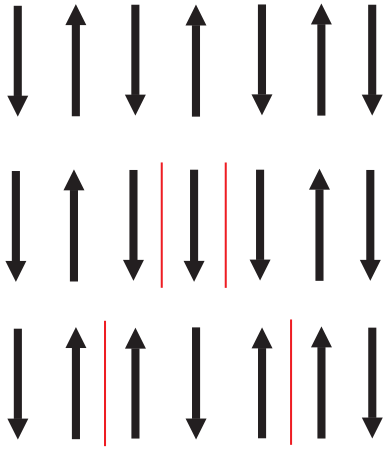

Figure 2.2: Spinons in a spin chain compound. In a perfectly ordered AFM chain (upper picture) two spinon excitations are created by flipping one spin (middle picture). These excitations can move outward (lower picture). The red lines indicate domain walls.

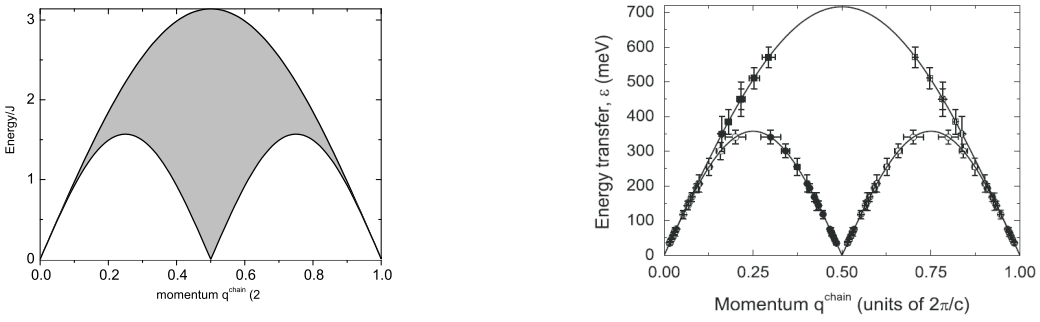

(a) (b)

Figure 2.3: a) Calculated dispersion relation of a spin chain compound. The c-direction is parallel to the chains. The two-spinon continuum in which excitations can be created lies in the shaded area. b) Measured two-spinon continuum bounds in $SrCuO_2$. Round and square black dots are independent measurements. Open dots are the same point reflected by symmetry. Measurements are obtained by inelastic neutron scattering. Picture taken from [71].

the coupling along the ladder direction, J_z, is much larger than the coupling between the rungs of the ladder, J_x. In this case effectively one deals with decoupled parallel chains. The properties are therefore the same as for the spin chain materials described in paragraph 2.1. The other limit assumes that the coupling along the ladder direction J_z, is much smaller than the coupling between the rungs of the ladder, J_x. In this idealization the rungs only interact weakly with each other and the dominant configuration in the ground state is the product state with the spins on each rung forming a spin singlet. The singlet state spin part of the wavefunction is given by

$$\Psi_S = \frac{1}{\sqrt{2}} \left(|\uparrow\downarrow\rangle - |\downarrow\uparrow\rangle \right) \tag{2.4}$$

where $\uparrow$ and $\downarrow$ are the spin-up and spin-down eigenvectors of the spin operator in the z direction. The ground state has total spin $S = 0$ because each rung forms a spin singlet. The energy of the ground state is given by

$$E_{gs} = -\frac{3}{4} J_x N \tag{2.5}$$

where N is the number of rungs and J_x is the exchange interaction parallel to the rung. To produce a $S = 1$ excitation, which is called a magnon or triplon, a rung singlet must be promoted to the triplet state

$$\Psi_T = \left[\frac{1}{\sqrt{2}} \left(|\uparrow\downarrow\rangle + |\downarrow\uparrow\rangle \right), |\uparrow\uparrow\rangle, |\downarrow\downarrow\rangle \right]. \tag{2.6}$$

An isolated rung in the triplet state has an energy J_x above the energy of the singlet state. Because of the coupling along the chain a band of $S = 1$ magnons is created of which the dispersion can be described by

$$\omega(k) = J_x + J_z cos(k) \quad \text{if} \quad J_x >> J_z \tag{2.7}$$

where k is the wave vector. The spin gap is the minimum excitation energy $\Delta_{spin} = \omega(\pi) \approx J_x - J_z$ which in this limit is large. In this limiting case the spins are mostly uncorrelated between rungs because the spin-spin correlations decay algebraically with distance along the chains and there is never any long-range order, even at T=0 [74]. This is the so-called spin-liquid ground state.

To bring together the two limits for the behaviour, it was proposed that the spin gap should slowly decrease and should only be zero when $J_x/J_z = 0$ [75]. This means that the spin-ladder system would always be in a spin-liquid state with a nonzero spin gap. In real spin ladders typically $J_x/J_z \approx 1$ so there is no small parameter that can be used as a perturbation. Therefore techniques such as Jordan-Wigner [47] and exact diagonalization have been used to simulate the behaviour of the spin gap as a function of J_x/J_z [76] [75]. It is found that the spin gap is > 0 for all $J_x/J_z \neq 0$. At the realistic coupling $J_x = J_z$ the spin gap is 0.5 J_z.

2.4 The two-leg ladders $Ca_9La_5Cu_{24}O_{41}$ and $Sr_{10}La_4Cu_{24}O_{41}$

The main material used for experiments in the work described in this thesis is the spin ladder compound $Ca_9La_5Cu_{24}O_{41}$. Furthermore, some experiments are performed on $Sr_{10}La_4Cu_{24}O_{41}$. The main difference between those two compounds is that $Sr_{10}La_4Cu_{24}O_{41}$ has hole-doped ladders. The family of spin ladder materials to which they belong was discovered as a byproduct of the high T_c superconductors in 1988 [77]. Some relevant properties are described below. The structure of $Ca_9La_5Cu_{24}O_{41}$ is shown in figure 2.4. The structure of $Sr_{10}La_4Cu_{24}O_{41}$ is the same, apart from one type of chain which consists of Sr^{2+} and La^{3+} ions instead of Ca^{2+} and La^{3+} ions. The left part of the figure shows the full structure which consists of two types of chains and ladder planes. The part of the structure forming the parallel ladders is shown on the right. Between the copper ions along the ladder direction and between the two copper ions forming the rung there are 180 degrees bonds, which leads to strong antiferromagnetic interactions. Between the copper ions of two adjacent ladders there are 90 degrees bonds, which leads to $\sim$ 10 times weaker ferromagnetic interactions, as can be derived from the Goodenough-Kanamori rule [68]. Furthermore, the spins of copper ions on adjacent ladders are frustrated, thereby decreasing the interactions between ladders to almost zero. The copper ions are connected through superexchange interaction, leading to a large exchange energy. If the ladders are undoped, $J_x = J_z = 110$ meV and the spin gap is 35 meV [39] [78]. For $Sr_{10}La_4Cu_{24}O_{41}$ inelastic neutron scattering one- and two-triplon specta were fitted with a model using J_x (rung) = 124 meV, J_z (leg) = 186 meV, and J_{cyc} (cyclic exchange) = 31 meV and a spin gap of 26.4 meV [79]. The size of the spin gap is influenced by the composition of the chains with the Sr, La and Ca ions. Substitution of Sr^{2+} ions with Ca^{2+} ions decreases the spin gap [40], while it increases when it is doped with trivalent ions (La^{3+}, Y^{3+}) [32]. The orientation of the chains (or ladders) defines the crystallographic c-axis, where the lattice constants of these two subsystems satisfy in a good approximation $10c_{chain} \approx 7c_{ladder}$. The lattice parameters are a=11.479 Å, b=13.406 Å, and c_{ladder} = 3.934 Å[25]. The lattice is orthorhombic with space group $CCCM$ [80]. $Ca_9La_5Cu_{24}O_{41}$ has a Néel temperature T_N =9.7 K [12]. For $Sr_{10}La_4Cu_{24}O_{41}$ a Néel temperature could not be determined, suggesting that above a certain amount of hole doping there is no long-range AFM ordering [20]. The copper ions are intrinsically hole doped for $Sr_{14}Cu_{24}O_{41}$ with nominal Cu valence +2.25. Optical conductivity and x-ray absorption experiments suggest that the substitution of Ca^{2+} for Sr^{2+} increases the chemical pressure, thereby inducing a transfer of holes from the chains to the ladders [19, 81, 82, 83]. On La^{3+} substitution the intrinsic doping is reduced, reaching the undoped state with nominal Cu valence +2.00 for $Ca_8La_6Cu_{24}O_{41}$. Unfortunately, this composition is not stable. However, the hole doping in the stable compound $Ca_9La_5Cu_{24}O_{41}$ is so small that it can usually be neglected.

A magnetic excitation (magnon) is created by flipping one spin so that the two spins on a rung are transformed from a singlet state to a triplet state. This is illustrated in figure 2.5. Although an exact model to describe the spin ladder does not exist, the magnon dispersion relation along the ladder direction can be described by an emperical function which is an interpolation between the solutions for the limiting

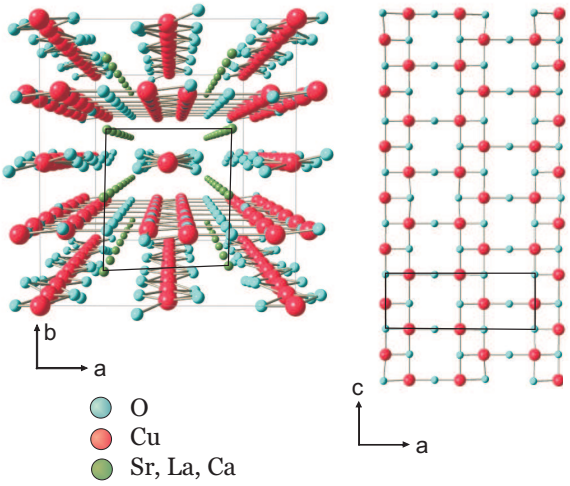

Figure 2.4: Structure of the spin ladder compound family $(Sr,La,Ca)_{14}Cu_{24}O_{41}$. On the left the full crystal structure is shown. The black square indicates the dimensions of the unit cell in the a and b-direction. On the right the part of the structure forming parallel ladders is depicted. The black square indicates the dimensions of the ladder unit cell in the a and c-direction. The copper ions carry spin 1/2. Two parallel ladders are depicted.

cases of independent chains or spin dimers [75, 84]

$$\epsilon(k)^2 = \epsilon(0)^2 cos^2(k/2) + \epsilon(\pi)^2 sin^2(k/2) + c_0 sin^2(k) \tag{2.8}$$

where $\epsilon(0), \epsilon(\pi)$ and c_0 are fitting parameters. The typical shape of such a dispersion relation, together with the experimental dispersion relation for $Sr_{10}La_4Cu_{24}O_{41}$ obtained by inelastic neutron scattering is shown in figure 2.6.

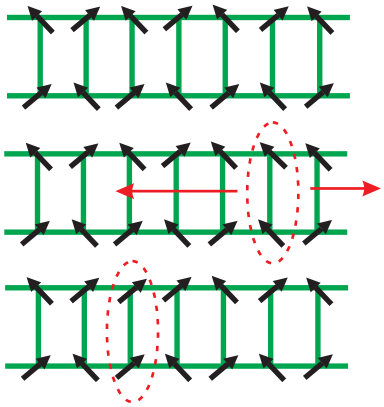

Figure 2.5: A magnon in a spin ladder compound. In a perfectly ordered AFM ladder (upper picture) an excitation is created by flipping one spin (middle picture) so that the two spins on a rung are in a triplet state. This excitation can move along the ladder in two directions. Movement to the left is shown (lower picture).

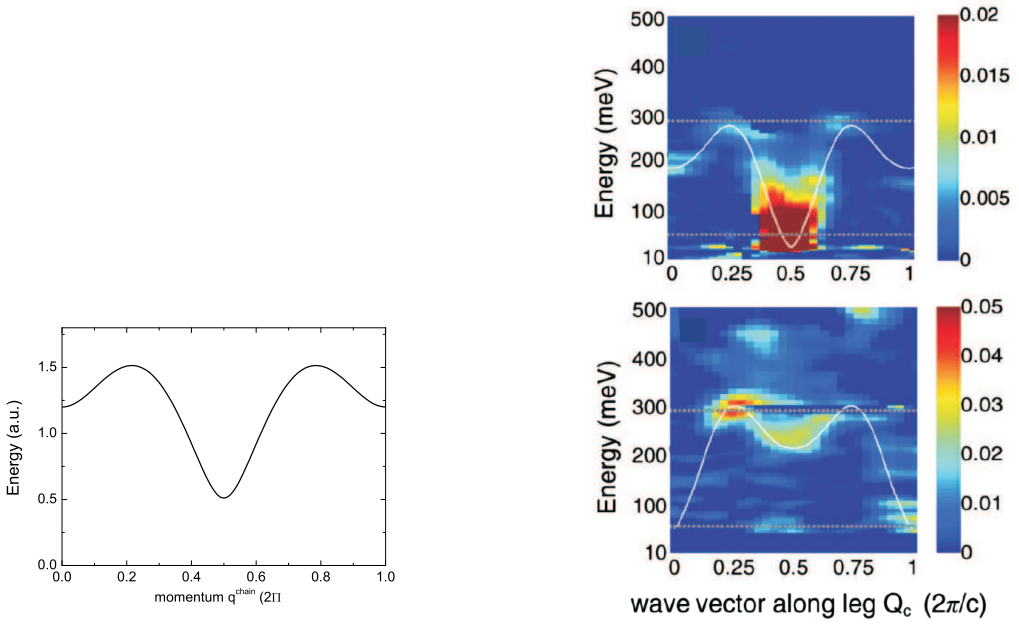

(a) (b)

Figure 2.6: a) Dispersion relation of a spin ladder compound. The c-direction is parallel to the chains. The minimum energy needed to create a magnon is given by the size of the spin gap. b) The upper picture shows the measured one-magnon dispersion relation as measured by inelastic neutron scattering for $Sr_{10}La_4Cu_{24}O_{41}$. The lower picture shows the lower bound of the two-magnon continuum. Both have a spin gap. The white lines give the calculated curves for the dispersion. The color is a measure for the local scattering intensity. Picture taken from [85].

3. Thermal transport in spin chains and spin ladders

In this chapter two theoretical descriptions of heat transport will be treated. The first one is a well known diffusion model, which can be used for single particle macroscopic diffusive process and multi-particle diffusive processes when the particles are in thermal equilibrium. The second one is a macroscopic diffusion model starting from two species having different thermal diffusivities and are converted into one another at a certain rate. After explaining the models, the thermal properties of the spin chain and spin ladder relevant for this work will be discussed.

Heat transport by magnetic excitations, as is present in spin ladders and spin chains, was already predicted 75 years ago [86], but it took 30 years before a convincing experimental proof of heat transport by classical spin waves was found [87]. The field has been expanding tremendously since it was predicted theoretically that heat conduction in one-dimensional antiferromagnetic Heisenberg chains is dissipationless [4, 49]. Furthermore, it was found experimentally that also in the quantum spin ladder material $(Sr,Ca,La)_{14}Cu_{24}O_{41}$ there is a huge (diffusive) magnetic contribution to the heat transport, even at room temperature [88, 5, 6].

3.1 One-particle three-dimensional heat conduction equation

The derivation of the heat conduction equation is explained following Carslaw and Jaeger [56]. Consider a rectangular parallelepiped, its edges parallel to the coordinate axes as is shown in figure 3.1, with point P at the center and dimensions $2dx$, $2dy$ and

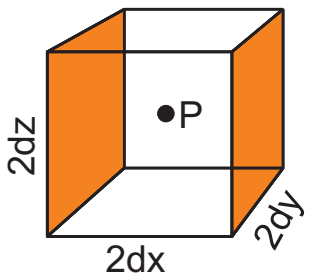

Figure 3.1: Parallelepiped with middle point P and axes of lengths $2dx$, $2dy$ and $2dz$ used in the derivation of the heat conduction equation. The faces at $x - dx$ and $x + dx$ are colored orange.

$2dz$. The rate at which heat flows into the parallellepiped over the face at $x - dx$ is given by

$$4\left(f_x - \frac{\partial f_x}{\partial x}dx\right)dydz,$$

where f_x is the flux at P over a parallel plane. Similarly, the rate at which heat flows out over the face at $x + dx$ is given by

$$4\left(f_x + \frac{\partial f_x}{\partial x}dx\right)dydz.$$

Thus the rate of gain of heat from the flow across these two faces is given by

$$-8dxdydz\frac{\partial f_x}{\partial x}. \tag{3.1}$$

The expressions for the other parallel pairs of faces are similar. By adding these the total rate of gain of heat of the parallelepiped from flow across its faces is found to be

$$-8\left(\frac{\partial f_x}{\partial x} + \frac{\partial f_y}{\partial y} + \frac{\partial f_z}{\partial z}\right)dxdydz = -8dxdydz\ \nabla\ \mathbf{f}. \tag{3.2}$$

This rate of gain of heat is also given by

$$8\rho c\frac{\partial T}{\partial t}dxdydz, \tag{3.3}$$

where ρ is the density and c is the specific heat (at temperature T) of the solid. Combining these equations gives

$$\rho c\frac{\partial T}{\partial t} + \left(\frac{\partial f_x}{\partial x} + \frac{\partial f_y}{\partial y} + \frac{\partial f_z}{\partial z}\right) = 0. \tag{3.4}$$

This equation holds at any point in the solid, provided no heat is supplied at that point.

For a homogeneous isotropic solid whose thermal conductivity κ is independent of temperature, f_x, f_y and f_z are given by

$$f_x = -\kappa\frac{\partial T}{\partial x} \quad f_y = -\kappa\frac{\partial T}{\partial y} \quad f_z = -\kappa\frac{\partial T}{\partial z},$$

so that equation 3.4 becomes

$$D\left(\frac{\partial^2 T}{\partial x^2} + \frac{\partial^2 T}{\partial y^2} + \frac{\partial^2 T}{\partial z^2}\right) - \frac{\partial T}{\partial t} = D\nabla^2 T - \frac{\partial T}{\partial t} = 0, \tag{3.5}$$

where

$$D = \frac{\kappa}{\rho c}$$

is called the thermal diffusion constant or thermal diffusivity. If heat is produced at point P at a rate $A(x, y, z, t)$ per unit time per unit volume, a term $8Adxdydz$ has to be added to equation 3.2 and equation 3.5 becomes

$$D\nabla^2 T - \frac{\partial T}{\partial t} = -\frac{A(x, y, z, t)}{\rho c}. \tag{3.6}$$

For an anisotropic solid the situation is in general more complex. When the crystal symmetry is such that the axes are not perpendicular, one has to deal with a second-order tensor with nine conductivity coefficients. However, a transformation can be made to a coordinate system with perpendicular axes. Furthermore, the thermal properties κ, ρ and c can depend on position and temperature. Taking into account all this, the heat equation for three perpendicular axes has to be modified to

$$\rho(x,y,z,T)\, c(x,y,z,T)\frac{\partial T}{\partial t} = \frac{\partial}{\partial x}\left(\kappa(x,T)\frac{\partial T}{\partial x}\right) + \frac{\partial}{\partial y}\left(\kappa(y,T)\frac{\partial T}{\partial y}\right) + \frac{\partial}{\partial z}\left(\kappa(z,T)\frac{\partial T}{\partial z}\right) + A(x,y,z,t). \quad (3.7)$$

If κ and A are functions of position only, an analytical solution exists for a variety of initial and boundary conditions. If the thermal properties depend on temperature, the situation becomes more complex and a full numerical analysis has to be performed.

3.1.1 Steady state solution

If one considers a linear, steady flow of one type of heat carrier in a solid bound by a pair of parallel planes at $x = 0$ and $x = L$ the one-dimensional differential equation becomes [56]

$$\frac{d^2T}{dx} = 0, \quad (3.8)$$

and thus

$$\frac{dT}{dx} = \text{constant} = \frac{T_L - T_0}{L}, \quad (3.9)$$

in which T_0 and T_L are the temperatures at the surfaces $x = 0$ and $x = L$, respectively. Also, the heat flux J is given by

$$J = -\kappa\frac{dT}{dx} = -\frac{\kappa(T_L - T_0)}{L}. \quad (3.10)$$

This relation is analogous to Ohm's law for the steady flow of electrical current. In the general, three-dimensional case, κ is a matrix. In the experiment the problem can be reduced to one dimension by choosing the experimental conditions carefully; the sample has a brick-like shape and is oriented such that heating is done homogenously over the small surface at $x = 0$, and a heat sink is connected to the small surface at $x = L$. Then by measuring the temperature difference between two points on the rectangular top surface, κ in the direction of the heat flow, i.e. from heater to heat sink along the long axis of the brick-like sample, can be determined. This simple analysis, assuming negligible radiation losses from the sample surface, gives a linearly decreasing temperature between the heater and heat sink and thus between the two contacts of the thermocouple. Therefore, by determining the temperature difference and distance between the thermocouple contacts, κ can directly be extracted.

3.1.2 Dynamic solution for flash method

In most of the experiments described in this work, the thermal conductivity is determined by measuring the temperature change at a surface as a function of time. If one

considers a sample with two parallel surfaces at $x = 0$ and $x = L$ with initial temperature distribution $T(x,t)$, the temperature distribution at any later time t is given by [56]

$$T(x,t) = \frac{1}{L}\int_0^L T(x,0)dx + \frac{2}{L}\sum_{n=1}^{\infty}\exp\left(\frac{-n^2\pi^2 Dt}{L^2}\right) \times \cos\frac{n\pi x}{L}\int_0^L T(x,0)\cos\frac{n\pi x}{L}dx, \tag{3.11}$$

where D is the diffusion constant. Now it is assumed that the front surface (at $x = 0$) is heated by a laser pulse of energy density Q, which is instantaneously and uniformly absorbed in a small depth μ. Then the inital conditions are given by

$$T(x,0) = Q/\rho C\mu \quad \text{for} \quad 0 < x < \mu$$
$$T(x,0) = 0 \quad \text{for} \quad \mu < x < L.$$

Using this initial condition, equation 3.11 can be written as

$$T(x,t) = \frac{Q}{\rho CL}\left[1 + 2\sum_{n=1}^{\infty}\cos\frac{n\pi x}{L}\frac{\sin(n\pi\mu/L)}{(n\pi\mu L)} \times \exp\left(\frac{-n^2\pi^2}{L^2}Dt\right)\right], \tag{3.12}$$

where ρ is the density and C is the heat capacity. Only a few terms are needed, usually around 20 are sufficient. Furthermore, μ is very small for opaque materials, therefore $\sin n\pi\mu/L \approx n\pi\mu/L$. At the back surface, where $x = L$, the temperature can be expressed as [89]

$$T_l(L,t) = T_m\left[1 + 2\sum_{n=1}^{\infty}(-1)^n \exp\left(\frac{-n^2\pi^2}{L^2}Dt\right)\right] \tag{3.13}$$

where $T(L,t)$ is the temperature at the back surface at time t, and $T_m = Q/(\rho CL)$ is the maximum temperature at the back surface. This formula is called Parker's formula. It is only valid if there is just one type of heat carrier or if the various heat carriers are in thermal equilibrium.

3.2 Two particle one-dimensional diffusion equation

The diffusion model in the previous section is a one-particle model. However, it turns out that in order to fully understand the thermal transport in the spin ladder material $Ca_9La_5Cu_{24}O_{41}$ the two-particle origin of the transport has to be taken into account, as is done in this section. An important point to realize is that in experiments to determine the thermal conductivity, only the phonon temperature is directly accessible. The temperature sensor, in this work either a fluorescent dye or a thermocouple, measures the temperature of the sample surface from the strength of the transmitted lattice vibrations. Furthermore, the heating process, either electrical or optical, mainly creates phonons, since this process is more efficient than creating magnons. In the absence of interaction between magnons and phonons, the only way the directly excited magnons can contribute to the measured temperature is by inelastic scattering at the surface, which is a weak process. If there is interaction between the magnons and phonons,

but the two heat carriers are not in thermal equilibrium, the thermal conductivity measured in an experiment is not equal to the sum of the thermal conductivities of the two species, as would be the case in a thermal equilibrium situation [90].

Suppose that in a solid in a certain direction two types of heat carriers exist, which are not in thermal equilibrium initially. Both types are travelling diffusively through the solid. Then the coupled heat equations for the two types of heat carriers, in our case magnetic excitations (magnons/spinons) and lattice excitations (phonons), are given by [90]

$$\begin{aligned} \frac{\partial T_l}{\partial t} &= D_l \frac{\partial^2 T_l}{\partial x^2} - g_l \left(T_l - T_m\right) + P(x) \\ \frac{\partial T_m}{\partial t} &= D_m \frac{\partial^2 T_m}{\partial x^2} + g_m \left(T_l - T_m\right) \\ \text{where} \quad g_m = \frac{c_m}{c_T \tau_{ml}} &\quad g_l = \frac{c_l}{c_T \tau_{ml}} \quad c_T = c_m + c_l \end{aligned} \tag{3.14}$$

where l stands for the lattice excitation (phonon) and m for the magnetic excitation (spinon or magnon). $P(x)$ is the rate at which phonons are created, τ_{lm} is the thermalization time between lattice and magnetic excitations and g is the conversion rate between the two types of particles.

3.2.1 Steady state solution

In the most common experimental configuration, the conventional steady state method, a steady heat flow is put through a brick-shaped sample along the long axis. The temperature difference along the long axis is measured between two thermocouple contacts attached to the surface. For this configuration the effective thermal conductivity κ_{eff} is analyzed by Sanders and Walton [90]. In a thermally isolated system, a total heat flux Q is supplied at $x = -1/2L$ and absorbed at $x = +1/2L$. In general, the temperature of the magnon system $T_m(x)$ is different from the temperature of the phonon system $T_p(x)$ for every x. The contribution of a small length dx to the heat flux in the magnon system is

$$dQ_m(x) = \frac{dP(x)}{A} = \frac{c_l c_m}{c_T} \frac{T_l(x) - T_m(x)}{\tau_{ml}} dx \tag{3.15}$$

where P is the heating power, A is the surface area, and T_l and T_m are the lattice and magnon temperatures, respectively. All the heat is coming from the phonon system, since no magnons are inserted directly.

Now the total magnon heat flux at any point x is given by

$$Q_m(x) = \frac{c_l c_m}{c_T} \frac{1}{\tau_{ml}} \int_{-L/2}^{x} \left[T_l(x') - T_m(x')\right] dx'. \tag{3.16}$$

But in a steady state experiment the magnon conductivity is also given by

$$Q_m(x) = -\kappa_m \frac{dT_m(x)}{dx}. \tag{3.17}$$

By combining and differentiating these equations one finds a second-order differential equation for the magnon temperature

$$\frac{d^2 T_m(x)}{dx^2} + \frac{c_l c_m}{c_T} \frac{1}{\kappa_m \tau_{ml}} \left[T_l(x) - T_m(x)\right] = 0. \tag{3.18}$$

The total heat flux Q is divided between the magnons and phonons according to

$$Q = Q_l(x) + Q_m(x) = -\kappa_l \frac{dT_l(x)}{dx} - \kappa_m \frac{dT_m(x)}{dx}, \tag{3.19}$$

so $T_l(x)$ is related to $T_m(x)$ by

$$\frac{dT_l(x)}{dx} = -\frac{Q}{\kappa_l} - \frac{\kappa_m}{\kappa_l}\frac{dT_m(x)}{dx}. \tag{3.20}$$

Solving equation 3.20 with the boundary condition that at the center of the sample, at $x = 0$, the phonon and magnon temperatures are both equal to the average sample temperature T_0, gives

$$T_l(x) = \frac{\kappa_T}{\kappa_l}T_0 - \frac{Q}{\kappa_l}x - \frac{\kappa_m}{\kappa_l}T_m(x), \tag{3.21}$$

where $\kappa_T = \kappa_l + \kappa_m$. By substituting equation 3.21 in equation 3.18, one finds

$$\frac{d^2T_m(x)}{dx^2} + A^2\left(T_0 - \frac{Q}{\kappa_T}x - T_m(x)\right) = 0, \tag{3.22}$$

where

$$A^2 = \frac{c_l c_m}{c_T}\frac{\kappa_T}{\kappa_l\kappa_m}\frac{1}{\tau_{ml}}. \tag{3.23}$$

This equation is solved with the boundary condition of equal T_m and T_l in the center of the sample and the requirement that heat only enters or leaves the sample through the phonon system, therefore the magnon heat flux must be zero at both ends. The magnon temperature is found to be

$$T_m(x) = T_0 - \frac{Q}{\kappa_T}\left(x - \frac{\sinh Ax}{A\cosh\frac{1}{2}AL}\right). \tag{3.24}$$

By substituting this expression into equation 3.21 the phonon temperature can be expressed as

$$T_l(x) = T_0 - \frac{Q}{\kappa_T}\left(x + \frac{\kappa_m}{\kappa_l}\frac{\sinh Ax}{A\cosh\frac{1}{2}AL}\right). \tag{3.25}$$

The parameter A is related to the coupling between magnons and phonons. If they are perfectly coupled, $\tau_{ml} = 0$ and $A = \infty$. In this limit the magnon and phonon temperatures are the same. In the other limit, $\tau_{ml} = \infty$, $A = 0$ and the magnon temperature is constant over the whole interval and equal to T_0.

Now the measured, *effective*, thermal conductivity κ_{eff} is given by

$$\kappa_{\text{eff}} = -QL/\Delta T_l, \tag{3.26}$$

which, with $\Delta T_l = T_l - T_0$ from equation 3.25, is given by

$$\kappa_{\text{eff}} = (\kappa_l + \kappa_m)\left(1 + \frac{\kappa_m}{\kappa_l}\frac{tanh\ \frac{1}{2}AL}{\frac{1}{2}AL}\right)^{-1}. \tag{3.27}$$

3.2.2 Dynamic solution for flash method

It is possible to derive from the formalism explained in section 3.2 an analytical formula similar to Parker's formula for two types of heat carriers taking into account the thermalization time. In this derivation isolation boundary conditions are assumed, i.e.

$$\frac{\partial T_{l,m}}{\partial z} \mid_{z=0} = \frac{\partial T_{l,m}}{\partial z} \mid_{z=L} = 0.$$

The initial condition is a step function

$$T_{l,m}(z,0) = \begin{cases} \Delta T_{l,m} & 0 < z < \mu \\ 0 & \mu < z < L \end{cases}$$

where $\mu << L$ is the skin depth. Now the two temperatures can be expanded in a Fourier series over the interval $[0, L]$. The boundary conditions are only fulfilled for a selection of all terms, which gives a restriction on the possible wavenumbers. The two coupled differential equations can now be expressed in the Fourier series and the 2x2 matrix eigenvalues can be found. Then from the boundary conditions the solution for the lattice temperature versus time at $x = L$ is found to be

$$T_l(L,t) = \frac{\mu}{L}\frac{\Delta T_m + \alpha/\beta \Delta T_l}{1+\alpha/\beta} - \frac{\mu}{L}\frac{\Delta T_m - \Delta T_l}{1+\alpha/\beta} e^{-(\alpha+\beta)t} + \frac{\mu}{L}\sum_{n=1}^{\infty}(-1)^n \, cos\frac{\pi\mu n}{2L} \, sinc\frac{\pi\mu n}{2L}$$
$$\left\{ \left[\left(1 - \frac{G_n}{\phi_n} \right) \Delta T_l - \frac{2\beta}{\phi_n}\Delta T_m \right] e^{-(F_n+\phi_n)\frac{t}{2}} + \left[\left(1 \frac{G_n}{\phi_n} \right) \Delta T_l + \frac{2\beta}{\phi_n}\Delta T_m \right] e^{-(F_n-\phi_n)\frac{t}{2}} \right\} \tag{3.28}$$

where

$$\begin{aligned} G_n &= \alpha - \beta - (\delta - \gamma)n^2 \\ F_n &= \alpha + \beta + (\delta + \gamma)n^2 \\ \phi_n &= \sqrt{\alpha^2 + 2\alpha\left[\beta + (\gamma - \delta)n^2\right] + \left[\beta - (\gamma - \delta)n^2\right]^2} \\ \alpha &= \frac{g}{c_m}, \beta = \frac{g}{c_l}, \delta = \frac{\kappa_l}{c_l}, \gamma = \frac{\kappa_m}{c_m}. \end{aligned} \tag{3.29}$$

In the limit of $g \to 0$ (g is the conversion rate between different types of particles) this formula reduces to Parker's formula 3.13.

3.3 Heat transport in low dimensional quantum magnets

The most widely used approach to describe heat transport in quantum many body systems is the calculation of transport coefficients via time-dependent current-current correlation functions, as was first done by Kubo [91]. In this formalism, the real part

of the thermal conductivity κ at a finite frequency ω can be decomposed into a dc part and a frequency dependent part [46]:

$$Re\,\kappa(\omega) = D_{th}\delta(\omega) + \kappa_{reg}(\omega), \tag{3.30}$$

where the weight of the singular part D_{th} is the so-called thermal Drude weight. The experimentally accessible quantity in a steady state experiment is the dc conductivity $Re\kappa(\omega \to 0)$. In a dynamic experiment the ac conductivity is accessible too. A nonzero D_{th} implies a nondecaying energy current and therefore ballistic heat transport. With this equation several situations can be described:

- thermal insulators if $D_{th}(\mathrm{T}) = 0$ and $\kappa_{reg}(\omega, T) = 0$;
- conventional thermal conductors if $D_{th}(T) = 0$ and $\kappa_{reg}(\omega, T) > 0$;
- ideal thermal conductors if $D_{th}(\mathrm{T}) > 0$ for any value of $\kappa_{reg}(\omega, T)$.

An experimentally observed, anomalously large dc thermal conductivity can be due to ballistic transport or to anomalously large values of $\kappa_{reg}(\omega)$ for low ω due to slowly decaying energy currents. In any real system, perturbations such as phonons and defects have to be taken into account. Then the model cannot be solved exactly. As an approximation, one assumes broadening of the Drude weight. Therefore, only a comparison of experimental data with theoretical calculations, taking into account both the dc part and the frequency dependent part of the conductivity spectrum, can give insight in the type of transport present in the system.

In experimental analysis, the most widely used way to separate the thermal conductivity due to magnetic excitations κ_m from the lattice contribution κ_l is by assuming that κ_l is isotropic, while κ_m is only present along the ladder or chain. Then by measuring two different directions, one parallel and one perpendicular to the ladder or chain, it is possible to distinguish different contributions. This method only works well if the thermal conductivity due to electrons κ_e is absent or small and if κ_m is comparable to or larger than κ_l [46]. For the spin chain and the spin ladder compound described in this thesis these requirements are met for all temperatures above 50 K.

3.4 Scattering mechanisms

When one considers a defect-free crystal of infinite size with non-interacting excitations, the lattice excitations (phonons) are described by a system of coupled harmonic oscillators. In such case an infinite thermal conductivity could be ascribed to the phonons (although it could not be measured directly since in order to measure the phonons have to interact with the measuring tool), because the phononic states remain stationary in a harmonic potential, and therefore the distribution of phonons is constant over time and thus the heat current is never changed. Such a situation is, however, not found in nature, because in every material phonons scatter, thereby making the thermal conductivity finite. Scattering can occur from different types of crystal defects or from the crystal surface. These processes do not depend on temperature. Furthermore, there is Umklapp scattering between two particles. When these have such high momentum

that the sum of the two is so large that it lies outside the first Brillouin zone, the total wavevector is changed and effectively transformed back to the first Brillouin zone, thereby changing the momentum. This process depends strongly on the amount of particles and therefore on temperature. When this process is dominant, the thermal conductivity depends on temperature as 1/T. For both phonons and magnons, at low T scattering from defects is the most important process, while at higher T Umklapp scattering becomes dominant.

Magnetic defects are major scattering centers for magnetic excitations. The effect of these has been studied, for example, by introducing defects in the material and compare the mean free path or thermal conductivity with that of the pure compound [19, 38, 33, 31]. Furthermore, at not too low temperatures, magnetic excitations can scatter with phonons, other magnetic excitations or charge carriers. In the spin ladder family $(Ca,La,Sr)_{14}Cu_{24}O_{41}$ also mobile holes are present in the ladder structure, which can act as scattering centers. The concentration of them depends on the exact chemical composition.

The mean free path, giving insight in the scattering behaviour of the magnetic excitations, can be calculated from the measured thermal conductivity using the kinetic equation

$$\kappa_m(T) = c_m(T)v_m(T)l_m(T), \tag{3.31}$$

where v_m is the mean velocity and c_m is the specific heat of the magnetic excitations. The mean free path is related to the relaxation time τ by $l_m = v_m\tau$. To get the total $\kappa_m(T)$ one has to sum over all the magnetic excitations in the material. If one assumes that the different scattering mechanisms act independently of each other, a good approximation for the mean free path is

$$l_m^{-1}(k,T) = \sum_i l_{m,i}^{-1}(k,T), \tag{3.32}$$

where each term corresponds to an independent scattering channel which depends on momentum k and temperature T. To make the analysis easier, it is usually assumed that the scattering rates are k-independent, even though this is not necessarily true. When doing so, equation 3.31 can be used to estimate the value and temperature dependence of the average mean free path.

For applications one would like to have a way to control the size of the heat flow by changing the thermal conductivity. From equation 3.31 it is seen that the thermal conductivity will go up when one increases the speed of the heat carriers, the mean free path and/or the specific heat. Several ways of doing so are possible; for example by creating more heat carriers through direct optical pumping, or changing the mean free path by changing the temperature or the amount of scattering centers. It has been measured that, although partially quenching the thermal conductivity peak at low temperature, doping with non-magnetic calcium ions does not influence the room temperature thermal conductivity [92, 93]. However, magnetic impurities do, because they introduce additional scattering centers. Therefore, doping with magnetic defects which can be switched on and off potentially makes tuning of the thermal conductivity achievable [50, 94]. In such case one could use low spin ($S = 0$)/high spin ($S \neq 0$) switchable magnetic impurities, e.g. Co or Fe, to control the magnetic heat transport in these materials. These ions have split d-orbitals which can be occupied in different

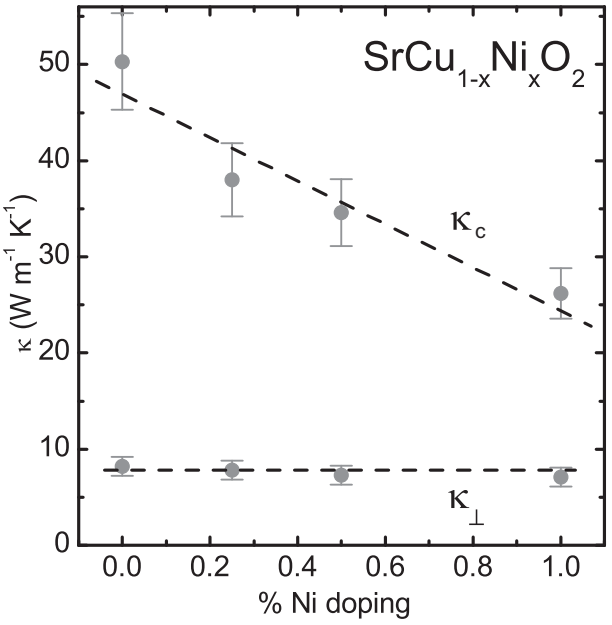

Figure 3.2: Doping dependence of the thermal conductivity κ of the spin chain compound $SrCu_xNi_{1-x}O_2$ obtained using a steady state method. The dashed lines are guides to the eye. Only the spinon transport parallel to the chains is influenced by the Ni doping.

ways depending on the gap between the levels and the interelectronic repulsive energy. One of the configurations has a low spin, while the other has a high spin. Switching between states can be achieved by an optical or magnetic pulse.

The steady state thermal conductivity κ of $SrCuO_2$ with Ni doping ($S = 1$) as a function of doping is shown in figure 3.2. This measurement was performed by N. Hlubek at the IFW Dresden. The motivation for this measurement is twofold. First, the influence of magnetic impurities on the thermal conductivity at room temperature has to be investigated to test the feasibility of a switchable thermal conductivity. Second, in this work the results obtained are compared with measurements on samples from the same batch done with the dynamic fluorescent flash method (described in section 6.3.1) to see the effect of a variable heat source on the thermal conductivity. As expected, κ_c (parallel to the chain) is substantially higher than $\kappa_\perp$ (perpendicular to the chain) due the contribution of anisotropic spinon transport which dominates over the phonon contributions near room temperature [7, 34]. The extreme sensitivity to magnetic impurities is evidenced by the strong decrease of κ_c upon doping: even a small amount of 1% Ni reduces κ_c by a factor of two, while $\kappa_\perp$ is insensitive to Ni doping.

Ballistic transport can be defined in several ways. One is that the mean free path of the excitations in the sample is only limited by the sample dimensions. However, this was never found in experiments on spin ladders or spin chains. It was found, however, for other materials like LiF [95]. A more appropriate definition, which does not rely on the quasi-particle approach, is given by the presence of nondecaying contributions to the energy current which is equivalent with a nonzero Drude weight, as was discussed in the beginning of this section. If one wants to use this criterion, one has to demonstrate

that the measured κ_m exceeds the value of κ_{reg} in equation 3.30. Comparison of data for different spin chains and spin ladders with a calculated high-temperature limit of κ_{reg} suggest that for spin ladders intrinsic diffusion is the dominant process, while for spin chains it is ballistic and only limited by external perturbations. This is in agreement with theoretical predictions and simulations [4, 49, 96].

3.5 Thermal conductivity of the spin chain $SrCuO_2$

The thermal conductivity of $SrCuO_2$ as a function of temperature is shown in figure 3.3 [34]. It is measured by a conventional steady state method, in which a steady heat current flows through a brick-like sample, such that the simple equation 3.10 can be used to extract the thermal conductivity. These measurements were performed by our collaborators from the IFW Dresden. It is seen that along the chain at all temperatures above T $\approx$ 20 K the spinon contribution to the thermal conductivity is much larger than the phonon contribution. Furthermore, the phonon contribution is assumed to be isotropic, making the separation of the two contributions possible. The general behaviour of the thermal conductivity as a function of temperature can be understood in the following way: at low temperature an increase of the thermal conductivity with temperature is seen which is due to the increased amount of heat carriers (phonons, spinons) by thermal activation. As the amount of heat carriers increases, also the contribution of Umklapp scattering increases, leading to two competing processes, therefore giving a peak at a certain temperature. The exact position of the peak depends on the energy of the excitations and the exact dependence of the scattering processes on temperature. For $SrCuO_2$ the magnon and phonon thermal conductivity maximum nearly overlap. In the data there is a clear difference between samples of 99% purity (2N) and of 99.99% purity (4N). From the thermal conductivities for different purities the mean free path can be determined. It is as large as 1.5 μm for the 4N sample but only 0.3 μm for the 2N sample at low temperature, indicating that the thermal conductivity is only limited by extrinsic scattering processes. This shows the ballistic nature of the heat transport, as predicted by theory and simulations.

3.6 Thermal conductivity of the spin ladders $Ca_9La_5Cu_{24}O_{41}$ and $Sr_{10}La_4Cu_{24}O_{41}$

The thermal conductivity of $Ca_9La_5Cu_{24}O_{41}$ and $Sr_{10}La_4Cu_{24}O_{41}$ as a function of temperature, measured by a conventional steady state method is shown in figure 3.4 [6]. These measurements were performed by our collaborators from the IFW Dresden. It is seen that along the ladder at every temperature above T $\approx$ 50 K the magnon contribution to the thermal conductivity is much larger than the phonon contribution, making the separation of the two contributions possible (again assuming that the phonon contribution is isotropic). For the perpendicular thermal conductivity, for $Ca_9La_5Cu_{24}O_{41}$ the a-direction is measured, while for $Sr_{10}La_4Cu_{24}O_{41}$ the b-direction is measured, which is usually about 50 % lower. From the thermal conductivity the mean free path can be determined. It is as large as 0.3 μm at low temperature for $Ca_9La_5Cu_{24}O_{41}$ [6]. Because the peak in κ_c lies at lower temperature for $Sr_{10}La_4Cu_{24}O_{41}$, it is likely that

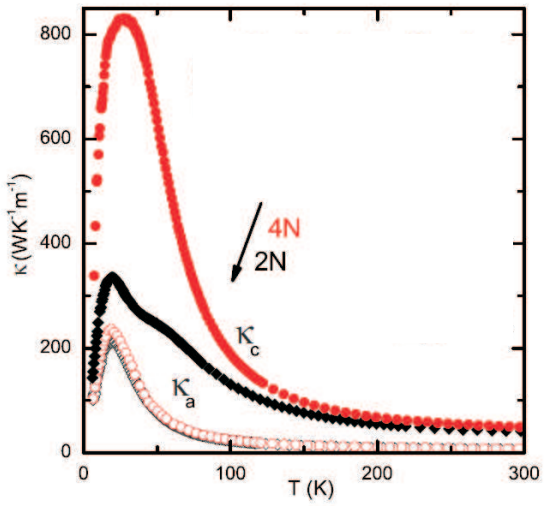

Figure 3.3: Thermal conductivity of the spin chain compound $SrCuO_2$ as a function of temperature. The c-direction is parallel to the chains and has a contribution from both phonons and spinons. The a-direction is perpendicular to the chains and only has a phonon contribution. 2N indicates a sample purity of 99% and 4N indicates a sample purity of 99.99 %. Picture taken from [34].

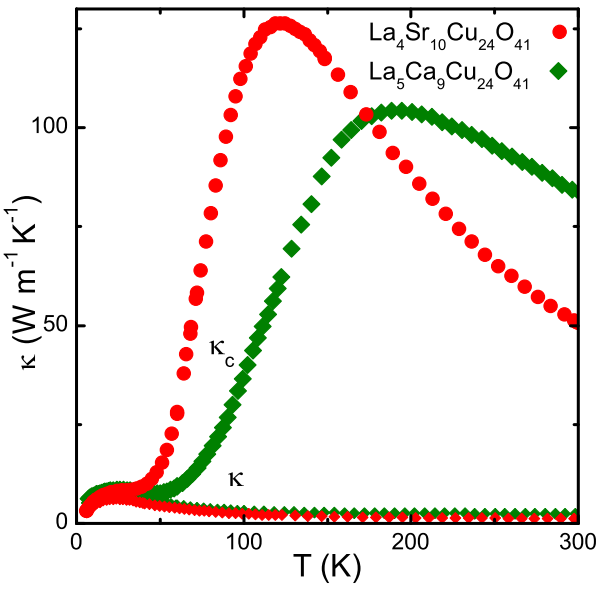

Figure 3.4: Thermal conductivity of the spin ladder compounds $Ca_9La_5Cu_{24}O_{41}$ (green) and $Sr_{10}La_4Cu_{24}O_{41}$ (red) as a function of temperature. The c-direction is parallel to the ladder and has a contribution from both phonons and magnons. The a-direction and b-direction are perpendicular to the ladder and only have a phonon contribution. Measurements performed by N.Hlubek, IFW Dresden.

the scattering processes are stronger and the mean free path somewhat shorter. In the spin ladders the long mean free path is not due to ballistic transport, but is caused by the low scattering probability between magnons and other excitations and defects [9]. The main phonon branches important for magnon-phonon scattering are the optical braches at 38 and 73 meV, respectively [47], which are only weakly populated for the full temperature range measured.

Comparing the spin ladders to the spin chain, it is seen that the magnetic contribution to the heat transport is higher at room temperature for the ladders, especially for $Ca_9La_5Cu_{24}O_{41}$. Therefore, for practical applications these materials are more promising. The spin chain however shows a much higher peak value of the thermal conductivity, which lies unfortunately at too low temperature to be interesting for most applications. The phonon thermal conductivity peaks at low temperature (~ 30 Kelvin) and is very low at room temperature. Therefore, at elevated temperatures there is a high anisotropy between the directions perpendicular and parallel to the ladder/chain.

4. Experimental methods

In this chapter the details of the experimental procedures and setups used will be described in detail. The data obtained in the experiments, together with the analysis and discussion, will be presented in the next chapters.

4.1 Materials

4.1.1 Sample preparation

Single crystals were grown by the traveling solvent floating zone method [97, 10]. This was done by our collaborators from the Laboratoire de Physico-Chimie de l'Etat Solide at the Université Paris Sud. In this method, two rods of the material (seed and feed) are melted using a laser directed with mirrors. In order to ensure homogeneity of the melt, both rods are counter-rotating. Via a vertical movement of the rods, the melting zone travels through the rod. This leads to a directional solidification and crystallisation. Impurities usually stay within the melt or stay at the surface of the crystal and can therefore easily be removed. Control and optimization of the crystal growth is done by supervising and adapting the growth parameters such as the type of gas and the pressure of the gas, speed of rotation, speed of pulling, composition of the rods and temperature of the melt.

For the spin ladder $Ca_9La_5Cu_{24}O_{41}$ one starts with powders of La_2O_3 (Alfa Aesar), $CaCO_3$ (Alfa Aesar), and CuO (Chempur), from which feed rods are prepared. The batch of stoichiometrically mixed powders are pelletized and annealed at 900 degrees for 24 h. The material is reground, treated at 950 degrees for 24 h, and hydrostatically pressed at 2500 bar and sintered in air at 950 degrees for another 24 h. Steady state conditions can be reached from the very beginning of the growth experiment by (in addition to this polycrystalline feed) using support rods with the same composition and placing between them a pellet of solvent, composed of 70 Mole % CuO and 30 Mole % SrO, which is equal in weight to the future molten zone. The starting crystal and feed rod are rotated in opposite directions at 40 rpm, leading to a growth rate of 1 mm/h. A picture of the sample is shown in figure 4.1. For $SrCuO_2$, as is shown in figure 4.2, the starting material was prepared by a solid state reaction of stoichiometric amounts of $SrCO_3$, $CaCO_3$. The material was thermally treated several times (around 4 times) at 900 degrees for 24 h. The pellet of solvent was composed of CuO.

Thin platelets (0.4 to 3.5 mm) were cut by a wire saw or a blade saw and polished from single crystals of the spin ladders $Ca_9La_5Cu_{24}O_{41}$ and $Sr_{10}La_4Cu_{24}O_{41}$ (both 99.99 % pure, 4N), and the spin chain $SrCuO_2$ (99.99 and 99.9999 % pure, 4N and 6N). Surface polishing was done in several ways. Most samples were polished by hand

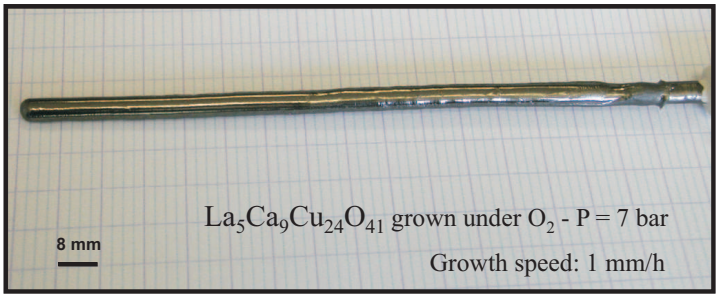

Figure 4.1: $Ca_9La_5Cu_{24}O_{41}$ single crystal grown by the travelling floating zone method.

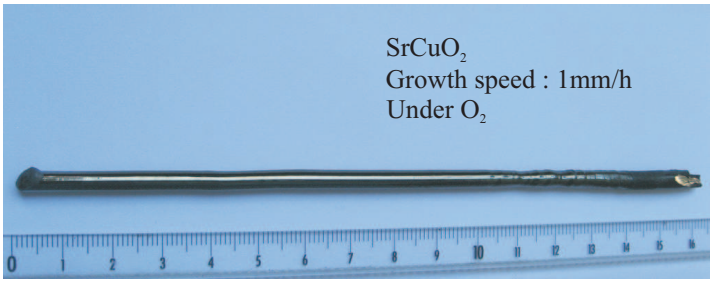

Figure 4.2: $SrCuO_2$ single crystal grown by the travelling floating zone method.

with SiC paper, which led to a RMS roughness of about 1 μm. When a flat surface was critical for the measurement, the surface was machine polished by SiC paper (5 μm grains) and subsequently by a cloth with 1 μm diamond suspension. The surface roughness was measured by a confocal microscope. By careful polishing the surface RMS roughness of the well-polished $Ca_9La_5Cu_{24}O_{41}$ sample was brought down to only 20 nm.

4.1.2 Sample characterization

Different characterization measurements have been performed on the single crystals. All data are acquired by our collaborators from the Laboratoire de Physico-Chimie de l'Etat Solide at the Université Paris Sud. After growing the crystals, Energy-Dispersive X-ray spectroscopy (EDX) was performed for elemental analysis. The pattern is shown in figure 4.3 for $Ca_9La_5Cu_{24}O_{41}$. From the analysis of the data it was found that there are 8 % La-vacancies present in the material. For $SrCuO_2$ the data is shown in figure 4.4. No vacancies are found.

After that, powder X-ray diffraction was performed, as is shown in figure 4.5 for $Ca_9La_5Cu_{24}O_{41}$. All reflections could be indexed using four indices in order to take into account the two sublattices of the ladder and the chain part of the crystal structure, where the third index belongs to the ladder sublattice and the fourth to the chain sublattice. The pattern is shown in figure 4.6 for $SrCuO_2$. The lattice parameters obtained from the analysis of this data are in agreement with literature. From these measurements it is seen that good quality single crystals are grown.

The steady state thermal conductivity along different crystallographic axes as a function of temperature was measured by our collaborators at the IFW Dresden. The data for both the spin chain and the spin ladder were shown in section 3.5 and 3.6,

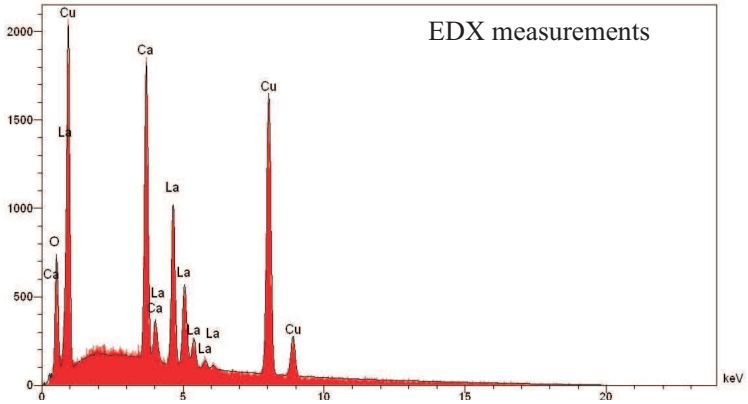

Figure 4.3: EDX measurement for the spin ladder $Ca_9La_5Cu_{24}O_{41}$. From the elemental analysis based on this data it is found that there are La-vacancies present in the lattice.

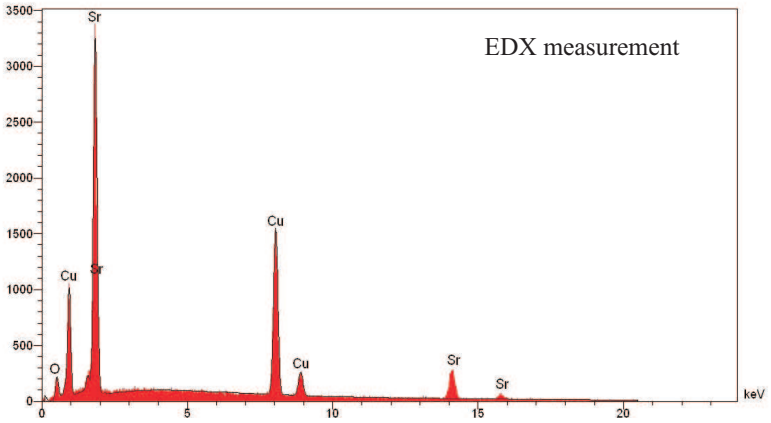

Figure 4.4: EDX measurement for the spin chain $SrCuO_2$. No lattice vacancies are found.

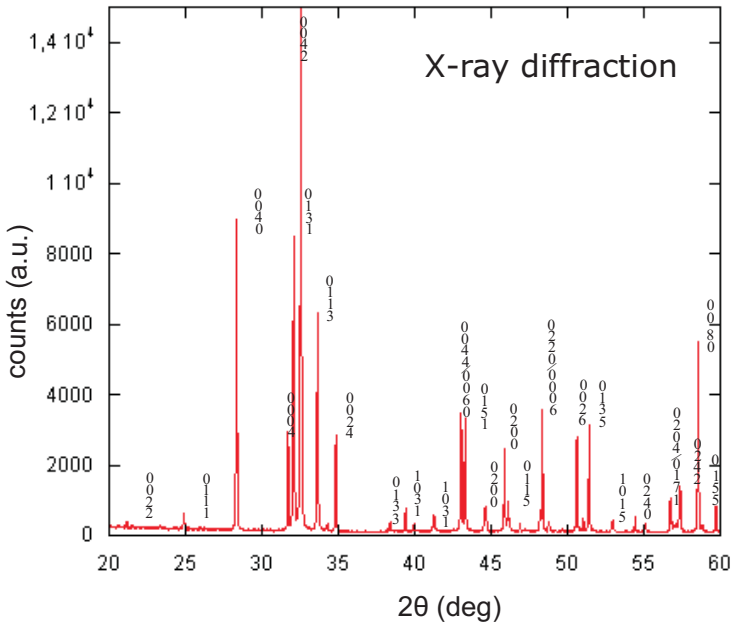

Figure 4.5: X-ray powder diffraction pattern for the spin ladder $Ca_9La_5Cu_{24}O_{41}$. Peaks coming from the chain and ladder sublattices and the overall lattice are observed. The structural analysis based on this data gives lattice parameters in agreement with literature [80].

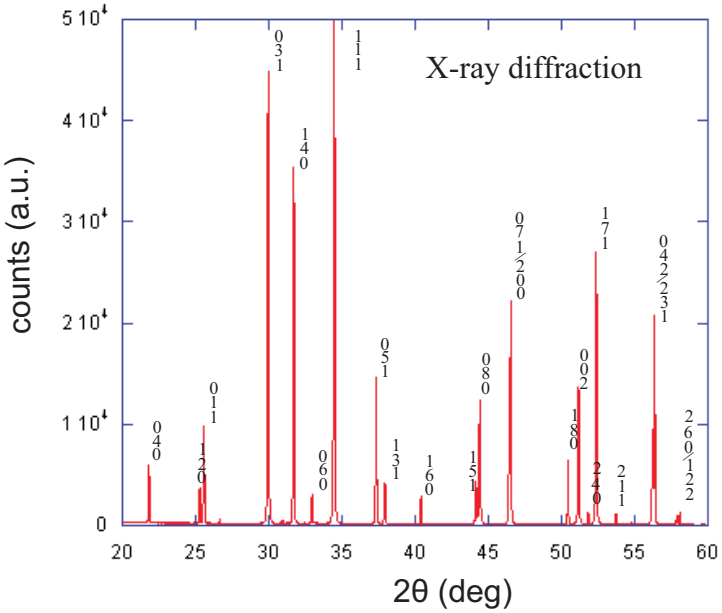

Figure 4.6: X-ray powder diffraction pattern for the spin chain $SrCuO_2$ for different temperatures. The structural analysis based on this data gives lattice parameters in agreement with literature [67].

respectively.

Furthermore, Raman measurements were performed on both spin chain and spin ladder crystals. The Raman measurements were performed in a backscattering configuration, using a three-grating micro-Raman spectrometer (T64000 Jobin Yvon) equipped with a liquid nitrogen-cooled charged coupled device (CCD) detector. The frequency resolution was better that 1 cm^{-1} for the frequency region considered. The samples were placed in an optical microscope cryostat. The temperature was kept at 4.5 K with the aid of RhFe resistor which was placed near the sample. Also, measurements were performed outside the cryostat at room temperature. The scattering was excited by the second harmonic light of a Nd:YVO4 laser (532 nm CW) or a Krypton laser (674 nm CW), focused down to $\sim$30 μm^2 with the power density on the sample kept below 0.1 $mW/\mu m^2$. The polarization was controlled both on the incoming and outgoing beams, making all polarization combinations possible. All measurements were done with cc or aa polarization.

Raman data for both cc and aa polarization for $SrCuO_2$ are shown in figure 4.7. For the cc polarization, 674 nm light is used since for this wavelength the excitation is below the bandgap, leading to a lower electronic background. The data are taken at room temperature. The spectra look very similar to published data [98], and the different peaks can be assigned accordingly. There are two almost degenerate A_g oxygen modes (543 and 558 cm^{-1}) seen in the cc spectrum. At 188 cm^{-1} the Sr vibration is found. It is visible in the aa configuration too. At 262 cm^{-1} lies the Cu ion vibration. It is only seen in the cc-oriented measurements. Furthermore, peaks are seen at 430 cm^{-1}, 900 cm^{-1}, and 1400 cm^{-1} for cc polarization. Those might be ascribed to phonons, coupled to an exchange term (the motion of an electron along the chain is correlated with that of others). Another explanation, given for a similar compound [99], is that those peaks are due to resonantly enhanced two-phonon scattering. The 2-magnon peak is expected to lie around 4600 cm^{-1}. Unfortunately in this range no unambiguous sign of this peak was observed in the experiment.

The Raman spectra for cc and aa polarization for $Sr_{10}La_4Cu_{24}O_{41}$ are shown in figure 4.8. The spectra are very similar to what is reported in literature [42], and the different peaks are assigned accordingly. For the cc polarization, there are modes at 176 cm^{-1}, which is most probably the vibration of Sr-ions, and at 573 cm^{-1}, which is caused by chain oxygen vibration. For the aa-polarization, a mode is seen at 180 cm^{-1} and a weak one at 555 cm^{-1}. These peaks probably have the same origin as for the cc-polarization. At low temperatures for cc polarization the phonon modes narrow and some additional modes appear. An important difference is that now the 2-magnon peak can be seen in the cc-polarization around 2760 cm^{-1}, as is shown in figure 4.9. This is a bit lower than for other similar compounds, which usually have this peak around 2900 cm^{-1}.

For the spin ladder $Ca_9La_5Cu_{24}O_{41}$, the low temperature Raman spectrum for the cc polarization is shown in figure 4.10. The spectrum for $Sr_{10}La_4Cu_{24}O_{41}$ is shown for comparison. It is seen that they are the same, and therefore the peaks are assigned similarly. Several experiments were performed to observe the 2-magnon peak around 2900 cm^{-1}, but unfortunately no reproducible signature was found. This is probably due to the low intensity of this peak, together with its position in a range for which the Raman setup is not optimized.

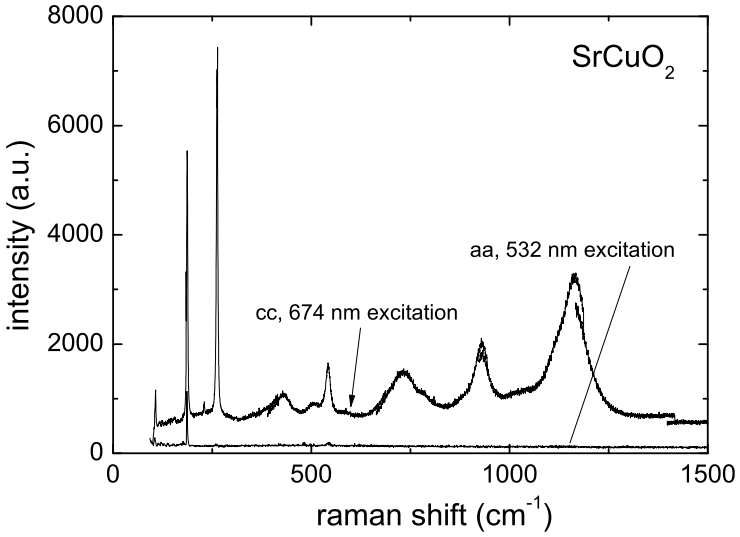

Figure 4.7: Raman measurements at room temperature for cc and aa polarization on the spin chain compound $SrCuO_2$.

Furthermore, the infrared (IR) transmission spectrum of a 82 μm thick $Ca_9La_5Cu_{24}O_{41}$ single crystal has been measured by means of Fourier Transform Infrared (FTIR) spectroscopy in the 1000-6000 cm^{-1} wavenumber range. In this technique a broad band IR source continuously irradiates the sample. By comparing the interference spectrum from a reference measurement (without sample) with the sample measurement and taking the Fourier Transform, the absorption spectrum over a wide range of wavelengths can be obtained at once. The data are shown and discussed in section 8.1. They are in agreement with data published in literature [47, 27].

4.2 Description of experiments

4.2.1 Optical temperature detection

Following a slightly modified version of the procedure invented by Kolodner *et al.* [100], a solution of 3 wt% deuterated PMMA and 2 wt% rare-earth chelate europium thenoyltrifluoroacetonate (EuTTA, Acros Organics) in chlorobenzene was prepared and spincoated onto the samples, resulting in a thin ($\sim$ 400 nm) layer of EuTTA/PMMA on the back side of the platelets. This layer is acting as a thermometer for the sample surface temperature.

An optical excitation of TTA molecules in a wide band around 345 nm results in intersystem crossing and energy transfer to the Eu^{3+}-ions, populating the f and d levels. Finally, the Eu^{3+}-ions emit at several wavelengths corresponding to transitions from their f and d levels, which is strongest at 612 nm (Eu^{3+} 5d level) [101]. The measured absorption spectrum is shown in figure 4.11. The sequence of processes is shown in figure 4.12. The overall quantum efficiency of the EuTTA layer photoluminescence decreases monotonically with temperature in the interval from 273 to $\sim$ 330 K, as a

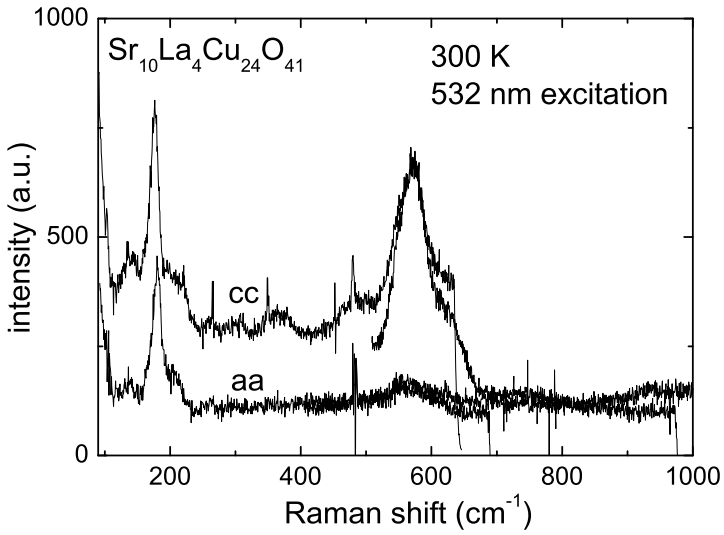

Figure 4.8: Raman measurements at room temperature for cc and aa polarization on the spin ladder compound $Sr_{10}La_4Cu_{24}O_{41}$.

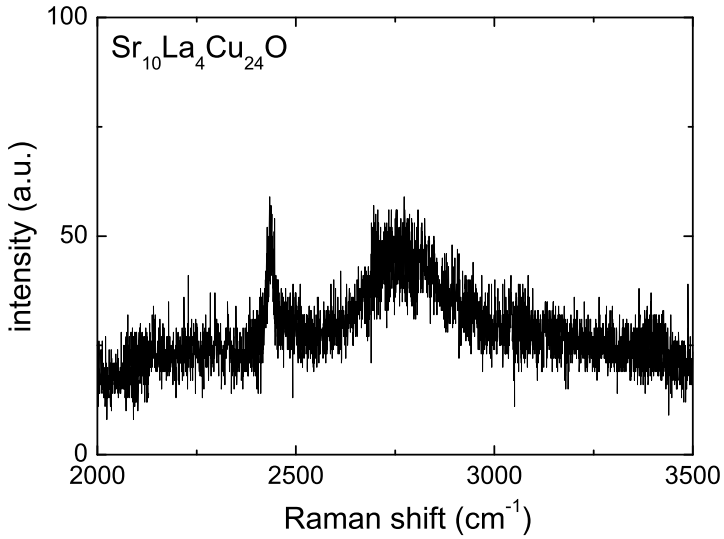

Figure 4.9: Raman measurements at 4.5 K for cc polarization on the spin ladder compound $Sr_{10}La_4Cu_{24}O_{41}$. The 2-magnon peak is observed at 2760 cm^{-1}.

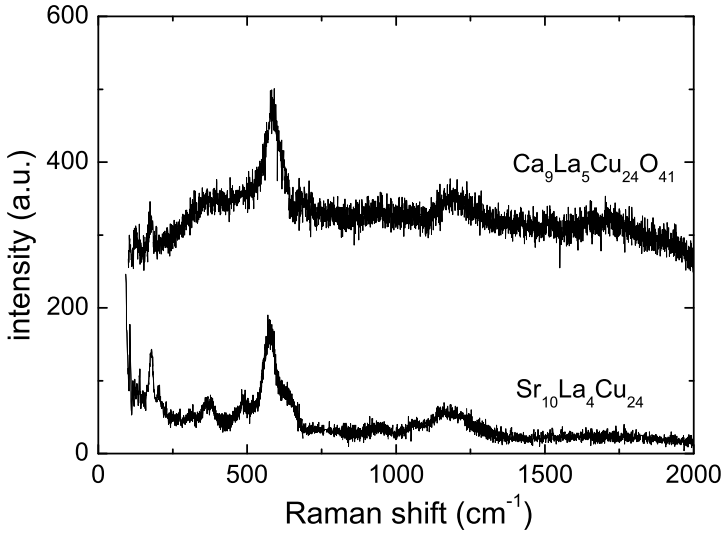

Figure 4.10: Raman measurements at 4.5 K for cc polarization on the spin ladder compound $Ca_9La_5Cu_{24}O_{41}$. The data for $Sr_{10}La_4Cu_{24}O_{41}$ is shown for comparison.

result of thermal activation of non-radiative decay processes from the emitting Eu^{3+} 5d level (612 nm) to the Eu^{3+} 7f manifold [102]. Also within the Eu^{3+}-ion there are losses due to non-radiative processes to the ground state [103].

The efficiency decrease between 294 and 340 K was determined by calibration. In the calibration experiment a sample was put under a steel cover on a hot plate. With a temperature sensor the temperature under the cover was measured and for several temperatures the intensity of the EuTTA layer was determined. The general behaviour can be described by the function $I(T) = A + Be^{-CT}$ [104]. The coefficient C is determined from the measurement of $I(T)$ over the range of temperatures of interest. Then by taking the natural logarithm of the function $I(T)/I(T_{\text{cold}})$, where $I(T_{\text{cold}})$ is the intensity at the lowest temperature (in our case room temperature), and fitting the data with a straight line, the slope of this line gives the efficiency decrease C. The measured calibration curve is shown in figure 4.13. The efficiency decrease was found to be around 4.4 % K^{-1}. This is approximately twice larger than that of a EuTTA/non-deuterated-PMMA layer, showing that the coupling to the environment influences the ratio between radiative and non-radiative processes in EuTTA. Furthermore, the working range can be extended below room temperature. In such case, over the large temperature range for which the compound can be used, the sensitivity is not constant. Therefore, at every temperature the percentage change per Kelvin has to be determined. It was found that EuTTA can be used down to 130 K.

For even lower temperature measurements, EuTTA is not suitable, because below 120 K the fluorescence intensity is reaching the maximum level and the temperature sensitivity is (nearly) zero. Therefore, another compound with similar properties has to be used. Europium tris[3-fluoromethylhydroxymethylene-(+)-camphorate] (EuTFC, Sigma-Aldrich) was chosen because it has the largest temperature sensitivity in the range from 0 to 150 K [105]. The temperature sensitivity occurs due to the same

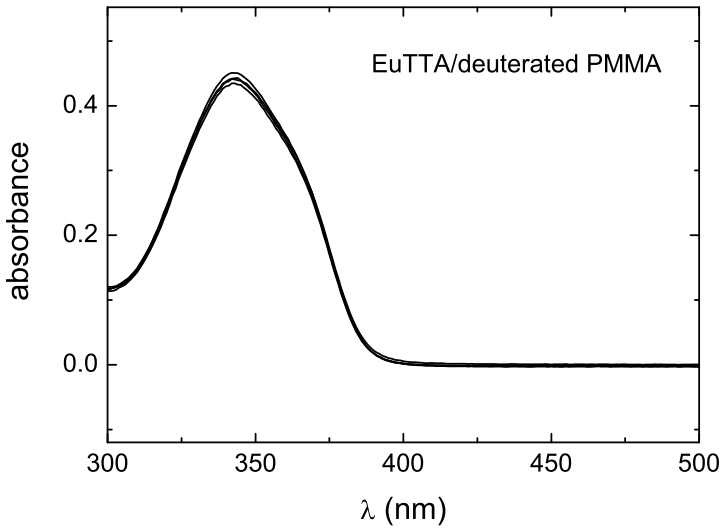

Figure 4.11: Absorption spectrum of a spin-coated layer of EuTTA/deuterated PMMA. Every different line represents a measurement on a different sample. The wide absorption band around 345 nm is clearly seen. Furthermore, the absorption band is well separated from the emission peak at 613 nm, making the separation of the two processes possible.

reasons as for EuTTA, however, the absorption band maximum for TFC lies around 300 nm. Although based on literature a matrix of PMMA should give the highest temperature sensitivity [106], this was not seen in test measurements. Therefore a matrix of polystyrene (PS) is used instead. A solution of 3 wt% PS and 2 wt% EuTFC in chlorobenzene was prepared and spincoated onto the samples, resulting in a thin ($\sim$ 400 nm) layer of EuTTA/PS on the back side of the platelets. The measured calibration curve is shown in figure 4.14. Since the temperature sensitivity is less than for EuTTA, the range over which the compound can be used is larger. However, this comes at the cost of a lower accuracy with which the temperature change can be determined.

4.2.2 Fluorescent flash method

In the fluorescent flash method (FFM), of which the setup is shown in figure 4.15, a heat pulse was provided by a YAG laser operating at 1064 nm and 60 μs (fundamental frequency, free run mode) for the spin ladders or 532 nm and 5 ns (SHG, Q-switch mode) for the spin chains at the front surface of the sample. A 360 nm UV LED (250 mW max, used at approximately 50 mW) was used to excite the EuTTA layer, spin coated onto the back side of the sample. For low temperature measurement, an optical fiber is used to guide the 300 nm third harmonic of a Ti:Sapphire laser to the optical table where the YAG is standing. The fiber output is a nearly collimated 7 mW pulse train which excites the EuTFC layer. The photoluminescence was detected by a GaAsP photodiode with a 610 $\pm$ 10 nm interference filter in front of it to filter out all background light, digitized and stored in a computer that also triggers the heating laser pulse. Because the heating pulse has a very high intensity, always a little bit

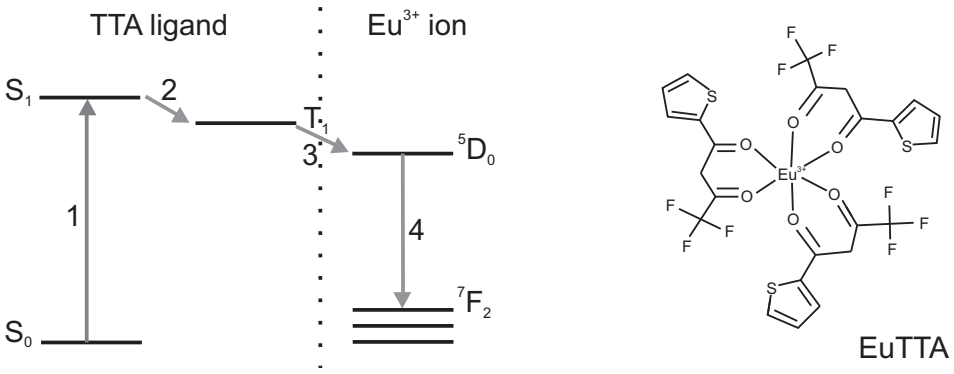

Figure 4.12: Excitation and fluorescence mechanism in EuTTA. 1) The TTA-ligand is excited by UV light with a wavelength around 345 nm. 2) Intersystem crossing to the triplet state, from which relaxation to the TTA ground state is dipole forbidden. 3) Energy transfer from the TTA-ligand to the Eu^{3+} ion. The efficiency of this process depends on temperature, because there is a competition with temperature dependent non-radiative processes. 4) Phosphorescence within the Eu^{3+} ion from the excited state to the ground state. Also here there is competition with non-radiative processes. It has been measured that the total time for steps 1-3 to take place is < 100 ns, therefore on the timescale of the experiment it can be assumed to be instantaneous [107]. On the right the EuTTA molecule is depicted.

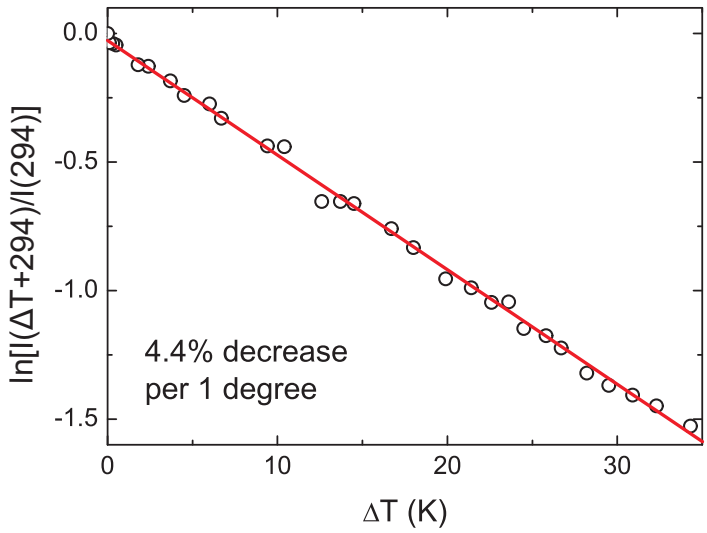

Figure 4.13: Measured calibration curve for EuTTA. $\Delta T = 0$ corresponds to room temperature (294 K). Shown is the logarithm of the relative change when the temperature increases. The best fit gives an intensity decrease of 4.4 % per degree Kelvin temperature increase.

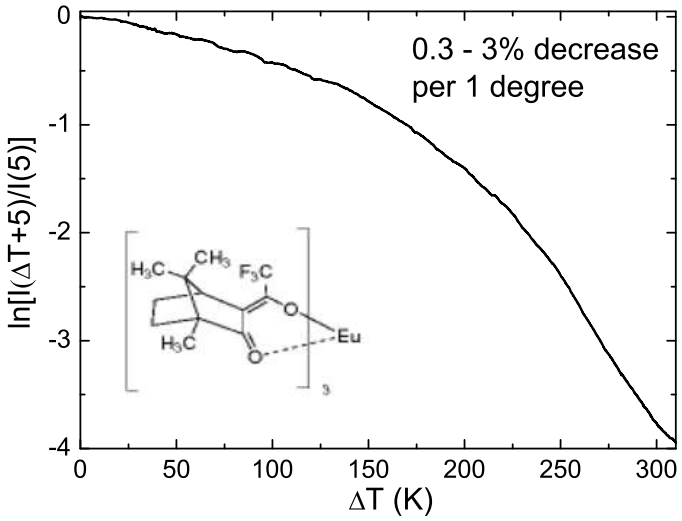

Figure 4.14: Measured calibration curve for EuTFC. $\Delta T = 0$ corresponds to the lowest temperature reached (5 K). Shown is the logarithm of the relative change when the temperature increases. The intensity decrease per degree Kelvin temperature increase is not equal at every temperature. It is found to vary between 0.3 and 3 %.

of light is collected on the detector, thereby allowing to determine the exact zero in time. Then, the temperature increase has been determined using the calibration data. For the low-temperature measurements the sample was placed in a helium flow-cryostat with a temperature controller. The mean values and standard deviations were obtained by averaging of at least hundred measurements.

A room temperature test measurement was done on a nickel single crystal. Nickel was chosen because it is a well-documented material of which the thermal conductivity at room temperature is 90.9 W m^{-1} K^{-1} which is very close to that of the spin ladder compound $Ca_9La_5Cu_{24}O_{41}$. The data is shown in figure 4.16 and the best fit gives a value for the thermal conductivity which is in agreement with literature [108]. The details about the model are explained in section 3.1.2. Other tests have been performed to validate the method. It was measured that the maximum temperature increase at the back side of the sample increased linearly with heating power, showing that the heat capacity and density can be considered constant, and that non-linear processes do not play a role. Furthermore, coating the heated surface with a layer of carbon black, in which all the light of the heating laser is absorbed, after which the heat is transferred to the sample, does not alter the results.

4.2.3 Fluorescent microthermal imaging

Single crystals

In the fluorescent microthermal imaging method (FMI), a focused 488 nm light beam (spot size ∼50 μm FWHM, power ∼100 mW) heats a small volume of the sample. The EuTTA/PMMA layer is transparent for this wavelength. The area around the heat

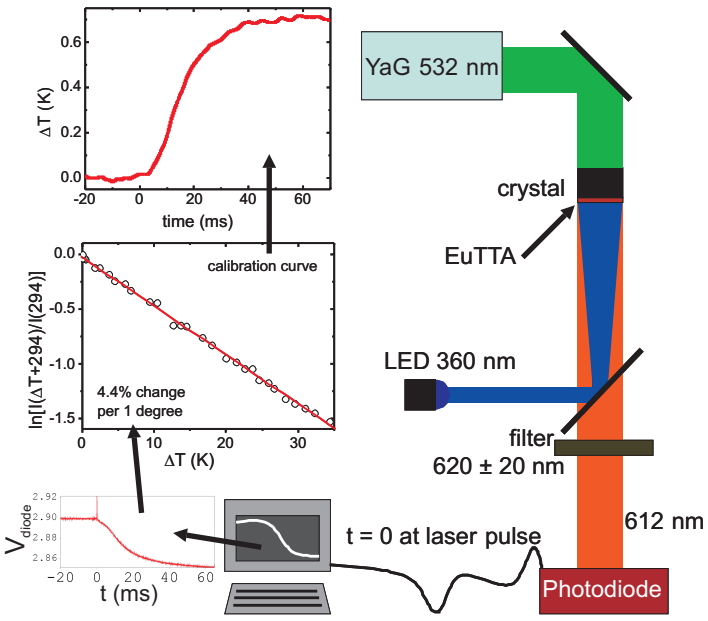

Figure 4.15: Setup for the fluorescent flash method (FFM). The front surface of the sample is excited with a laser pulse from a YAG-laser. The back surface of the sample is illuminated with a 360 nm UV LED to continuously excite the EuTTA layer which is spincoated onto the back surface. The fluorescence coming from this layer is collected by a few lenses and focused onto a GaAsP photodiode. The independently measured calibration curve is used to calculate the time-dependent temperature profile from the voltage profile. A typical curve, measured on nickel, is shown.

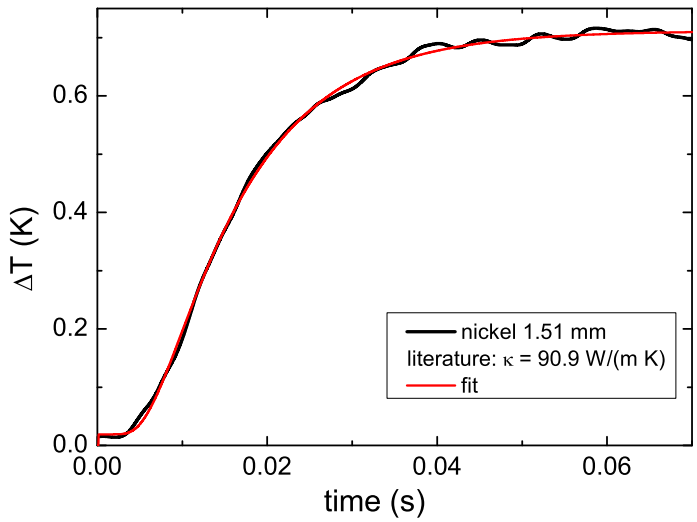

Figure 4.16: Test measurement on a nickel single crystal. From fitting with a one-dimensional diffusion model the thermal conductivity is extracted. It is found to be 85 $\pm$ 4 W m^{-1} K^{-1}, which is in agreement with the literature value.

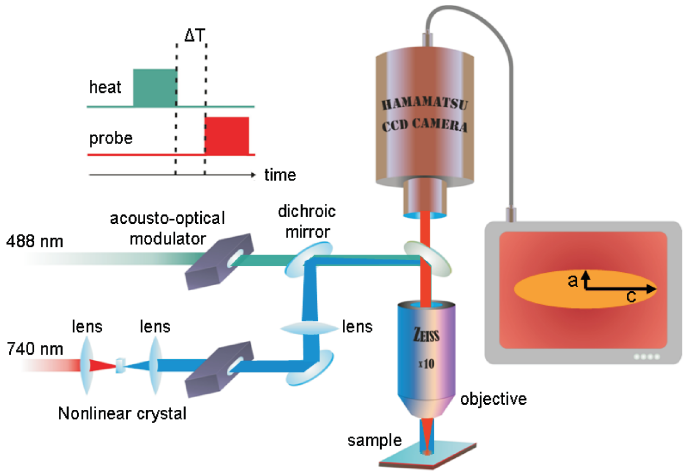

Figure 4.17: Setup for the fluorescent microthermal imaging method (FMI). The sample is heated with a 488 nm laser pulse. During and after the laser pulse, the temperature at the surface of the crystal is measured in a time-resolved (pump-probe) fashion. This is done by exciting a spin-coated EuTTA-layer with 370 nm light and collecting the temperature dependent fluorescence with a CCD camera. For more details, see text.

pulse was illuminated by a pulsed 370 nm defocused laser beam (the second harmonic of a Ti:Sapphire laser, power on the sample ∼1 mW) to excite the EuTTA/PMMA layer. The photoluminescence was collected by an objective, filtered from heating/excitation radiation, and imaged onto a Peltier-cooled CCD-camera. A schematic of the setup is shown in figure 4.17. The magnification of the objective is 10 or 20 times, which for the present system corresponded to a resolution of 1.6 or 0.8 μm per CCD pixel. The measurements were performed in a pump-probe fashion. Typically, the sample was heated for a few tenths of microseconds after which the heating beam was switched off. Then the surface was imaged with different delays between heating and imaging laser and with an integration time of a few tenths of μs. The CCD camera signal was converted into a temperature difference by means of a calibration curve. The mean values and standard deviations were obtained by averaging of at least a hundred measurements.

A room temperature test measurement was done on a thin piece of gold foil ($\sim$ 10 μm). Nickel could not be used because the reflectivity of the 532 nm heating pulse is too high for imaging. Furthermore, a 3-dimensional material with a high thermal conductivity in every direction would cool down too fast to do time-resolved measurements at the same timescales as for the spin chains and spin ladders, even if the maximum laser power is used for heating. The gold foil, with a thicknes of a few tenths of a μm does allow for time-resolved measurements at the same timescales as for the spin chains and spin ladders. A 10 $\times$ objective was used with a heating time of 0.05 ms. The integration time is 0.05 ms. The measured temperature profiles are shown in figure 4.18. From these profiles a normalized cross-section is taken, showing

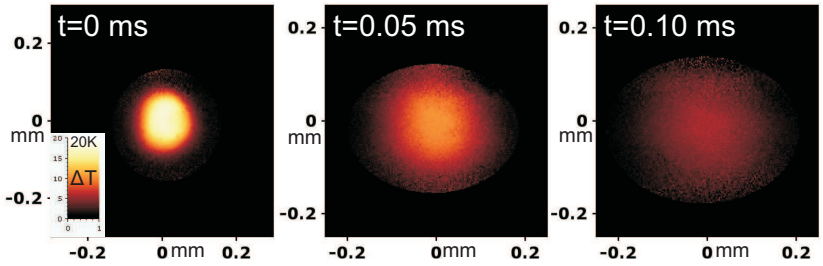

Figure 4.18: FMI on $\sim$ 10 μm gold foil. The temperature profile for different delays during and after the heating pulse is shown.

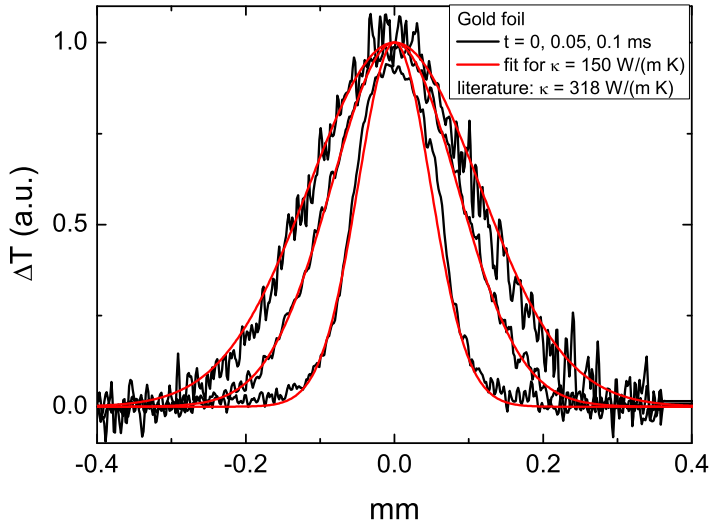

Figure 4.19: Normalized cross-section parallel to the x-axis of the gold foil data shown in figure 4.18. The temperature profile for different delays during and after the heating pulse is shown, together with the best fit to the data. The fitted thermal conductivity, 150 $\pm$ 15 W m^{-1} K^{-1}, is half the literature value of 318 W m^{-1} K^{-1}.

the broadening of the profile as a function of time, as is shown in figure 4.19. The best fit to this cross-section gives a value for the thermal conductivity which is about half of the literature bulk value [108]. This is reasonable taking into account the wrinkled surface on which the measurements were performed. The details about the analysis will be explained in the chapter with FMI measurement results (chapter 7).

Device

To mimic a device, a cross shaped gold structure was deposited by DC magnetron sputtering of Au thin films through a shadow mask on the polished ac-plane of the sample. The width of the strips was designed to be 10-12 μm, which was optimal for the 10 times magnification objective of the microscope. The design of the cross structure on the ac-plane of a $Ca_9La_5Cu_{24}O_{41}$ crystal with its dimensions, as well as

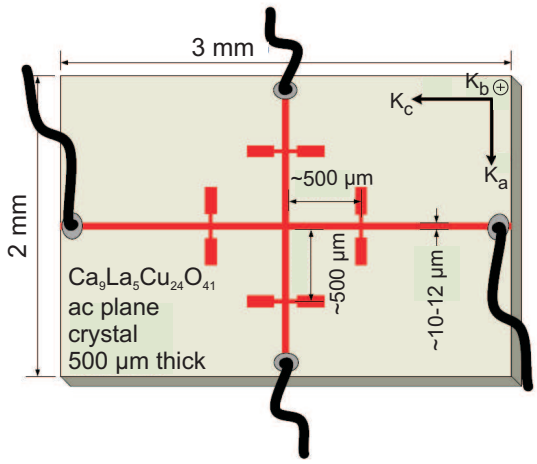

Figure 4.20: Schematic picture of the gold cross (red) deposited on the ac surface (light green) of the $Ca_9La_5Cu_{24}O_{41}$ crystal. The dimensions of the cross and the sample are indicated. The thermal conductivities along the crystallographic axes a, b, c are indicated by K_a, K_b and K_c, respectively.

the direction of the strips with respect to the crystal axis, is shown in Fig. 4.20. The shadow mask is made out of hard, electroformed, sulphamate nickel. It is 50 μm thick and thinned to 5 μm thickness around the apertures in order to avoid problems during metal deposition associated with the mean free path of the metal ions, which needs to be of sufficient size for the ions to be able to travel through the entire thickness of the mask. A shadow mask was preferred in order to avoid the chemical treatment of the surface used in photolithography. Gold was chosen for the fabrication of the cross since it is not susceptible to oxidation. Because of its poor adhesion to oxides, a thin pre-layer of chromium was used as an adhesion promoter. Fig. 4.21 shows a 3D profile, measured by an optical profiler, of a deposited chromium/gold part of the cross structure, showing well-defined lines. The inset shows a stereomicroscope photo of the sample. The red circle indicates the part of the sample whose profile is shown. The thickness of the deposited chromium and gold cross is ∼30 nm and ∼100 nm, respectively, and its width, which was measured by an optical profiler and a scanning electron microscope (SEM), was ∼12 μm. The metal lines were inspected for constant width throughout their length using both an optical microscope and an optical profiler. After the deposition of the metal line, wire leads were connected to the pads. Wire bonding, a technique used during packaging of microelectronic devices, could not be employed due to the very thin metal layers (∼130 nm) that prevent wire bonder's adhesion. Instead, silver paste was used to connect 25 μm gold wires to the sample pads. The sample was mounted on a dual-in-line ceramic package, as shown in Fig. 4.22.

The measurement is performed as on the single crystals. The only difference is that the heating is done electrically, by heating one of the gold strips by a voltage pulse of 0.05 ms. This gives the possibility to average over the direction parallel to the gold strip, thereby increasing the temperature resolution.

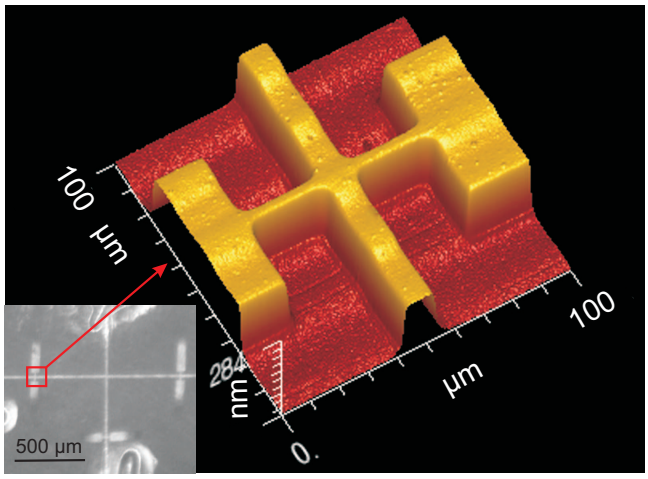

Figure 4.21: 3D profile, measured by an optical profiler, of a small part of the deposited chromium/gold structure, showing well-defined lines. The inset shows a stereomicroscope photo of the sample. The red square indicates the part of the sample whose profile is shown.

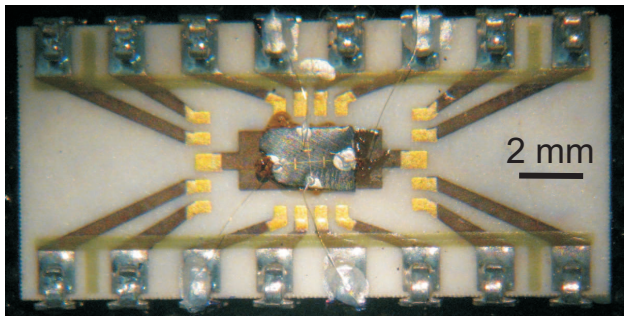

Figure 4.22: Photograph of a dual-in-line ceramic package with the $Ca_9La_5Cu_{24}O_{41}$ single crystal, together with the deposited the gold structure and the wire contacts, mounted on it.

Optical and conventional steady state method

The results obtained by the dynamic FFM are compared to conventional four probe steady state method results, obtained by our collaborators in Dresden (IFW Dresden, group of C. Hess). These measurements are done in the following way [109]: brick-shaped samples with typical dimensions of (3x0.5x0.5)mm were cut with an abrasive slurry wire saw. Measurements of the thermal conductivity in the range from 7-300 K were then performed by applying a heat current with a resistive heater along the principal axes. The resulting temperature gradient was determined by measuring the temperature difference between the junctions of a differential Au/Fe-Chromel thermocouple.

The optical steady state method as applied in this work makes use of the EuTTA layer as a temperature sensor. In this case a sample, of which the three sides to which the heater, heat sink and EuTTA layer are connected are carefully polished, is glued with silver paste or GE varnish to a chip resistor (2-4 kΩ) for heating on one side and a water-cooled copper block for cooling on the other side. The polished side in between the connected sides is covered with EuTTA and the spatially resolved temperature profile is measured. From the thermal gradient between heater and heat sink the thermal conductivity can be extracted. It was found that to create a homogeneous, steady heat flux in the sample, there are a few critical issues; first of all, the sample surface to which the heater and heat sink are connected should be smooth and flat in order to make a good thermal contact. Furthermore, the surface on which the EuTTA layer is attached should be reasonably smooth as well so that the heat can flow with constant resistance. Finally, the heat sink should be actively cooled to keep the temperature constant while adding heat. Still, the temperature profile will consist of a constant background heating, which is growing with the heat power density, plus a thermal gradient from heat sink to heater, which is also growing with growing heat power density. Deviations from linearity occur in the thermal gradient when the thermal contact between heater and sample and/or sample and heat sink is not good. Therefore, in the optical steady state method the quality of the thermal contacts can directly be checked, which is not possible for the conventional steady state method.

The same nickel single crystal as was used as a test sample in FFM was measured by the conventional steady state method to be able to directly compare the results. The data, measured by our collaborator N. Hlubek from IFW Dresden, is shown in figure 4.23. The red dots are the measured data, the black line is a comparison to the literature [108]. It is seen that the steady state measurement and the FFM are in good agreement.

This sample was also used as a test sample in the optical steady state method. The thermal conductivity was measured at room temperature for different heat power densities, as will be discussed in more detail in chapter 5. The thermal conductivity found is in agreement with the conventional steady state method and with literature [108].

4.2.4 Visible pump - visible/near-infrared probe measurements

The room temperature time evolution of the reflectivity change in $Ca_9La_5Cu_{24}O_{41}$ has been investigated by a femtosecond pump-probe technique, using a Ti:sapphire laser

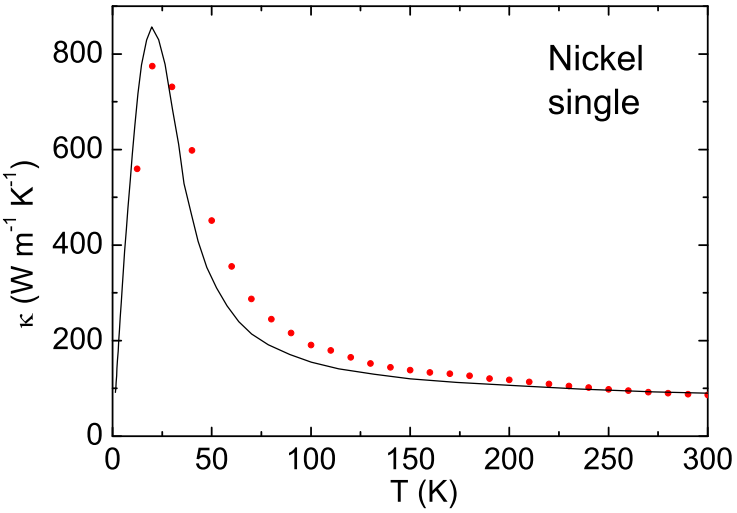

Figure 4.23: Conventional steady state thermal conductivity measurements for different temperatures for the same nickel single crystal that was tested by the FFM. The red dots are the measured data, the black line is a comparison to the literature [108]. It is seen that the steady state measurement ($\kappa = 86 \pm 4$ W m^{-1} K^{-1}) and the FFM ($\kappa = 85 \pm 4$ W m^{-1} K^{-1}) are in good agreement. The steady state data are measured by our collaborator N. Hlubek from IFW Dresden.

(central wave length 785 nm, pulse width 70 fs, repetition rate 81 MHz). This work was done by D.A. Fishman. Both pump and probe beams were focused on the sample surface by an achromatic objective into a spot of 20 μm diameter. The pump beam (760 nm) was chopped at a frequency of 260 Hz. The intensity of the probe pulse reflected from the sample surface was measured as a function of the delay time relative to the pump pulse. With an interference filter only a small range of wavelengths was selected. This was done for several ranges between 785 and 850 nm, thereby giving access to the response at different energies. The measurement was done on a sample with the a and c-axes parallel to the surface. The polarization of the pump pulse E_{pump} is parallel to the c-axis, and perpendicular to the probe pulse polarization E_{probe} which is parallel to the a-axis. Figure 8.6 gives an overview of the reflectance change for all different probe energies measured.

In a follow-up experiment, the time evolution of the reflectivity change in $Ca_9La_5Cu_{24}O_{41}$ has been investigated as a function of temperature. The same femtosecond pump-probe technique was used. Both pump (760 nm, 50 μJ/cm^2) and probe (820 nm, 5 μJ/cm^2) beams were focused on the sample surface by an achromatic objective into a spot of 20 μm diameter. The pump beam was chopped at a frequency of 204 Hz. The intensity of the probe pulse reflected from the sample surface was measured as a function of the delay time relative to the pump pulse. E_{pump} was parallel to the c-axis or parallel to the a-axis. E_{probe} was parallel to the c-axis.

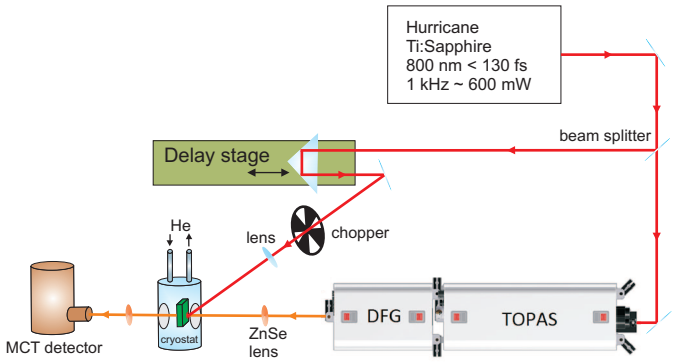

Figure 4.24: Setup for the pump-probe experiment. A 800 nm pulse is split in two pulses. One is delayed by a delay stage and used as a pump. Of the other, the frequency is changed to the infrared by an optical parametric amplifier (difference frequency generation, DFG) and after that focused onto the sample with a zinc selenide lens and used as a probe. The sample is placed inside a cryostat and the changes in transmission are measured by a mercury cadmium telluride (MCT) detector. The signal is sent to a lock-in amplifier which is synchronized with a chopper at 500 Hz.

4.2.5 Near-infrared pump - infrared probe measurements

Pump-probe time resolved transmission measurements have been performed on the same sample to investigate the magnon dynamics and scattering at the ps timescale. A schematic picture of the setup is shown in figure 4.24. A 800 nm (1.5 eV), 100 fs long pulse from a Ti:Sapphire 1 kHz laser has been employed as a pump, while the probe pulse wavelength has been tuned in the 2700 nm - 5500 nm range to probe different parts (phonons, magnons and electron-induced) of the sample spectrum. This is done using the idler of an optical parametric amplifier. The beam diameter of the pump, $\sim$ 550 μm, is slightly larger than that of the probe, $\sim$ 530 μm. The energy densities are 0.93 μJ/cm^2 and 23 nJ/cm^2 at maximum power, respectively. Four different frequencies have been used, of which two have been tuned in resonance with the two magnon dips at 4700 nm 3500 nm, respectively. For detection a lock-in amplifier has been used at a frequency of 500 Hz.

5. Steady state thermal conductivity

Traditionally, steady state heat transport is measured using the temperature difference which is determined between two points at the sample surface. This chapter describes the initial development of an alternative method to determine the heat conductivity of bulk materials through optical imaging of the two-dimensional heat pattern originating from an applied heat flow through a material. The method is demonstrated both for a metallic heat conductor (nickel) as well as for a low dimensional magnetic heat conductor ($Ca_9La_5Cu_{24}O_{41}$). In the following chapters, the steady state thermal conductivity will be compared to thermal conductivities obtained with dynamic methods. The sample preparation and principle of the steady state method were described in section 4.1.1 and 4.2.3, respectively.

5.1 Advantages of an optical steady state method

In the steady state method (SSM), with which thermal conductivities are measured, it is very important that there is a good thermal contact between the heater, the sample and the heat sink, to set up a homogenous flow through the sample, leading to a constant temperature gradient in the direction from heater to heat sink. If this is not the case, the simple analysis from section 3.1.1 cannot be used, because the heat flow is not fully one-dimensional. In the conventional steady state method, the measured quantity is the temperature difference between the two thermal contacts of the thermocouple at the surface, from which the presence of a linear temperature decrease between heater and heat sink cannot directly be verified. Therefore, usually the temperature range is measured back and forth at least once to see if the results are reproducible and no hysteresis is seen.

However, it would be much more convenient if the full temperature profile could be measured, from which one could evaluate directly if the conditions needed to justify the use of the simple analysis are fulfilled. In order to do so, we have used EuTTA as a temperature sensor with which we can measure the temperature of the surface locally, therefore giving access to the local temperature of the sample. With this method one can directly check the presence of a constant temperature gradient in the direction perpendicular to the heater and the absence of a temperature gradient in the direction parallel to the heater which are the desired conditions to perform the experiment.

In this optical SSM, as in the conventional SSM, the thermal conductivity is directly extracted from the measured temperature change (instead of being calculated from the diffusion constant as in the dynamic methods), making a direct comparison between results of both methods straightforward. Compared to the conventional SSM,

the optical SSM gives more scalability in heat power densities and sample size; the experiment can be performed for a large range of heat power densities since the best resolution in temperature is about 0.02 K, and for both small and large length scales, since the spatial resolution is determined by the diffraction limit, which is about 300 nm, rather than by the size of the thermal contacts as in the conventional SSM, which are typically in the order of 200 μm. Going to such a small length scale close to the diffraction limit opens the intriguing possibilities of measuring at length scales below the diffusion length, allowing to observe ballistic transport, or at small distances from the heater, where thermal equilibrium between magnons and phonons has not yet been reached [90]. In the last situation, one measures an effective thermal conductivity which is lower than the total thermal conductivity, since the temperature that is measured is the phonon temperature. Therefore, magnons can only contribute to the thermal transport by interaction with phonons. For the conventional SSM in the spin ladder $Ca_9La_5Cu_{24}O_{41}$, one always measures the total thermal conductivity, since the thermal gradient is determined between two points on the sample which are both at a position where magnons and phonons are in thermal equilibrium.

5.2 Optical steady state measurements on nickel

Optical steady state measurements were performed on a nickel single crystal. Nickel was used as a test material, because its thermal properties are well understood. The amount of averages and integration times were different for different measurements. It was found that making a good thermal contact between heater, sample and heat sink is not trivial. Several times the contacting was not good enough to give a uniform heat profile and the sample had to be reglued. A chip resistor (2.2 or 2.4 kΩ) was used as a heater and connected to the sample with GE varnish glue. The sample had a cube shape, all sides were approximately 1.3 mm long.

Figure 5.1 shows the EuTTA fluorescence intensity on the nickel sample without (left) and with heat flowing through the sample (right). The voltage used for heating is 15 V, corresponding to a heating power density of 60 mW/mm^2. Throughout this chapter we will use x to designate the direction of the applied heat current, and y the direction in the crystal face perpendicular to this. The intensity is given in arbitrary units, white being most intense and black being least intense. By eye no difference is seen between the cold and hot image, because very small temperature differences are detected. Every part of the sample is covered by the EuTTA layer, apart from the darker right down corner, which has some glue on the surface. The left down part of the sample is most intense, which is due to an inhomogeneous energy density of the UV excitation beam, and probably partially due to EuTTA layer thickness variations over the sample. The three darker round spots are a feature of the UV beam and are probably caused by some dust inside the acousto-optical modulator. The cracked structure in the intensity is due to small variations in the EuTTA layer thickness. This occurs because even with spin-casting it is difficult to get a completely homogeneous layer for such a small sample.

The calculated temperature profile of the sample is shown in figure 5.2a. The positions of the heater and the heat sink are indicated. The temperature profile is reasonably homogeneous. The structure in the layer as was seen in the intensity profiles

is almost invisible in the temperature profile, since the relative difference between two images is used to calculate this. To further check the homogeneity of the temperature profile, the local derivative in the y-direction is calculated for every position of the sample, as shown in figure 5.2b. This is done by fitting the data in this direction with a 3rd order polynomial using 4 adjacent values to calculate the local derivative, unless stated otherwise. The derivative is constant over the largest part of the sample, i.e. the gradient is constant in the y-direction and the simple one-dimensional analysis can be used.

As an additional check the data is averaged in the x-direction for different parts of the sample and the derivative of the average slope is taken. Because there is some glue on the sample in the right lower corner and a black spot in the right upper corner, to determine the average gradient, the y-region from 0.3 to 1.2 mm is selected. The average temperature as a function of the y-coordinate for different averaging regions is shown in figure 5.3. The dotted lines are best fits to the temperature curve with the same color. All temperature curves are linear, except the one for averaging over x = 0.8 to 1.2 mm. From the temperature picture it is seen that in this region there are some darker and brighter spots on the surface, indicating a non-linear behaviour in temperature drop between heater and heat sink. Therefore, this region is not taken into account. From the other 3 regions the average temperature derivative is taken. Using κ = - $J/(dT/dy)$, with κ the thermal conductivity, J the heating power density in the y-direction and dT/dy the temperature derivative in the y-direction, a κ of 79 $\pm$ 8.7 W m^{-1} K^{-1} is calculated. This is in agreement with the literature value of 85 $\pm$ 5 W m^{-1} K^{-1}, which was measured by our collaborators of the IFW in Dresden.

The experimental error is estimated by taking into account different sources. The error in dT/dy is mainly due to the error in the calibration of the particular EuTTA layer on the sample, since calibration data of another layer was used. From a comparison of the response of different EuTTA/PMMA layers we estimate the calibration error to be less than 10 %. In the error in J, on has to consider the error in the sample area to which the heater is connected, and the heat current applied. Together, it is estimated to be 5 %, leading to a total error in the thermal conductivity κ of 11 %. What is neglected in this analysis are possible losses by radiation and air convection.

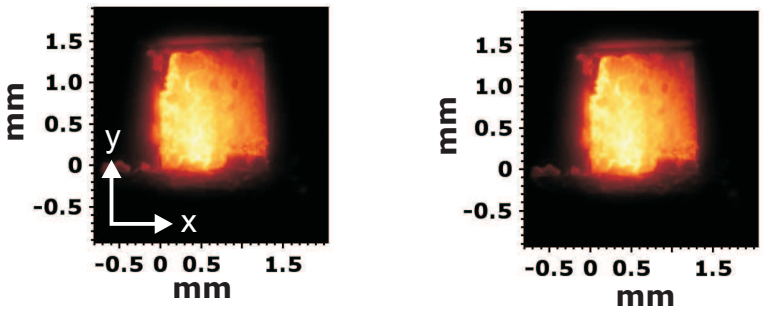

Figure 5.1: EuTTA layer fluorescence intensity for a nickel sample. The heater is parallel to y=0 mm and the heat sink is parallel to y=1.4 mm. Left: without heat flowing through the sample. Right: while heat is flowing through the sample, with a heating power density of 60 mW/mm^2.

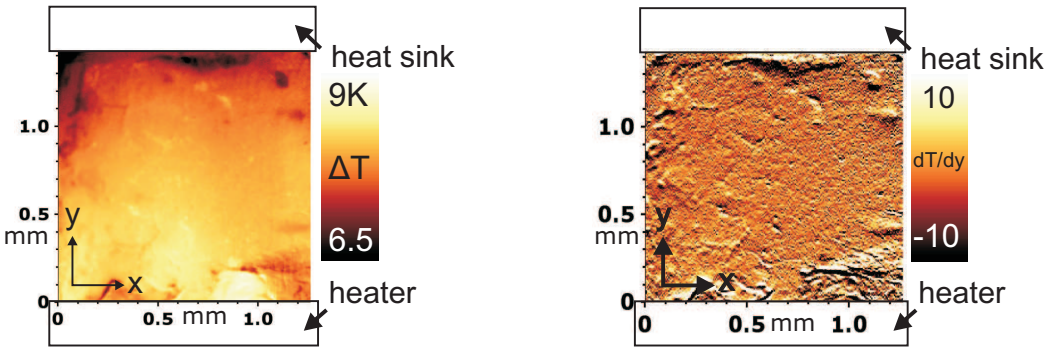

Figure 5.2: a) Temperature profile of a nickel single crystal while heating continuously with a heating power of 60 mW/mm^2. The sides of the sample connected to the heater and heat sink are indicated; the image only displays the sample. b) Derivative along the y-direction from the temperature profile. Over the largest part of the sample surface the derivative is constant, indicating that the simple one-dimensional analysis can be used to extract the thermal conductivity.

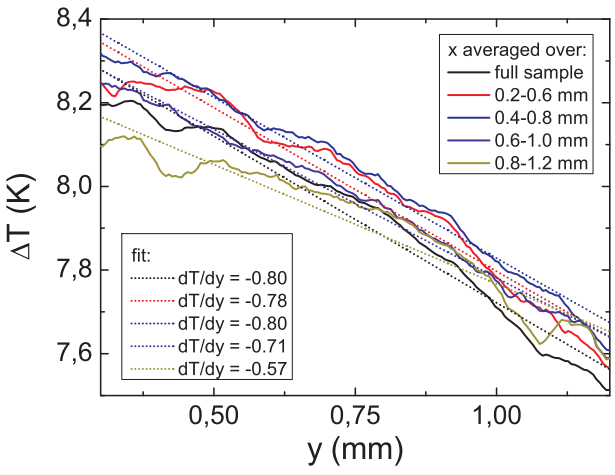

Figure 5.3: Temperature profile in the y-direction for different regions of the sample for a heating power density of 60 mW/mm^2. The average is taken over the x-direction for different ranges. The 3 regions x = 0.2 - 0.6 mm, x = 0.4 - 0.8 mm, and x = 0.6 - 1.0 mm are used to determine the average derivative of the temperature in the y-direction, which is used to calculate $\kappa = 79 \pm 8.7$ W m^{-1} K^{-1}.

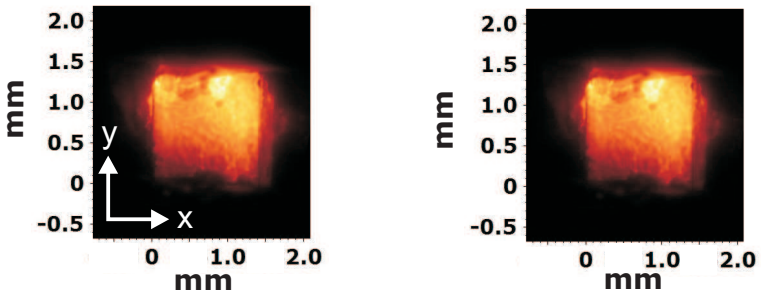

Figure 5.4: EuTTA layer fluorescence intensity for a nickel sample. The heater is parallel to y=0 mm and the heat sink is parallel to y=1.4 mm. Left: without heat flowing through the sample. Right: while heat is flowing through the sample, with a heating power density of 45 mW/mm^2.

In the following paragraphs, additional measurements will be shown to illustrate the issues found using the optical steady state method and discuss how they can be avoided. Figure 5.4 shows the EuTTA fluorescence intensity on the nickel sample without (left) and with heat flowing through the sample (right). The voltage used for heating is 13 V, corresponding to a heating power density of 45 mW/mm^2. A modulation in the intensity of the fluorescence is seen in the center for both images. This could be due to thickness modulations of the EuTTA-layer, however, it is more likely that the UV beam exciting the layer is not homogeneous. It is observed that by somewhat changing the alignment of the UV-beam this modulation is gone. Furthermore, again a dark spot is seen, coming from the passing of the beam through the AOM. Calculating the temperature profile, as is shown in figure 5.5a, the modulations are clearly visible in the center. Also when calculating the derivative in the y-direction, as is shown in figure 5.5b, this modulation is clearly visible. If this effect was due to modulations in the EuTTA layer, it would not be visible in the temperature profile, since the relative intensity change is used to calculate this. Therefore we conclude that the modulation is due to a purely optical effect.

The smooth side regions on the left and right side of the sample are analyzed. On the left, averaging over x = 0.81 to 1.07 mm, dT/dy is -0.18 K/mm. On the right, averaging over x = 1.9 to 2.07 mm, the gradient is -0.22 K/mm. When taking the average over the full sample, the gradient is -0.2 K/mm. Since the difference is so small, the average value is taken and κ = 134 $\pm$ 14.7 W m^{-1} K^{-1}. An explanation for the higher value can be that in this experiment, which was a first try, a heater was used with a surface area much larger than the sample surface, which might lose part of its heat to the surroundings, more than for a heater that has a size only slightly larger than the sample. Then the actual heating power density applied to the sample will be overestimated and κ too.

Furthermore, measurements were done at a lower heating power density of 27 mW/mm^2 (10 V). The first measurement was done in the same series as the one at 60 mW/mm^2. Therefore the EuTTA fluorescence intensity on the nickel sample without and with heat flowing through the sample (both not shown) look exactly the same as in that measurement. The temperature profile is shown in figure 5.6a, and the derivative in the y-direction is shown in figure 5.6b. The average dT/dy is -1.05 K/mm, which gives a thermal conductivity of only 25 $\pm$ 2.8 W m^{-1} K^{-1}. The reason for this discrep-

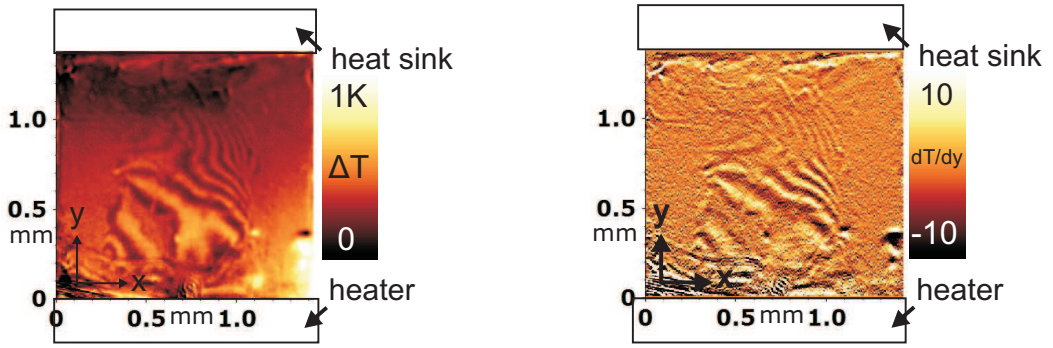

(a) (b)

Figure 5.5: a) Temperature profile of a nickel single crystal while heating continuously with a heating power of 45 mW/mm^2. The sides of the sample connected to the heater and heat sink are indicated; the image only displays the sample. The modulations in intensity, as were observed in figure 5.4 are also seen in the temperature profile. b) Derivative along the y-direction from the temperature profile. The modulations in intensity, as were observed in figure 5.4, are also seen in the derivative.

ancy is not fully understood, because there are no clear signs that there was a problem in this measurement. The temperature profile and the derivative seem ok. The most probable explanation is that the active water cooling used decreased the temperature of the copper block so much that an additional gradient was induced between heater and copper block (heat sink), even when the heater is off. Then the total flow measured is larger, and the extracted thermal conductivity is smaller. Therefore, it is important to measure the ambient temperature independently and set the temperature of the heat sink at exactly that temperature. This was done in later measurements.

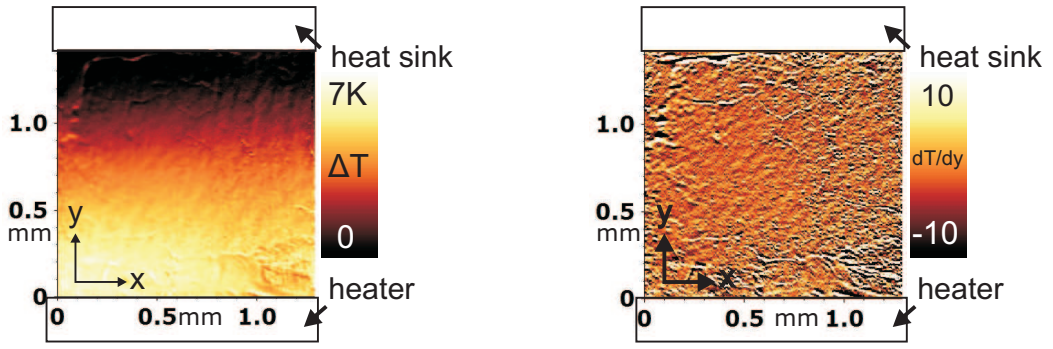

(a) (b)

Figure 5.6: a) Temperature profile of a nickel single crystal while heating continuously with a heating power of 27 mW/mm^2. The sides of the sample connected to the heater and heat sink are indicated; the image only displays the sample. A homogeneous temperature decrease is seen in the y-direction, while the temperature in the x-direction is constant. b) Derivative along the y-direction from the temperature profile in a.

In a measurement which was done at a heating power density of 39 mW/mm^2 (12

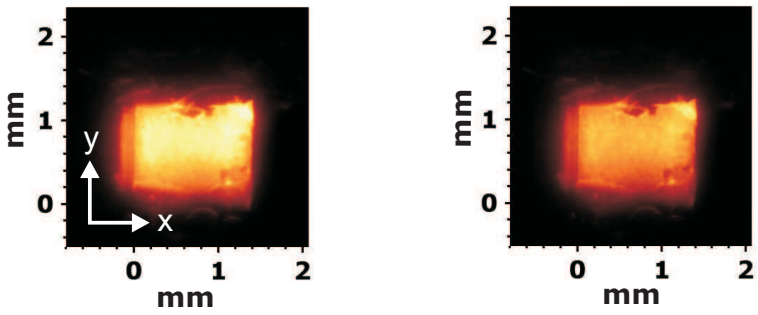

Figure 5.7: EuTTA layer fluorescence intensity for a nickel sample. The heater is parallel to y=0 mm and the heat sink is parallel to y=1.2 mm. Left: without heat flowing through the sample. Right: while heat is flowing through the sample, with a heating power density of 39 mW/mm^2.

V), no good thermal contact between the heater, sample and heat sink was achieved. The EuTTA fluorescence intensity on the nickel sample without (left) and with heat flowing through the sample (right) is shown in figure 5.7. Apart from glue on the lower edge of the sample no special features are observed. The temperature profile is shown in figure 5.8a. The parts which are covered by glue are colder than the sample, which is contrasting other measurements, and indicates a poor thermal contact. Furthermore, the hottest part of the sample is located in the middle, instead of on the heater side. When looking at the derivative in the y-direction, as shown in figure 5.8b, one sees that it is not constant over the sample. In the lower half of the sample it is positive and higher than in the upper half, where it is negative. In this derivate, 10 adjacent values are used to calculate the derivative, thereby showing better contrast between the upper and lower half of the sample. In all measurements with a poor thermal contact, a similar temperature profile along the y-direction was found, as is shown in figure 5.9, which is averaged over the full sample in the x-direction. The highest temperature is measured in the center region of the sample, leading to a variable temperature gradient over the sample. From such profiles the thermal conductivity cannot be extracted. In such case the sample has to be reglued. Unfortunately, it is difficult to know beforehand if the thermal contact is good. What should be avoided for sure is very rough surfaces and too much glue.

Sometimes (part of) the layer degrades, leading to a loss of temperature sensitivity. For example, as shown in figure 5.10, in another measurement with a heating power density of 27 mW/mm^2, with another layer of EuTTA, the EuTTA fluorescence intensity on the nickel sample without (left) and with heat flowing through the sample (right) looks ok, apart from some glue in the left down corner. However, when calculating the temperature profile, as shown in figure 5.11, it is seen that the upper and lower part of the layer are not indicating any temperature dependence. In such case the layer of EuTTA is removed and a fresh layer is put on the sample.

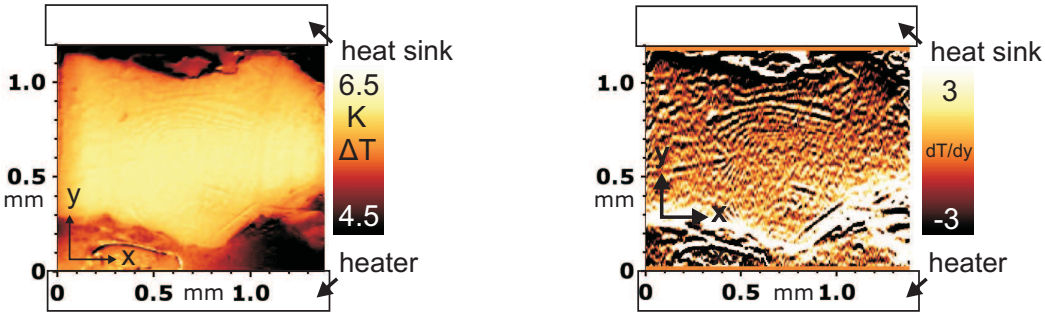

(a) (b)

Figure 5.8: a) Temperature profile of a nickel single crystal while heating continuously with a heating power of 39 mW/mm^2. The sides of the sample connected to the heater and heat sink are indicated; the image only displays the sample. The small modulations in intensity, as were observed in figure 5.7, are also seen in the temperature profile. b) Derivative along the y-direction from the temperature profile in a. The derivative is higher in the lower half of the sample than in the upper half of the sample.

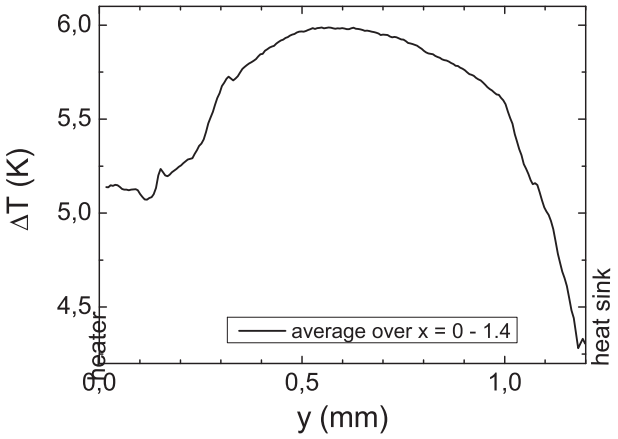

Figure 5.9: Average temperature profile in the y-direction. Only the region between heater at y=0 and heat sink at y=1.2 is shown. When the thermal contact between heater, heat sink and sample is poor, a typical temperature profile is observed, with the highest temperature in the center region of the sample.

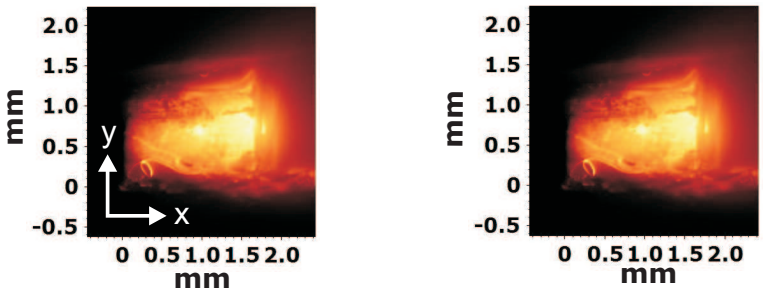

Figure 5.10: EuTTA layer fluorescence intensity for a nickel sample. The heater is parallel to y=0 mm and the heat sink is parallel to y=1.4 mm. Left: without heat flowing through the sample. Right: while heat is flowing through the sample, with a heating power density of 27 mW/mm^2. This is a different measurement for this heating power density as was described previously, with a different EuTTA layer.

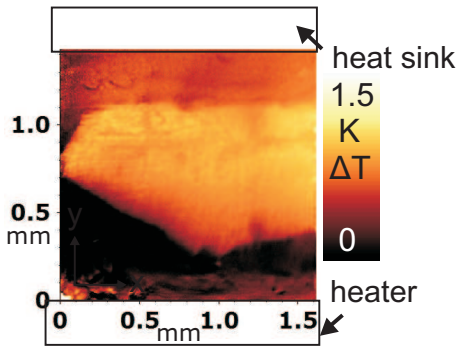

Figure 5.11: Temperature profile of a nickel single crystal while heating continuously with a heating power of 27 mW/mm^2. The sides of the sample connected to the heater and heat sink are indicated; the image only displays the sample. No clear temperature gradient is seen and at the lower part of the sample the temperature increase seems to be zero. Therefore, such data cannot be used with the simple model.

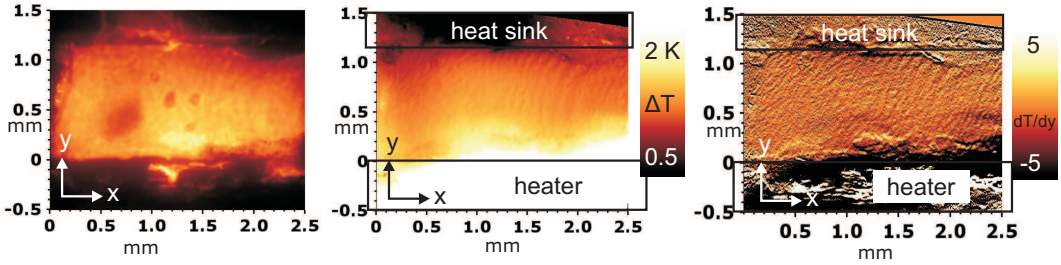

Figure 5.12: EuTTA fluorescence intensity on the $Ca_9La_5Cu_{24}O_{41}$ sample without heat flowing through the sample (left), the temperature profile (center) and the derivative in the y-direction (right) for a heating power density of 54 mW/mm^2.

5.3 Optical steady state measurements on $Ca_9La_5Cu_{24}O_{41}$

Even though the test measurements on nickel were not yet perfect, further measurements were performed on a sample of $Ca_9La_5Cu_{24}O_{41}$ with the c-direction parallel to the temperature gradient between heater and heat sink. Some smooth temperature profiles with good thermal contact were obtained for different heating power densities of 54, 78 and 96 mW/mm^2 (15, 18 and 20 V chip resistor voltage), all measured with the same layer of glue and the same EuTTA layer. The average is taken over 100 measurements, each with integration time 250 ms. Figure 5.12 shows the EuTTA fluorescence intensity on the $Ca_9La_5Cu_{24}O_{41}$ sample without heat flowing through the sample (left), the temperature profile (center) and the derivative in the y-direction (right) for a heating power density of 54 mW/mm^2. It is seen that the inhomogeneities in the EuTTA fluorescence intensity are gone in the temperature profile, as should be the case. Furthermore, the temperature is lower at the sample sides than at the middle part. The right lower corner of the sample contains some glue, as can be seen in the cold image. This region is white in the temperature profile, showing that the glue has a higher temperature than the crystal, ΔT is about 4-6 K in the area close to the sample. Therefore, it will act as a heat source applying heat at the top of the sample. The calculated derivative is constant over the sample, apart from the region in which the glue is covering the surface and the two slightly darker spots on the sample surface, which are regions in which the sample surface is somewhat warmer. Now the temperature profile in the y-direction is calculated for 3 different regions, i.e. by averaging over 3 different ranges of x-coordinates, as is shown in figure 5.13. The best linear fit to the data over the glue free region of the surface is shown. This region is different for different parts of the sample. The temperature gradient is somewhat lower on the left side of the sample. This can be due to a non-homogeneous heat flux distribution, since the sample is rather wide. Therefore, the average of the other two regions is taken to determine dT/dy.

Now exactly the same procedure is followed for a heating power density of 78 mW/mm^2, shown in figures 5.14 and 5.15, and 96 mW/mm^2, shown in figures 5.16 and 5.17, respectively. For all heating power densities the thermal conductivity κ is calcutated and shown in figure 5.18, together with the values obtained by a conventional steady state method on samples from the same batch, as indicated by the grey area.

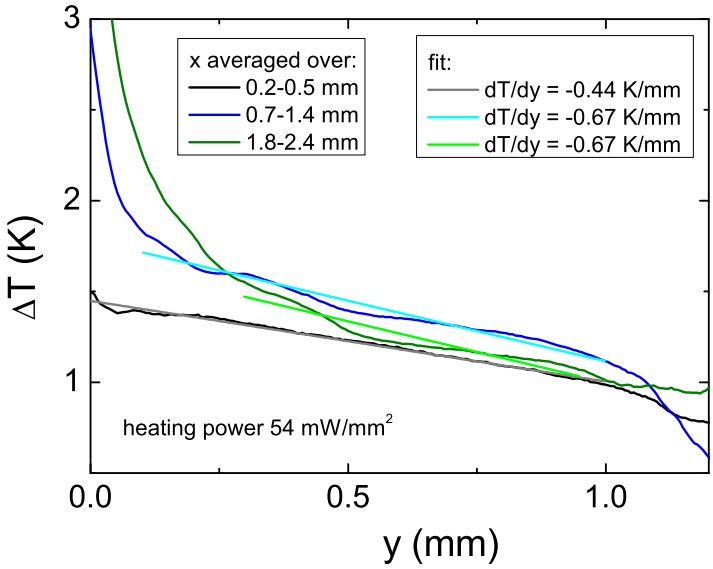

Figure 5.13: Temperature profile in the y-direction for different regions of the sample for a heating power density of 54 mW/mm^2. The average is taken over the x-direction for different ranges. The 2 regions x = 0.7 - 1.4 mm, and x = 1.8 - 2.4 mm are used to determine the average derivative of the temperature in the y-direction, which is used to calculate κ (shown in figure 5.18.

The values obtained by the OSSM are in good agreement with those. The error bar is 11 %, as was discussed for the measurements on nickel.

5.4 Discussion

The first measurements with the new optical steady state method are in reasonable agreement with the results from the conventional steady state method. However, it turns out that establishing the experimental conditions under which the heat flow is constant throughout the sample, such that the problem is simplified to an analytically solvable one, is not straightforward. Different crucial issues will now be discussed.

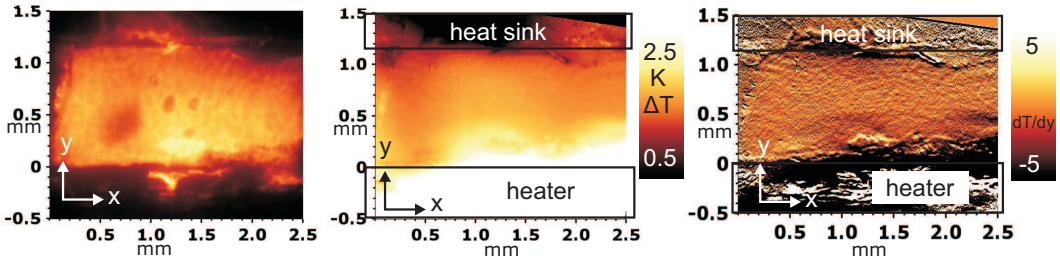

Figure 5.14: EuTTA fluorescence intensity on the $Ca_9La_5Cu_{24}O_{41}$ sample without heat flowing through the sample (left), the temperature profile (center) and the derivative in the y-direction (right) for a heating power density of 78 mW/mm^2.

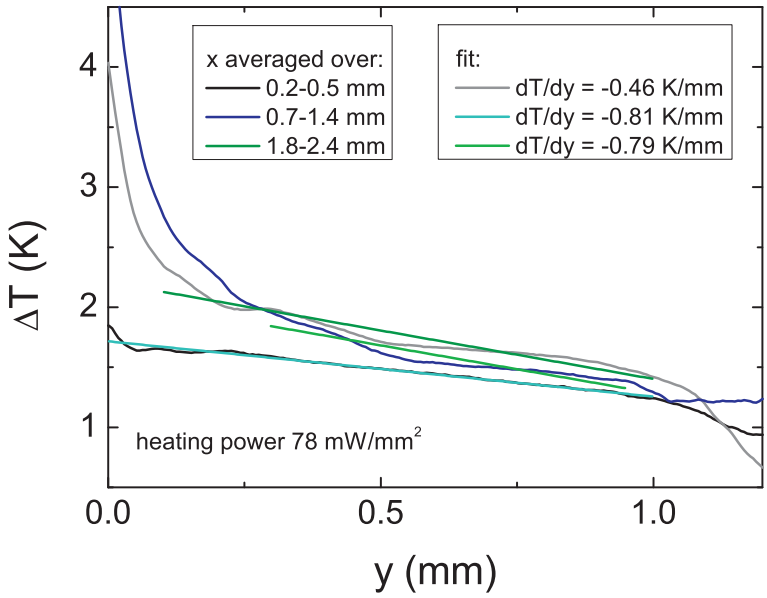

Figure 5.15: Temperature profile in the y-direction for different regions of the sample for a heating power density of 78 mW/mm^2. The average is taken over the x-direction for different ranges. The 2 regions x = 0.7 - 1.4 mm, and x = 1.8 - 2.4 mm are used to determine the average derivative of the temperature in the y-direction, which is used to calculate κ (shown in figure 5.18.

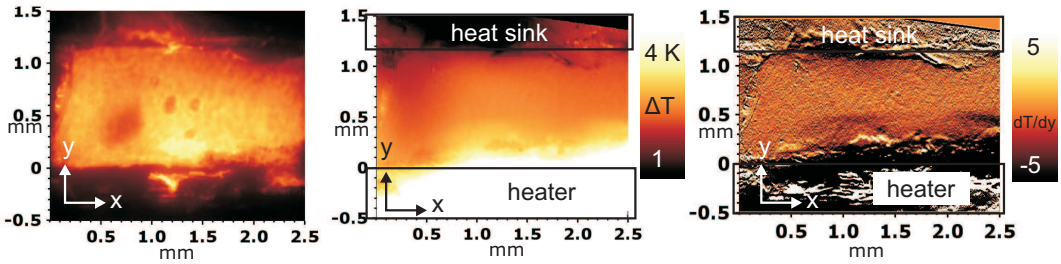

Figure 5.16: EuTTA fluorescence intensity on the $Ca_9La_5Cu_{24}O_{41}$ sample without heat flowing through the sample (left), the temperature profile (center) and the derivative in the y-direction (right) for a heating power density of 96 mW/mm^2.

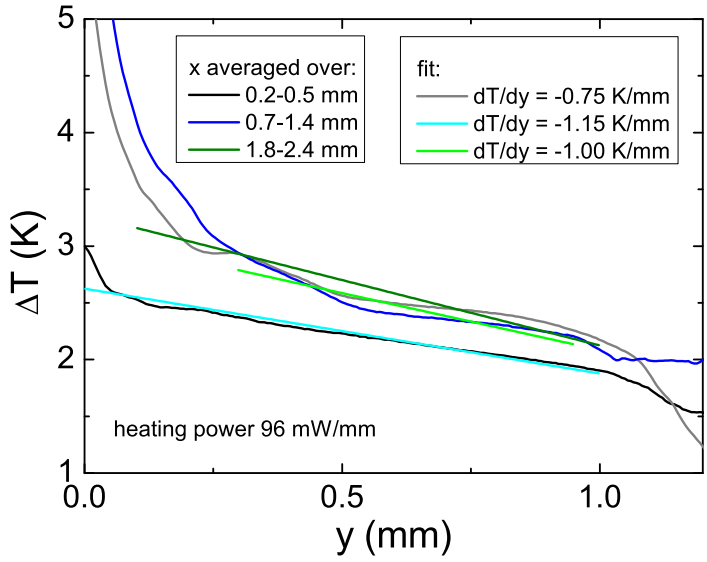

Figure 5.17: Temperature profile in the y-direction for different regions of the sample for a heating power density of 96 mW/mm^2. The average is taken over the x-direction for different ranges. The 2 regions $x = 0.7$ - 1.4 mm, and $x = 1.8$ - 2.4 mm are used to determine the average derivative of the temperature in the y-direction, which is used to calculate κ (shown in figure 5.18.

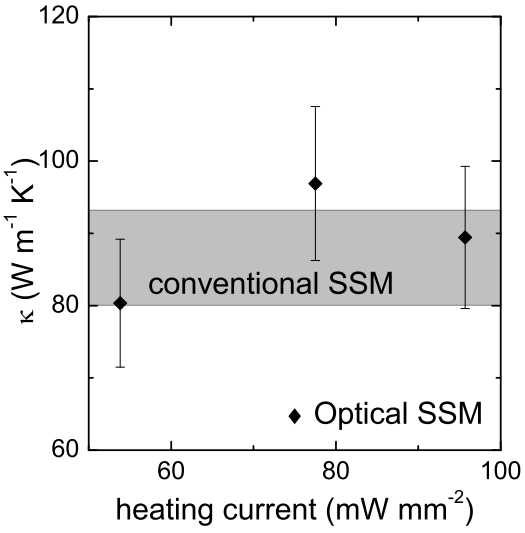

Figure 5.18: Extracted thermal conductivity κ from fitted thermal gradients as a function of heating power density. The values are in agreement with the values obtained by a conventional steady state method, which are in the range indicated by the grey bar.

Concerning the design of the experiment:

- The sample should be rectangular in shape, with flat, well-polished surfaces. Preferably the surface to which the heater is connected is equal to or smaller than the surface which is covered with EuTTA. In such case it is easier to set up a homogeneous heat flux. Our $Ca_9La_5Cu_{24}O_{41}$ sample had a non-ideal shape, leading to a lower temperature at one side of the sample.

- Air conduction losses can be limited by performing the experiment in vacuum. By choosing a heater size close to the size of the sample surface to which it is attached, the homogeneity of the heating is increased and heat losses by radiation are decreased.

- Placing the sample in a holder will improve the stability of the setup, decreasing vibrations and forces on the glued parts. The holder material has to be chosen such that the temperature of the sample environment is constant, and that the heat flow through the sample is not disturbed.

Concerning the thermal gradient:

- The quality of the thermal contacts between the heater and sample, and heat sink and sample, is of uttermost importance. The amount of glue used should be limited as much as possible and glue on the other sample surfaces should be avoided. This was especially challenging in the current experimental design, since the sample was free-standing, and a minimum amount of glue had to be used to fix the sample.

- The heat sink, in the current experimental design a copper block, should be kept at a constant temperature equal to the ambient temperature. Making the temperature of the heat sink lower than the ambient temperature sets up additional heat gradients in the sample and therefore should be avoided. It was found that this can best be done by active water cooling through a copper block of at least several cm^3.

- A glue with a thermal conductivity as high as possible should be chosen, ideally equal to the thermal conductivity of the sample or higher. However, it should be electrically isolating as well. By choosing isolating glue with highest thermal conductivity possible and making the layer as thin as possible the thermal contact is optimized.

Concerning the use of EuTTA as a temperature sensor:

- The EuTTA layer should be calibrated in situ to account for layer-to-layer variations, thereby strongly decreasing the experimental error in the temperature increase, since the relative error in this quantity is *directly* determining the minimum relative error in the thermal conductivity.

- The intensity of the UV-source exciting the EuTTA-layer should be very stable, to avoid variations in intensity between measurements.

- The UV-source should have a (nearly) constant intensity over the sample surface, to avoid variations between different parts of the sample surface.
- The UV-beam should not move in space, to avoid intensity variations, therefore long beam paths should better be avoided.
- The EuTTA layer should be reasonably homogeneous to avoid marks of inhomogeneities in the temperature profile.
- The EuTTA layer should be thin enough (maximum approximately 500 nm) to avoid an influence on the thermal transport in the material on which it is spin-casted.

5.5 Conclusion

In conclusion, an alternative, optical, steady state method was demonstrated to measure the static thermal conductivity in nickel and along the spin structure in the spin ladder material $Ca_9La_5Cu_{24}O_{41}$. For both materials the thermal conductivity found is in agreement with the value determined by a conventional steady state method. For both methods similar heating power densities and sample sizes were used.

The optical steady state method potentially has several advantages over the conventional steady state method; by measuring the temperature at every postion of the sample, it is directly visible if there is a one-dimensional heat flow through the sample. Furthermore, a few orders of magnitude higher spatial resolution can be achieved, thereby opening the possbility to measure at length scales below the diffusion length or close to the heater, where thermal equilibrium between magnetic and lattice excitations has not been established.

During the first experiments using the optical steady state method, which are described in this chapter, it was challenging to get full control over all the critical parameters influencing the thermal gradient and to obtain an accurate and reproducible temperature measurement of the full sample surface. However, these problems are solvable by improving the experimental setup and procedure.

6. Dynamic measurements of the bulk thermal conductivity

6.1 Introduction

As discussed in section 3.6, quasi-1D antiferromagnetic two-leg spin ladder systems show an exceptionally large thermal conductivity κ_c along the ladder, [8] even though the transport by gapped magnon excitations is predicted to be dissipative according to most calculations [112]. At room temperature, the electrically insulating spin ladder material $Ca_9La_5Cu_{24}O_{41}$ shows $k_c \sim 100$ W m^{-1} K^{-1} (c is the ladder axis). Since the magnetic excitations, called magnons, only contribute to the heat transport along the spin structure, the conductivity is highly anisotropic; $k_a \sim 2.5$ W m^{-1} K^{-1} (a axis perpendicular to the ladders) at room temperature [6]. In the spin chain material $SrCuO_2$, the magnetic excitations are predicted to transport energy ballistically, thereby making these systems of fundamental interest [4].

In such a material with magnetic and phononic excitations, the spin-phonon coupling becomes a key parameter to properly describe [90] and eventually control the heat conduction in magnetic materials, since in a typical heat conduction experiment, to a first-order approximation, only the phonon temperature is directly measured; the (fast) spin contributes to the measured, effective, conductivity only trough the interaction with the (slow) phonons. This is schematically shown in figure 6.1. By laser heating electrons are put in the system. These are in a negligible amount of time converted into phonons. Then these phonons are interacting with the magnons while diffusing. At the other side of the sample the lattice temperature (which is determined by lattice vibrations, i.e. phonons) is measured by an optical temperature sensor. This idea has been already used to qualitatively explain measured static heat conductivities in bulk magnetic materials [90]; however, no attempt to measure the spin-phonon interaction has been reported, in part due to the limitations of conventional (static) experimental techniques in measuring such an inherently dynamic property.

In this chapter, it is shown that the dynamic thermal conductivity is not necessarily equal to the static thermal conductivity. Furthermore, it is shown that if they are not equal, dynamic thermal conductivity measurements on different sample thicknesses allow for determination of the spin-phonon interaction time, because in such situation this time has the same order of magnitude as the typical time scale of the experiment. The time scale used can be tuned by adjusting the sample thickness, thereby adjusting

Part of this chapter is in preparation for publication [110]. The FFM principle has been published in *Journal of Magnetism and Magnetic Materials* [111].

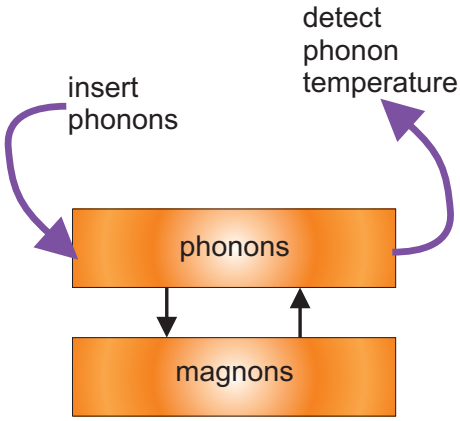

Figure 6.1: Schematic idea of a dynamic experiment. By optical heating electronic excitations are created in the system. These are in a negligible amount of time converted to phonons. Then these phonons are interacting with the magnons while diffusing. At the other side of the sample the lattice temperature (which is determined by lattice vibrations, i.e. phonons) is measured by an optical temperature sensor.

the time needed for diffusion from the side of the sample where the phonons are injected to the other side where the phonon temperature is measured. This information is very valuable, since a better understanding of the spin-phonon coupling in 1D quantum magnets is instrumental for the understanding of various low-dimensional phenomena, such as spin-Peierls instabilities in insulating crystals such as $CuGeO_3$ [113], in which the interplay between spin dimerization and lattice distortion determines the dynamics of the transition and is still not completely understood.

6.2 Experimental procedure

The measurements in this chapter have been performed using the time-domain fluorescent flash method (FFM) as was described in section 4.2.2. They are compared to the data obtained with a steady state method (optical or conventional), performed as is described in section 4.2.3. Single crystals platelets (thickness 0.39 - 3.25 mm) were cut and polished by hand with SiC paper (grain size 5 μm) along different crystallographic axes from a single rod of the spin ladder materials $Ca_9La_5Cu_{24}O_{41}$ and $Sr_{10}La_4Cu_{24}O_{41}$. Furthermore, samples with different Ni doping concentrations of the spin chain compound $SrCu_{1-x}Ni_xO_2$ with 99.99 % purity (4N) were prepared. Finally, different thicknesses (0.53 - 3.25 mm) of 99.9999 % pure (6N) $SrCuO_2$ samples were cut and polished. Details about sample growth were described in section 4.1.1.

Thermal conductivities have been measured along (c-axis) and perpendicular to (a/b axis) the ladder/chain direction. The temperature traces are fitted with Parker's equation [89] to extract the diffusion constant. Furthermore, from the increase in temperature ΔT, the specific heat C_p is extracted. From the diffusion constant the thermal conductivity is calculated by multiplying by the factor $\rho\, C_p$, in which ρ is the molar density. For the experiments at room temperature the temperature increase is small and therefore one can safely neglect the temperature dependence of both ρ and C_p. At lower temperature the temperature dependence of C_p is taken into account.

However, literature values were used for C_p, since those were measured more accurately than the values determined by FFM. The following numbers were used: for the molar density $\rho = 1690$ m^{-3} [80] and for the specific heat $C_p = 1700$ J Mole$^{-1}K^{-1}$ [114] for the spin ladder $Ca_9La_5Cu_{24}O_{41}$, $\rho = 1590$ m^{-3} [77] and $C_p = 1700$ J Mole$^{-1}K^{-1}$ [114] for the spin ladder $Sr_{10}La_4Cu_{24}O_{41}$, and $\rho = 29000$ m^{-3} [115] and $C_p = 87$ J Mole$^{-1}K^{-1}$ [116] for the spin chain $SrCuO_2$, respectively.

The total error is estimated from analyzing different error sources. To calculate C_p, the error in ΔT is important. This depends on the layer-to-layer reproducability of the temperature dependence of the EuTTA layer. From calibration measurements on different layers in different temperature intervals this is found to be around 10 %. Furthermore, an estimation of the energy density Q has to be made from the measured pulse energy and the beam profile. This is done by assuming a trapezoid beam shape and only let the flat part fall on the sample. However, when the beam is slightly misaligned the actual Q is lower. Also the laser output can fluctuate somewhat. The error is estimated to be 10 %. Finally, the error in sample thickness. Even for the thinnest samples this is ≤ 2 %. Furthermore, one has to correct for the reflectivity, which is taken from literature and for which the error is not specified. It is estimated to be ~ 10 %. Therefore, the total relative error in C_p, which is the square root of the sum of all the individual relative errors squared, ≤ 18 %.

For extracting the diffusion constant by fitting with Parker's formula, ΔT is not important. Other factors do play a role. First, the zero in time, but this can be determined exactly because a small portion of the heating laser light is collected by the detector. Second, the precision of the measured sample thickness. Even for the thinnest samples this is ≤ 2 %. Third, the noise in the data. The noise in the extracted diffusion constant is estimated from trying different values. It differs from sample to sample but in general, if the data is good, it is about 4 %, while for the noisiest traces it increases up to 15 %. Fourth, the density is calculated from the lattice parameters, for which the variations with temperature are negligibly small. The final source of error is in the heat capacity. It has been measured in literature [114] but also by our collaborators in Dresden. The difference between both curves is never more than 5 %, which is therefore used as an estimate for the error. It is clear that the noise in the data and the fitted diffusion constant are the largest sources of error. Therefore, the error in general will vary between 6.7 % and 16 %, since κ is determined by multiplying D and C_p so therefore square root of the sum of the squared relative errors add up.

6.3 Results

6.3.1 Spin chain $SrCuO_2$

Figure 6.2 shows normalized FFM temperature traces measured for $SrCuO_2$ with different Ni doping concentrations. It is clear that there is a delay in temperature rise with increasing Ni doping concentration, resulting in a decrease of the diffusion constant. The red solid curves are fits to Parker's equation [89], which is described in section 3.1.2. The samples have approximately the same thickness, which is around 1.3 mm. The heating laser wavelength for all $SrCuO_2$ measurements is 532 nm (2nd harmonic of the YAG), because it was found that the fundamental wavelength has a too large

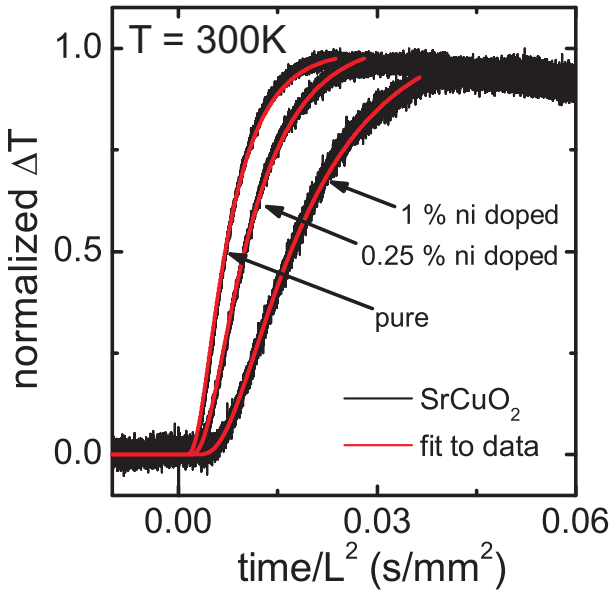

Figure 6.2: Normalized temperature increase at the back side of $SrCuO_2$ samples with different nickel doping concentrations. The heat transport is measured along the chains. The sample length is normalized to 1 mm for all samples. The decrease of the diffusion constant with the increasing doping concentration is clearly seen from the longer delay between heat pulse and temperature rise. The red curves indicate the best fit to the data, using Parker's equation.

penetration depth in this material and is partially transmitted in thin samples. To facilitate the comparison of different delays, a time axis transformation is applied to normalize to a standard sample thickness. This is done by dividing the time axis by the sample thickness squared, because from Parker's equation it is seen that the factor in the exponent is $(n^2\pi^2)/(L^2Dt)$, which involves L^2D as a fitting term instead of D. In figure 6.3 this is shown for two curves measured on undoped $SrCuO_2$ samples of 0.95 and 1.92 mm, respectively. The diffusion constant is the same for both, therefore the curves fall on top of each other after the transformation, as is seen in the right graph.

The thermal conductivity of Ni-doped $SrCuO_2$ measured with the FFM and conventional SSM as a function of doping is shown in figure 6.4. The agreement between both methods is good. This indicates that the thermalization time between spinons and phonons is neglibibly small compared to the time scale of the experiment. As already mentioned in section 3.4 when discussing the SSM data dependence on scattering, κ_c (parallel to the chain) is substantially higher than $\kappa_\perp$ (perpendicular to the chain) due the contribution of anisotropic spinon transport which dominates over the phonon contributions near room temperature [7, 34]. The agreement between the FFM and SSM measurements shows that the heat transport is not influenced by the character of the heat supply. For heat transport in applications, which usually deal with varying non-homogeneous heat sources, this is an advantageous property.

From the temperature increase at the back surface of the sample ΔT(back), an estimate can be made of the temperature increase at the front surface ΔT(front) during the heating laser pulse. In the most simple case, assuming that the heat capacity is constant or changing very little over the interval of the temperature increase, energy

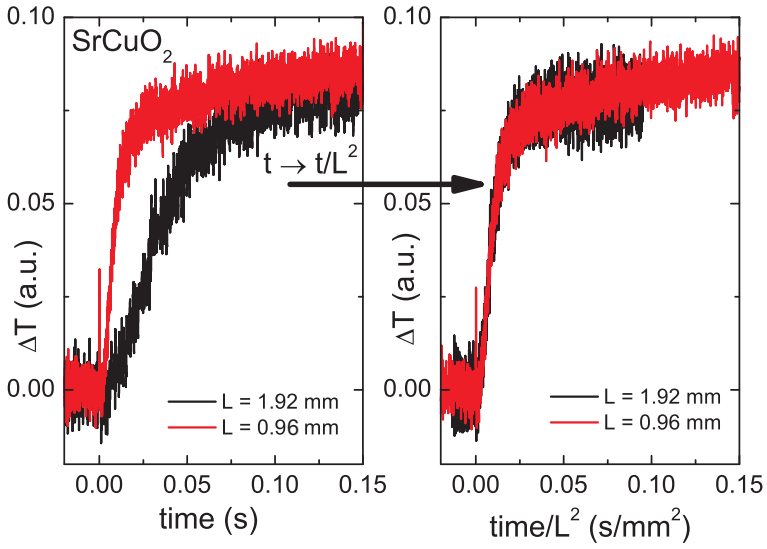

Figure 6.3: Principle of time axis transformation to facilitate the comparison of the temperature traces for different sample thicknesses. Left: temperature traces for two different samples of undoped $SrCuO_2$ as a function of time. Since the sample thickenesses are different, it is not clear in which sample the diffusion is faster. Right: after transforming the time axis by dividing by the sample length L^2 there is no influence of the sample length on the curve. Now it is immediately clear that the curves fall on top of each other and thus the diffusion constant is equal.

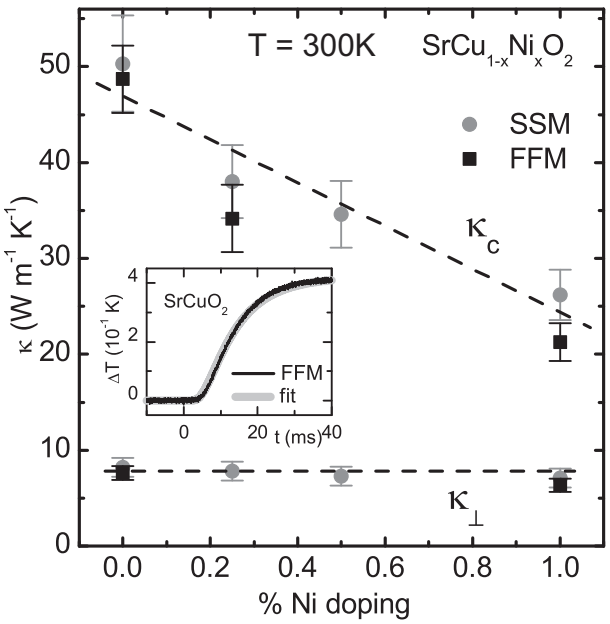

Figure 6.4: Doping dependence of the thermal conductivity κ of the spin chain compound $SrCu_xNi_{1-x}O_2$ obtained using conventional SSM (dots) and FFM (squares) experiments. The dashed lines are guides to the eye. The inset shows a typical result of an FFM time trace (black) together with a fit of Parker's formula [89] to the data (grey).

conservation requires the following relation to hold: $\Delta T(\text{front})\ \mu = \Delta T(\text{back})\ L$, where μ is the heat penetration depth and L is the sample length. μ is not equal to the optical penetration depth. On the timescale of the slow diffusion processes, the electron-phonon thermalization time (a few tenths of ps, [117]) is negligible and has to be taken into account to calculate the heat penetration depth, together with the particle diffusion constant [117]. Only a rough estimate can be made (since these numbers are not know exactly), which is ~ 1 μm.

Another advantage of these materials is seen when looking at the energy density dependence and estimated initial front surface temperature of the thermal conductivity, as is shown in figure 6.5. Even when the energy density is varied by one order of magnitude, no change in thermal conductivity is observed. From the absense of an energy density dependence, one can conclude that the high initial temperature does not influence the measured (average) thermal conductivity. This could be the case, since in the first few moments after heating, the temperature of the front surface goes up by a few hudreds of Kelvin for the highest laser power applied, which means that the local thermal conductivity is lower than the value at room temperature. However, apparently the system is in this state for such a short time that it does not measurably contribute to the measured thermal conductivity. Another observation supporting this conclusion is the linear increase of the temperature rise at the back surface with increasing heating power (not shown). Differences in estimated inital front surface temperature for the different samples are assigned to differences in laser alignment. These measurements show the applicability of this material for directional heat transport over a wide range of heating energy densities, as long as the sample thickness is much longer than the heat penetration depth (≈ 1 μm).

From the maximum ΔT, the sample length L and the heating energy density Q one can estimate the specific heat $C_p = Q/(\Delta T L)$. For the b-direction one finds 2.9×10^6 J m^{-3} K^{-1}. In this calculation the reflection from the surface is neglected. This is around 0.2 for $SrCuO_2$ [118]. Taking this into account $C_p = 2.3 \times 10^6$ J m^{-3} K^{-1}, which is in good agreement with the literature value of $C_p = 2.5 \times 10^6$ J m^{-3} K^{-1} as is calculated from the molar heat capacity and the lattic parameters. For the c-direction $C_p = 1.7 \times 10^6$ J m^{-3} is found. The extracted heat capacity should just be considered as a rough estimate, since slight changes in the alignment of the heating beam the energy density lead to variantions in the measured ΔT up to 30 %, as is seen from different measurements on the same sample.

The measured temperature traces for different sample thicknesses for pure $SrCuO_2$ crystal platelets along the chain direction are shown in figure 6.6, together with the best fit to Parker's formula [89]. The time axis for every trace is normalized for a sample length of 1 mm. It is seen that the traces for the thinnest and thickest sample are somewhat different from the other three, the trace for the thinnest sample being somewhat delayed and the trace for the thickest sample being somewhat expedited. The inset shows the extracted κ_c as a function of sample thickness. Two datapoints for the same sample thickness are two different measurements on the same sample. The result obtained in the conventional SSM is indicated by the grey bar. The distance between two arms of the temperature sensor is $\sim$ 0.5 - 1 mm in this method. It is seen that the agreement with the 3.25 mm sample is good, while for the other sample thicknesses the FFM gives an up to 25% lower thermal conductivity which possibly

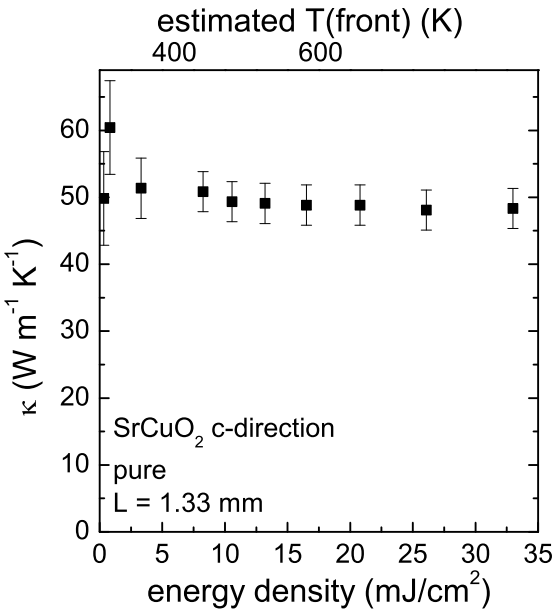

(a)

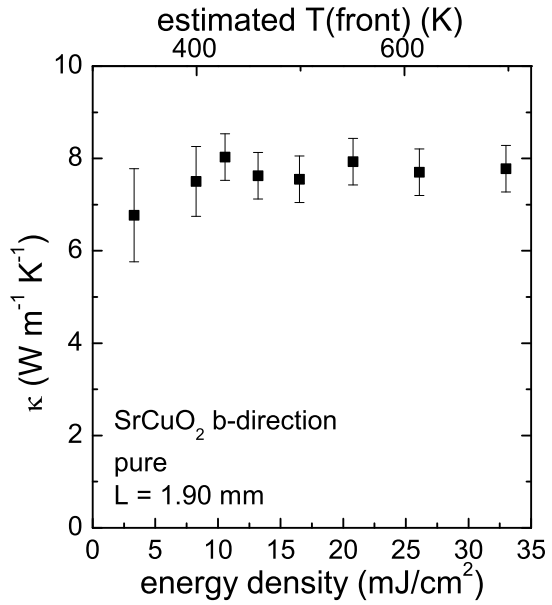

(b)

Figure 6.5: a) Thermal conductivity of $SrCuO_2$ as a function of energy density of the heating laser (lower x-axis) and estimated front surface inital temperature (upper x-axis) for the direction parallel to the chains (c-direction). Even when varying the energy density over an order of magnitude, no change in thermal conductivity is found. b) Thermal conductivity of $SrCuO_2$ as a function of energy density (lower x-axis) of the heating laser and estimated front surface inital temperature (upper x-axis) for the direction perpendicular to the chains (b-direction). Even when varying the energy density over an order of magnitude, no change in thermal conductivity is found.

shows a thickness dependence. On both the 1.00 mm and the 0.95 mm sample a heating power dependence was measured. Up to a decrease in heating power by a factor 20 no change in the measured κ_c was observed, in agreement with the measurement on the Ni-doped $SrCuO_2$ sample.

Also for these samples the heat capacity is extracted. After correcting for the reflectivity of the sample and the reflectivity of the window of the cryostat (which was at that time part of the setup), for three samples $C_p = 4.3 \pm 0.2 \times 10^6$ J m^{-3}. For two samples it was around 6×10^6 J m^{-3}. This is 2-3 times higher than the literature value. Probably this is due to heat losses, which are not taken into account in the model. An additional pathway for diffusion could be created by the connection between the cryostat and the sample. However, it should be small, since the order of magnitude for the heat capacity is correct.

Unfortunately, the $SrCuO_2$ rod was not long enough to prepare all samples at the same time. Therefore, first the thickest 3.25 mm sample was measured, from which the 1.92 and 0.95 mm sample were cut. After measuring these, the 1.92 mm sample was cut in two pieces of 1.00 mm and 0.53 mm, respectively. Therefore, making mechanical treatment necessary between measurements, it is possible that additional cracks are introduced in the material, which are lowering the thermal conductivity. So, from these data, one cannot distinguish between a lower κ_c due to more cracks and a lower κ_c due to intrinsic processes.

In conclusion, the dynamic thermal conductivity of $SrCuO_2$ has been measured as a function of Ni-doping, sample thickness, and heating power, and was compared to results obtained by a conventional steady state method. A strong decrease of the thermal conductivity with Ni doping was observed. The values found in the FFM are in agreement with the SSM. Furthermore, the thermal conductivity along the chain for pure $SrCuO_2$ samples with different thicknesses was measured. For the thickest sample the FFM value is in agreement with the SSM value. For thinner samples the thermal conductivity is up to 25 % lower. Since the thinner samples had additional mechanical treatment, the cause for this lower thermal conductivity could be both due to sample preparation and due to intrinsic processes. The absence of a change in the thermal conductivity with changing energy density of the heating laser by an order of magnitude shows the applicability of this material for a wide range of heating powers.

6.3.2 Spin ladders $Ca_9La_5Cu_{24}O_{41}$ and $Sr_{10}La_4Cu_{24}O_{41}$

In the inset of figure 6.7 a typical temperature trace measured with the FFM on the spin ladder compound $Ca_9La_5Cu_{24}O_{41}$ along the c-axis is shown, along with the fit to Parker's formula giving an extracted conductivity of κ_c(FFM)$\sim$ 35 W m^{-1} K^{-1}. This result strongly deviates from the one obtained with the SSM, κ_c(SSM)$\sim$ 85 W m^{-1} K^{-1} for a sample from the same batch; the discrepancy can be rendered more evidently by simulating the relative FFM temperature time trace, using the thermal conductivity value found in the SSM. This simulated curve is given by the thin blue line. Since κ_c(FFM) is so much lower than κ_c(SSM), probably an effective value is measured. Therefore, the subscript 'eff' is added for the spin ladder. Moreover, $\kappa_{\mathrm{eff},c}$(FFM) shows a remarkable dependence on the measured sample thickness; data are shown in the main graph of figure 6.7. In contrast to the pure $SrCuO_2$ samples, these samples come from

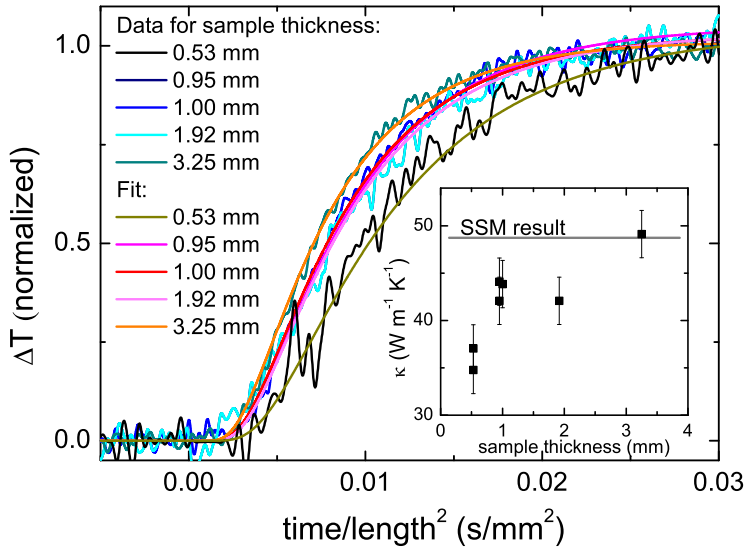

Figure 6.6: Thickness dependence of the thermal conductivity parallel to the chain κ_c of the spin chain compound $SrCuO_2$ (6N purity) obtained using FFM. The main graph shows temperature traces for different sample thicknesses, normalized to a 1 mm thick sample. The best fit of Parker's formula to the data is shown as well. The inset shows the extracted thermal conductivity as a function of sample thickness. The grey line indicates the steady state value. For the thickest sample the FFM and SSM thermal conductivity are in agreement, for the other thicknesses the FFM thermal conductivity is somewhat lower.

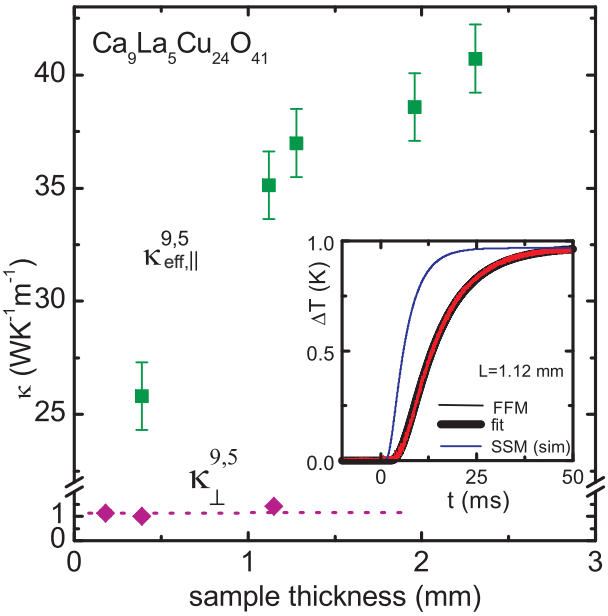

Figure 6.7: Thickness dependence of the thermal conductivity parallel to the ladder $\kappa_{\mathrm{eff},c}$ and perpendicular to the ladder κ_b of the spin ladder compound $Ca_9La_5Cu_{24}O_{41}$ obtained using FFM. The main graph shows the extracted thermal conductivity as a function of sample thickness. The data for the thermal conductivity parallel to the ladder show a thickness dependence. Even for the thickest sample the FFM and SSM thermal conductivity are in disagreement, the FFM value being ≈ 50 % lower. The data for the thermal conductivity perpendicular to the ladder show no thickness dependence and are in agreement with the SSM data. The inset shows the time versus temperature trace from which $\kappa_{\mathrm{eff},c}$ is extracted for the 1.12 mm sample thicknesses. The best fit of Parker's formula to the data is shown by the red line. A simulation of the temperature versus time trace using the SSM thermal conductivity is shown by the blue line.

the same batch and they were cut simultaneously, under the same conditions. All samples are from the same rod, apart from the 0.39 mm sample, which is from another rod, grown under the same conditions. On the other hand, along the a-direction, the FFM and SSM give consistent results, namely κ_b(FFM)$\sim\kappa_b$(SSM)$\sim$ 1.3 W m^{-1} K^{-1} and no thickness dependence in the FFM results is visible. The extracted $C_p = 2.0 \pm 0.5 \times 10^6$ J m^{-3} for three samples and $C_p \approx 4.5 \times 10^6$ J m^{-3} for the other two. It is not clear why the result differs so much for different samples, however, from changes in ΔT when the sample is remounted it is likely that it is related to the thermal contact between the sample and the sample holder. Furthermore, if the laser is slightly misaligned, the actual energy density on the sample will be lower, leading to an overestimation of C_p.

The thermal conductivity shows no dependence on energy density and wavelength of the heating laser, as is shown in figure 6.8. In the upper x-axis the estimated initial front surface temperature is shown. For the fundamental frequency (1064 nm) which is more powerful than the second harmonic, very high initial temperatures can be reached. Even when the energy density is varied by one order of magnitude, no change in thermal conductivity is observed. From the absense of an energy density

dependence one can conclude that the high inital temperature does not influence the measured (average) thermal conductivity.

Figure 6.9 shows the time trace obtained using the FFM for the spin ladder $Sr_{10}La_4Cu_{24}O_{41}$, together with three fits to Parker's formula. Again, the best fit is for κ_c(FFM) = 37 W m^{-1} K^{-1}, which is considerably lower than the value found by the SSM, κ_c(SSM) = 52 W m^{-1} K^{-1}. The extracted $C_p = 2.2 \times 10^6$ J m^{-3}, which is in agreement with literature.

Furthermore, $\kappa_{\mathrm{eff},c}$ was measured as a function of temperature for two samples of $Ca_9La_5Cu_{24}O_{41}$. In one measurement (blue squares), EuTTA was used as a temperature sensor, allowing to span the temperature range from 120 to 320 K. In the other measurement (orange squares), EuTFC was used, allowing to span the temperature range from 10 to 280 K. Furthermore, FFM measurements were done by our collaborator O. Mityashkin at the IFW Dresden for higher temperatures on the same 1.12 mm sample (black squares). In these measurements a commercial flash machine was used which detects the emitted infrared (IR) radiation from the sample surface and calculates the temperature increase from that. All these data are shown in figure 6.10. The inset shows a comparison with the thermal conductivity measured by the steady state method. The dynamic thermal conductivity $\kappa_{\mathrm{eff},c}$(FFM) peaks at the same temperature as the steady state thermal conductivity κ_c(SSM). Both samples measured with the FFM are in agreement in the overlapping range. The 1.62 mm sample has been cut from a thicker sample, which probably has introduced some additional cracks, and therefore it is not added to the thickness dependence data. κ_c(SSM) is higher for every temperature, with the highest discrepancy around the magnon peak temperature.

To have a better insight in the difference between κ_c(SSM) and κ_{eff_c}(FFM), the ratio of the two as a function of temperature is plotted in figure 6.11. The data can be devided into three regions. i) Below 50 K the ratio is getting larger with decreasing temperature. ii) Between 50 and 170 K the ratio is growing with increasing temperature and increasing magnon contribution to the thermal transport. iii) Above 170 K the ratio is slowly decreasing with increasing temperature and decreasing magnon contribution to the thermal transport. For cryostat temperatures $\leq$ 50 K we are in the non-linear regime. In this region the heat capacity C_p is small en strongly temperature dependent. By heating, the front surface temperature increases so much that also C_p increases considerably, thereby increasing the amount of energy needed to heat a certain volume. Therefore the maximum temperature will be lower than expected from the simple analysis assuming a constant C_p. This is consistent with non-linear dependence on energy density which will be shown below. Not only C_p is ill-defined in this regime. Also the diffusion constant will vary strongly because of the high induced temperature changes. Therefore, in this regime one measures an effective value of both quantities and therefore a κ at some effective temperature. Since it is not clear what exactly is going on in this non-linear regime, it is decided to discard this region in the later discussion of the data.

The thermal conductivity for every temperature is calculated from the diffusion constant determined by fitting the temperature trace with Parker's model [89]. From the maximum temperature increase ΔT at the back side of the sample, obtained from the same temperature trace, the specific heat C_p can be calculated, using $C_p = Q/(\Delta T\ L)$, where Q is the energy density of the laser pulse at the front surface and L is the sam-

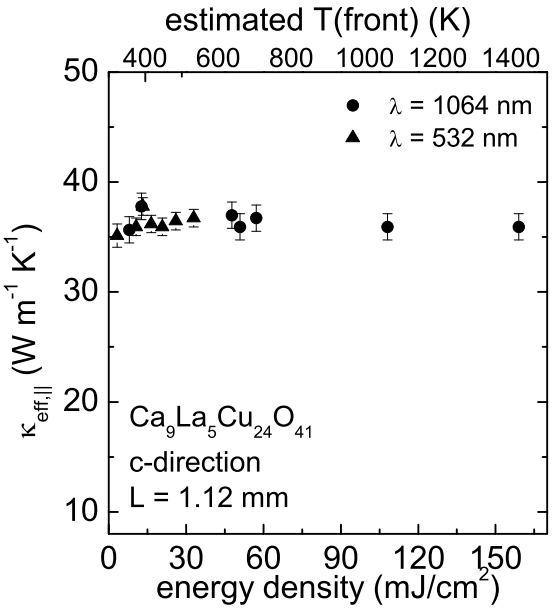

(a)

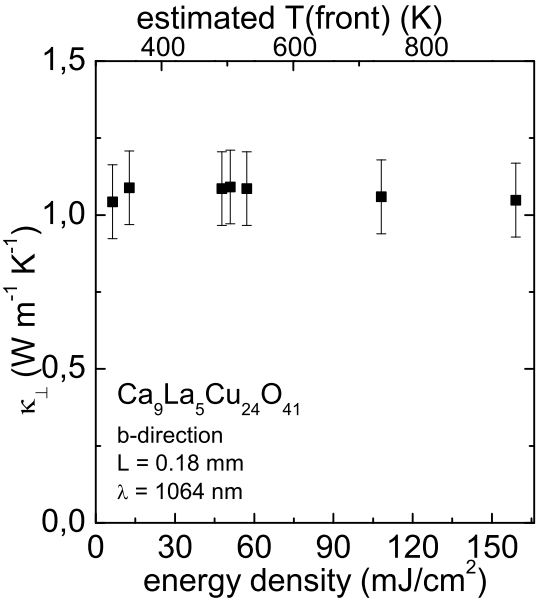

(b)

Figure 6.8: a) $\kappa_{\mathrm{eff},c}$ of $Ca_9La_5Cu_{24}O_{41}$ as a function of energy density (lower x-axis) and wavelength of the heating laser for the direction parallel to the chains. The estimated front surface inital temperature is shown in the upper x-axis. Even when varying the energy density over an order of magnitude, no change in thermal conductivity is found. b) κ_b of $Ca_9La_5Cu_{24}O_{41}$ as a function of energy density (lower x-axis) of the heating laser for the direction perpendicular to the chains (b-direction). The estimated front surface inital temperature is shown in the upper x-axis. Even when varying the energy density over an order of magnitude, no change in thermal conductivity is found.

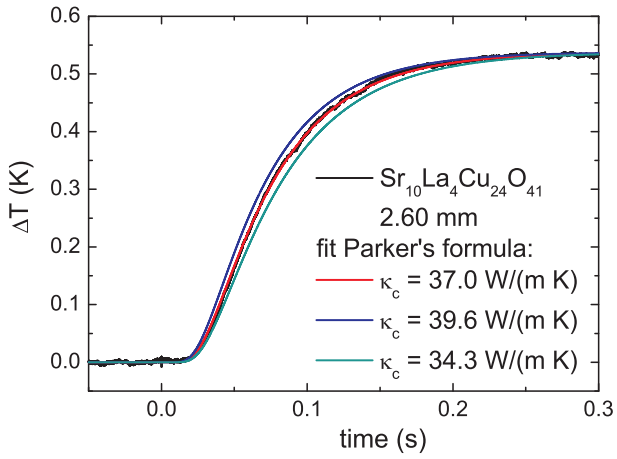

Figure 6.9: Time versus temperature increase at the back surface of a sample of the spin ladder $Sr_{10}La_4Cu_{24}O_{41}$ obtained using FFM. κ_c is extracted for the 2.60 mm sample thicknesses. The best fit of Parker's formula to the data is shown by the red line. The other lines, shown for comparison, are a plot of Parker's formula using a somewhat higher or lower thermal conductivity.

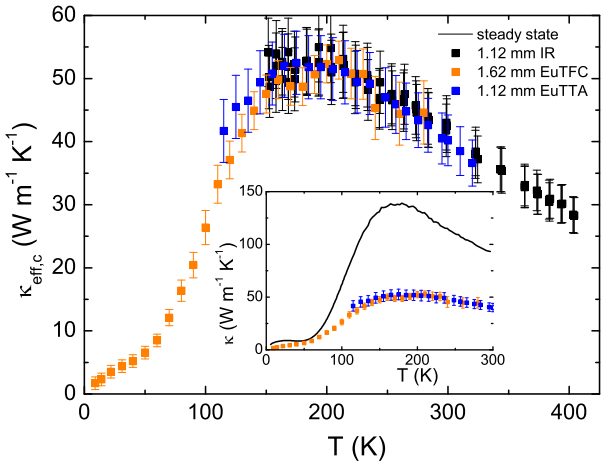

Figure 6.10: $\kappa_{\mathrm{eff},c}$, obtained by FFM, for the spin ladder $Ca_9La_5Cu_{24}O_{41}$ as a function of temperature. Two different samples are measured, one sample (orange squares) using EuTFC as a temperature sensor, and one (blue squares) using EuTTA as a temperature sensor. This sample was also measured by our collaborator O. Mityashkin for higher temperatures, using a commercial flash machine which is calculating the temperature of the surface from the emitted infrared (IR) radiation. The inset shows the data measured in Groningen, together with κ_c obtained with the SSM, which is higher, but peaks around the same temperature.

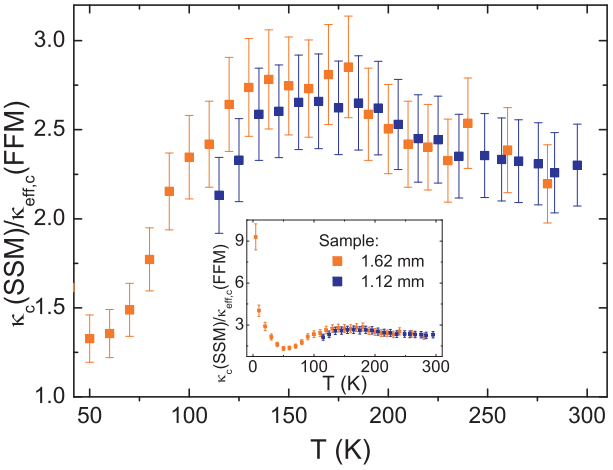

Figure 6.11: $\kappa_c(\mathrm{SSM})/\kappa_{\mathrm{eff},c}(\mathrm{FFM})$ for the spin ladder $Ca_9La_5Cu_{24}O_{41}$ above 50 K as a function of temperature. Two different samples are measured, one sample (orange squares) using EuTFC as a temperature sensor, and one (blue squares) using EuTTA as a temperature sensor. The inset shows the full range of the data.

ple thickness. This is done at every temperature and compared to the C_p measured in a standard calorimetry measurement by our collaborators at the IFW Dresden for a sample from the same batch, as is shown in figure 6.12. The extracted C_p is somewhat higher than the calorimetric C_p. This is probably due to the fact that, even though heating the front surface by a few hundreds of Kelvin, we neglect radiative losses in the simple analysis. Furthermore, the energy density at the front surface is estimated from the heating laser beam profile and incident power. This might contain a systematic error. For the calculation of $\kappa_{\mathrm{eff},c}$ the heat capacity determined by calorimetric means is used, since this is obtained more accurately and it is in agreement with literature data on $Sr_{14}Cu_{24}O_{41}$, with a maximum difference between the curves of 5 % [114].

From the temperature increase at the back surface of the sample $\Delta T(\mathrm{back})$, an estimate is made of the temperature increase at the front surface $\Delta T(\mathrm{front})$ during the heating laser pulse. At low temperatures, the simple formula used for room temperature measurements is not applicable, since the heat capacity C_p is small and very strongly temperature dependent. Therefore, $\Delta T(\mathrm{front})$ and $\Delta T(\mathrm{back})$ have to be found by integration. If one of the two is known the other can be calculated from the energy conservation requirement:

$$L \int_{T_0}^{T_{back}} C_p(T)dT = \mu \int_{T_0}^{T_{front}} C_p(T)dT$$
$$\Delta T_{back} = T_{back} - T_0$$
$$\Delta T_{front} = T_{front} - T_0$$

This equation is solved numerically for T_{front} for every cryostat temperature T_0. Again, the heat penetration depth μ is estimated to be ~ 1 μm. The data are plotted in figure 6.13. The inset shows the temperature increase at the front $\Delta T(\mathrm{front})$ as a function of the temperature in the cryostat. After growing with increasing temperature, the temperature increase at the front surface seems to stabilize around 250 K, probably due to the fact that at higher temperatures C_p saturates as well. For low cryostat

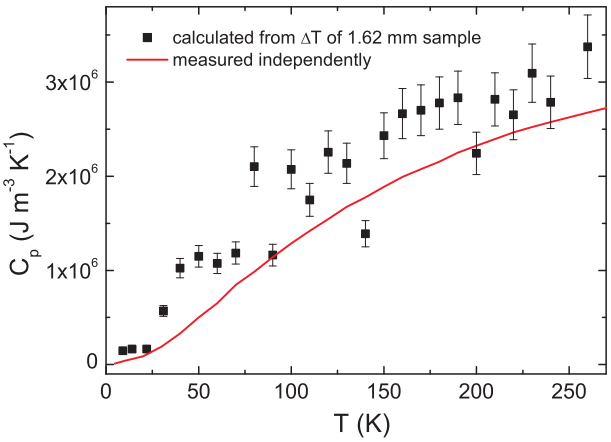

Figure 6.12: Heat capacity C_p for the spin ladder $Ca_9La_5Cu_{24}O_{41}$ as a function of temperature, extracted from the measured maximum temperature increase at the back surface. The data are compared to the heat capacity measured by standard calorimetry (red line). Although the behaviour with temperature is the same, the C_p extracted from the FFM is somewhat higher.

temperatures we are in the non-linear regime, as explained when discussing figure 6.11. By heating the temperature increases so much that C_p increases considerably, thereby increasing the amount of energy needed to heat a certain volume. Thereby the maximum temperature will be lower than expected from the simple analysis with a constant C_p, which is consistent with the data. Furthermore, the temperature increase is never so high to reach typical temperatures at which ions in the material start reacting ($\approx$ 960 K [119]), which is consistent with the absence of signatures of melting on the front surface.

Another indication that at low temperatures non-linear processes take place is found when looking at the heating laser power dependence of the thermal conductivity at 14 K, shown in figure 6.14. The main window shows the extracted thermal conductivity as a function of heating power. For lower heating powers κ_c goes up, which is different from what was found in power dependence measurements at room temperature. Furthermore, the inset shows ΔT(back) as a function of energy density of the heating laser. A non-linear relation between those is observed, due to the large variations of C_p and κ_c with temperature, inducing non-linearities in the behaviour.

6.4 Discussion

This discussion will concentrate on the thickness dependence of the thermal conductivity along the ladder $\kappa_{\mathrm{eff},c}$ of the spin ladder $Ca_9La_5Cu_{24}O_{41}$ and the difference in κ_c measured in a dynamic and a static measurement. There are several reasons to do so. First, the discrepancies for the spin chain $SrCuO_2$ and the spin ladder $Sr_{10}La_4Cu_{24}O_{41}$ are much smaller. Second, for pure $SrCuO_2$ a difference due to cracks in the sample (caused by cutting the thin samples from the thick samples after measuring those) is likely, since for the Ni-doped $SrCuO_2$ samples, which were all prepared simultaneously, no discrepancy between the fluorescent flash method (FFM) and the steady state

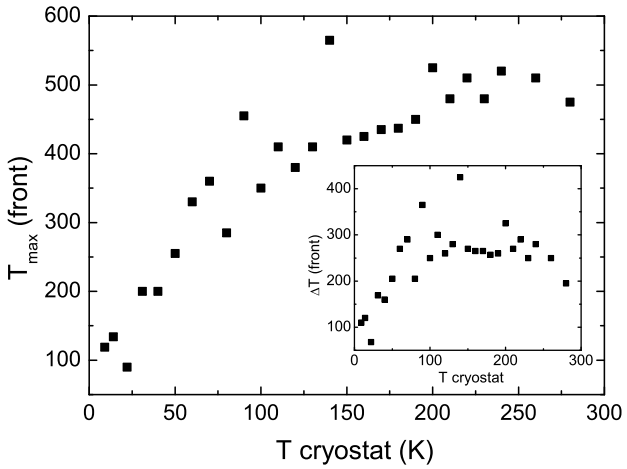

Figure 6.13: T(front) as a function of cryostat temperature, for a heating pulse energy density of 30 mJ/cm^2. The inset shows ΔT(front)=T(front)-T(cryostat). Both are numerically extracted from energy conservation requirements. At higher temperatures, where C_p reaches saturation, also ΔT(front) reaches saturation.

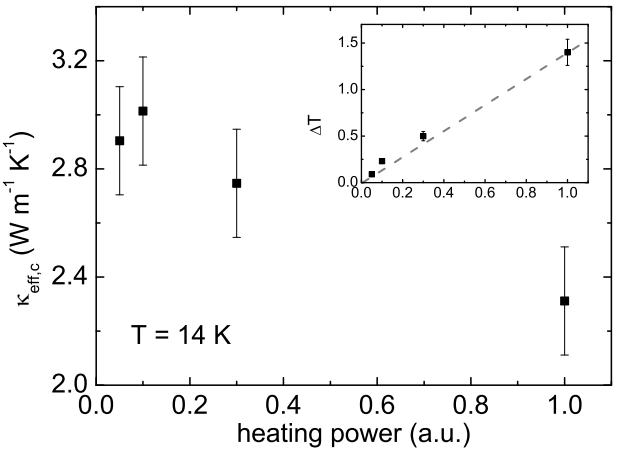

Figure 6.14: $\kappa_{\mathrm{eff},c}$ as a funtion of normalized heating power at the front surface. It increases with decreasing heating power. The inset shows ΔT(back) as a function of heating power. There is not a linear increase with increasing heating power. The grey line is a guide to the eye. Both are indications that variations in C_p and $\kappa_{\mathrm{eff},c}$ are large and cannot be neglected.

method (SSM) was found. Third, for the spin ladder $Sr_{10}La_4Cu_{24}O_{41}$, just one sample has been measured. Even though the two crystals used for FFM and SSM are from the same crystal rod, the presence of (more) cracks in one of the samples cannot be excluded. Therefore it is not clear if the difference is due to extrinsic properties or intrinsic processes related to the different nature (dynamic versus static) of the different experiments. Unfortunately no more samples were available to perform measurements on. Furthermore, understanding the heat transport in this system is more complicated because the compound is hole doped (see section 2.4); the holes can contribute to the heat transport differently for FFM and SSM.

The thickness dependence in the spin ladder compound $Ca_9La_5Cu_{24}O_{41}$ in the direction parallel to the ladder can be rationalized considering: i) that along the ladder direction heat is carried by interacting magnons and phonons, which thermalize as they diffuse across the sample; ii) the fact that, under the SSM and FFM experimental conditions, the sample is excited and probed through its phonon degrees of freedom only.

In the experiments, one expects a high degree of non-equilibrium in the magnetic-lattice initial temperatures: the optical pulse illuminating the sample at time zero creates high-energy electron-hole pairs that, through electron-phonon interactions, decay predominantly and quickly ($\approx$ 10 ps) into phonons; As they diffuse through the sample, phonons are then converted into magnons, with a thermalization time constant t_{lm}. In addition, the EuTTA fluorescent layer on the sample front side is mainly sensitive to the phonon temperature at the sample surface. Thus, as in the static case [90], diffusion of magnetic excitations is detected mainly because of their coupling to the lattice. In this framework, the relation between the diffusion times and the thermalization times determines the measured effective thermal conductivity. In particular, if the thermalization time is much shorter (longer) than the typical phonon diffusion time, $\kappa_{\text{eff}} \sim \kappa_l + \kappa_m$, ($\kappa_{\text{eff}} \sim \kappa_l$), being κ_{eff}, κ_l and κ_m the effective, phononic and magnetic thermal conductivity.

In this framework, an effective two-temperature model can be constructed for the lattice (l) and magnetic (m) degrees of freedom, as was explained in section 3.2. These coupled diffusion equations are solved with thermal insulation boundary conditions at the sample front ($x = 0$) and back ($x = L$) sample surfaces. Initial conditions are $T_l(x, 0) = T_0$ and $T_m(x, 0) = T_0 + \Delta T_0\, \theta(x - \mu)$, where θ is the Heaviside step function, μ the penetration depth of the exciting radiation and L the sample thickness [89] and T_0=300 K is the baseline temperature. A similar analysis has been carried out by Sanders and Walton [90] for the SSM. Thermal conductivities κ_l and κ_m have been fixed to their room temperature extracted from SSM measurements [8].

Due to the gapped nature of the excitation spectrum, the magnon specific heat shows an exponential behavior at low temperature, complicating its separation from the phonon contribution; therefore, theoretical estimates have to be used to fix the value of C_l and C_m. Since the Debye temperature for this compound class is $\theta_D \approx 240$ K$< T_0$, the phonon specific heat has been taken equal to the saturated Dulong-Petit value for the spin ladder, i.e. $C_l = 3k_BN/V$, where N and V are the number of atoms and volume of the unit cell considered. However, from figure 6.12 it is seen that this maximum value is not yet reached, therefore the real C_l will be somewhat lower. The value obtained, $C_l = 2.3 \times 10^6$ J m^{-3} K^{-1} (listed in Table 6.1), forms the largest

k_l	1	W m^{-1} K^{-1}	
k_m	85	W m^{-1} K^{-1}	
C_l	2.3×10^6	J K^{-1} m^{-3}	Ref. [47, 9]
C_m	1.5×10^5	J K^{-1} m^{-3}	Ref. [47, 9]
Δ_{1M}	280	cm^{-1}	Ref. [47, 9]

Table 6.1: Parameters for $Ca_9La_5Cu_{24}O_{41}$ used in the model.

contribution to the measured (total) specific heat $C_p = 2.8 \times 10^6$ J m^{-3} K^{-1}, as would be expected.

The magnon specific heat is determined by the dispersion of the two relevant, gapped, magnon bound states: the triplet (single magnon - 1M) and the singlet (double magnon - 2M) states, being $\epsilon_{1M}(\pi) = \Delta_{1M}$ the single magnon gap and $\epsilon_{2M}(0) = \Delta_{2M} = 2\Delta_{1M}$ the double magnon gap. Here, $\epsilon_{2M}(p_{||})$, and $\epsilon_{1M}(p_{||})$ are the 1M and 2M magnon dispersion relations and $p_{||}$ is the momentum along the rung direction. Since $k_B T_0 \approx \Delta_{1M} < \Delta_{2M}$, the specific heat can be obtained using an Einstein-like model for the density of states (DOS), using the appropriate triplet (1M) [6] and Bose-Einstein (2M) occupancy:

$$C_m(T) = k_B \frac{N_R}{V} \left[\mathcal{G}\left(\frac{\Delta_{1M}}{k_B T} \right) + \mathcal{D}\left(\frac{\Delta_{2M}}{k_B T} \right) \right], \tag{6.1}$$

where $\mathcal{G}(x) = 3x^2 \exp(x) / [3 + \exp(x)]^2$ and $\mathcal{D}(x) = x^2 \exp(x) / [1 - \exp(x)]^2$. Here, N_R is the number of ladder rungs in the unit cell and k_B is the Boltzmann constant. Due to the low temperature differences in the experiment, the temperature dependence of C_m has been neglected, taking $C_m = C_m(T_0)$. In this way we obtain $C_m \approx C_l/10$. This estimate is too low, since it is known from the estimation of C_l that $C_m = C_p - C_l$ should be $\geq 5 \times 10^5$ J m^{-3} K^{-1}, i.e. $C_l/5$. Currently it is not clear what is the reason for the difference from both estimates. Possibly the magnon excitation modes are partially hybridizing with optical phonon modes, which are, especially at higher temperature, substantially contributing to the measured C_p. Another possibility is that taking into account the temperature dependence is necessary to get a reasonable estimate.

The parameters used in 3.15 are listed in Table 6.1. The solution for 3.15 evaluated at $x = L$, equation 3.28, has been fitted to the thickness-dependent FFM data of the spin ladder compound to extract the value of the magnon-phonon thermalization time. Results are reported in figure 6.15, with the obtained values for the thermalization time τ_{lm}. An average value of $\tau_{lm} \approx 2.8 \times 10^{-4}$ s has been obtained, indicating a quite long magnon-phonon thermalization time. By comparison, the highest τ_{lm} is observed in 3D antiferromagnetic compounds like the classical antiferromagnet MnF_2, where $\tau_{lm} \approx 10^{-4}$ s [90].

In the spin chain compound $SrCuO_2$, no clear thickness dependence of k_c(FFM) is observed. In the framework of the preceding analysis, this would indicate that the spin-lattice thermalization time is much shorter than in the spin ladder case. This occurrence can be explained by considering i) the details of the spin-phonon scattering, and in particular the role of spin conservation requirements in determining the phase space available for the scattering process; and ii) the different spin-phonon energy

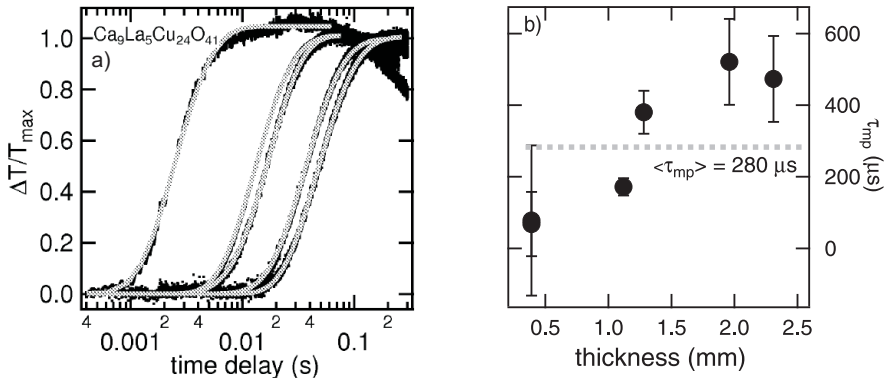

Figure 6.15: a) Temperature traces for all sample thicknesses with a fit to the 2-temperature model. b) Extracted magnon-phonon thermalization time τ_{lm} for all sample thicknesses.

overlap, determined by the differences in the excitation spectrum of spin chain and spin ladder.

In spin chains (spin ladders), due to *spin conservation* requirements, the magnetic and lattice subsystems interact via a two-spinon (two-magnon)/one-phonon scattering processes [120], in which one phonon state scatters with the two-spinon (two-magnon) state. The magnetic excitation spectra and the relevant phonon states are shown in figure 6.16 for the two cases. For the integrable spin chain model, shown in 6.16 a), the boundaries of the gapless two-spinon continuum are determined by the de Cloiseaux-Pearson dispersion relations [72]: $\pi J/2\,|\sin q| \leq \epsilon(q) \leq \pi J\,|\sin q/2|$, with the lower bound being the the single spinon (1S) dispersion. The antiferromagnetic exchange parameter $J = 1820$ cm^{-1} for $SrCuO_2$ [121]. In the spin ladder, the interchain rung coupling hybridizes the two spinon dispersions in a gapped triplet one magnon (1M) and singlet two magnon (2M) bound states, which also bounds the 1M-induced two-magnon continuum (2Mc) in the first half ($[0, \pi/2]$) of the ladder brillouin zone.

It is well known that in this class of 1D cuprate antiferromagnets the c-axis optical phonon modes dominates in the scattering process, having the highest magneto-elastic coupling. In particular, the 560 cm^{-1} A_g Cu-O stretching mode appears to be mainly responsible for the Lorenzana-Sawatzky phonon-mediated bi-magnon light scattering in $Ca_9La_5Cu_{24}O_{41}$ [47]. For the spin ladder, the spin gap ($\Delta_M = 280$ cm^{-1} for $Ca_9La_5Cu_{24}O_{41}$ [47, 79]) in the 1M state shifts the 2M and 2Mc dispersion far above the low-lying phonon dispersion. In the spin chain, the 2Sc dispersion has a seizable energy-momentum superposition with the c-axis phonons, enhancing in turn the phase space available for the scattering between spinons and phonons. From these considerations one can understand that the spinons in the spin chain have a higher probability to scatter with the phonons which are relevant in this experiment than the magnons in the spin ladder. This would lead to only a weak or absent thickness dependence in κ_c for the spin chain $SrCuO_2$, in agreement with our experimental findings.

Let us look a in a bit more detail at this idea. In figure 6.17 the phonon dispersion relation of a similar spin ladder compound $Sr_{0.5}Ca_{0.5}CuO_2$ is shown [122] (The exact phonon dispersion relation has not been measured for $Ca_9La_5Cu_{24}O_{41}$, but is supposed

to be similar because of the similarities in structure). The added red and blue line are the one- and two-magnon brands, respectively. It is seen that there is no crossing of the lowest (acoustical) phonon brands and the magnon brands. Therefore, taking into account the requirement of conserving energy, momentum and spin, it is only possible to convert the abundantly present acoustical phonons into magnons in a limited number of ways. An example is by annihilating an optical phonon and creating two magnons with opposite spin which together have an energy equal to the phonon energy. Because of the magnon gap, only (optical) phonons with an energy of at least two times 32 meV are available for this process. Therefore, low-order processes involving two or three acoustic phonons (maximum energy around 20 meV) are not possible. Another possibility is the creation of one magnon plus one phonon and the annihilation of a magnon. In this case one or more acoustic phonons could be involved in the scattering only if they are of long wavelength and low energy, because the magnon dispersion is very steep [24]. However, from the exponential increase of magnons with temperature below 100K it can be understood that processes involving acoustic phonons, which are already abundantly present at low temperature, are not significant [6, 9].

If one would estimate the thermalization time from the mean free path determined from κ(SSM), 50 nm at room temperature [9], and the magnon velocity, $\approx$ 2500 m/s from linearizing the dispersion relation, a much shorter scattering time for the spin ladder, $\sim 10^{-11}$ s, is expected. Why it is so different is understood by realizing the asymmetry of the conversion from phonons to magnons and vice versa. As was sketched in figure 6.1, in the dynamic experiment both conversions have to take place, since phonons are inserted and measured. In the static experiment one starts from a situation in which the magnons are already there (the thermocouple arms are placed at a considerable distance from the heating source, where there is thermal equilibrium) and measures how well they diffuse, thereby only being sensitive to the conversion from magnons to phonons. These processes are very asymmetric because to create magnons, several acoustical phonons with suitable spin, momentum and energy have to be present to create a magnon. The magnons already present, however, can scatter with any phonon present. Even though probably more acoustical phonons will be present in the material, *all* optical phonons present can easily scatter with the magnon, because they have an energy above the magnon gap. Scattering with acoustical phonons is less likely but possible too [9]. Therefore, the magnon to phonon conversion process has a higher scattering probability, thereby leading to a smaller thermalization time.

The temperature dependence of $\kappa_{\mathrm{eff},c}$ depicted in figures 6.10 and 6.11 strengthens the conclusion that the long magnon-phonon thermalization time is responsible for the discrepancy between the FFM and SSM data. The region below 50 K is difficult to analyze because for these temperatures there are strong non-linear effects, as was discussed before when discussing figure 6.11. Around 50 K, where in the SSM the magnon contribution to the heat transport is still small, the FFM and SSM give results which are only 30 % different. When the temperature and thus the magnon contribution to the heat transport is increasing, the ratio κ_c(SSM)/$\kappa_{\mathrm{eff},c}$(FFM) is increasing too. It is striking that the shape of the ratio (and thus the discrepancy) versus temperature follows exactly the shape of κ_c(SSM) at higher T, where the phonon contribution is negligible. If we assume for the moment that the temperature dependence of τ_{lm} is negligible, the ratio κ_c(SSM)/$\kappa_{\mathrm{eff},c}$(FFM) for a certain sample thickness would only

be determined by the anisotropy between κ_l and κ_m, growing when κ_m (which only partially contributes in the effective κ_c measured in FFM) grows. This is in agreement with our data. It is not very likely that τ_{lm} is strongly temperature dependent in the temperature range measured, since at every T the energy of the phonons which are excited is below the spin gap, such that the scattering phase space is very limited.

Apart from demonstrating surprisingly long phonon-magnon scattering times in the spin ladder compounds, the present results, combined with a quantitative two excitation diffusion based on a microscopic scattering model of the magnon and spinon scattering rates, enable a quantitative, easy, and robust experimental measurement of magnon-phonon lattice thermalization times. Thereby they are contributing to the still open discussion on spin-lattice relaxation in 1D quantum magnets [8]. For application of 1D quantum magnets in devices, the results from this chapter imply that spin chain materials are more suitable for quickly varying heating sources than spin chain materials, while for constant heating sources there is no difference. For the spin ladder and spin chain investigated in this chapter, however, even in the FFM the anisotropy is higher for the spin ladder (because κ_b is much lower), which is therefore more promising in heat channeling applications. Further discussion about applications is described in section 7.5, in which also the results from measurements on a prototype device (described in chapter 7) are considered.

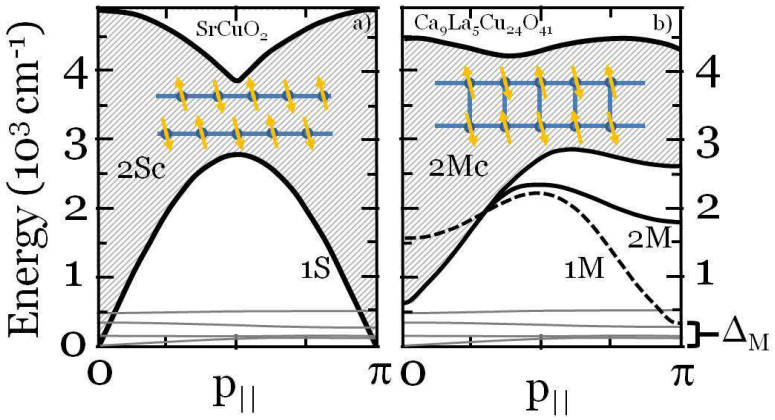

Figure 6.16: Magnetic excitation spectrum and phonon dispersion. (a) Spin chain $SrCuO_2$: the two spinon continuum (2Sc - shaded area) crosses the low liying c-phonon bands (gray lines, from [122]) near the $q = 0$ and $q = \pi$ Brillouin zone points; whereas in (b) spin ladder $Ca_9La_5Cu_{24}O_{41}$ the gap in the single-magnon (1M) bound state shifts the two-magnon continuum (2Mc) above the phonon dispersion. The two-magnon bound state (2M) is also shown for completeness.

6.5 Conclusion

In this chapter, fluorescent flash method (FFM) measurements have been performed on the spin ladders $Ca_9La_5Cu_{24}O_{41}$ and $Sr_{10}La_4Cu_{24}O_{41}$, and the spin chain $SrCuO_2$. The thermal conductivity has been extracted as a function of heating laser energy density and sample temperature. Results are compared to the conventional steady state method (SSM). Surprisingly, while the FFM method gives comparable results

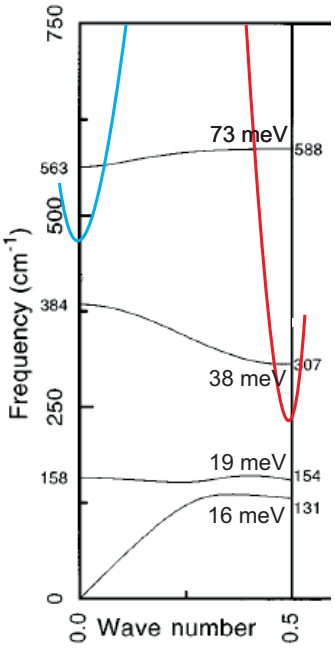

Figure 6.17: Phonon dispersion of the spin ladder compound $Sr_{0.5}Ca_{0.5}CuO_2$ with added one-magnon (red) and two-magnon (blue) dispersion bands. The shaded area indicates the two-magnon continuum. It is seen that the magnon dispersion gap is such that the lower lying phonon bands do not cross the magnon bands. This, together with the requirement of conserving energy, momentum and spin, gives rise to a low scattering probability. Picture adapted from [122].

for the spin chain compound $SrCuO_2$, both in undoped and Ni-doped crystals, the thermal conductivity extracted from the FFM measurements in the ladder direction of $Ca_9La_5Cu_{24}O_{41}$, $k_{eff,c}$(FFM), is found to: i) be substantially lower than the one obtained by the SSM method; and ii) show a remarkable and unexpected dependence on the sample thickness. This is interpreted as the signature of the failure of the single-fluid diffusion theory to describe the thermal transport in the ladder compound. For the spin ladder $Sr_{10}La_4Cu_{24}O_{41}$, only one sample has been measured. Also for this sample the thermal conductivity along the ladder direction is substantially lower than the one obtained by the SSM method.

Interpreted in the framework of the interacting magnon-phonon heat diffusion, the thickness dependent data allow to extract a particularly long estimate of the magnon-phonon scattering time for the spin ladder compound (i.e. in the microsecond range). This is supported by the temperature dependence of the discrepancy between the FFM and SSM, which follows precisely the dependence of the magnon contribution to the heat transport, being largest when the magnon contribution peaks and going to unity when the magnon contribution vanishes. The differences between the spin ladder and the spin chain compounds can be rationalized by considering that in the spin chain compound the absence of a gap in the spinon spectrum enhances the energy superposition between the 2-spinon excitation continuum and the phonon dispersions, increasing the magnon-phonon scattering phase space.

The measurements and analysis performed in this chapter show that by choosing samples with suitable thicknesses (i.e. in which diffusion times are the same order of magnitude as thermalization times), the spin-phonon thermalization time can be extracted from a fit with a two-fluid model to the FFM temperature traces for different sample thicknesses. The spin-phonon thermalization time is a dynamic quantity and cannot be extracted easily from SSM measurements. It is instrumental for the understanding of low-dimensional phenomena.

7. Imaging of anisotropic heat transport

7.1 Introduction

The spin ladder compound with the highest anisotropy in thermal conductivity at room temperature, which is therefore most promising for applications, is the spin ladder $Ca_9La_5Cu_{24}O_{41}$. This material has a structure which consists of two types of non-magnetic chains, and a sheetlike arrangement of parallel, but only weakly interacting, Cu_2O_3 two-leg ladders. The ladder structure is formed by the Cu ions with S=1/2 spins, which are strongly coupled via Cu-O-Cu superexchange interactions. The full structure is described in chapter 2.4. As is explained there, the magnetic excitations only contribute to the heat transport along the spin ladder structure. From dispersion relation measurements a spin gap as large as 35 meV between the singlet ground state and the triplet excited state was found [79, 47, 124]. On the other hand, the lattice excitations (phonons) are isotropic. This leads to a high anisotropy with a ratio between the thermal conductivity coefficients parallel ($\kappa_{||}$) and perpendicular ($\kappa_{\perp}$) to the spin structure of ~ 40 at room temperature, with $\kappa_{||}$ is 95 $Wm^{-1}K^{-1}$, i.e. a value comparable to that of a metal [9]. Since the cuprate compounds are Mott insulators they provide an escape route from the apparent paradox of having both a high thermal conductivity and an electrically insulating behavior. Also, doping with switchable magnetic defects potentially makes tuning of the thermal conductivity achievable.

Apart from the spin ladder $Ca_9La_5Cu_{24}O_{41}$ another spin ladder with a high anisotropy is investigated; $Sr_{10}La_4Cu_{24}O_{41}$. For this compound the thermal conductivity along the ladder is $\sim$ 52 $Wm^{-1}K^{-1}$, while the phonon thermal conductivity is the same as for $Ca_9La_5Cu_{24}O_{41}$, making this compound suitable for directional heat transport too. Furthermore, the spin chain compound $SrCuO_2$ is measured, comparing a pure sample with one containing 0.25 % Ni. For the pure compound the themal conductivity along the chain is 48 $Wm^{-1}K^{-1}$ and for the doped compound it is 34 $Wm^{-1}K^{-1}$, while the thermal conductivity perpendicular to the chain is 7 $Wm^{-1}K^{-1}$. The spin chain compounds are interesting, since ballistic spinon heat transport has been predicted in these materials [49].

In order to investigate the application of quantum magnets to thermal management of microelectronics, the experimental method employed should reproduce the spatially inhomogenous, pulsed heat imprint characteristics of miniaturized electronic devices.

Part of this chapter has been published in *The international journal of mass and heat transfer* [123].

Also, the ensuing thermal evolution has to be probed in a time-resolved fashion in order to measure the spatial-temporal thermal response of the device. The standard four-probe steady state method employed so far [125] for studying bulk heat conductivity in the compounds investigated here requires a uniform, constant heat current to allow reliable measurements and has certain limitations concerning sample size and shape. In the work described here the front surface of the sample is heated optically, using a laser pulse, or electrically, using a deposited gold strip. The laser pulse is used to create a hot spot at the sample surface, while the gold strip on top of the sample resembles a microelectronic device consisting of a heat producing structure with a cooling substrate attached. Time-resolved fluorescent microthermal imaging (FMI)[89, 104, 100] is used to probe the time- and position-resolved temperature profile by detecting variations in the fluorescence intensity of a thin rare-earth chelate layer deposited onto the sample [111]. Distinctive advantages of this non-conventional optical technique arise when compared to the steady state method, such as the possibility to vary the heating volume and power and the short measurement time, combined with a broad applicability, ranging from thin films to the observation of heat transport patterns on real microchips and small electronic devices [104, 100].

7.2 Experimental procedure

The $Ca_9La_5Cu_{24}O_{41}$, $Sr_{10}La_4Cu_{24}O_{41}$, and $SrCuO_2$ single crystals were grown by the travelling solvent floating zone method [97]. See also section 4.1.1. Two $SrCuO_2$ crystals were used in the experiment; one 99.9999 % pure crystal and one 99.99 % pure crystal with Ni doping ($SrCu_{1-x}Ni_xO_2$ with x=0.0025). Thin platelets with the b-axis out of plane were cut from all crystals, giving a crystal surface parallel to the c-axis (magnon/spinon plus phonon transport) and the a-axis (only phonon transport). The surface was machine polished by SiC paper (5 μm grains) and subsequently by a cloth with 1 μm diamond suspension. The surface roughness was measured by a confocal microscope. By careful polishing the surface RMS roughness of the $Ca_9La_5Cu_{24}O_{41}$ sample with the cross on top was brought down to only 20 nm. The other samples, which were polished with just the SiC paper, had a RMS roughness of about 1 μm.

For temperature detection, the FMI method was used with an EuTTA layer as a temperature sensor, as is described in section 4.2.3. The gold cross was deposited on the sample as described in section 4.2.3. In the optical heating experiment, a focused 488 nm Argon-ion CW laser beam (spot size $\sim 40\,\mu$m FWHM, power $\sim 20\,$mW) heated a small volume of the sample at a position were no gold was deposited. An acousto-optical modulator (AOM) was used to produce the desired pulse duration. The EuTTA/dPMMA layer is transparent for this wavelength. In the electrical heating experiment, the two perpendicular gold strips forming a cross structure were heated electrically, one at a time. For both heating methods, the area around the heat pulse was illuminated by a pulsed 370 nm defocused laser beam (the second harmonic of a Ti:Sapphire laser, repetition rate 80 MHz, power on the sample $\sim 1.5\,$mW) to excite the EuTTA/dPMMA layer. Pulse trains with the desired duration were produced by a second AOM. The photoluminescence was collected by an objective, filtered from heating/excitation radiation, and imaged onto a Peltier-cooled CCD-camera. The magnification of the objective was 10 times, which for the present system corresponded to

a resolution of 1.6 μm per CCD pixel. The measurements were performed in a time-resolved fashion. The sample was heated for 0.02 ms for the optical heating or 0.05 ms for the electrical heating, after which the heating was switched off. Then the surface was imaged with different delays between heating and imaging laser, with integration time 0.02 or 0.03 ms. The mean values and standard deviations were obtained by averaging 300 to 400 measurements. The synchronisation between the two AOM's and the processing of the images from the CCD-camera was done by a PC. The improvement of this technique compared to the method used by Kolodner *et al.* [100] is that it is used in a time-resolved fashion. The smallest time-resolution achieved is 20 μs. This resolution allows to follow the time-evolution of the heat spread along the surface in different directions. From that, the diffusion constant in different directions can be determined by fitting the data with the heat equation as will be described in the following section.

7.3 Model

The observed temperature dynamics can be described by the anisotropic three-dimensional heat diffusion equation

$$\frac{\partial T}{\partial t} = \vec{\nabla}\left(\vec{D}\cdot\vec{\nabla}\right)T + S(\vec{r},t), \tag{7.1}$$

where T is the temperature, S is a source term depending on time t and position $\vec{r}$, and $\vec{D}$ is the (diagonal) diffusivity tensor. Equation 7.1 has been integrated numerically using both ad-hoc written software and the commercially available software package TransAT developed by ASCOMP GmbH [126]. After extracting the diffusion constant from fitting, the thermal conductivity is calculated by $k_i{=}\rho c_p D_i$, using for the molar density $\rho = 1690$ m^{-3} [80] and for the specific heat $c_p = 1700$ J Mole$^{-1}K^{-1}$ [114] for the spin ladder $Ca_9La_5Cu_{24}O_{41}$, $\rho = 1590$ m^{-3} [77] and $c_p = 1700$ J Mole$^{-1}K^{-1}$ [114] for the spin ladder $Sr_{10}La_4Cu_{24}O_{41}$, and $\rho = 29000$ m^{-3} [115] and $c_p = 87$ J Mole$^{-1}K^{-1}$ [116] for the spin chain $SrCuO_2$, respectively. The density is assumed to be constant over the temperature interval (T, T+ ΔT), which is valid for small temperature changes or when the temperature dependence is weak.

It was shown that neglecting the duration of the probe pulse does not alter the results, since the duration of the probe pulse has the same length as the time difference between two consecutive pump-probe delay times. This shortens the calculation time since no time convolution of the simulation results has to be performed before comparing them with the experimental results. This equation is solved numerically with thermal insulation boundary conditions. In the x and y direction the spatial heat profile is taken as measured. In the z direction the penetration depth of the light ($\approx$ 500 nm) is taken into account, as are the pulse duration of both pump and probe beam.

However, equation 7.1 can be simplified. Note that the diffusion dynamics along the z-axis can be factorized out and ignored, since it does not couple with the diffusion parallel to the surface. Moreover, if the temperature dependence of the thermal parameters (thermal conductivity and specific heat) in equation 7.1 can be neglected,

then the anisotropic heat diffusion equation at the surface reduces to [56]:

$$\frac{\partial T}{\partial t} = \sum_{\nu=x,y} D_\nu \frac{\partial^2 T}{\partial \nu^2} + S(\vec{r}, t). \tag{7.2}$$

Equation 7.2 can be solved analytically through the Green's function formalism. With open boundary conditions, the in plane Green's function of the problem results in a product of two Gaussians:

$$G(x - x', y - y') = \prod_{\nu=x,y} \frac{1}{2\sqrt{\pi D_\nu(t)}} \exp\left(-\frac{(\nu - \nu')^2}{4D_\nu t}\right). \tag{7.3}$$

As said, the diffusion along the z direction (perpendicular to the surface) is neglected, since it does not influence the Gaussian width in the parallel directions. To find the solution for the experimental conditions used in this work, the Green's function has to be convolved with the initial conditions induced by the Joule heated strip and the optical heating profile, respectively:

- For the Joule heating experiment, a temperature profile coinciding with the heated gold strip, rectangular in section and 10 μm wide along one direction, and of infinite length along the perpendicular direction, heated with a constant power in time for 50 μs.
- For the optical heating, a two-dimensional Gaussian with full width half maximum 40 μm in space, with constant power in time for 20 μs.

Both heating methods produce temperature profiles that after the excitation quickly converge to a Gaussian shape. Therefore, a Gaussian-shaped initial temperature profile has been used in both cases as initial conditions. By performing the convolution we obtain

$$\Delta T = \Delta T_0 \prod_{\nu=x,y} \sqrt{\frac{t_{0,\nu}}{t - t_{0,\nu}}} \exp\left(-\frac{(\nu - \nu')^2}{4D_\nu(t - t_{0,\nu})}\right). \tag{7.4}$$

Here ΔT_0 is the maximum of the t=0 temperature profile. For the Joule heating experiment, there is no temperature gradient in the direction parallel to the strip. Therefore only one direction is considered. From equation 7.4 the Gaussian width σ (or the full width at half maximum FWHM = 2.355σ) can be extracted:

$$\sigma(\nu) = \sqrt{2D_\nu(t - t_{0,\nu})} \quad \nu = x, y \tag{7.5}$$

Following a standard approach, the introduced timeshift $t_{0,\nu}$ (representing the time at which the heating pulse is applied) is not treated as an independent fitting parameter, but is a direct function of the diffusivity and the value of the first data point collected after the heating pulse has vanished, by applying equation 7.5 to this data point we get:

$$t_{0,\nu} = t_m - \frac{\sigma_{t_m}^2}{2D_\nu} \tag{7.6}$$

where t_m is the time at which the first measurement after the heat pulse is performed (in our case 20 or 30 μs), σ_{t_m} is the standard deviation of the Gaussian at $t = t_m$ and D_ν

is the diffusion constant in the direction ν. In this treatment, the value of $t_{0,\nu}$ depends on the diffusion constant along that specific direction. Equation 7.5 is used to directly extract the thermal conductivity from the best fit to the standard deviation evolution in time for the optical and Joule heating experiments on $Ca_9La_5Cu_{24}O_{41}$. In the other optical experiments the initial temperature profile is different from a Gaussian shape, and therefore the full numerical analysis is performed.

As mentioned, this model can be applied only if the temperature dependence of the thermal constants of the problem can be safely ignored. This seems to be a reasonable assumption, since under the present experimental conditions the maximum temperature rise induced in the material by either the laser or the Joule heating is evaluated to be $\Delta T_0 \approx 45$ K. Considering the temperature before the excitation to be T_0=300 K, ΔT_0 induces an initial 15% thermal conductivity decrease and a 5% specific heat increase, and therefore a 20% decrease of the diffusivity. After the heating pulse has vanished, the temperature and the thermal parameter values relax back to their pristine values as $\Delta T \propto t^{-1}$ (see equation 7.4). This assures that the maximum effect on the evolution of temperature profile widths would be less than 5% for most of the pump probe delays time considered here, i.e. well within the experimental uncertainties of the technique. This is also confirmed by comparing the solution to the one dimensional thermal diffusion model, where the thermal parameters have been fixed at their room temperature values, and a numerical solution of equation 7.1, where the full temperature dependence of the thermal parameters as reported in literature is taken into account [9, 8].

7.4 Results

7.4.1 Optical heating

Heat spread along 1 μm RMS surface roughness samples

In figure 7.1 the time evolution of the heat spread from a hot spot, created by a laser pulse, along the surface of the spin ladder compound $Sr_{10}La_4Cu_{24}O_{41}$ is shown for 3 different delay times between pump and probe beam. The left column shows the data, while the right column shows a two-dimensional Gaussian fit to the data. Not all delay times are shown. In total, 10 delay times were measured, ranging from 0 to 0.18 ms, in steps of 0.02 ms. The data are normalized in order to enhance the contrast at later times. The maximum temperature increase reached is 7 Kelvin. Figure 7.2 shows the width of the fitted Gaussian as a function of delay time extracted from the temperature profile of the spread parallel and perpendicular to the ladder. Fitting by the Gaussian one-dimensional model (equation 7.5) is shown. The first datapoint is not considered in the fit, because it is measured during heating. The thermal conductivities found are $\kappa_{||} = 18 \pm 3$ W m^{-1} K^{-1} and $\kappa_{\perp} = 1.3 \pm 0.5$ W m^{-1} K^{-1}. The thermal conductivities found in a bulk dynamic experiment are $\kappa_{||} = 37 \pm 4$ W m^{-1} K^{-1} and $\kappa_{\perp} = 2.5 \pm 0.2$ W m^{-1} K^{-1}.

In figure 7.3 the time evolution of the heat spread from a hot spot, created by a laser pulse, along the surface of the spin ladder compound $Ca_9La_5Cu_{24}O_{41}$ is shown for 3 different delay times between pump and probe beam. The left column shows the

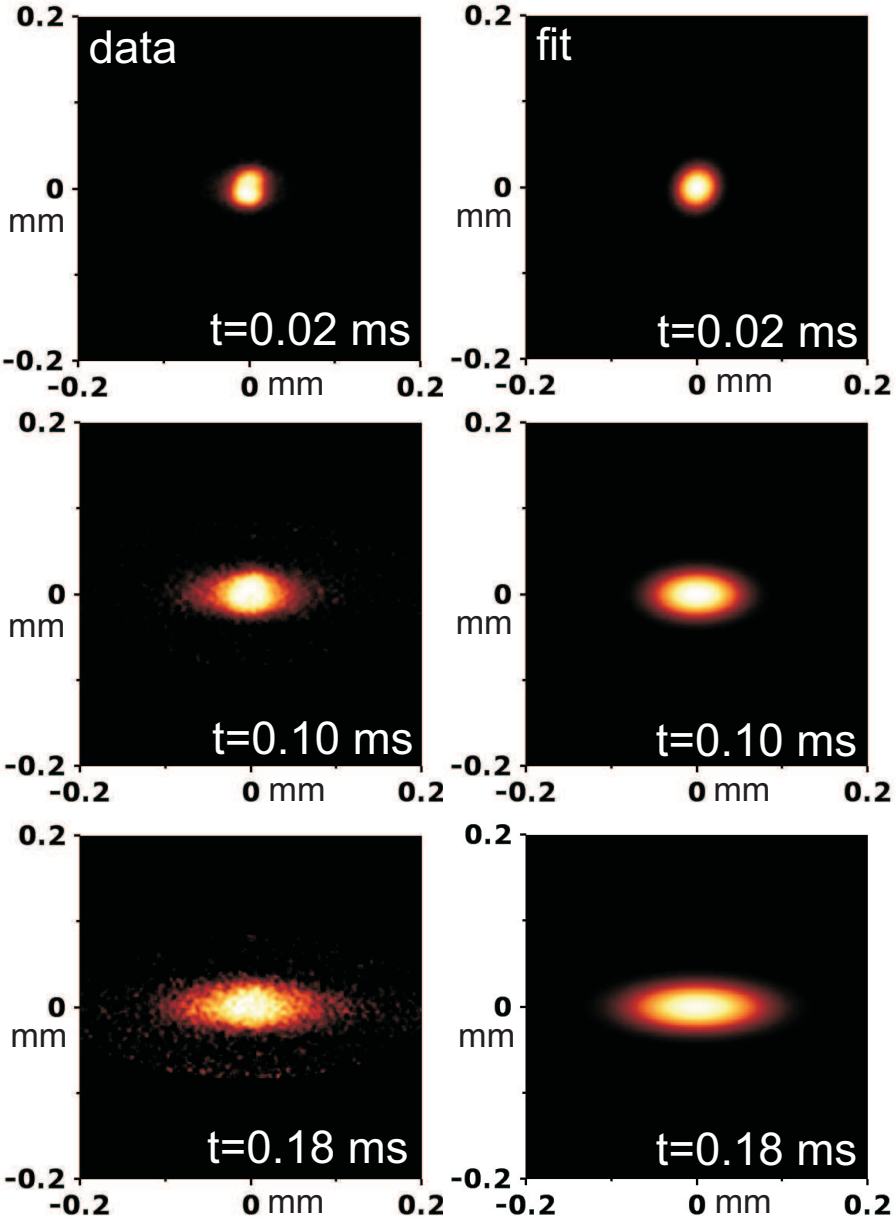

Figure 7.1: Time evolution of the heat spread from a hot spot in the spin ladder $Sr_{10}La_4Cu_{24}O_{41}$. The left column shows the data, while the right column shows the best Gaussian fit to the data. Heating is done by a laser with a pulse duration of 0.02 ms. The integration time for the probe UV-pulse is 0.02 ms. The ladder direction is horizontal. The anisotropy of the diffusion process is clearly seen.

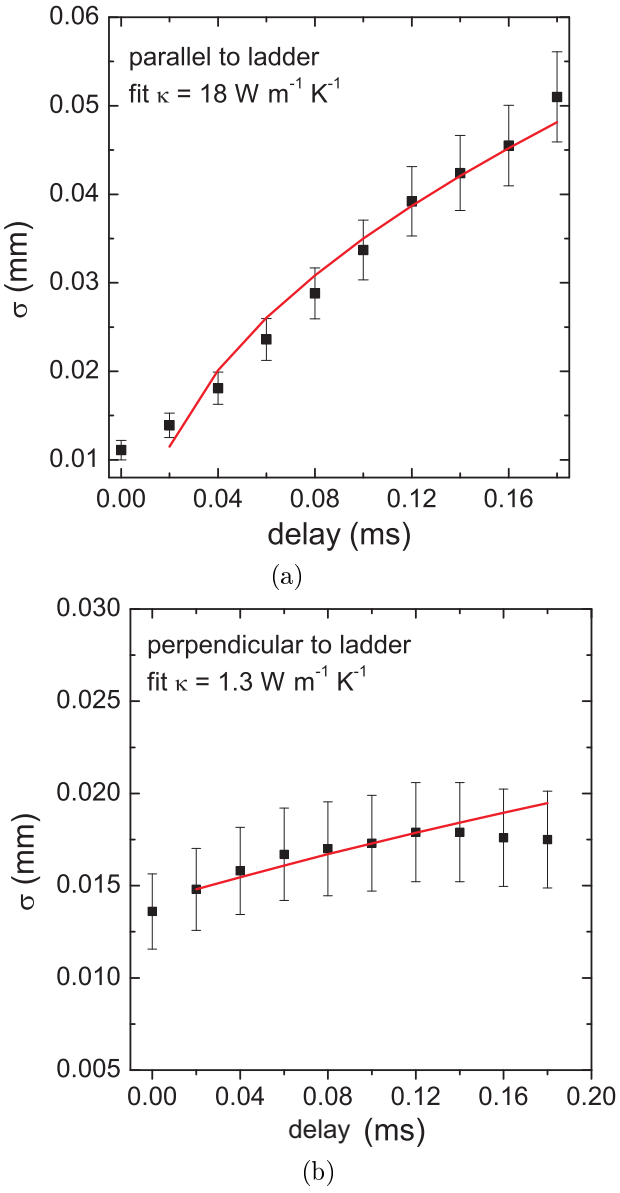

Figure 7.2: a) Squares: width of the fitted Gaussian in figure 7.9 as a function of delay time extracted from the temperature profile of the heated surface parallel to the ladder. Line: fitting by the Gaussian one-dimensional model. The thermal conductivity is $\kappa_{||} = 18 \pm 3$ W m^{-1} K^{-1}. b) Squares: width of the fitted Gaussian in figure 7.9 as a function of delay time extracted from the temperature profile of the surface perpendicular to the ladder. Line: fitting by the Gaussian one-dimensional model. The thermal conductivity is $\kappa_{\perp} = 1.3 \pm 0.4$ W m^{-1} K^{-1}.

data, while the right column shows a two-dimensional Gaussian fit to the data. Not all delay times are shown. In total, 10 delay times were measured, ranging from 0 to 0.18 ms, in steps of 0.02 ms. The data are normalized in order to enhance the contrast at later times. The maximum temperature increase reached is 16 Kelvin. In this experiment the heating beam was not Gaussian. Therefore, it was decided to analyse the data by comparing with a simulation of the full three-dimensional anisotropic heat equation. The heat pulse is rectangular in the time domain and is equal in shape to the measured heat profile in space. Figure 7.4 shows the measured and fitted temperature profiles as a function of delay time in the direction parallel to the ladder. The thermal conductivities found are $\kappa_{||} = 23.5 \pm 3$ W m^{-1} K^{-1} and $\kappa_{\perp} = 0.55 \pm 0.3$ W m^{-1} K^{-1}. The thermal conductivities found in a bulk dynamic experiment are $\kappa_{||} \sim 37 \pm 5$ W m^{-1} K^{-1} and $\kappa_{\perp} = 2.5 \pm 0.2$ W m^{-1} K^{-1}.

Obtaining good quality data for the spin chain compound $SrCuO_2$ is more complicated than for the spin ladders. Because of the higher reflectivity of the sample surface, a lower maximum temperature increase can be reached. A way to overcome this difficulty is to make the heating pulse longer. However, if the pulse is too long, all the dynamics take place within the heating pulse so no dynamics after the pulse can be measured. Furthermore, the heating beam creates a reflection which cannot be filtered out completely. This reflection is measured separately and subtracted from the data, which leads to a slightly higher noise level at the center part of the heat profile. In figure 7.5 the time evolution of the heat spread from a hot spot, created by a laser pulse, along the surface of the spin chain compound $SrCuO_2$ (pure, 99,9999 %) is shown for 3 different delay times between pump and probe beam. The left column shows the data, while the right column shows a two-dimensional Gaussian fit to the data. Not all delay times are shown. In total, 8 delay times were measured, ranging from 0 to 0.18 ms, in steps of 0.03 ms. The data are normalized in order to enhance the contrast at later times. The maximum temperature increase reached is 12 Kelvin. Figure 7.6 shows the measured and fitted temperature profiles as a function of delay time in the direction parallel and perpendicular to the chain. The thermal conductivities found are $\kappa_{||} = 25 \pm 4$ W m^{-1} K^{-1} and $\kappa_{\perp} = 1.3 \pm 0.3$ W m^{-1} K^{-1}. The thermal conductivities found in a bulk dynamic experiment are $\kappa_{||} = 48 \pm 3$ W m^{-1} K^{-1} and $\kappa_{\perp} = 7 \pm 0.5$ W m^{-1} K^{-1}.

In figure 7.7 the time evolution of the heat spread from a hot spot, created by a laser pulse, along the surface of the spin chain compound $SrCuO_2$ with 0.25 % Ni-doping is shown for 3 different delay times between pump and probe beam. For this particular experiment, a larger spotsize of ~ 100 μm was used. The left column shows the data, while the right column shows a two-dimensional fit to the data. Not all delay times are shown. In total, 10 delay times were measured, ranging from 0 to 0.9 ms, in steps of 0.1 ms. The data are normalized in order to enhance the contrast at later times. The maximum temperature increase reached is 9 Kelvin. In this experiment the heating beam was not Gaussian. Furthermore, the temperature profile in the first timesteps was not Gaussian, making the analysis with the simple model impossible. Therefore, it was decided to analyse the data by comparing with a simulation of the full three-dimensional anisotropic heat equation. The heat pulse is rectangular in the time domain and is equal in shape to the measured heat profile in space. Figure 7.8 shows the measured and fitted temperature profiles as a function of delay time in the

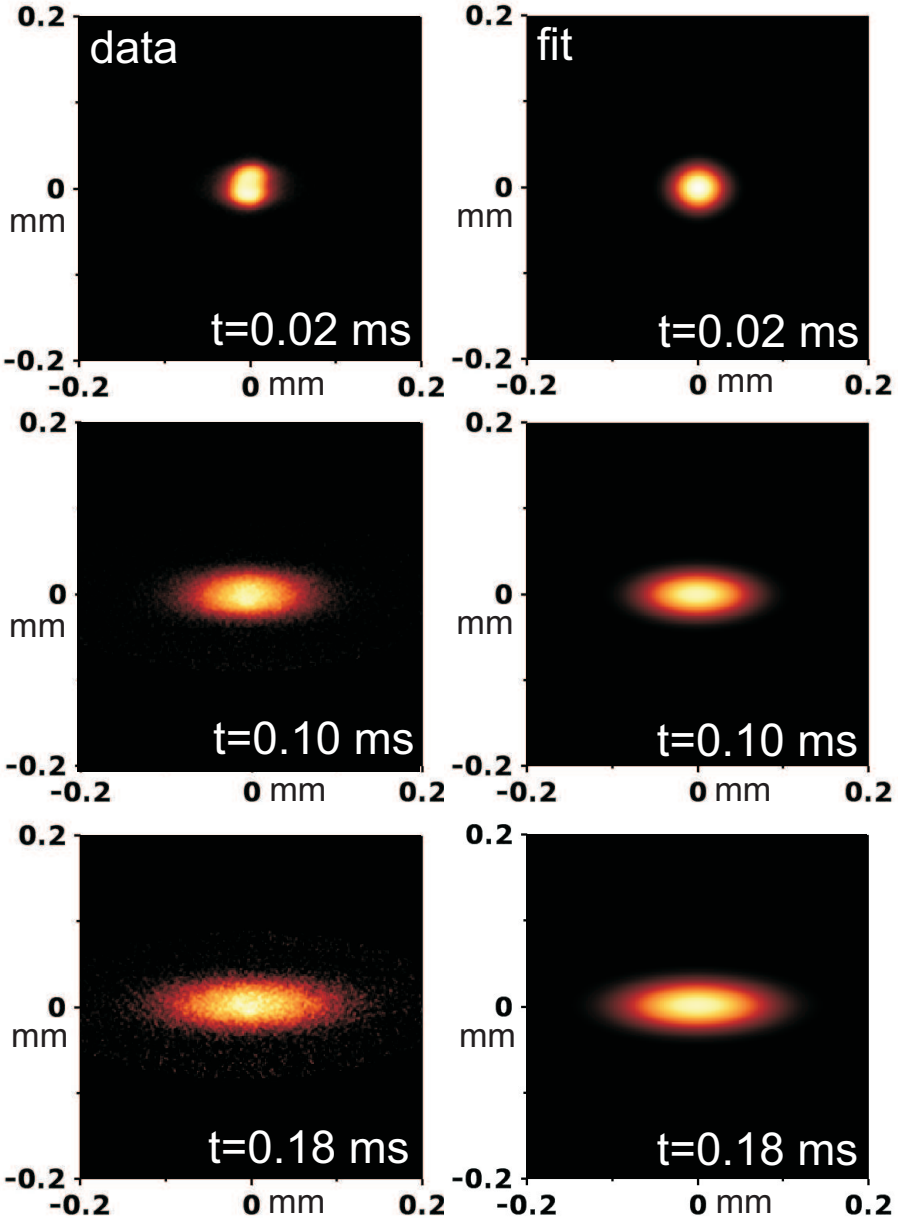

Figure 7.3: Time evolution of the heat spread from a hot spot in the spin ladder $Ca_9La_5Cu_{24}O_{41}$. The left column shows the data, while the right column shows the best Gaussian fit to the data. Heating is done by a laser with a pulse duration of 0.02 ms. The integration time for the probe UV-pulse is 0.02 ms. The ladder direction is horizontal. The anisotropy of the diffusion process is clearly seen.

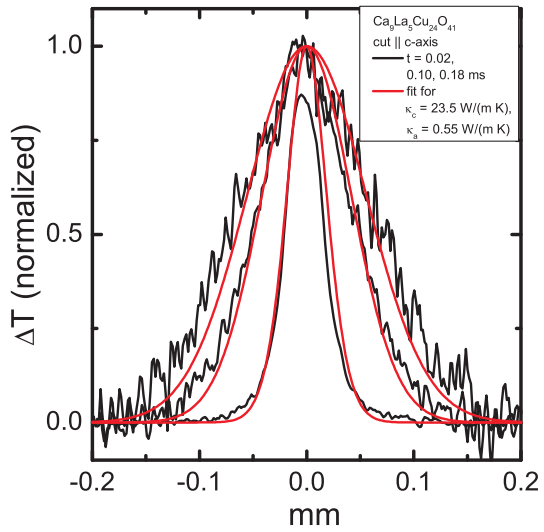

Figure 7.4: Black line: normalized temperature profile for different delay times in $Ca_9La_5Cu_{24}O_{41}$. Red line: fitting by the anisotropic 3-dimensional model. The thermal conductivity along the ladder is $\kappa_{||} = 23.5 \pm 3$ W m^{-1} K^{-1}. In the direction perpendicular to the ladder (not shown) $\kappa_{\perp} = 0.55 \pm 0.3$ W m^{-1} K^{-1}.

direction parallel to the ladder. The thermal conductivities found are $\kappa_{||} = 10 \pm 3$ W m^{-1} K^{-1} and $\kappa_{\perp} = 0.75 \pm 0.3$ W m^{-1} K^{-1}. The thermal conductivities found in a bulk dynamic experiment are $\kappa_{||} = 34 \pm 3$ W m^{-1} K^{-1} and $\kappa_{\perp} = 7 \pm 0.5$ W m^{-1} K^{-1}.

Heat spread along 20 nm RMS surface roughness sample

In figure 7.9 the time evolution of the heat spread from a hot spot, created by a laser pulse, along the surface of the spin ladder compound $Ca_9La_5Cu_{24}O_{41}$ is shown for 4 different delay times between pump and probe beam. The left column shows the data, while the right column shows a 2-dimensional Gaussian fit to the data. Not all delay times are shown. In total, 10 delay times were measured, ranging from 0 to 0.18 ms, in steps of 0.02 ms. The data are normalized in order to enhance the contrast at later times. The maximum temperature increase reached is 35 Kelvin. Figure 7.10 shows the width of the fitted Gaussian as a function of delay time, extracted from the temperature profile parallel and perpendicular to the ladder. Fitting by the Gaussian one-dimensional model is shown. The first datapoint is not considered in the fit, because it is measured during heating. The thermal conductivities found are $\kappa_{||} = 39 \pm 3$ W m^{-1} K^{-1} and $\kappa_{\perp} = 2.6 \pm 0.5$ W m^{-1} K^{-1}. This is in agreement with the thermal conductivity in a dynamic bulk experiment. However, the thermal conductivities found in a bulk steady state experiment are $\kappa_{||} = 85 \pm 5$ W m^{-1} K^{-1} and $\kappa_{\perp} = 2.5 \pm 0.2$ W m^{-1} K^{-1}.

7.4.2 Gold strip heating

Figure 7.11 shows the time evolution of the heat spread from a hot gold strip, heated for 0.05 ms, along the surface of the spin ladder $Ca_9La_5Cu_{24}O_{41}$ single crystal for 5

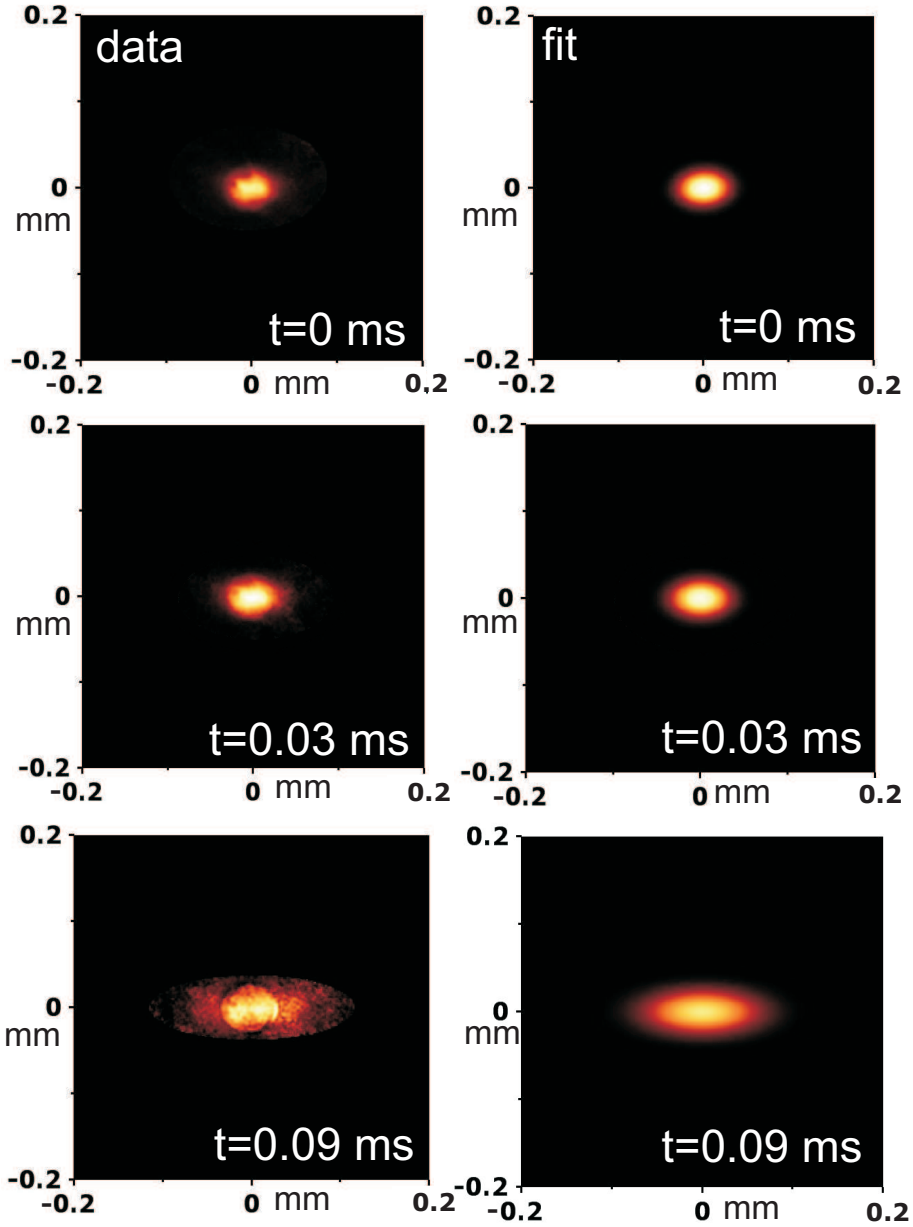

Figure 7.5: Time evolution of the heat spread from a hot spot in the pure spin chain $SrCuO_2$. The left column shows the data, while the right column shows the best Gaussian fit to the data. Heating is done by a laser with a pulse duration of 0.03 ms. The integration time for the probe UV-pulse is 0.03 ms. The chain direction is horizontal. The anisotropy of the diffusion process is clearly seen.

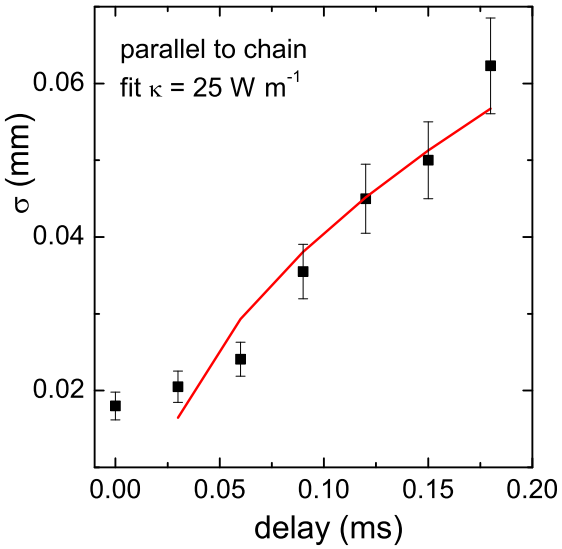

(a)

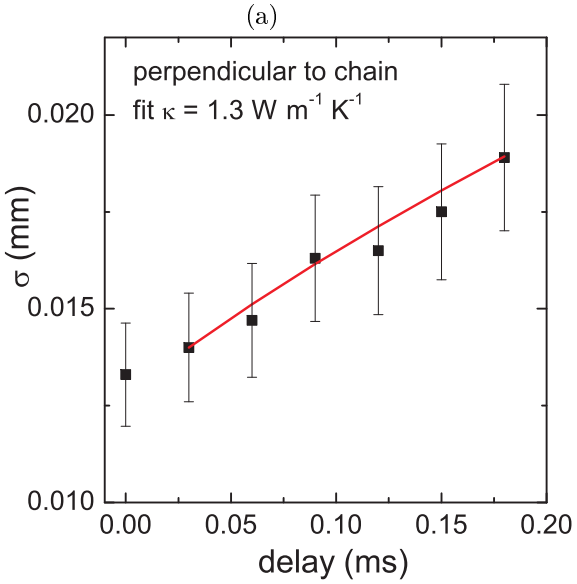

(b)

Figure 7.6: a) Squares: width of the fitted Gaussian in figure 7.5 as a function of delay time extracted from the temperature profile of the heated surface parallel to the chain. Line: fitting by the Gaussian one-dimensional model. The thermal conductivity is $\kappa_{||} = 25 \pm 4$ W m^{-1} K^{-1}. b) Squares: width of the fitted Gaussian in figure 7.5 as a function of delay time extracted from the temperature profile of the surface perpendicular to the ladder. Line: fitting by the Gaussian one-dimensional. The thermal conductivity is $\kappa_{\perp} = 1.3 \pm 0.3$ W m^{-1} K^{-1}.

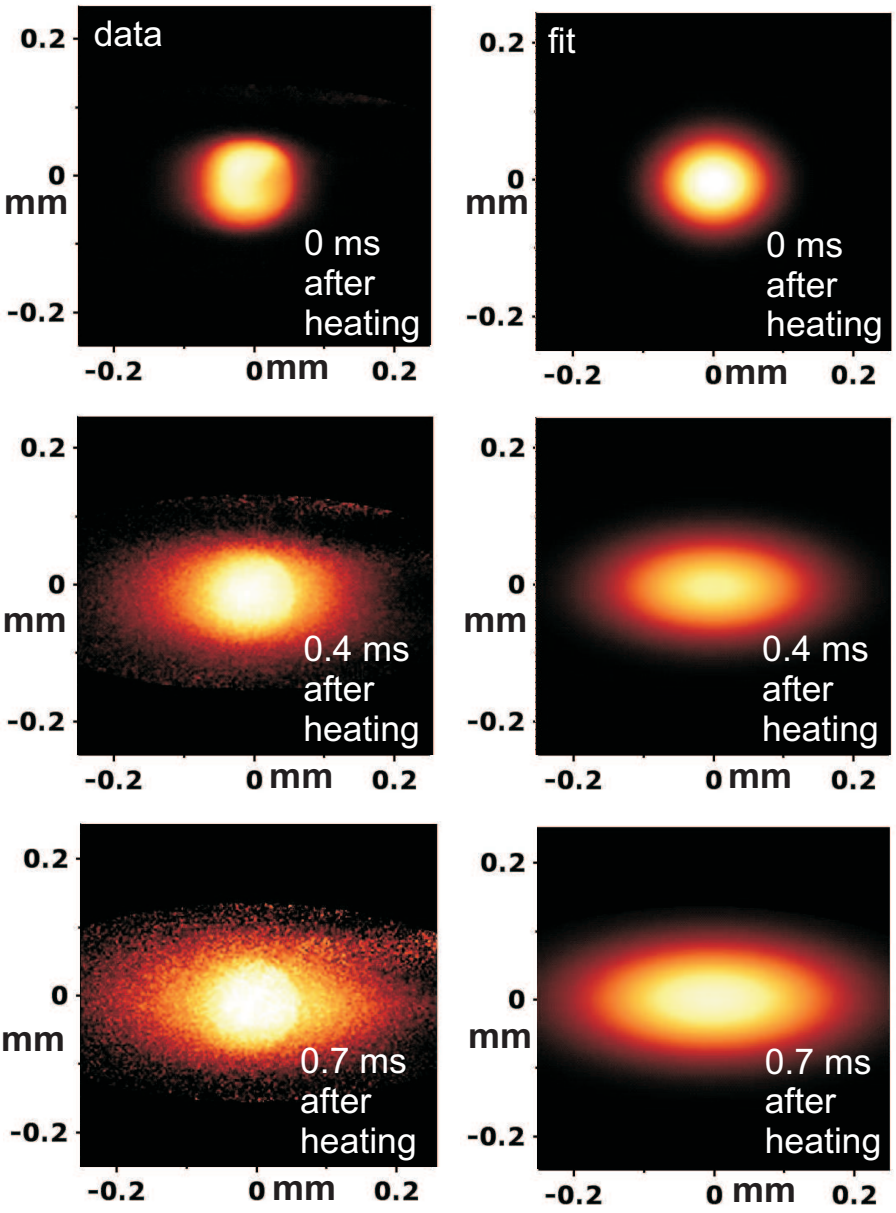

Figure 7.7: Time evolution of the heat spread from a hot spot in the spin chain $SrCuO_2$. The left column shows the data, while the right column shows the best fit to the data, obtained with a simulation of the three-dimensional anisotropic diffusion equation. Heating is done by a laser with a pulse duration of 0.1 ms. The integration time for the probe UV-pulse is 0.1 ms. The chain direction is horizontal. The anisotropy of the diffusion process is clearly seen.

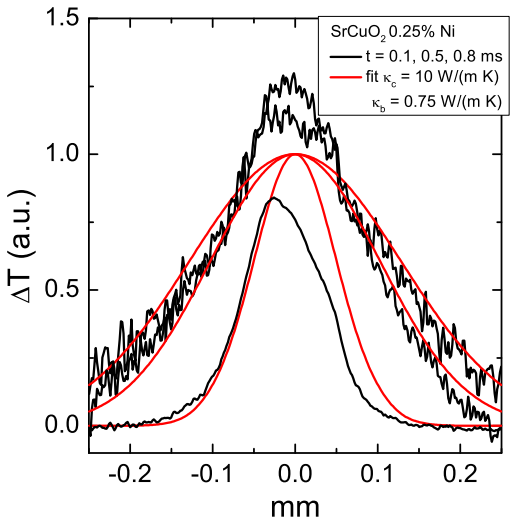

Figure 7.8: Black line: normalized temperature profile for different delay times in $SrCuO_2$ with 0.25 % Ni-doping. Red line: fitting by the anisotropic three-dimensional model. The deviation at the center between the data and the fit is due to the strong reflection of the heating beam, for which a full correction is not possible. The thermal conductivity along the ladder is $\kappa_{||} = 10 \pm 3$ W m^{-1} K^{-1}. In the direction perpendicular to the ladder (not shown) $\kappa_{\perp} = 0.75 \pm 0.3$ W m^{-1} K^{-1}.

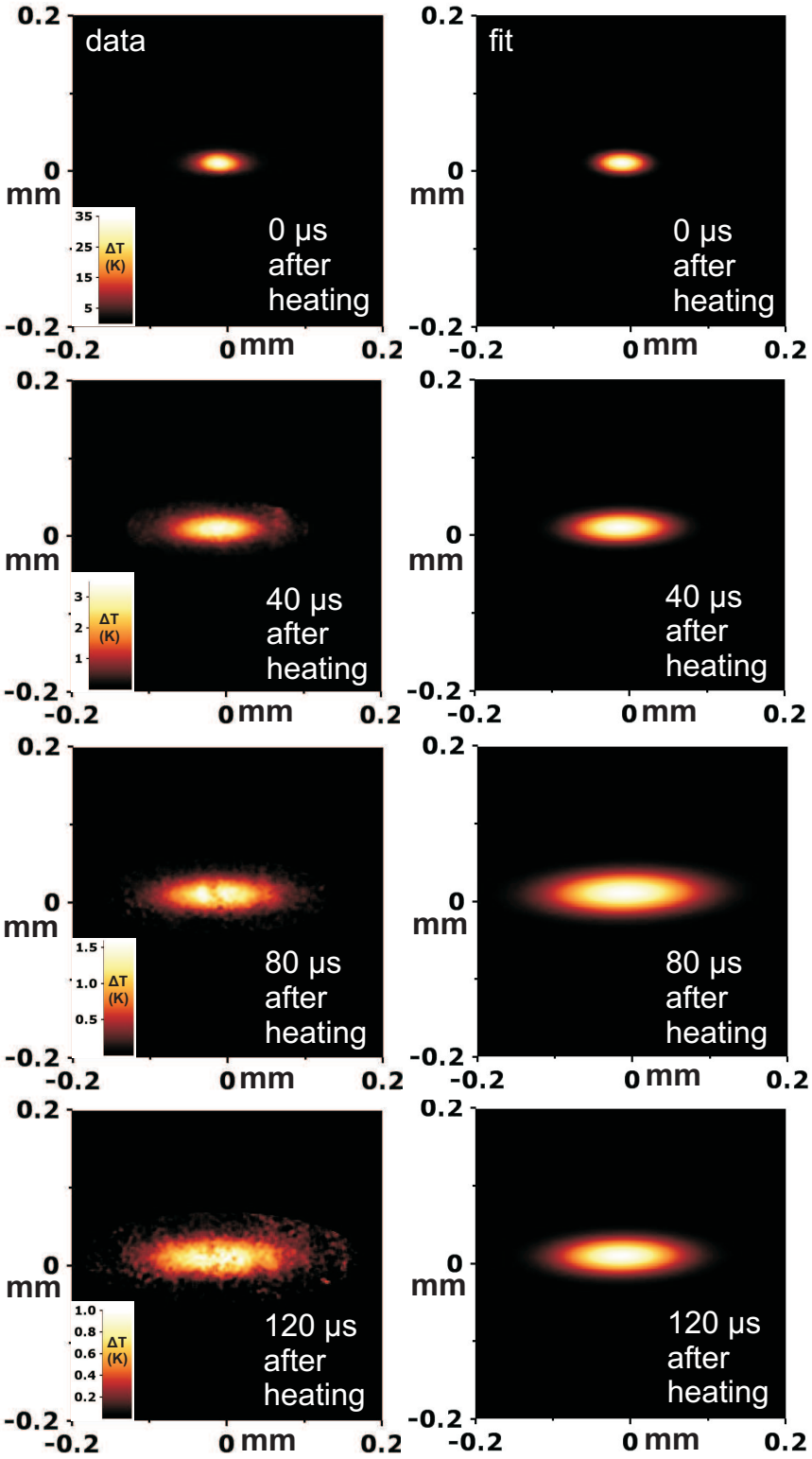

Figure 7.9: Time evolution of the heat spread from a hot spot in the spin ladder $Ca_9La_5Cu_{24}O_{41}$. The left column shows the data, while the right column shows the best Gaussian fit to the data. Heating is done by a laser with a pulse duration of 0.02 ms. The integration time for the probe UV-pulse is 0.02 ms. The ladder direction is horizontal. The anisotropy of the diffusion process is clearly seen.

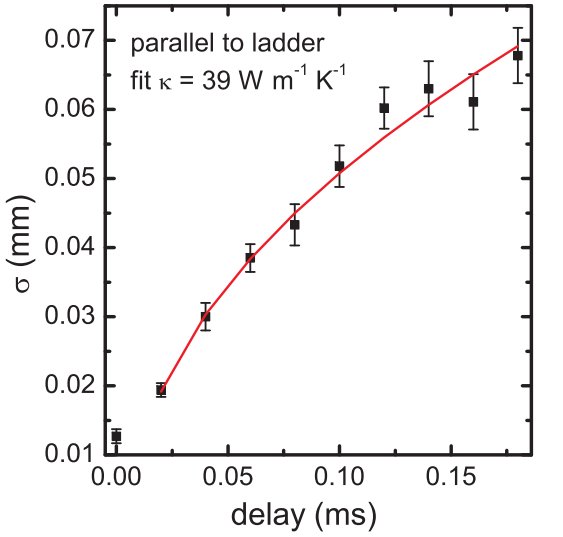

(a)

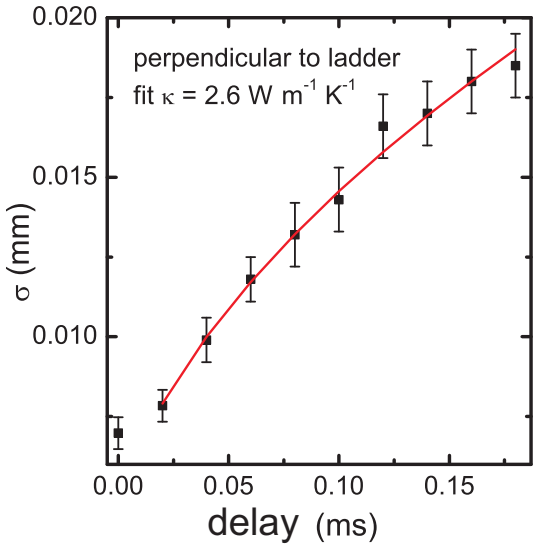

(b)

Figure 7.10: a) Squares: width of the fitted Gaussian in figure 7.9 as a function of delay time extracted from the temperature profile of the heated surface parallel to the ladder. Line: fitting by the Gaussian one-dimensional model. The thermal conductivity is $\kappa_{||} = 39 \pm 3$ W m^{-1} K^{-1}. b) Squares: width of the fitted Gaussian in figure 7.9 as a function of delay time extracted from the temperature profile of the surface perpendicular to the ladder. Line: fitting by the Gaussian one-dimensional. The thermal conductivity is $\kappa_{\perp} = 2.6 \pm 0.5$ W m^{-1} K^{-1}.

different delay times between pump and probe beam. In the left column, the data with the ladders perpendicular to the gold strip (parallel to the x-axis) are presented. In the right column, the data with the ladders parallel to the gold strip and the y-axis are presented. Not all delay times are shown. In total 12 delay times were measured, from 0 to 0.35 ms, in steps of 0.03 ms. The data are normalized in order to enhance the contrast at later times. The maximum temperature increase reached is 45 Kelvin. The normalized temperature profiles, averaged over the y-direction, for the same delay times are presented in figure 7.12 for diffusion parallel and perpendicular to the ladder direction. A simulation using TransAT software for this evolution is shown for the direction parallel to the ladders in figure 7.13. The initial conditions are a temperature of 300 K everywhere. The domain is 5 x 5 x 1 mm, and the minimum cell size is dx=0.6 μm (ladder direction), dy=12 μm, and dz=0.6 μm (out of plane direction). In total, there are 265x100x60 cells. Time steps are 0.05 ms during heating and 0.01 ms after that. The thermal conductivity used parallel to the ladders is 34.5 W m^{-1} K^{-1} and perpendicular to the ladders 2.5 W m^{-1} K^{-1}. It is seen that the simulation reproduces the data quite well. From the time evolution data, the full width half maximum (FWHM) is extracted as a function of delay time, as shown in figure 7.14. This is fitted with the Gaussian one-dimensional model (equation 7.5). The first datapoint is not considered in the fit, because it is measured during heating. The fitted thermal conductivities are $\kappa_{||} = 34.5 \pm 3$ W m^{-1} K^{-1} and $\kappa_{\perp} = 2.3 \pm 0.5$ W m^{-1} K^{-1}, respectively. The thermal conductivities found in a bulk steady state experiment are $\kappa_{||} = 85 \pm 5$ W m^{-1} K^{-1} and $\kappa_{\perp} = 2.5 \pm 0.2$ W m^{-1} K^{-1}.

7.5 Discussion

7.5.1 Influence of surface roughness

In order to test the influence of surface roughness, the optical heating experiment was not only performed on a very well-polished sample surface, but also on several sample surfaces with a RMS roughness of ~ 1 μm. The $Ca_9La_5Cu_{24}O_{41}$ single crystal came from the same batch as the 20 nm RMS roughness sample. For this rougher sample, the thermal conductivity parallel to the ladders was about 40 % lower than the dynamic bulk value, while perpendicular to the ladder it was about 70 % lower than the bulk dynamic value, showing the role of surface defects. The other single crystals show a reduction of 65 % along the ladder and 50 % perpendicular to the ladder for $Sr_{10}La_4Cu_{24}O_{41}$, and 50 % along the chain and 80 % perpendicular to the chain for $SrCuO_2$, respectively. A possible explanation for the difference for measurements along surfaces with different roughness is the introduction of structural strain and/or static imperfections at the surface by polishing [127].

Since the exact surface roughness of these samples has been estimated instead of measured precisely, it is not possible to qualitatively determine the influence of the surface roughness on the thermal conductivity along the sample surface. However, it is clear that a rough surface decreases the thermal conductivity for both phonon and magnon/spinon transport. More accurate measurements on the influence of the surface roughness have to be done to draw strong conclusions about how exactly both conductivities are influenced and to answer the question if there is any difference of

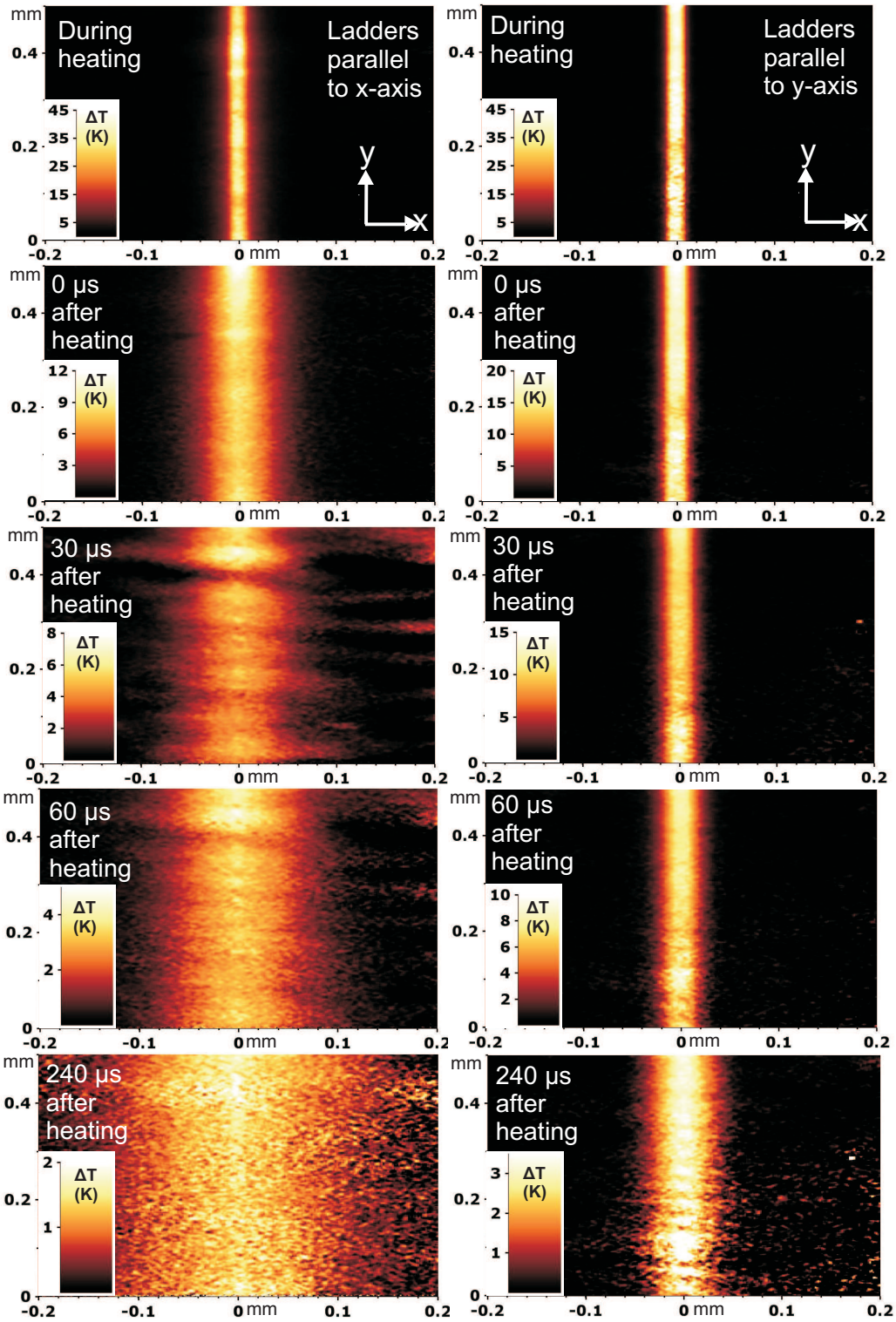

Figure 7.11: Time evolution of the heat profile during and after electrically heating a hot gold strip for 0.05 ms in the spin ladder $Ca_9La_5Cu_{24}O_{41}$. The integration time for the probe UV-pulse is 0.03 ms. The ladder direction is horizontal for the images in the left column and vertical for the images in the right column. The anisotropy of the diffusion process is clearly seen.

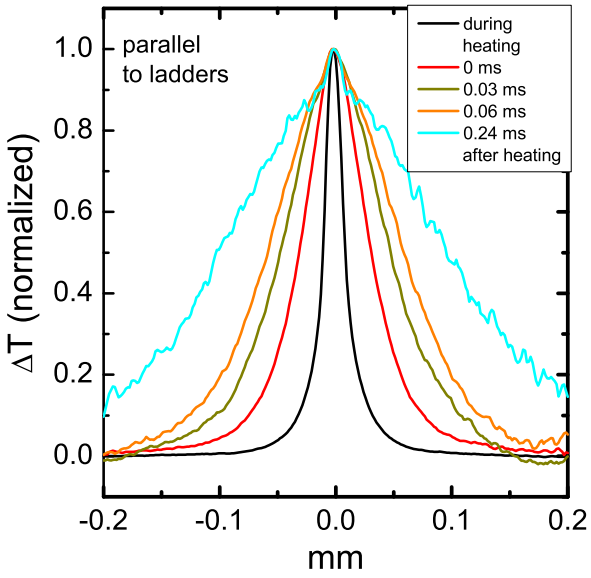

(a)

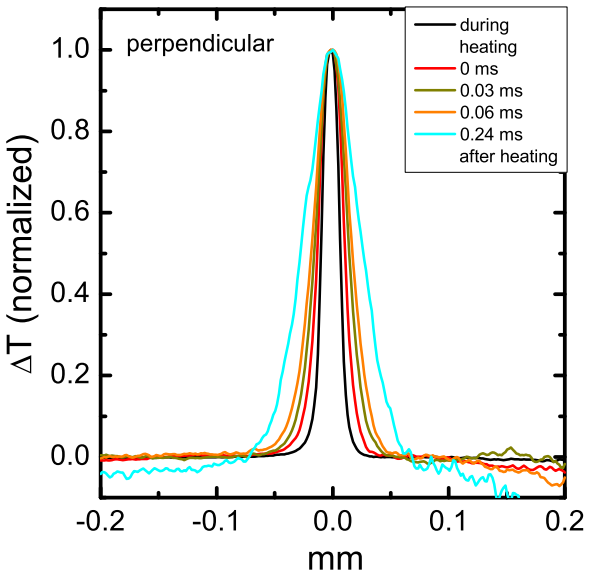

(b)

Figure 7.12: a) Normalized temperature profiles parallel to the ladder for several delay times extracted from the left column of figure 7.11. The data are averaged over the y-direction. b) Normalized temperature profiles perpendicular to the ladder for several delay times extracted from the right column of figure 7.11. The data are averaged over the y-direction.

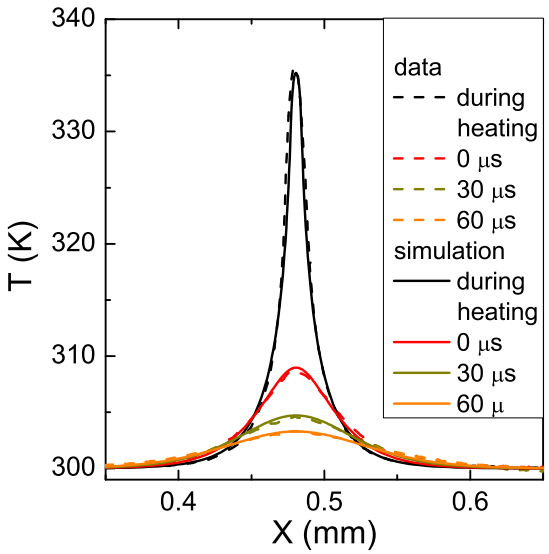

Figure 7.13: Time evolution of the heat profile during and after electrically heating a hot gold strip for 50 μs in the spin ladder $Ca_9La_5Cu_{24}O_{41}$ parallel to the ladders. A comparison to a numerical simulation using TransAT software is shown, which is performed using a thermal conductivity parallel to the ladders of 34.5 W m^{-1} K^{-1}

the influence of the surface roughness between spin ladder compounds and spin chain compounds.

7.5.2 Influence of doping

By comparing the pure $SrCuO_2$ sample and the 0.25 % Ni-doped sample, it is seen that the thermal conductivity along the chain structure, which is lower than in the bulk dynamic measurement due to surface roughness, goes down even more, by about 60 %, when the sample is Ni doped. This trend is equal to what was found in the dynamic bulk measurements and in conventional steady state measurements, as was described in chapter 6. However, in the FMI measurement, the thermal conductivity is decreasing more. This can be due to a different surface roughness at the spot where the measurement is performed for the doped and undoped sample. The polishing procedure is the same, however, the Ni-doped $SrCuO_2$ sample had some patterns on the surface which were not removable with e.g. ethanol, methanol or acetone. Maybe the surface has reacted with oxygen or water from the air and developed some surface layer, which can cause a lowering in the measured thermal conductivity. The phonon thermal conductivity perpendicular to the chain structure seems to be very much hindered by the surface roughness, since both for the doped and the pure $SrCuO_2$ sample it less than 20 % of the bulk value. However, as a critical note it has to be mentioned here that the thermal conductivity in this direction cannot be determined with high accuracy. Furthermore, although for the doped $SrCuO_2$ the measured phonon thermal conductivity is lower than for the pure compound, it is not clear that this is due to the doping. Another explanation could be that at the spot where the measurement is

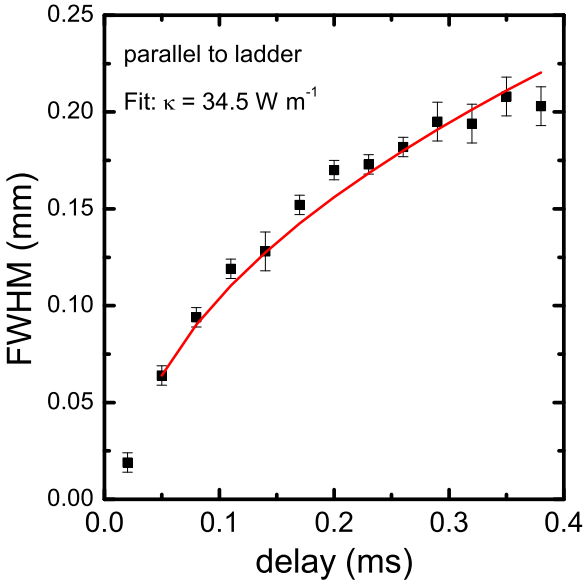

(a)

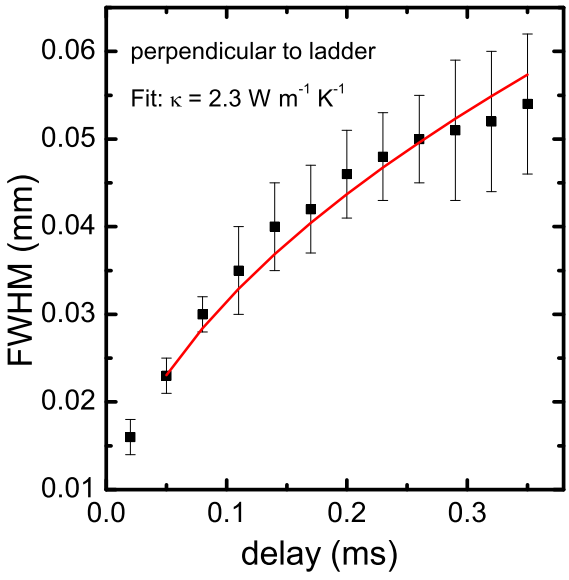

(b)

Figure 7.14: a) Squares: full width half maximum (FWHM) as a function of delay time extracted from the temperature profile of the spread parallel to the ladder. Line: fitting by a one-dimensional model. The thermal conductivity found is 34.5 ± 2 W m^{-1} K^{-1}. b) Squares: full width half maximum (FWHM) as a function of delay time extracted from the temperature profile of the spread perpendicular to the ladder. Line: fitting by a one-dimensional model. The thermal conductivity found is 2.3 ± 0.2 W m^{-1} K^{-1}.

performed the surface roughnesses are slightly different, which might affect the phonon thermal conductivity more than the spinon thermal conductivity. Furthermore, the formed surface layer on the doped sample can cause an additional decrease of the phonon thermal conductivity.

7.5.3 Comparison between dynamic and static results

The thermal conductivity of the 20 nm RMS roughness $Ca_9La_5Cu_{24}O_{41}$ single crystal extracted from the FMI experiment along the ladder is about 60 % lower than the bulk value measured in a steady state experiment, which is 85 W m^{-1} K^{-1} for a crystal from the same rod. However, for different dynamic bulk experiments, a similar reduced value of $\kappa_{||}$ has been reported; the dynamic methods used being the 3ω method [14] and the fluorescent flash method [110], chapter 6. The fluorescent flash method furthermore reveals a thickness dependence, suggesting that in a dynamic measurement at the μs timescale no full thermal equilibrium between magnons and phonons has been reached. In such case one measures an effective thermal conductivity which is lower than the static (magnon + phonon) thermal conductivity. The thermal conductivity perpendicular to the ladder is the same as in the bulk steady state method and the bulk dynamic method. This idea was explained in detail in chapter 6. The measurements on the samples with rough surfaces cannot fairly be expected to be equal to the dynamic bulk results, since from the measurement on $Ca_9La_5Cu_{24}O_{41}$ it was seen that the thermal conductivity for both magnons and phonons is lowered in the sample with the rougher surface.

The reason that in the dynamic method along the surface an influence of the long magnon-phonon thermalization time is measured, is that the heat transport is monitored from the heating source, where the particles are excited and no thermal equilibrium has been reached. In order to follow thermalization dynamics, one needs a time resolution shorter than the thermalization time. The smallest time resolution achieved in the experiment is 20 μs, which is much shorter than the thermalization time of 300 μs, extracted from the model to fit the FFM data in chapter 6. The timescale in the FMI experiments is the same order of magnitude as in the dynamic bulk measurements, explaining the same reduced magnon thermal conductivity values. For the static method, simulations have shown that when one measures close to the heating source (i.e. at a distance < 100 μm) also influences of the long magnon-phonon thermalization time should be visible. In the conventional steady state method the thermal contacts are too bulky to have such a space resolution. In the optical steady state method in principle it is possible to measure this region.

7.5.4 Application of spin ladders/chains in devices

This work highlights the potential of these materials as a directional heat transport channel. For spin ladder compounds, however, when using quickly varying heat sources, the value of the thermal conductivity along the ladders is lower than under steady state conditions. Therefore, if a high value of the thermal conductivity is the main criterion, the directional heat transport channel can only be applied to slowly varying heat sources and over distances long enough such that the first part in which there

is no thermal equilibrium is negligible. However, if a large anisotropy is the most critical parameter, then this material, the dynamic anisotropy still being ~ 15, suits application as a directional heat transport channel for quickly varying heat sources as well. Unfortunately, at the position of the heat producing component, i.e. exactly where one would like to cool most, the effective thermal conductivity is lowest. For spin chain compounds the steady state bulk and dynamic bulk thermal conductivity are in agreement. No measurements on a very smooth surface were performed. Already for the ~ 1 μm surface roughness samples the reflection from the heating beam was so strong that the analysis of the data is complicated. However, since for bulk the dynamic and steady state thermal conductivity are in agreement, it is expected that, as for the spin ladder, the thermal conductivity along a well-polished surface is the same, making the spin chain compound suitable for directional heat transport as well.

Concerning efficiency, let us make the comparison to a typical material from the semiconductor industry: silicon. Silicon has a thermal conductivity of 140 W m^{-1} K^{-1} at room temperature, and a diffusion constant of 90 mm^2/s [128]. In the spin ladder compound the steady state thermal conductivity is 85 W m^{-1} K^{-1} along the ladder and the diffusion constant is 30 mm^2/s. Even though thermal conductivity is usually used to indicate how well heat is transported, this is only true in a steady state situation. When dynamic heat transport is considered, the diffusion constant (also called diffusivity sometimes) defines how fast the heat is spreading from the heat source. Compared to silicon, both thermal conductivity and diffusion constant are lower in the spin ladder material. Therefore, a heat producing component will be cooled less efficient. However, the big advantage over all the materials that conduct heat well, is that the spin ladder conducts heat directionally. This opens the possibility to design a structure in which the heat is transported to areas which are less sensitive to overheating. One more thing that one has to realize is that the directionality comes at a cost: if one compares two materials with the same diffusion constant, of which one is a normal three-dimensional conductor, while the other is a one-dimensional conductor, the last material spreads the heat over a much lower volume, and therefore the increase in temperature in this volume will be higher. Ideally, one would like to have a material with a diffusion constant in one direction as high as possible. For example, the highest diffusion constant ever measured in a bulk material is in diamond, 1850 mm^2/s, [129]. For suspended graphene the thermal conductivity can be as high as 5000 W m^{-1} K^{-1}, 2.5 $\times$ as high as for diamond, but it decreases by a factor of 10 when it is contacted to a substrate [130]. A one-dimensional diffusion constant of the order of magnitude of diamond would compensate for the fact that the heat is spread over a lower volume then in a three-dimensional conductor. Unfortunately, a material like that has not been discovered.

7.6 Conclusion

In this chapter, a time-resolved thermal imaging technique is used to monitor heat diffusion along the surface in different directions in the spin ladder materials $Ca_9La_5Cu_{24}O_{41}$ and $Sr_{10}La_4Cu_{24}O_{41}$, and the spin chain material $SrCuO_2$. These materials show a highly anisotropic bulk thermal conductivity due to large uni-directional magnetic heat transport along the ladder/chain structure. The thermal conductivity of the ~ 1 μm

RMS roughness samples is at least two times lower than the dynamic bulk value in both the direction parallel to the ladder/chain and the direction perpendicular to the ladder/chain. The thermal conductivity for the very flat 20 nm RMS surface roughness $Ca_9La_5Cu_{24}O_{41}$ sample is measured using optical heating as well as using electrical heating. The results of both methods are in good agreement; 37 ± 3 W m^{-1} K^{-1} for the fast direction parallel to the ladders and 2.5 ± 0.5 W m^{-1} K^{-1} for the slow direction perpendicular to the ladders, respectively. The thermal conductivities in the fast and slow direction, measured in a dynamic way, are in agreement with other dynamic measurements in the bulk material. However, in the fast direction the dynamic thermal conductivity is about 60 % lower than the steady state value. The highly anisotropic heat transport properties of this material, both in the bulk and along the surface, can potentially be applied in directional cooling of microelectronics.

We kindly thank Gert ten Brink for sample preparation. This work was supported by the European Commission through the NOVMAG project (FP6-032980) and through the LOTHERM project (PITN-GA-2009-238475).

8. Ultra-fast dynamics in the spin ladder $Ca_9La_5Cu_{24}O_{41}$

This chapter forms a preliminary report on pump-probe experiments performed to get more insight in the short timescale (ps) dynamics in the spin ladder compound $Ca_9La_5Cu_{24}O_{41}$. Specifically, one would like to have an understanding of the magnon dynamics in this material, and the interplay between magnons, electrons and phonons at short timescales. This information would complement our current understanding of the longer timescale (ms) diffusion dynamics described in chapters 6 and 7.

In section 6.4 it was discussed that the Lorenzana-Sawatzky bi-magnon-phonon interaction is the main mechanism to create magnons from phonons [120], and that the low probability of this interaction in gapped spin ladder systems leads to a long magnon - phonon thermalization time. To study the magnon - phonon dynamics, ultra-short pulses have to be used in order to coherently excite magnons, shorter than the oscillation period for magnons and phonons. For the single-magnon bound state this is 120 fs and for low energy acoustical phonons it can go up to a few hundred fs. For the two-magnon bound state it is 20 fs and for optical phonons and electrons even shorter. Therefore we have chosen to use femtosecond pump-probe techniques, for which the pulse duration can be in this range. When the pump pulse hits the sample, first electrons are excited which are converted to phonons. Part of these phonons are converted to magnons. At which timescale these processes occur is not yet known.

First, a near-infrared (NIR) pump - visible/NIR probe transient reflectivity experiment was done, to have some insights in short time scale dynamics in the visible. Then, the NIR pump - visible probe experiment was repeated for different pump and probe polarizations as a function of temperature. In the follow-up experiment, excitations were created by pumping with a strong NIR pulse, after which the response of the material was probed in the infrared as a function of temperature, with a pulse energy lying in one of the two magnon absorption bands. Therefore, these probe pulses are mainly sensitive to the magnon dynamics. For comparison, two more probe pulse energies were used which lie outside these bands. Therefore, these are not (so much) sensitive to the magnon dynamics, and can be used to obtain an understanding of the electron and phonon response.

8.1 Temperature dependent infrared absorption

The infrared (IR) transmission spectrum of a 82 μm $Ca_9La_5Cu_{24}O_{41}$ single crystal has been measured by means of Fourier Transform Infrared (FTIR) spectroscopy in the

1000-6000 cm^{-1} range for different temperatures. The sample surface has been cut parallel to the c-axis (ladder direction). The surface was machine polished by SiC paper (5 μm grains) and subsequently by a cloth with 1 μm diamond suspension. The RMS surface roughness was $\approx$ 10 nm, as measured by a confocal microscope. Results are in agreement with data reported in the literature [47, 27]. Figure 8.1 shows a typical spectrum for polarization parallel to the ladder direction for a temperature T=5 K. The magnon-induced absorption dips are visible in the 2000-3000 cm^{-1} region, between the low energy (single) phonon induced features and the high energy onset of the charge transfer interband excitations above 3000 cm^{-1} (electronic excitations), together with the two-magnon continuum above 4000 cm^{-1} [47]. The exponentially decreasing transmissivity with energy, on top of which the magnon features are visible, is also due to charge tranfer interband excitations. These visibly contribute, but are not yet dominant in this range. The two magnon-induced dips (henceforth called A and B) are the signature of the two Van Hove singularities in the density of the 2-magnon bound state, due to two flat points in the dispersion located at the Brillouin zone boundary (A) and at the middle point (B), as shown in figure 8.2. Both dips are due to the Lorenzana - Sawatsky 2-magnon plus phonon absorption [120]. Direct magnon absorption is not possible due to momentum and spin conservation requirements.

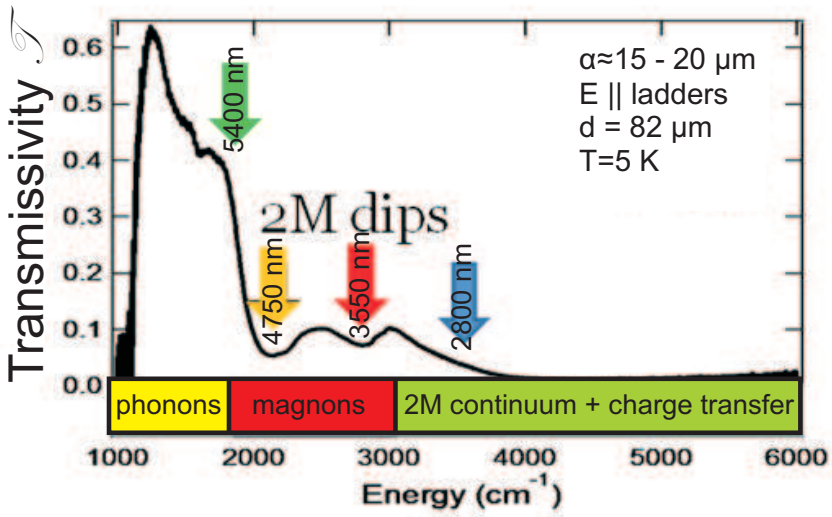

Figure 8.1: IR transmission spectrum of $Ca_9La_5Cu_{24}O_{41}$ with the electric field polarization parallel to the c-axis (ladder direction). The arrows indicate the frequency where the time resolved transmissivity experiments were performed. The two magnon-induced dips (yellow and red arrow) are clearly visible.

The temperature dependence of the magnon part is shown in figure 8.3. These data have never been reported in literature. The two magnon features (due to the two flat points in the dispersion, A and B) show a strong dependence on temperature, with the dip contrast diminishing with raising temperature. Whereas the A feature is still visible as a shoulder at room temperature, the B dip vanishes above 120 K. This behavior can be quantified by extracting the optical conductivity $\sigma(\omega,T)$, which is obtained by fitting the transmissivity data with a multiple Lorentz oscillator model.

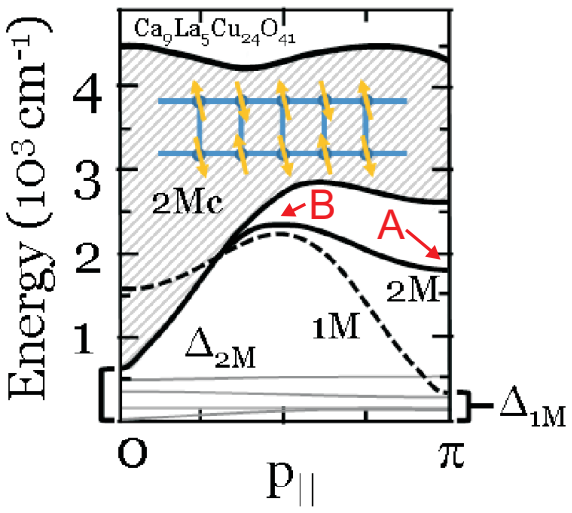

Figure 8.2: Dispersion of $Ca_9La_5Cu_{24}O_{41}$ versus the ladder momentum $p_{||}$. The single-magnon (dashed line) and two-magnon (solid line) bound states are shown; the two-magnon continuum is dashed. The two Van Hove singularities lie at $p_{||}=\pi$ (A) and at $p_{||}=\pi/2$ (B).

In figure 8.4 the relative spectral weight of the oscillators for the A and B magnon features are plotted;

$$\text{relative spectral weight} = \frac{\int \sigma_i d\omega}{\int \sigma_{\text{total}} d\omega} \quad i = \text{A,B.} \tag{8.1}$$

Both oscillator strengths show a possible drastic quenching between 100 and 150 K, with a characteristic temperature of $\approx$ 120 K. This quenching might happen because the phonon mode responsible participating in the two-magnon plus phonon absorption, the 560 cm^{-1} A_g Cu-O stretching mode [47], is so much broadened with temperature that the absorption process is becoming less efficient. At temperatures higher than 150 K the magnon features become broad, presumably due to the short phonon and magnon lifetimes. For the spectra measured at 180 and 295 K the peaks are so broad that their oscillator strength cannot be determined accurately. Already at 100 and 120 K the error in the fit is much larger than at lower temperature.

The temperature dependent IR transmissivity for the direction perpendicular to the ladders shows no signs of magnon peaks and the changes with temperature are rather small, as is shown in figure 8.5. Also for this direction, the measured low temperature spectra are in agreement with literature [27], however, the features around 1500 cm^{-1} and 3000 cm^{-1} are resolved in more detail in our experiments.

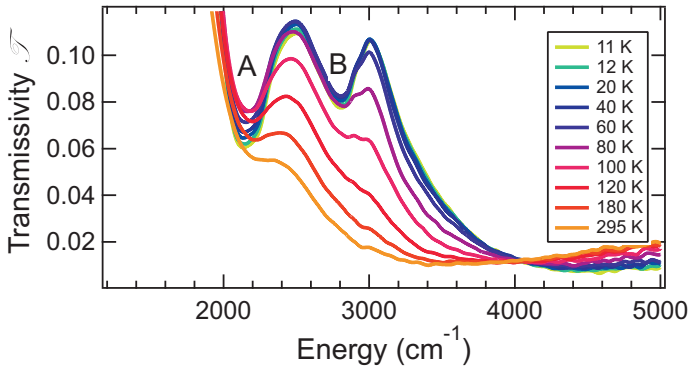

Figure 8.3: Temperature dependent IR transmission spectra for $Ca_9La_5Cu_{24}O_{41}$ with electric field polarization parallel to the ladders.

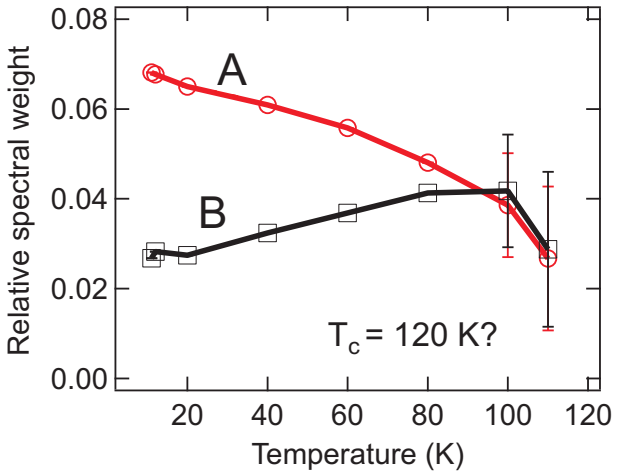

Figure 8.4: Relative spectral weight of the magnon oscillators versus the temperature. The characteristic temperature $T_c \approx 120$ K of a possible quenching of the oscillator strength is highlighted.

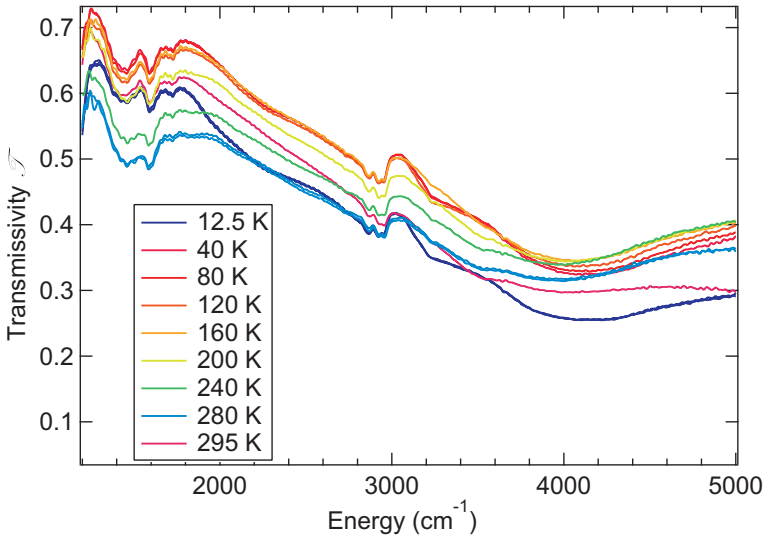

Figure 8.5: Temperature dependent IR transmission spectra for $Ca_9La_5Cu_{24}O_{41}$ with electric field polarization perpendicular to the ladders. No signs of magnon absorption are observed.

8.2 Visible pump - visible/near-infrared probe dynamics

8.2.1 Room temperature measurements

The room temperature time evolution of the reflectivity change in $Ca_9La_5Cu_{24}O_{41}$ has been investigated by a femtosecond pump-probe technique, as is described in section 4.2.4. This work was done by D.A. Fishman. The penetration depth of the pump and probe pulse are about 200 nm as was calculated from dielectric constant measurements [42], therefore the pulses are mainly sensitive to the surface layer of the crystal. The curves for all probe wavelengths are shown in figure 8.6. The data are stacked for clarity. The pump fluence was about 50 μJ/cm^2, the probe fluence approximately ten times lower. Figure 8.7 shows the response of the reflectance change for a probe energy of 1.57 eV (790 nm). A small negative signal with ΔR/R in the order of 10^{-6} with a short lifetime ($\sim$ 1 ps) was observed. This negative signal is common in semiconductors and is due to the excitation of electrons and the conversion to phonons thereafter. The lifetime is interpreted as the electron-phonon equilibration time.

The inset in figure 8.7 shows the difference between the reflectivity change at positive and negative delay times. It is seen that both the reflectivity change and the difference between positive and negative delay times (blue squares) are increasing with increasing pump pulse energy density. There might be a saturation plateau around 0.9 mJ/cm^2. Both increasing effects are probably due to laser heating. Two processes can play a role. One is single pulse heating which is expected within a time shorter than the time constant of cooling due to thermal conduction (ballistic or diffusive) across the excited volume. In this case the rise of temperature can be expressed as $Q/(C_p(T)V)$, where Q is the heat energy deposited by one pulse, $C(T)$ is the temperature dependent

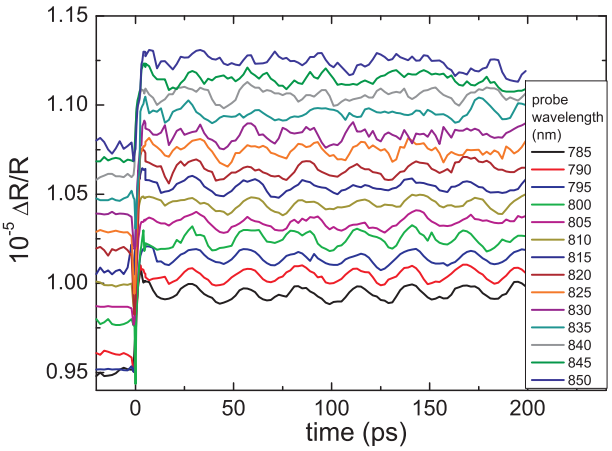

Figure 8.6: Reflectivity change for $Ca_9La_5Cu_{24}O_{41}$ with Epump parallel to the ladders and E_{probe} perpendicular to the ladders. The pump pulse has an energy of 1.63 eV (760 nm), while the probe pulse has different energies between 1.44 and 1.58 eV (785-850 nm). The pump fluence was about 50 $\mu J/cm^2$, the probe fluence approximately ten times lower. The data are stacked for clarity, with increasing probe wavelength 10^{-7} $\Delta R/R$ is added for every next trace.

specific heat and V is the heated volume. This is only a first approximation; if the temperature variations are large, $C_p(T)$ has to be replaced by an integration over the temperature range. Another effect is average heating, accumulated from many pump pulses, and governed by thermal conduction. It is given by the difference between how much heat is put into the sample and how much flows away. This difference depends on the fluence of the pump laser, the thermal conductivity and specific heat of the sample, and the thermal contact to the sample holder. The background component, which does not depend on the delay time, can be caused by average heating. The peak in the signal due to a change in temperature has a build-up time of 10 ps around room temperature, which reflects the time required for the redistribution of energy from the excited phonon states by phonon-phonon scattering. The excited charges are long-lived; in 200 ps, the maximum delay time of the experiment, they have not decayed measurably. Therefore, the decay time, which can give information about the thermal conductivity, cannot be extracted. However, it is unlikely to be a thermal effect, since the estimated temperature increase due to single pulse heating is about 1 K.

Furthermore, the transient reflectivity change traces show an oscillating component with a period $T \sim 28$ ps. It is found that the period of this oscillation is approximately proportional to the wavelength of the probe light in the medium, as is shown in figure 8.8. The error is estimated as three times the standard deviation from the sinusoidal fit to the data. The phase is the same for all probe wavelengths. This oscillation is ascribed to the interference of the probe light reflected at the surface and the wave front of the induced acoustic wave propagating into the sample. In such case, $T = \lambda/(2nv\cos\theta)$, with probe wavelength λ, refractive index n and speed of sound v. Here $\sin\theta = (1/n)\sin\theta_{probe}$, with an angle of incidence θ_{probe} [131, 132]. The linear dependence of the oscillation period on λ is explained by the interference of the light beams reflected from the sample surface and the propagating phonon pulse. The light

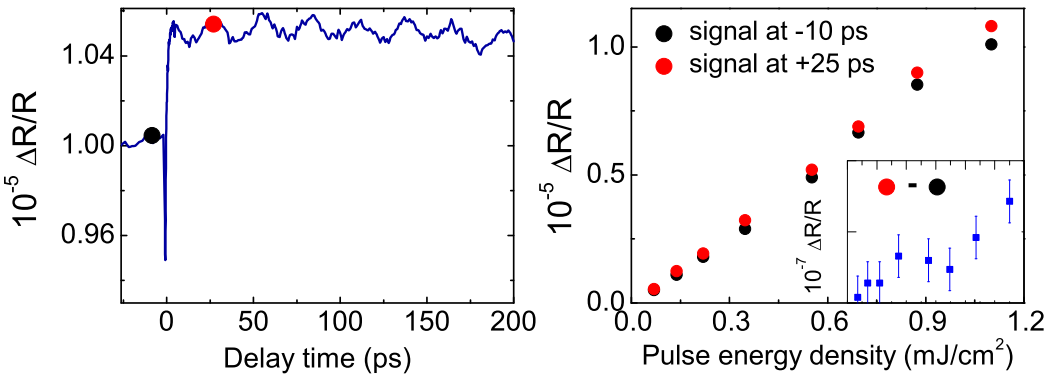

Figure 8.7: Left: reflectivity change for $Ca_9La_5Cu_{24}O_{41}$ with E_{pump} parallel to the ladders and E_{probe} perpendicular to the ladders. The pump pulse has an energy of 1.63 eV (760 nm), while the probe pulse has an energy of 1.57 eV (790 nm). Right: the reflectivity changes at positive and negative delay times and the difference between those. The error is estimated from the noise in the $\Delta R/R$ signal in the left graph. It is seen that both the reflectivity change and the difference between positive and negative delay times are increasing with increasing pump pulse energy density.

reflected by the phonon wave travels a distance of $2nvt/\cos\theta$ in the medium, leading to a phase shift $4\pi nvt\cos\theta/\lambda$, proportional to the delay time t, with respect to the light reflected by the surface. Therefore, a periodic oscillating intensity is generated for the overall reflection. The speed of sound is calculated as 7.7 ± 1 km/s, using a value for the refractive index calculated from the dielectric constant [42] and assuming that $\cos\theta \approx 1$. The error in the fit is quite large because the data is rather scattered. This value is in agreement with the speed of sound in the low-dimensional spin system $SrCu_2(BO_3)_2$, which is ≈ 7.7 km/s [133].

8.2.2 Temperature dependence

In a follow-up experiment, the time evolution of the reflectivity change in $Ca_9La_5Cu_{24}O_{41}$ has been investigated as a function of temperature. First, the temperature dependence was measured for both E_{pump} and E_{probe} parallel to the ladder direction. Figure 8.9 shows the change in reflectivity as a function of time for different temperatures. The traces for different temperatures are not stacked here, i.e. it is seen that $\Delta R/R$ goes down as a function of temperature. Since the change in $\Delta R/R \sim 5 \times 10^{-8}$ K^{-1}, which is $\sim 2 \times$ lower than the noise level, the absolute value of $\Delta R/R$ cannot be used as a precise thermomether. However, a rough estimate can be obtained.

A maximum level in $\Delta R/R$ is reached after about 50 ps. Over the full measurement interval (500 ps) no decay is seen from this maximum level. Furthermore, oscillations are seen due to acoustic phonons. These are most clear between 30 and 100 ps, because from 100 ps on the time step in the experiment was too coarse to resolve the oscillations. This time step was chosen because of measurement time considerations. From the

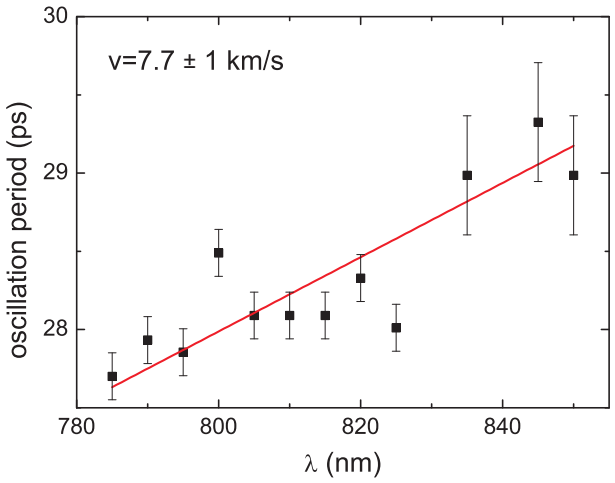

Figure 8.8: Extracted oscillation period as a function of probe wavelength. The error is estimated as three times the standard deviation from the sinusoidal fit to the data. From the slope of the best linear fit the acoustical phonon velocity is determined.

oscillation period of T=8.5 ps is determined. For the lowest temperature for which oscillations occur, 70K, T=9.2 ps. The phonon velocity is determined to be $\approx$ 18 km/s. This is higher than what was found in the previous experiment. It is not clear why this difference occurs.

Figure 8.10a shows the average background level and the maximum level of $\Delta R/R$. The average background level is taken between -50 and -1 ps. The average maximum level is taken between 200 and 500 ps. These values are plot for different temperatures. Two regions are observed, below 70 K the slope is less steep than above 70 K. That the difference between these two values decreases linearly with temperature is seen in figure 8.10b. Here only one slope is observed. The error in the difference is estimated from the error in $\Delta R/R$. Another interesting quantitity is the difference between the value of $\Delta R/R$ at the dip just after the pump beam and the average background level at negative times. It is normalized to this average background level, because this level changes strongly with temperature. The temperature dependence is shown in figure 8.11. It follows the inverse of the specific heat, indicating that the amplitude of the dip value is linear with the temperature in crease in the small volume heated by the pump pulse.

The rise of the signal after the dip can be described by a bi-exponential function. The fast and the slow decay times are shown as a function of temperature in figure 8.12. It is seen that the fast decay time, which is ascribed to electron-phonon thermalization, is nearly constant with temperature. Therefore, the fit for the long decay time is done while keeping the fast decay time constant at an average value. It is seen that this decay time, which is ascribed to phonon-phonon thermalization, is decreasing with increasing temperature. This is probably due to the fact that at higher temperature there are more phonons present for the thermalization process.

Second, the temperature dependence was measured for both the polarization of the pump pulse E_{pump} and the polarization of the probe pulse E_{probe} perpendicular to each other, with E_{pump} parallel to the ladder direction. Figure 8.13 shows the change

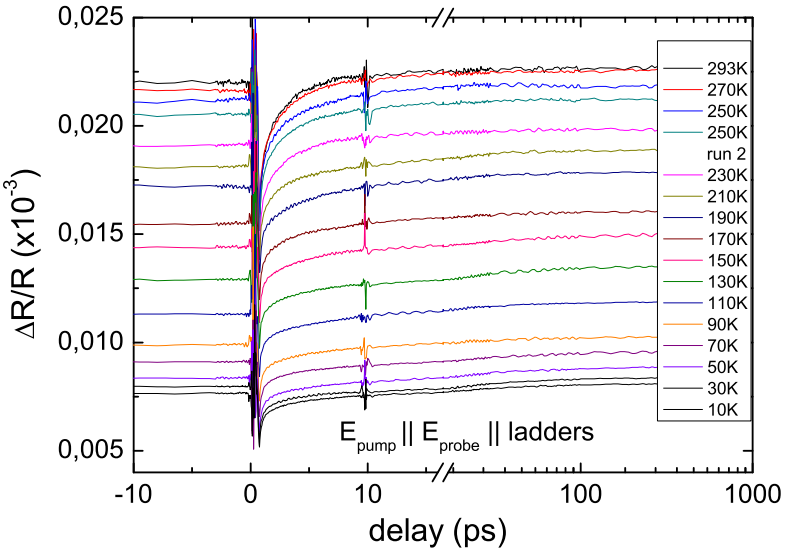

Figure 8.9: Reflectivity change for $Ca_9La_5Cu_{24}O_{41}$ with E_{pump} and E_{probe} parallel to the ladders. It is seen that the reflectivity change decreases with decreasing temperature. The data are not stacked.

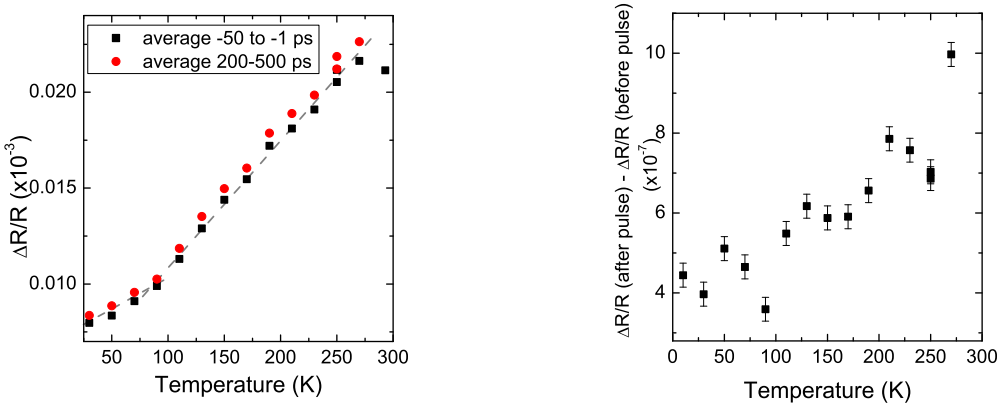

(a) (b)

Figure 8.10: a) Average background level and maximum level of $\Delta R/R$ as a function of temperature, with E_{pump} and E_{probe} parallel to the ladders. The average background level is taken between -50 and -1 ps. The average maximum level is taken between 200 and 500 ps. The error bar is smaller than the seize of the circle/square. The grey dotted lines are guides to the eye. b) The difference between the average background level and the average maximum level of $\Delta R/R$ decreases linearly with decreasing temperature.

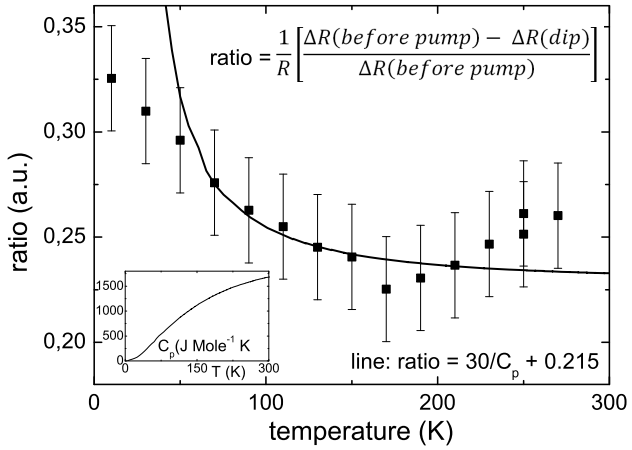

Figure 8.11: Difference between the value of $\Delta R/R$ at the dip induced by the pump pulse and the average background level at negative times as a function of temperature, with E_{pump} and E_{probe} parallel to the ladders. Since $\Delta R/R$ depends strongly on temperature, the data are normalized to the average background level. The shape of the curve follows the inverse of the specific heat, apart from the low temperature region in which the specific heat is strongly temperature dependent, indicating that the amplitude of the dip is linear with the temperature increase induced by the pump pulse.

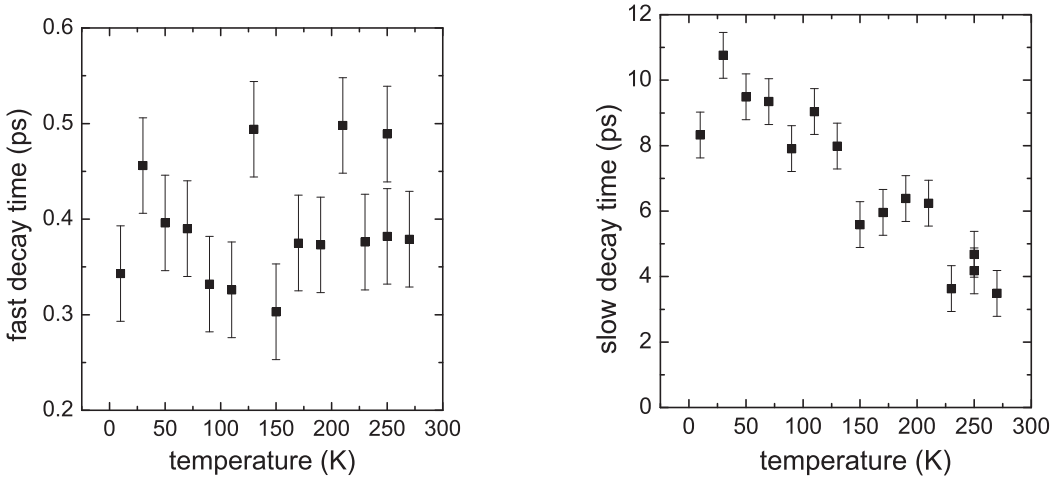

(a) (b)

Figure 8.12: a) Fast decay times as a function of temperature for the data with E_{pump} and E_{probe} parallel to the ladders. It is seen that the fast decay time, which is ascribed to electron-phonon thermalization, is nearly constant with temperature. b) Slow decay times as a function of temperature for the data with E_{pump} and E_{probe} parallel to the ladders. It is seen that this decay time, which is ascribed to phonon-phonon thermalization, is decreasing with increasing temperature.

in reflectivity as a function of time for different temperatures. It is seen that $\Delta R/R$ goes down as a function of temperature, the data are not stacked. In agreement with the measurements with E_{probe} parallel to the ladders, the maximum level is reached at about 100 ps, but for this polarization the level of $\Delta R/R$ decreases afterwards.

Figure 8.14a shows the average background level and the maximum level of $\Delta R/R$. The average background level is taken between -50 and -1 ps. The average maximum level is taken between 30 and 100 ps. These values are plot for different temperatures. Two different regions can be distinguished: below 70 K the increase with temperature is less steep than above 70 K. The difference between the two values decreases linearly when temperature decreases, as is seen in figure 8.14b. These data have a too large error to see if there are differences between the different regions. The difference between the value of $\Delta R/R$ at the dip just after the pump beam and the average background level at negative times, normalized to this average background level, is shown for different temperatures in figure 8.15. Also for this probe orientation, the normalized change follows the inverse of the specific heat indicating that the amplitude of the dip value is linear with the temperature increase induced by the pump pulse. However, the ratio is about three times smaller, reflecting the smaller changes induced by the pump. Also the temperature dependence is less strong and therefore the $1/C_p$ dependence, which is found comparing the best fitting curves for both polarizations. The data with E_{pump} parallel and E_{probe} perpendicular to the ladders has a smaller term dependent on C_p.

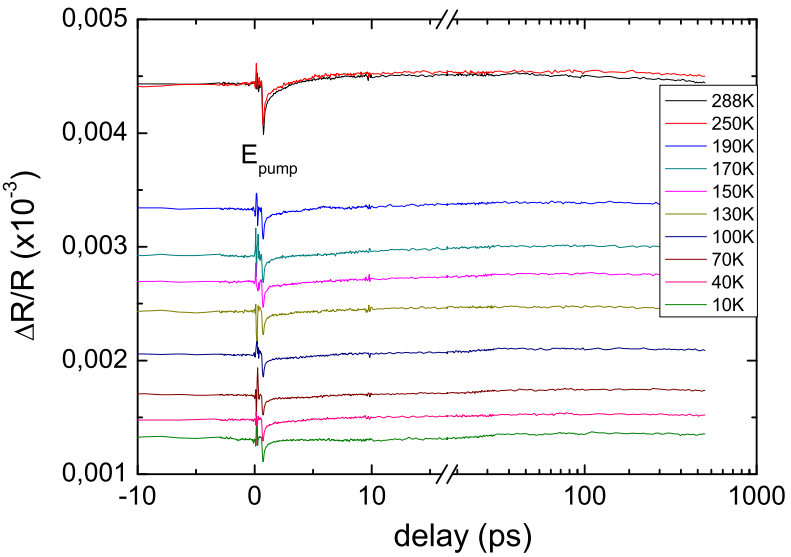

Figure 8.13: Reflectivity change for $Ca_9La_5Cu_{24}O_{41}$ with E_{pump} parallel and E_{probe} perpendicular to the ladders. It is seen that the reflectivity change decreases with decreasing temperature. The data are not stacked.

The rise of the signal after the dip is fitted with a single-exponential function. The fast decay time is shown as a function of temperature in figure 8.16. It is seen that

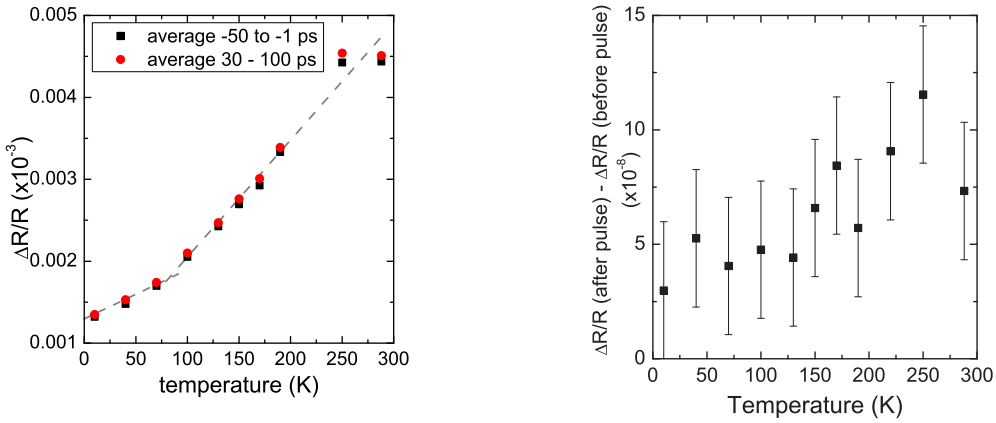

(a) (b)

Figure 8.14: a) Average background level and maximum level of $\Delta R/R$ as a function of temperature, with E_{pump} parallel and E_{probe} perpendicular to the ladders. The average background level is taken between -50 and -1 ps. The average maximum level is taken between 30 and 100 ps. The error bar is smaller than the seize of the circle/square. The grey dotted lines are guides to the eye. b) The difference between the average background level and the average maximum level of $\Delta R/R$ decreases linearly with temperature. The error in this measurement is much larger than for the other probe polarization, because the difference signal is orders of magnitude smaller.

the fast decay time, which is ascribed to electron-phonon thermalization, is somewhat shorter than found when E_{probe} is parallel to the ladders, and is slightly increasing with temperature. No slower decay time is needed to fit the data, which means that this component, if present, is longer than the timescale of the experiment, which is 0.5 ns. Therefore, it is constant at the time scale of the experiment and only one decay time plus a constant background is sufficient to fit the data.

Third, again the temperature dependence was measured for both E_{pump} and E_{probe} perpendicular to each other, with E_{pump} parallel to the ladder direction, this time zooming in on the shorter time scale. The data for different temperatures are shown in figure 8.17. They are fitted with a single exponential decay and similar results as for the long range data are found. The $\Delta R/R$ signal is about five times larger in this measurement, equal to the measurement with E_{probe} parallel to the ladders. This is probably due to a better overlap of pump and probe beam. Furthermore, in these data for some temperatures phonon oscillations are observed. The oscillation period T goes down slightly from 0.97 ps at 210 K to 1.33 ps at 40 K. Assuming this is an acoustical phonon, the sound velocity calculated is approximately 130 km/s. However, this is too high for an acoustical phonon in this compound. From the dispersion relation of a similar compound a typical acoustical phonon velocity of 12 km/s was calculated. Therefore, the interference is ascribed to an optical phonon.

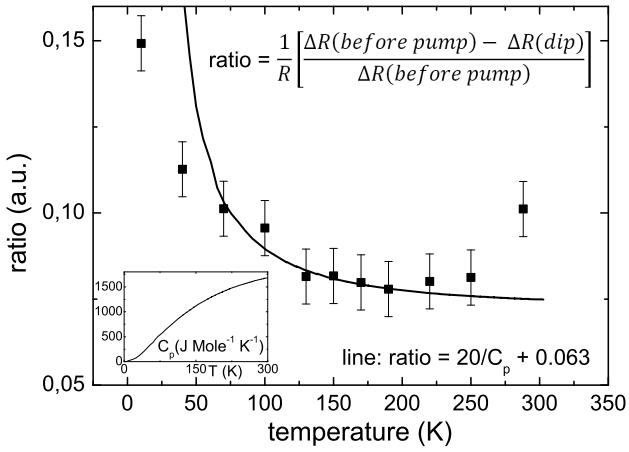

Figure 8.15: Difference between the value of $\Delta R/R$ at the dip induced by the pump pulse and the average background level at negative times as a function of temperature, with E_{pump} parallel and E_{probe} perpendicular to the ladders. Since $\Delta R/R$ depends strongly on temperature, the data are normalized to the average background level. The shape of the curve follows the inverse of the specific heat, apart from the low temperature region in which the specific heat is strongly temperature dependent, indicating that the amplitude of the dip is linear with the temperature increase induced by the pump pulse.

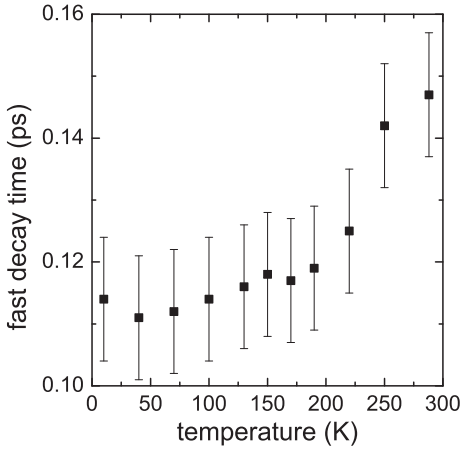

Figure 8.16: Fast decay times as a function of temperature, with E_{pump} parallel and E_{probe} perpendicular to the ladders. It is seen that the fast decay time, which is ascribed to electron-phonon thermalization, is nearly constant with temperature, apart from the highest temperatures.

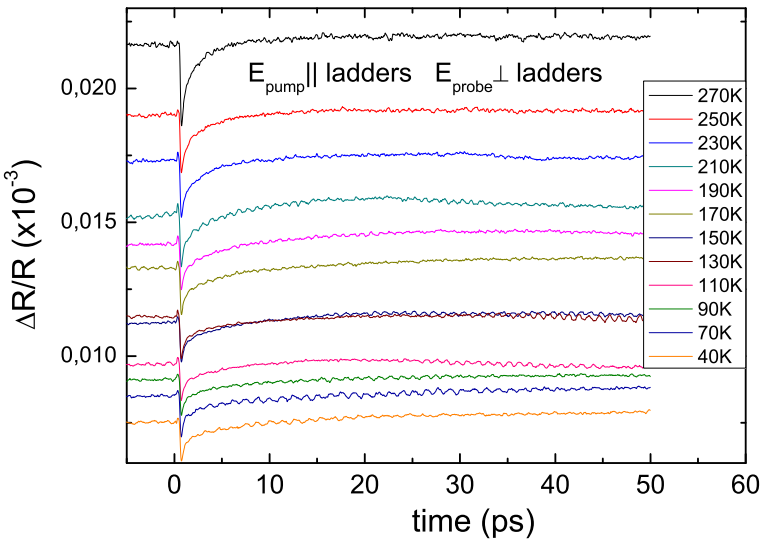

Figure 8.17: Reflectivity change for $Ca_9La_5Cu_{24}O_{41}$ with E_{pump} parallel and E_{probe} perpendicular to the ladders. Compared to figure 8.13 a smaller temperature domain is taken. The data are not stacked. It is seen that the reflectivity change decreases with decreasing temperature. Furthermore, phonon oscillations are observed for some temperatures.

8.3 Visible pump - infrared probe dynamics

Visible pump - IR probe time resolved transmission measurements have been performed on a 82 μm thick $Ca_9La_5Cu_{24}O_{41}$ sample in the attempt to investigate the magnon dynamics and scattering at the ps timescale. The advantage over reflectivity measurements is that surface effects are much less important when measuring through the sample. Unfortunately, pumping directly at the magnon absorption frequencies is not possible since the laser power is too low at these wavelengths. Therefore, 800 nm is chosen and the excitation will be mainly thermal. Furthermore, the pump beam is only exciting the first $\sim$ 200 nm of the sample, while the probe goes through completely, thus the volumes which are pumped and probed are very different. The details of the experiment and the experimental setup are described in section 4.2.5. Measurements were done for different probe wavelengths, temperatures, pump polarizations (parallel and perpendicular to the ladder) and pump and probe powers.

8.3.1 Temperature dependence

In figure 8.18 four differential transmissivity traces are shown, one for every probe wavelength used. These traces are measured at 5.5 K with the pump pulse polarization perpendicular to the ladders and the probe pulse polarization parallel to the ladders. In figure 8.18 and in the next figures the different probe wavelengths will be indicated with the same colors as in figure 8.1. The best fit to all the traces is shown. Fitting

is done with a bi-exponential decay with a constant background to take into account heating effects, convoluted with the width of the pump pulse.

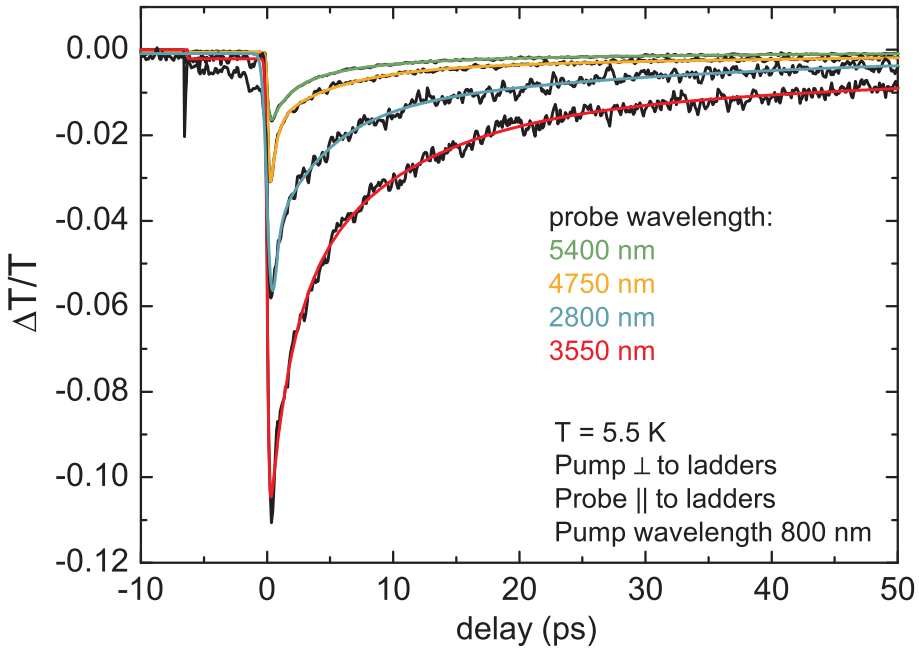

Figure 8.18: Transmissivity change for $Ca_9La_5Cu_{24}O_{41}$ with E_{pump} perpendicular to the ladders and E_{probe} parallel to the ladders. The pump pulse has an energy of 1.55 eV (800 nm), while the probe pulse has different energies: 0.23 eV (5400 nm), 0.26 eV (4750 nm), 0.35 eV (3550 nm) and 0.44 eV (2800 nm). The colors used for different wavelengths are similar to the ones in figure 8.1. The temperature is 5.5 K. The best fit to all the traces is shown. Fitting is done with a bi-exponential decay convoluted with the width of the pump pulse.

Figure 8.19 shows the dependence of the short decay time in the bi-exponential fit on temperature for the four different probing wavelengths used in the experiment. This decay time most probably corresponds to the electronic charge equilibration time. No dependence on probe wavelength or temperature is observed. However, when pumping parallel to the ladders, the decay is about 1.5 times faster than when pumping perpendicular to the ladders. This is probably related to the lower band gap in the ladder direction (1.4 eV) as compared to the a-direction (2.4 eV) [42]. This was also observed for GaAs [134]. The long carrier cooling time at wavelengths near or below the band edge (a-direction) is explained by the insufficient excess energy of the electrons for optical phonon emission, which is the most efficient electron cooling process for higher energy electrons, i.e. the ones created when exciting in the direction parallel to the ladder. The percentage transmissivity change for a certain temperature and probe wavelength but different pump polarization is the same, however.

Figure 8.20 shows the dependence of the long decay time in the bi-exponential fit on temperature for the four different probing wavelengths used in the experiment. For the longest wavelength and the shortest wavelength the probe pulse is most sensitive to the phonons and electrons, respectively. For both these probe wavelengths the same trend

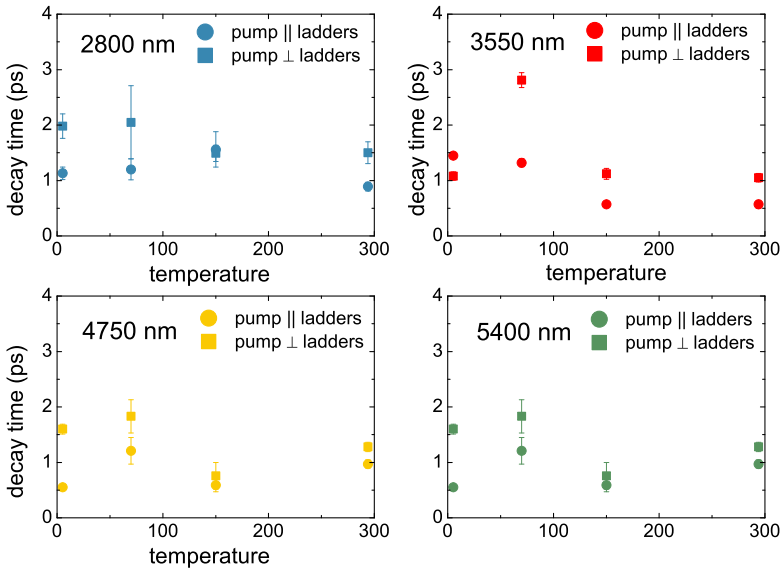

Figure 8.19: Short decay time from the bi-exponential decay fit function for different probe wavelengths as a function of temperature. Data for both pump pulse polarizations are shown. This decay time most probably corresponds to the electron-phonon relaxation time. No dependence on probe wavelength or temperature is observed. When pumping parallel to the ladders (circles) the decay time is about 1.5 times lower than when pumping perpendicular to the ladders (squares).

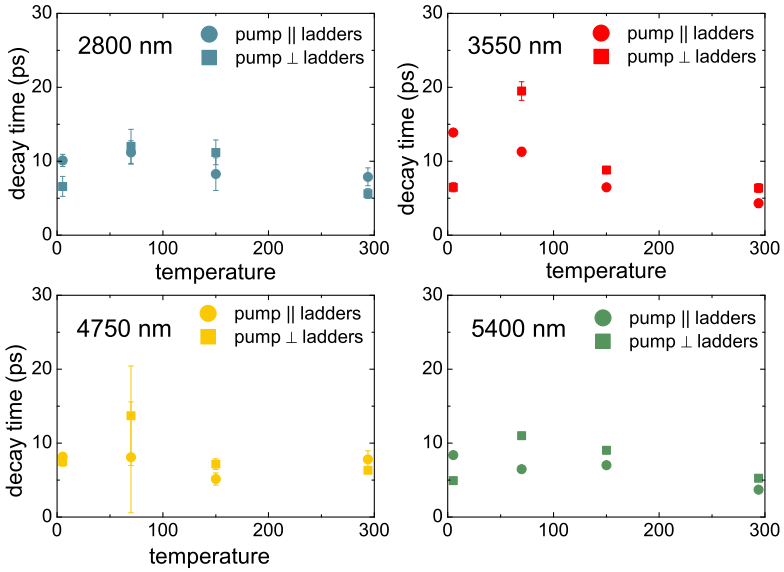

Figure 8.20: Long decay time from the bi-exponential decay fit function for different probe wavelengths as a function of temperature. Data for both pump pulse polarizations are shown.

is seen; at 5.5 K the decay time for E_{pump} perpendicular to the ladders is about 30 % lower than for E_{pump} parallel to the ladders. While the decay time for E_{pump} parallel to the ladders stays constant with temperature, E_{pump} perpendicular to the ladders has a maximum at 70 K and then slowly goes down with temperature. Since for both wavelengths the behaviour is the same, it is ascribed to electron-phonon thermalization times, which are typically in the order of 10 ps, in agreement with the experimental results. The difference in thermalization time behaviour for E_{pump} perpendicular or parallel to the ladders could be related to the different bandgap in these directions. Furthermore, it could be an influence of magnon dynamics, since the magnon absorption peaks are very broad, and the trend at the two center probe wavelengths is the same but stronger. At these wavelengths especially the decay time for E_{pump} perpendicular to the ladders at 70 K is significantly longer than for E_{pump} parallel to the ladders. The short decay time is tentatively interpreted as the electron-phonon thermalization time, and the long decay time as the phonon-phonon thermalization time.

A possible scenario for the difference in decay time for different pump pulse polarizations is the following: when pumping parallel to the ladder, i.e. over the bandgap, a lot of high energy electrons are created which are equilibrating by exciting high energy phonons and magnons. A similar trend was observed in GaAs [134]. The scattering probability for magnons with high energy phonons is much higher than for magnons with low energy (acoustic) phonons, because of energy, momentum and spin conservation requirements. This was extensively discussed in section 6.4. Therefore, the presence of these high energy phonons increases the scattering probability of the magnons, thereby decreasing their relaxation time. When pumping perpendicular to the ladder, only electrons at the bottom of the electron band are excited and less high energy phonons will be created, thereby decreasing the scattering probability of magnons and increasing their decay time. It is not clear however, why this effect would be strongest at 70 K.

In figure 8.21 the long decay time is plotted for different temperatures as a function of probe wavelength. The decay time for pumping with E_{pump} parallel to the ladders slightly decreases with temperature, showing no clear difference between the probe wavelengths sensitive to magnons and the ones mainly sensitive to electrons or phonons. Apparently, when pumping this way, a negligible concentration of magnons is created. The decay time for pumping with E_{pump} perpendicular to the ladders shows a maximum at 70 K, and especially the decay times for probe frequencies sensitive to the magnons are increased. Above 70 K there is not a clear difference in decay times for different probe frequencies. Furthermore, the decay times slowly decrease with increasing temperature. For pumping with E_{pump} perpendicular to the ladders the decay time is longer for every probe wavelenght at 70 K and 150 K, while at 5.5 K it is shorter. At room temperature no clear difference can be seen.

The average heating of the excited volume (after electrons and phonons are thermalized) due to a single pump pulse at maximum power ($\sim$ 75 mW) can be estimated from the beam diameter (550 μm) and the penetration depth at 800 nm ($\sim$ 200 nm), which is obtained from the imaginary part of the dielectric constant [42]. The rise of temperature ΔT can be quite high, therefore the temperature dependence of the heat capacity C_p has to be taken into account and an integration has to be performed as was done in formula 6.1. This formula was used to calculate the temperature increase

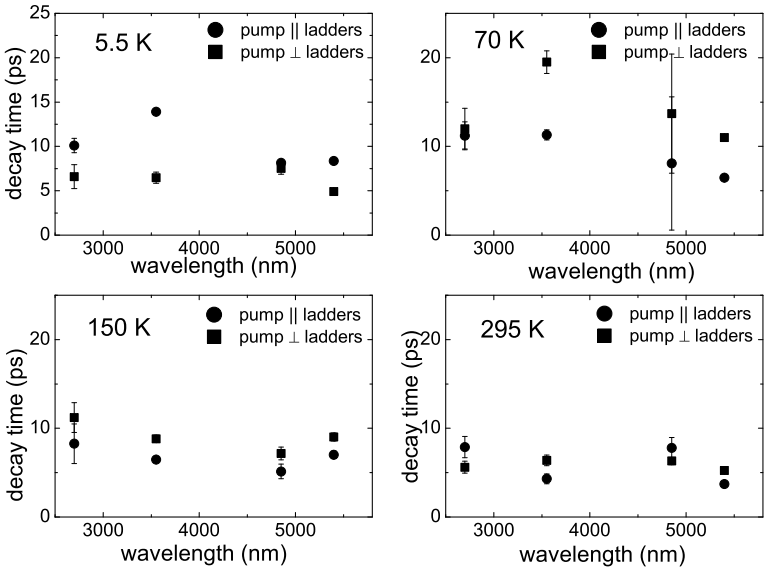

Figure 8.21: Long decay time from the bi-exponentioal decay fit function for different temperatures as a function of probe wavelength. Data for both pump pulse polarizations are shown.

at the front surface of the sample in the fluorescent flash method. In the pump-probe experiment the maximum temperature can be estimated numerically from

$$\Delta T = \frac{Q}{V \int_{T_0}^{T_{max}} C_p(T) dT}, \quad \Delta T = T_{max} - T_0 \tag{8.2}$$

in which Q is the energy deposited by the pump pulse, V is the volume in which it is deposited, T_{max} is the maximum temperature in the heated volume, and T_0 is the cryostat temperature. At 5.5 K, ΔT is $\approx$ 80 K. At 70 K, ΔT $\approx$ 30 K is much smaller. At 150 K ΔT $\approx$ 10 K and at 295 K ΔT $\approx$ 4 K. This has to be considered as an upper limit, since diffusion and reflection are neglected. Figure 8.22 shows the temperature increase and the maximum temperature reached as a function of cryostat temperature for a maximum pump fluence of 0.6 mJ/mm^2 and 0.3 mJ/mm^2. Especially at temperatures below 100 K the heating by the pump is large.

Figure 8.23 shows the maximum amplitude of ΔT/T as a function of pump fluence at 5.5 K for different probe wavelengths. It is seen that at 2800 nm and 4750 nm the pump fluence dependence is linear. At 3550 nm and 5400 nm it is linear at low pump fluences but possibly saturates at the highest pump fluence used. Furthermore, it is striking that at these two wavelengths, the maximum ΔT/T is about 3 times higher than at the other two wavelengths. This shows no correlation with different probe fluences used when measuring the pump fluence dependence. It is not clear why this occurs.

Figure 8.24 shows normalized ΔT/T traces for probe wavelengths 3550 nm (left upper corner) and 4750 nm (left lower corner) for different probe strengths at 5.5 K. One can see that the decay is independent of probe strength, showing that the

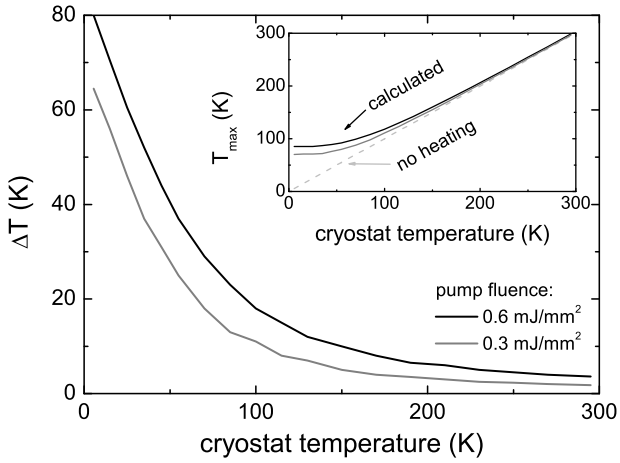

Figure 8.22: Nearly instantaneous temperature increase and maximum temperature reached in the volume heated by the pump pulse for two different pump fluences. Especially below 100 K the heating by the pump is large. Diffusion and reflection are neglected in this calculation, therefore it should be considered as an upper limit.

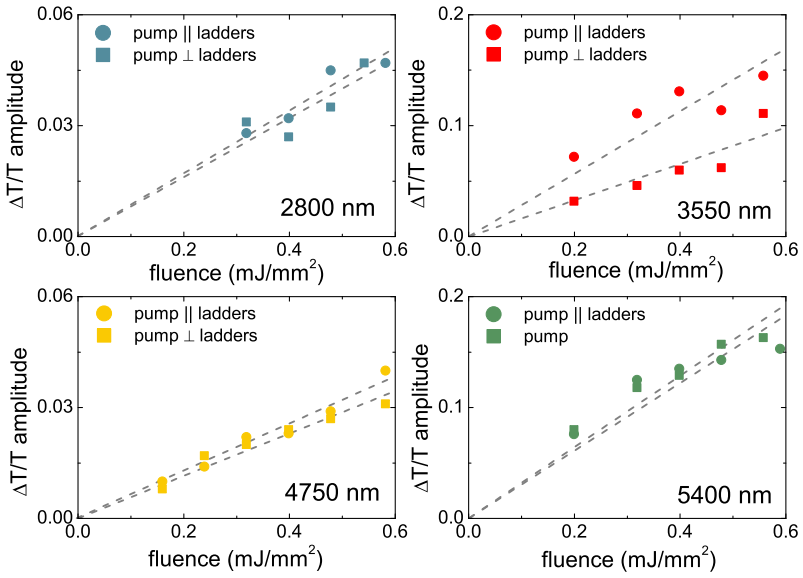

Figure 8.23: Pump fluence dependence of the maximum amplitude of $\Delta T/T$ at 5.5 K for different probe wavelengths. Data for both pump pulse polarizations are shown, together with a best linear fit to the data.

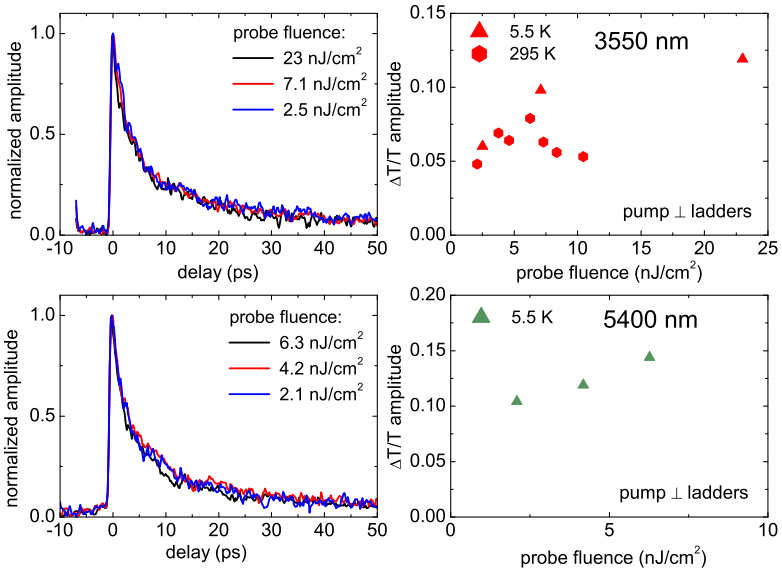

Figure 8.24: Left: normalized $\Delta T/T$ traces for probe wavelengths 3550 nm (left upper corner) and 4750 nm (left lower corner) for different probe strengths at 5.5 K Right: Probe strength dependence of the maximum amplitude of $\Delta T/T$ at probe wavelengths 3550 nm for 5.5 K (triangles) and 295 K (hexagonals) and 4750 nm for 5.5 K.

measurements are in the linear regime. On the right, the maximum amplitude of $\Delta T/T$ is shown for 3550 nm probe (right upper corner) for 5.5 K and 295 K and for 4750 nm probe (right lower corner) for 5.5 K. A decrease in $\Delta T/T$ for higher probe strenghts could be due to saturation of ΔT, when the probe pulse is stronger than needed to make all possible excitations. Then, since T keeps on increasing but ΔT saturates, the total $\Delta T/T$ will be lower. This trend is seen in the ΔT data. But the increase with probe strength for low strengths is not understood. This means that amplitudes $\Delta T/T$ cannot be compared between different wavelengths, since the probe strength used is somewhat different and it is not clear if the dependence is the same for every probe wavelength.

8.3.2 Magnon related oscillations

When looking at 5.5 K for medium pump fluences, 20 mJ cm^{-2}, coherent oscillations are observed for the probe wavelengths of 3550 and 4750 nm, i.e. the probe wavelengths sensitive to the magnon dynamics. The clearest oscillation is observed for a probe wavelength of 4750 nm with both E_{pump} and E_{probe} parallel to the ladder, and is shown in figure 8.25a. The difference between the measured pump-probe curve and the bi-exponential fit is plotted as a function of time. A clear beating pattern is seen from t=0 which can be fitted by a double sinusoidal function. By making a wavelet transformation the different frequencies are resolved, as is shown in figure 8.25b. Two peaks are observed at 0.147 THz (0.609 meV) and 0.175 THz (0.725 meV). The different frequencies are plotted as a function of time in figure 8.26. The oscillations are gone

after $\sim$ 20 ps. For the other pump polarization, perpendicular to the ladders, no oscillation was observed.

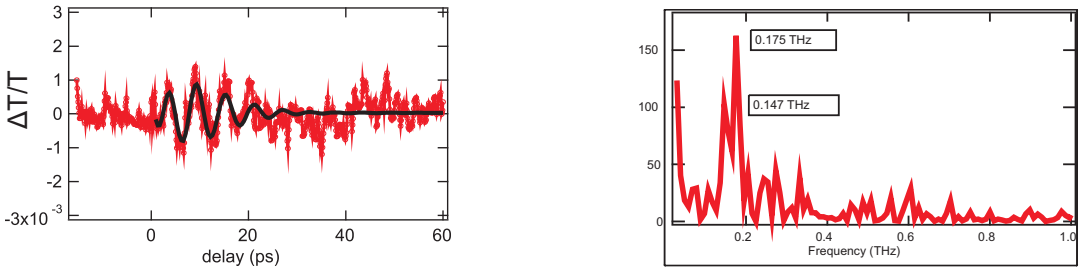

(a) (b)

Figure 8.25: a) Difference between measured pump-probe curve and bi-exponential fit at 5.5 K for a fluence of 20 mJ cm^{-2} and a probe wavelength of 4750 nm. A clear oscillation with beating is observed, which is fitted with a double sinusoidal function. b) Frequency analysis of the oscillation. Two main components of 0.147 THz and 0.175 THz are observed.

Also for the probe wavelength of 3550 nm at 5.5 K with 20 mJ cm^{-2} fluence oscillations are observed for both pump polarizations. These oscillations are not very clear in the pump-probe time traces, but are when looking at the Wigner transformation, as is shown in figure 8.27 for both pump polarizations. The Wigner transformation is used here because it gives a clearer output. For E_{pump} perpendicular to the ladders, a frequency of 0.332 THz (1.37 meV) is found, and for E_{pump} parallel to the ladders a frequency of 0.478 THz (1.98 meV) is found.

The oscillations are only present at the lowest pump fluences used in the experiment, and only for the probe wavelengths sensitive to magnon dynamics. The frequency is low and depends on the probe wavelength and the polarization of the pump. Different explanation are possible. For example, it might be the coherent excitation of an acoustical phonon. Something similar was observed in GaAs [135]. The fluence threshold could then be explained by a coherence loss when the fluence is too high. However, in this case two different acoustical phonons should have beating frequencies which are related as $f_1/f_2 = \lambda_2/\lambda_1$, which is not the case. Furthermore, the absense

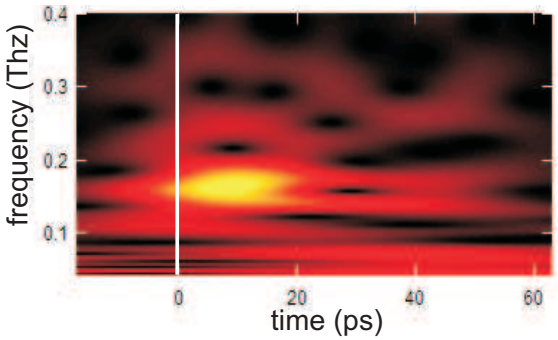

Figure 8.26: Wavelet transformation for data obtained with 4750 nm probe as a function of time. The oscillations are gone after $\sim$ 20 ps.

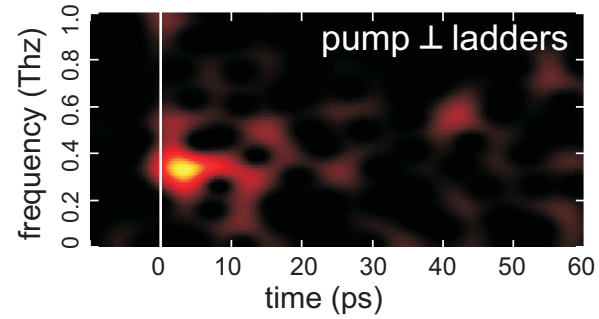

(a)

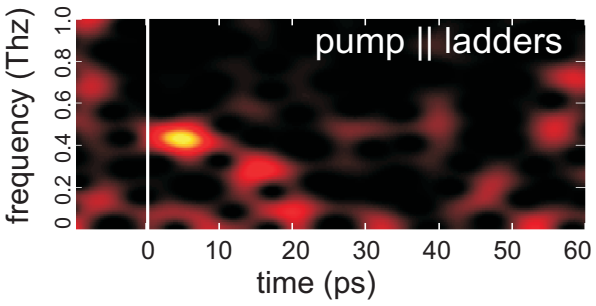

(b)

Figure 8.27: a) Wigner transformation for the data obtained with 3550 nm probe with E_{pump} perpendicular to the ladders as a function of time. An oscillation with a frequency of 0.332 THz is found. The oscillation is gone after $\sim$ 7 ps. b) Wigner transformation for the data obtained with 3550 nm probe with E_{pump} parallel to the ladders as a function of time. An oscillation with a frequency of 0.332 THz is found. The oscillation is gone after $\sim$ 10 ps.

of the oscillations at frequencies where there is no sensitivity to the magnon dynamics cannot be explained in this way. This obervation hints at an explanation involving magnon dynamics, for example coupling between charges and magnons or quantum beats of the single magnons with the 2-magnon continuum. The energy of the beating oscillations are around 0.6-0.7 meV, while the thermal energy k_bT is around 0.45 meV at this temperature.

8.4 Summary and conclusion

This chapter describes the femtosecond to picosecond dynamics in the spin ladder $Ca_9La_5Cu_{24}O_{41}$. The goal of these measurements is to gain an understanding of the magnon dynamics in this material, and the interplay between magnons, electrons and phonons at short timescales. First, temperature dependent infrared transmission measurements for both light polarizations parallel and perpendicular to the ladders are done. The low temperature data are in agreement with literature. For the light polarization parallel to the ladders, two magnon absorption bands are observed around 2300 and 2700 cm^{-1}, respectively. The temperature dependence of these bands shows a possible quenching of the oscillator strength at 120 K. Additional measurements have to be done to understand the reason for this possible quenching. For the light polarization perpendicular to the ladders, no signs of magnon absorption are observed and the spectra show only a weak temperature dependence.

Furthermore, room temperature and temperature dependent pump - probe transient reflectivity measurements are performed. The wavelength dependent room temperature measurements allow to extract the acoustical phonon velocity, which is 7.7 ± 1 km/s. The relative change in reflectivity $\Delta R/R$ increases with increasing pump pulse energy density. Also, $\Delta R/R$ decreases with temperature. A temperature dependence is measured for both probe pulse polarizations. When probing with polarization parallel to the ladders, oscillations due to acoustical phonons are observed. When probing with polarization perpendicular to the ladders, much faster oscillations are observed, which are probably due to optical phonons. For the probe with parallel polarization, using a bi-exponential fit, the fast decay time is in the order of 0.4 ps and constant with temperature, while the slow decay time is linearly decreasing with increasing temperature from 10 ps at 10 K to 4 ps at 300 K. These are ascribed to the electron-phonon thermalization time and the phonon-phonon thermalization time, respectively. When the probe polarization is perpendicular to the ladders, only a single-exponential fit is needed, and the decay time is slightly faster than the fast exponent in the parallel probe polarization measurement. For both probe polarizations, the difference between $\Delta R/R$ before and after the pump pulse increases with increasing temperature. The difference of $\Delta R/R$ before the pump pulse and the dip in $\Delta R/R$ induced by the pump pulse, normalized to the value before the pump pulse, follows the inverse of the specific heat, indicating that amplitude of the induced dip is linear with the temperature increase induced by the pump pulse.

The last measurement series consists of temperature dependent time-resolved transmission measurements. Four probe wavelengths in the infrared are used, two at the position of the magnon absorption bands and two outside these bands. The polarization of the light is parallel to the ladders. Pumping is done with 800 nm light. No

clear conclusions can be drawn from the short and long decay times, extracted from a bi-exponentional fit to the data. Some observations can be made; the short decay time is similar for every probe wavelength and no clear trend is seen in the temperature dependence. Especially at low temperature, short fast decay time for the pump polarization perpendicular to the ladders is higher than for the pump polarization parallel to the ladders. For the long decay time this is also the case. It is highest at 70 K. The difference in decay time could be due to the difference in band gap in the different directions. An estimation of the temperature increase due to the pump pulse shows that at 5.5 K, the lowest temperature used in the experiments, the temperature increase can be up to 80 K. For all probe wavelengths, the induced change in transmission increases linearly with pump pulse fluence. Furthermore, a probe pulse power dependence was observed due to saturation of the change ΔT in the probe signal. Finally, oscillations are observed at 5.5 K for medium pump pulse power and probe wavelengths in the magnon absorption band. Although these oscillations cannot be explained from the obtained data only, the absence at probe wavelengths outside the magnon absorption bands suggests that they are related to magnon dynamics.

Maybe even more than answering questions, these first time resolved data on the spin ladder $Ca_9La_5Cu_{24}O_{41}$ give rise to additional questions. Much more measurements have to be done to fully understand what is going on in this material at short timescales. Why pumping with E_{pump} perpendicular to the ladders seems to lead to a longer decay time of particles, probably magnons? Why this longer decay time is mainly observed for one of the two magnon absorption bands? What is the meaning for the dependence of the amplitude of $\Delta T/T$ on the probe power? Is it present for every probe wavelength? Why the longest decay time is observed at 70 K? And what are the low-frequency oscillations that are only present when one probes at the wavelengths sensitive to magnon dynamics?

One thing one would like to do is to directly and coherently excite magnons. Also, pumping in the infrared would make the penetration depth of pump and probe nearly equal, thereby probably increasing the probe signal. In the current measurements infrared pumping was not possible since the infrared pulses do not have enough energy. Furthermore, apparently there is a difference in response between the electric field polarizations with which one pumps, but there might be such a dependence on probe polarization too. Especially because from the static infrared transmissivity spectra it is clear that when probing perpendicular to the ladders no signatures of magnons are observed. Therefore, plans to supplement these measurements are under consideration by measuring the probe polarization anisotropy at the magnon frequency while resonantly pumping at the magnon frequencies. These experiments have to be carried out at an infrared free electron laser source facility.

9. Summary

In contrast to the well known ordered three-dimensional magnetism, one-dimensional quantum magnets show only short range correlations. In these materials there is a competition between two processes. On one hand, the system strives for the lowest energy, and therefore the most ordered ground state. On the other hand, quantum fluctuations prevent long range ordering in one or two dimensions, leading to the intermediate situation with strong correlations between nearby spins, but no magnetic order on longer length scales at room temperature. Since the spin correlations resemble the positional correlations as found in liquids, these low-dimensional magnetic systems are often referred to as 'spin liquids'. Many of the materials showing spin liquid behavior are part of a larger class of cuprate materials showing many unusual and intriguing phenomena, including high temperature superconductivity and Bose-Einstein condensation of magnons.

The goal of the work on low-dimensional quantum magnets presented in this thesis is twofold; on the one hand obtaining more knowledge on the interaction between the magnetic excitations and other types of excitations (electrons, phonons). On the other hand, understanding how the favorable properties of the one-dimensional magnetic system can be used in the cooling of microdevices, for example by making use of one-dimensional heat transport and controllable heat channels. It is well known that efficient heat removal is crucial to the performance of many electronic devices; overheating often leads to overall system failures. The spin ladder and spin chain materials investigated in this thesis, in which the magnetic structure forms a ladder and chain, respectively, are promising candidates for advanced cooling mechanisms for several reasons. First of all, heat is conducted primarily along one crystal axis, hence the material can thermally insulate in one direction and carry away heat along another. The ratio between the conductivities in the good and bad directions can be about 40. Second, the thermal conductivity in the conducting direction is $\kappa_{mag} \approx 100$ W m^{-1} K^{-1}, i.e. comparable to a metal. For example, for nickel $\kappa \approx 85$ m^{-1} K^{-1}, for copper $\kappa \approx 350$ m^{-1} K^{-1} and for the widely used material silicon $\kappa \approx 140$ m^{-1} K^{-1}. Third, these compounds are electrically insulating and can therefore be used to simultaneously electrically insulate electronic circuits and transport heat. Finally, heat is carried by localised spins which can be manipulated with magnetic fields or light. This opens the possibility of having a controllable thermal conductivity at room temperature.

The spin chain material $SrCuO_2$ and spin ladder materials $Ca_9La_5Cu_{24}O_{41}$ and $Sr_{10}La_4Cu_{24}O_{41}$, which are investigated in this thesis, are introduced in chapter 2. The magnetism in these systems are well described by the Heisenberg model. For the spin chain, the model can be solved analytically, leading to the interesting prediction of dissipationless magnetic heat transport. For the spin ladder, no analytical solution exists.

Some insight is gained by looking at two limiting cases; two parallel non-interacting chains on the on hand and a chain of non-interacting rungs on the other. The dispersion relation for both systems is very different, the most striking difference being that the spin ladder systems have a large spin gap of some tens of meV, while the spin chain dispersion is gapless. Chapter 3 starts with a mathematical description of (anisotropic) heat diffusion. Along the one-dimensional spin system both magnetic and lattice excitations participate in the heat transport. During a typical conductivity experiment, only the temperature of the lattice excitations can be measured. A standard macroscopic diffusion model can be used when the magnetic and lattice excitations reach thermal equilibrium at a time scale much faster than the time scale of the experiment. If this is not the case, both excitations have to be taken into account and a macroscopic two-temperature diffusion model is needed to describe the problem. If in such case the one-temperature diffusion model is used, an effective thermal conductivity is obtained, which size depends on the degree of thermalization between the lattice and magnetic excitations. This chapter also discusses scattering mechanisms and different parameters that determine the size of the thermal conductivity, as well as a proof-of-principle experiment on the spin chain $SrCuO_2$, showing that the thermal conductivity is easily controllable. Furthermore, the temperature dependence of the steady state thermal conductivity for spin chains and ladders is described, showing a huge magnetic contribution along the ladder/chain at most temperatures that dwarfs the lattice contribution, leading to a large anisotropy between the ladder/chain direction and the other directions.

Since heating in microelectronics can be both static and dynamic, one would like to measure the thermal conductivity for both situations. In this work, the temperature detection is done optically. A spin coated layer of EuTTA is used as temperature sensor, which has the property that when exciting the layer with UV light, the orange fluorescence intensity is strongly temperature dependent. This way of temperature detection can be used both in a static and a time-resolved fashion. To make a straightforward comparison possible between a conventional static experiment and a measurement using the optical temperature sensor, the static thermal conductivity is measured optically in chapter 5. The experiment is done by heating a brick-like sample continuously from one side and connecting the opposite side to a heat sink. The temperature of the surface of one of the sides between heater and heat sink is measured locally using a microscope. The advantage of this method over the conventional one is the increased spatial resolution it offers and therefore the possibility to see differences in behaviour between different parts of the sample. The spatial resolution is only limited by the diffraction limit. By measuring close to the heat source, the part of the sample where thermal equilibrium between different heat carriers has not yet been reached can be accessed. Although different critical experimental parameters like a one-dimensional heat flow, the cooling of the heat sink, the stable mounting of the sample, and heat losses have to be controlled better, some first results are obtained showing the advantages of the method. The initial experiments showed a good agreement between this new method and the conventional method for both nickel as well as for the spin ladder compound.

Chapter 6 describes dynamic bulk thermal conductivity measurements on both the spin chain $SrCuO_2$ and the spin ladders $Ca_9La_5Cu_{24}O_{41}$ and $Sr_{10}La_4Cu_{24}O_{41}$. From

the experiments insight has been obtained on the magnon dynamics at the microsecond timescale, which is not easily accessible in a steady state experiment. The measurements are performed using the newly developed fluorescent flash method, in which a platelet of material is heated with a laser pulse on one side, while the temperature is detected as a function of time on the other side, using the same layer of EuTTA as in the static experiment as a temperature sensor. Interestingly, while for the spin chain the effective dynamic bulk thermal conductivity is equal to the steady state bulk thermal conductivity, for the spin ladders it is considerably lower, around 40 W m^{-1} K^{-1}. Furthermore, it shows a thickness dependence, as was measured on $Ca_9La_5Cu_{24}O_{41}$. Therefore, instead of the macroscopic model, the macroscopic two-temperature diffusion model is used to analyze the thickness-dependent dynamic thermal conductivity. Changing the sample thickness effectively changes the time scale in the experiment and therefore the degree of thermalization. This allows to extract the thermalization time between magnons and phonons in $Ca_9La_5Cu_{24}O_{41}$. It is found to be a few hundreds of μs at room temperature, which is extremely long. This can be explained by the low conversion probability between phonons and magnons. In spin ladder materials the dispersion shows a large spin gap, which is a bottle neck for the conversion of slow phonons into the fast magnons, since such scattering processes violate spin, momentum and energy conservation rules. Using another temperature sensitive compound, EuTFC, the thermal conductivity of $Ca_9La_5Cu_{24}O_{41}$ is measured for different temperatures from 10 to 300 K. It is found that the effective thermal conductivity for a certain sample thickness is closer to the steady state thermal conductivity when the magnon contribution is smaller, as would be expected from our two-temperature model.

In chapter 7 dynamic heat transport along the sample surface is investigated. The surface is imaged by a microscope, again using a EuTTA layer as temperature sensor. The anisotropic spread of heat from a hot spot, created by a laser, is followed in time. From these data the diffusion constant is extracted. Both the spin chain $SrCuO_2$ and the spin ladders $Ca_9La_5Cu_{24}O_{41}$ and $Sr_{10}La_4Cu_{24}O_{41}$ are measured for different surface roughnesses. It is found that the thermal conductivity of the ~ 1 μm RMS roughness samples is at least two times lower than the dynamic bulk value determined in the fluorescent flash method in both the direction parallel to the ladder/chain and the direction perpendicular to the ladder/chain. Furthermore, a prototype microelectronic device was created by depositing a gold cross structure on the surface of the spin ladder $Ca_9La_5Cu_{24}O_{41}$. One strip was parallel to the ladders and the other one perpendicular. The strips are electrically heated, one at a time for a few tens of microseconds, thereby simulating a hot strip as can appear in a real microdevice. The thermal conductivity for this very flat 20 nm RMS surface roughness sample is measured using optical heating as well as using electrical heating. The results of both methods are in good agreement; 37 ± 3 W m^{-1} K^{-1} for the fast direction parallel to the ladders and 2.5 ± 0.5 W m^{-1} K^{-1} for the slow direction perpendicular to the ladders, respectively. The thermal conductivities in the fast and slow direction, measured in a dynamic way, are in agreement with bulk dynamic measurements at similar timescales on samples from the same batch. These experiments show that the sample surface can be prepared such that it does not influence the heat transport measurably, and that the heat transport does not depend on the way that the heat is put into the system. Chapter 6 and 7 highlight the potential of spin ladder materials as a directional heat transport channel. However,

when using quickly varying heat sources, the value of the thermal conductivity along the ladders is lower than under steady state conditions. Therefore, if a high value of the thermal conductivity is the main criterion, the directional heat transport channel can only be applied to slowly varying heat sources and over distances long enough such that the first part in which there is no thermal equilibrium is negligible. However, if a large anisotropy is the most critical parameter, then this material, the dynamic anisotropy still being ~ 15, suits application as a directional heat transport channel for quickly varying heat sources as well.

Finally, chapter 8 explores the femtosecond to picosecond dynamics in the spin ladder $Ca_9La_5Cu_{24}O_{41}$. The goal of these measurements is to gain an understanding of the short timescale magnon dynamics in this material, and the interplay between magnons, electrons and phonons. First, temperature dependent infrared transmission measurements for both light polarizations parallel and perpendicular to the ladders are done to determine the position of the magnon peaks. The low temperature data are in agreement with literature. For the light polarization parallel to the ladders, two magnon absorption bands are observed. The temperature dependence of these bands shows a possible quenching of the oscillator strength at 120 K. Additional measurements have to be done to understand the reason for this possible quenching.

Then, temperature dependent pump - probe transient reflectivity measurements are performed for a first understanding of electron and phonon dynamics. It is observed that $\Delta R/R$ decreases with temperature. Furthermore, when probing with polarization of light parallel to the ladders, oscillations due to acoustical phonons are observed. When probing with polarization perpendicular to the ladders, much faster oscillations are observed, which are probably due to optical phonons. For the probe with parallel polarization, using a bi-exponential fit, the fast decay time is in the order of 0.4 ps and constant with temperature, while the slow decay time is linearly decreasing with increasing temperature from 10 ps at 10 K to 4 ps at 300 K. These are ascribed to the electron-phonon thermalization time and the phonon-phonon thermalization time, respectively. When the probe polarization is perpendicular to the ladders, only a single-exponential fit is needed, and the decay time is slightly faster than the fast exponent in the parallel probe polarization measurement.

The last measurement series consisted of temperature dependent time-resolved transmission measurements. Four probe wavelengths in the infrared were used, two at the position of the magnon absorption bands and two outside these bands. By comparing time traces for wavelengths within and outside the bands, some first insights can be obtained about magnon dynamics. The polarization of the light was parallel to the ladders. Pumping was done with 800 nm light. No clear conclusions can be drawn from the short and long decay times, extracted from a bi-exponentional fit to the data. Some observations can be made; the short decay time is similar for every probe wavelength and no clear trend is seen in the temperature dependence. Especially at low temperature, the short decay time for the pump polarization perpendicular to the ladders is higher than for the pump polarization parallel to the ladders. For the long decay time this is also the case. Also it is highest at 70 K. The difference could be due to the difference in band gap in the different directions. Finally, oscillations are observed at 5.5 K for medium pump pulse power for probe wavelengths in the magnon absorption band. Although these oscillations cannot be explained from the

obtained data only, the absence at probe wavelengths outside the magnon absorption bands suggests that they are related to magnon dynamics.

10. Samenvatting

In tegenstelling tot het bekende geordende driedimensionale magnetisme laten eendimensionale kwantummagneten alleen correlaties zien over een korte afstand. In deze materialen zijn twee competitieve processen aan het werk. Aan de ene kant streeft het systeem naar de laagste energie en daarom de meest geordende grondtoestand. Aan de andere kant voorkomen kwantumfluctuaties ordening over grote afstand in één of twee dimensies. Dit leidt tot de situatie hier tussenin, met correlaties over een korte afstand tussen spins die zich dichtbij elkaar bevinden, maar geen magnetische ordening over grotere afstand bij kamertemperatuur. Omdat de spincorrelaties lijken op de correlaties van posities in vloeistoffen worden deze laag-dimensionale magnetische systemen vaak 'spinvloeistoffen' genoemd. Veel van de materialen die zich gedragen als spinvloeistoffen zijn onderdeel van een grotere klasse van koperbevattende materialen. Hierin worden ongewone en intrigerende verschijnselen waargenomen, bijvoorbeeld hoge temperatuur supergeleiding en Bose-Einstein condensatie van magnonen.

Het doel van het werk aan laag-dimensionale kwantummagneten beschreven in dit proefschrift is tweeledig; aan de ene kant het verkrijgen van meer kennis van de interactie tussen de magnetische excitaties en andere typen excitaties (elektronen, fononen). Aan de andere kant begrijpen hoe de gunstige eigenschappen van het één-dimensionale magnetische systeem gebruikt kan worden in de koeling van microapparaten, bijvoorbeeld door één-dimensionaal warmtetransport of regelbare warmtekanalen. Het is bekend dat het efficiënt afvoeren van warmte cruciaal is voor de werking van vele elektronische apparaten; oververhitting leidt vaak tot falen van het complete systeem. Het spinketen systeem en het spinladder systeem die worden onderzocht in dit proefschrift en waarin de magnetische structuur respectievelijk een keten en een ladder vormen zijn veelbelovende kandidaten voor geavanceerde koelingsmechanismen om verschillende redenen. Ten eerste wordt de warmte voornamelijk langs één kristalas geleid. Daarom kan zo'n materiaal warmte isoleren in één richting en de warmte wegleiden in een andere. De verhouding tussen de geleiding in de goede en slechte richting kan rond de 40 liggen. Ten tweede is de warmtegeleidingscoëfficiënt langs de eendimensionale struktuur $\kappa_{mag} \approx 100$ W m^{-1} K^{-1}, vergelijkbaar met een metaal. Bijvoorbeeld, voor nikkel $\kappa \approx 85$ m^{-1} K^{-1}, voor koper $\kappa \approx 350$ m^{-1} K^{-1} en voor het veelgebruikte materiaal silicium $\kappa \approx 140$ m^{-1} K^{-1}. Ten derde zijn deze materialen elektrisch isolerend. Ze kunnen daarom gebruikt worden om elektronische circuits elektrisch te isoleren en tegelijkertijd de warmte af te voeren. Als laatste wordt de warmte getransporteerd door gelokaliseerde spins die kunnen worden gemanipuleerd met magnetische velden of licht. Dit geeft de potentiële mogelijkheid tot een regelbare warmtegeleiding bij kamertemperatuur.

De spinketen $SrCuO_2$ en de spinladder systemen $Ca_9La_5Cu_{24}O_{41}$ en $Sr_{10}La_4Cu_{24}O_{41}$,

die worden onderzocht in dit proefschrift, worden geïntroduceerd in hoofdstuk 2. Het magnetisme in deze systemen worden goed beschreven met het Heisenbergmodel. Voor de spinketen kan het model analytisch opgelost worden en volgt de interessante voorspelling van verliesloos magnetisch warmtetransport. Voor de spinladder bestaat er geen analytische oplossing. Enig inzicht wordt verkregen door naar twee grensgevallen te kijken; twee parallelle ketens zonder interactie of een keten met sporten zonder interactie. De dispersierelatie is heel verschillend voor beide systemen, het meest opvallende verschil is dat de spinladder systemen een grote energiegap (verboden zone) voor spins hebben van een tiental meV, terwijl de spinketen dispersie gaploos is. Hoofdstuk 3 begint met een wiskunde beschrijving van (anisotropische) warmtediffusie. Langs het eendimensionale spinsysteem dragen zowel magnetische als roosterexcitaties bij aan het warmtetransport. Tijdens een typisch warmtegeleidingsexperiment kan alleen de temperatuur van de roosterexcitaties worden gemeten. Een standaard macroscopisch diffusiemodel kan worden gebruikt wanneer de magnetische en roosterexcitaties thermisch evenwicht bereiken op een tijdschaal die veel sneller is dan de tijdschaal van het experiment. Als dit niet het geval is, moeten beide excitaties worden meegerekend en is een macroscopisch tweetemperaturendiffusiemodel nodig om het probleem te beschrijven. Als in zo'n geval toch het één-temperatuurmodel wordt gebruikt, wordt een effectieve warmtegeleidingscoëfficiënt verkregen, waarvan de grootte afhangt van de mate van warmteëvenwicht tussen de roosterexcitaties en magnetische excitaties. Verstrooiingsmechanismen en verschillende parameters die de grootte van de warmtegeleiding bepalen, worden besproken, net als een 'proof-of-principle' experiment aan de spinketen $SrCuO_2$, dat laat zien dat de warmtegeleiding makkelijk regelbaar is. Verder wordt de temperatuursafhankelijkheid van de steady state warmtegeleiding voor spinketens en ladders beschreven, die bij de meeste temperaturen een zeer grote magnetische bijdrage laat zien langs de ladder/keten die de roosterbijdrage overschaduwt. Dit leidt tot een grote anisotropie tussen de keten/ladderrichting en de andere richtingen.

Aangezien opwarmen in microelektronica zowel statisch als dynamisch kan zijn, willen we de warmtegeleidingscoëfficiënt voor beide situaties meten. In dit werk wordt de temperatuur optisch gemeten. Een dun laagje EuTTA wordt gebruikt als temperatuursensor, dat als eigenschap heeft, dat wanneer het laagje met UV-licht wordt bestraald, de intensiteit van de oranje fluorescentie sterk van de temperatuur afhangt. Deze manier van temperatuurdetectie kan zowel op een statische als tijdsopgeloste manier gebruikt worden. Om een directe vergelijking mogelijk te maken tussen een conventioneel statisch experiment en een meting die gebruik maakt van een optische temperatuursensor wordt de statische warmtegeleidingscoëfficiënt optisch gemeten in hoofstuk 5. Het experiment wordt gedaan door een blokvormig sample continu vanaf één kant te verwarmen en de tegenovergestelde zijde op constante temperatuur te houden met een koelblok. De temperatuur van het oppervlak van één van de zijden tussen warmtebron en koelblok wordt lokaal gemeten met een microscoop. Het voordeel van deze methode ten opzichte van de conventionele is de verhoogde resolutie in lengte en daarmee de mogelijkheid om verschillen te zien in gedrag tussen verschillende delen van het sample. De lengteresolutie wordt slechts beperkt door de diffractielimiet. Door dichtbij de warmtebron te meten kan informatie worden verkregen over het deel van het sample waarin nog geen warmteëvenwicht is tussen verschillende warmtedragers. Hoewel verschillende kritische experimentele parameters zoals de

één-dimensionale warmtestroom, de koeling van het koelblok, de stabiele bevestiging van het sample en warmteverliezen beter onder controle moeten worden gekregen, zijn enige eerste resultaten verkregen die de voordelen van de methode laten zien. De initiële experimenten laten een goede overeenstemming zien tussen deze nieuwe methode en de conventionele methode, zowel voor nickel als voor het spinladder systeem.

Hoofdstuk 6 beschrijft dynamische bulk warmtegeleidingscoëfficiëntmetingen aan zowel de spinketen $SrCuO_2$ als de spinladders $Ca_9La_5Cu_{24}O_{41}$ en $Sr_{10}La_4Cu_{24}O_{41}$. Uit de experimenten is inzicht verkregen over de magnonendynamica op een tijdschaal van microseconden, iets dat niet makkelijk toegankelijk is in een steady state experiment. De metingen zijn uitgevoerd met behulp van de nieuw ontwikkelde fluorescentie flitsmethode, waarin een schijfje van het materiaal verhit wordt met een laserpuls aan de ene kant, terwijl de temperatuur gedetecteerd wordt als functie van de tijd aan de andere kant, gebruikmakend van hetzelfde laagje EuTTA als temperatuursensor als in het statische experiment. Het is interessant dat, terwijl voor de spinketen de effectieve dynamische bulk warmtegeleidingscoëfficiënt gelijk is aan de steady state bulk warmtegeleidingscoëfficiënt, deze voor de spinladders beduidend lager is, rond 40 W m^{-1} K^{-1}. Verder wordt een dikteafhankelijkheid gezien in $Ca_9La_5Cu_{24}O_{41}$. Daarom wordt in plaats van het macroscopische model het macroscopische twee-temperaturendiffusiemodel gebruikt om de dikteafhankelijke dynamische warmtegeleiding te analyseren. Het veranderen van de sampledikte verandert effectief de tijdschaal in het experiment en daarom de mate van warmteëvenwicht. Dit maakt het mogelijk om de thermalizatietijd tussen magnonen en fononen in $Ca_9La_5Cu_{24}O_{41}$ te bepalen. Deze is een paar honderd μs bij kamertemperatuur, wat extreem lang is. Dit kan worden verklaard door de lage kans op conversie tussen fononen en magnonen. In spinladder materialen heeft de dispersie een grote spin gap, welke de beperkende factor is voor de conversie van langzame fononen naar snelle magnonen, aangezien zulke verstrooiingsprocessen spin, impuls en energiebehoudregels breken. Met een andere temperatuursafhankelijke stof, EuTFC, kan de warmtegeleidingscoëfficiënt in $Ca_9La_5Cu_{24}O_{41}$ worden gemeten voor verschillende temperaturen van 10 tot 300 K. Het blijkt dat de effectieve warmtegeleidingscoëfficiënt voor een bepaalde sampledikte dichterbij de steady state warmtegeleidingscoëfficiënt ligt, wanneer de bijdrage van magnonen kleiner is, zoals verwacht wordt wanneer gekeken wordt naar het twee-temperaturenmodel.

In hoofdstuk 7 wordt warmtetransport langs het sampleoppervlak bekeken. Het oppervlak wordt afgebeeld door een microscoop, waarbij weer gebruik wordt gemaakt van een EuTTA-laagje als temperatuursensor. De spreiding van warmte vanuit een warmtespot, gecreëerd door een laser, wordt gevolgd in de tijd. Uit deze data wordt de diffusieconstante verkregen. Zowel de spinketen $SrCuO_2$ als de spinladders $Ca_9La_5Cu_{24}O_{41}$ en $Sr_{10}La_4Cu_{24}O_{41}$ worden gemeten en verschillende oppervlakteruwheden worden gebruikt. Een uitkomst is dat de warmtegeleidingscoëfficiënt in het sample met ~ 1 μm RMS ruwheid tenminste twee keer lager is dan de dynamische bulkwaarde, zoals bepaald is met de fluorescentie flitsmethode, zowel in de richting parallel aan de ladder/keten als in de richting loodrecht op de ladder/keten. Verder werd een gouden structuur in de vorm van een kruis, lijkend op een echt microapparaatje, aangebracht op het oppervlak van de spinladder $Ca_9La_5Cu_{24}O_{41}$ door middel van depositie. Eén strip was parallel aan de ladders en de andere loodrecht erop. De strips worden elektrisch verhit, één tegelijkertijd, waarmee een warme strip wordt gesimuleerd, zoals

in het echt kan voorkomen in een klein apparaatje. De warmtegeleidingscoëfficiënt voor dit zeer gladde sample met 20 nm RMS oppervlakteruwheid wordt gemeten met optisch verhitten en elektrisch verhitten. Het resultaat van beide methoden is in overeenstemming: 37 ± 3 W m^{-1} K^{-1} voor de snelle richting parallel aan de ladders en 2.5 ± 0.5 W m^{-1} K^{-1} voor de langzame richting loodrecht op de ladders. De warmtegeleidingscoëfficiënten in de snelle en langzame richting, gemeten op de dynamische manier, zijn in overeenstemming met andere dynamische metingen in de bulk op gelijke tijdschalen aan samples van dezelfde batch. Deze experimenten laten zien dat het sampleoppervlak zodanig geprepareerd kan worden dat het geen meetbare invloed heeft op het warmtetransport en dat het warmtetransport niet afhangt van de manier waarop de warmte in het systeem wordt gebracht. Hooftstuk 6 en 7 belichten de potentiële toepassing van de spinladder materialen als directionele warmtetransportkanalen. Maar, wanneer snel variërende warmtebronnen gebruikt worden is de waarde van de warmtegeleidingscoëfficiënt langs de ladders lager dan bij steady state omstandigheden. Wanneer de hoge waarde van de warmtegeleidingscoëfficiënt het voornaamste criterium is, kan daarom het directionele warmtetransportkanaal alleen gebruikt worden voor langzaam variërende warmtebronnen en over afstanden die lang genoeg zijn om het eerste deel waarin nog geen warmteëvenwicht is te kunnen verwaarlozen. Wanneer echter de grote anisotropie het belangrijkste criterium is, is dit materiaal, met dynamische anisotropie nog steeds ~ 15, ook geschikt als directioneel warmtekanaal voor snel variërende warmtebronnen.

Tenslotte verkent hoofdstuk 8 de dynamica op femtoseconde tot picoseconde tijdschaal in de spinladder $Ca_9La_5Cu_{24}O_{41}$. Het doel van deze metingen is om inzicht te krijgen in de magnondynamica in dit materiaal en de interactie tussen magnonen, elektronen en fononen op korte tijdschalen. Eerst worden temperatuursafhankelijke infrarood transmissiemetingen gedaan met licht dat zowel parallel aan als loodrecht op de ladders gepolarizeerd is. De lagetemperatuurdata zijn in overeenstemming met de literatuur. Voor de polarisatie parallel aan de ladders worden twee magnonabsorptiebanden gezien. De temperatuursafhankelijkheid van deze banden laat zien dat de oscillatieënergie mogelijk uitdooft bij 120 K. Aanvullende metingen moeten worden gedaan om de reden van deze mogelijke uitdoving te begrijpen.

Daarna worden temperatuursafhankelijke pomp-probe transient reflectiemetingen gedaan. Een daling van $\Delta R/R$ met temperatuur wordt gezien. Verder worden oscillaties veroorzaakt door akoestische fononen gezien, wanneer geprobed wordt met lichtpolarisatie parallel aan de ladders. Wanneer wordt geprobed met de polarizatie loodrecht op de ladders worden veel snellere oscillaties gezien, die waarschijnlijk worden veroorzaakt door optische fononen. Voor de probe met de parallelle polarisatie is de snelle vervaltijd, bepaald uit een bi-exponentiële fit, in de orde van 0.4 ps en onafhankelijk van temperatuur, terwijl de langzame vervaltijd lineair afneemt met toenemende temperatuur, van 10 ps bij 10 K tot 4 ps bij 300 K. Deze worden respectievelijk toegeschreven aan de tijd om warmteëvenwicht te bereiken tussen elektronen en fononen, en fononen onderling. Wanneer de probe een polarizatie loodrecht op de ladders heeft, is slechts een enkel-exponentiële fit nodig, en de vervaltijd is ietwat sneller dan de snelle exponent in de meting bij parallele probepolarizatie.

De laatste meetserie bestond uit temperatuursafhankelijke tijdsopgeloste transmissiemetingen. Vier probegolflengtes in het infrarood werden gebruikt; twee gepo-

sitioneerd in de magnonabsorptiebanden en twee buiten deze banden. De polarisatie van het licht was parallel aan de ladders. Er werd gepompt met 800 nm licht. Er kunnen geen duidelijke conclusies worden getrokken uit de korte en lange vervaltijden, die zijn verkregen uit een bi-exponentiële fit van de data. Enkele observaties kunnen worden gedaan; de korte vervaltijd is vergelijkbaar voor elke probegolflengte en er is geen duidelijke trend in temperatuursafhankelijkheid. Vooral bij lage temperatuur is de korte vervaltijd voor de pomppolarisatie loodrecht op de ladders hoger dan voor de pomppolarisatie parallel aan de ladders. Voor de lange vervaltijd is dit ook het geval. Ook is deze het hoogste bij 70 K. Het verschil zou kunnen komen door het verschil in bandgap in de verschillende richtingen. Verder werd een afhankelijkheid van het vermogen van de probepuls gezien vanwege verzadiging van de verandering ΔT in het probesignaal. Tenslotte worden oscillaties gezien bij 5.5 K voor medium pomppulsvermogens voor probegolflengtes in de magnonabsorptieband. Hoewel deze oscillaties niet kunnen worden verklaard met alleen de verkegen data suggereert de afwezigheid bij probegolflengtes buiten de magnonabsorptiebanden dat ze te maken hebben met magnondynamica.

11. Acknowledgements

It is not just the work one does that makes a project successful. It is also the colleagues around that supply help and support, and the friends one can share successes and failures with. During my years in Groningen I was lucky to find many smart, wise, friendly, helpful and/or inspiring people on my way. Therefore I've been looking forward to write these acknowledgements, in which I have the possibility to thank many of them. I apologize beforehand, because I am quite sure I will forget some.

Let me start with my supervisor prof. Paul van Loosdrecht. Paul, I find your way of working very inspiring. In a world in which almost everthing is about the money, you try to give curiosity and interest a higher priority. Furthermore, you understand very well how important it is to teach and tell about ones work and you do that with great enthusiasm. You have taught me to be critical in my work, clear in my explanations and detailed in my knowledge. Sometimes you forced me outside my comfort zone, which was not always pleasant, but certainly necessary and very useful for personal development. I am very grateful for all your positive contributions to my PhD project.

Then I would like to thank my reading committee prof. Beatriz Noheda, prof. Bernd Büchner and prof. Xenophon Zotos for carefully reading my manuscript and giving useful feedback. It certainly improved the quality of the thesis.

Next, the collaborators of the NOVMAG project. I think we have shown that by collaborating more can be achieved than by working alone. I am grateful for the useful discussions, the help from different groups in experiments, theory and sample growth and preparation and the great meetings we had at most beautiful locations all over Europe. My special thanks goes to Nikolai, for the help in the project, the pleasant conversations about different aspects of life, the visit of several concerts of the type that others would consider terrible noise, and the days in Berlin.

The 'Optical Condensed Matter Physics' group has been a very pleasant environment to work in. The attitude of helping each other I value very much. Much experimental work would not have been possible without the help of Foppe, Ben and Arjen, who, I think, are highly appreciated by everybody in the group. Jeannette, you are the best secretary one can wish for, and a very social and open-minded person. Maxim, after I had known you a bit longer, I realized what a nice person you are and how many interesting things you have to say. I am very greatful to Dima Fishman, because he spent years in teaching me how to handle optics properly. Even though we were sometimes lost in translation, he managed to let me profit from his great knowledge and experience. Matteo, thank you for all the fruitful discussions and the critical reading of my papers and thesis. Katja, I very much enjoyed travelling together. All other past and present group members I will not address personally, but I want to thank you for the very pleasant interaction I had with all of you. Furthermore, there were the nice

coffee talks and outside work activities; movie nights, city nights, Christmas nights, and all other kinds of activities. It was great to be the party organizer!

I would like to thank my fellow topmaster students. We had many scientific discussions and we motivated each other to get the best out of ourselves. I am not so sure if I would have chosen a PhD if I had not been in this stimulating environment. Alex, you've been my housemate as well, part of the time together with Oksana. It was great, and now I know how to drink wodka properly.

During my PhD I had the chance to supervise several smart and motivated students. I found it very rewarding to do so, and in the end we came to a stage in which the results obtained by the students were useful for my project as well. Aisha, Morten and Martine, thank you very much.

Next, I would like to thank my paranimfs for supporting me during the defense. Erwin, you are the most relaxed person I know. Thank you for teaching me to be more like that myself and for always seeing the positive side of things. It is wonderful to have you as a friend. Artem, I very much admire your dedication to science. But apart from that you are a lovely and caring friend for me. You broadened my view in several ways. It is always great to have you around.

My friends are very important to me, and I was lucky to find several in Groningen and around. There are a few that I would like to thank personally. Karianne, I admire your wisdom and strength. Mirjam, being family and friends makes our connection even stronger. Rosie, thanks for the all the relaxing days. Laura, you are a very pleasant combination of enthusiastic, cheerful and down-to-earth. Hielke, after living in the same house in harmony for so many years, I think we can stay friends for the rest of our lives. You have many more interesting things to tell than you might think you have. Dan, thank you for the pleasant times we spent together over the years. Durk, for you just a few keywords: philosophic conversations, unconventional movies and hanging on the couch. Wim, thanks for the dinners and beach walks. Niels and Mirjam, thanks for the good conversations and wines and wiskeys. To all my other friends: you are great!

Then I would say thanks to my parents. You made sure that I got the chance to have good education and I am very grateful for that. You do not always understand my choices, but let me make them anyway. Furthermore, thanks to my brother, always willig to help, who has admirable social skills and dedication to his work. Also thanks to my grandmother for the interesting conversations, even though you are over 60 years older than me.

The last paragraph is for the most important person in my life. Dearest Willie, one kiss, and all was clear. Some things are meant to be, and happen when the time is right. Thank you for all the joy, care and love that we share, have shared and will share. My life is better with you next to me.

Bibliography

[1] S. Lee. How to select a heat sink. *Electronics Cooling*, June 1st 1995.

[2] Y.S. Ju. Self-heating in thin-film magnetic recording heads due to write currents. *Magnetics, IEEE Transactions on*, 41(12):4443 – 4448, dec. 2005.

[3] K.G. Brill. 2005-2010 heat density trends in data processing, computer systems, and telecommunications equipments: perspectives, implications, and the current reality in many data centers. *White paper, The Uptime Institute Inc., Version 2.0, New York, USA*, pages 1–16, 2006.

[4] X. Zotos, F. Naef, and P. Prelovsek. Transport and conservation laws. *Phys. Rev. B*, 55:11029, 1997.

[5] A. V. Sologubenko, K. Giannò, H. R. Ott, U. Ammerahl, and A. Revcolevschi. Thermal conductivity of the hole-doped spin ladder system $Sr_{14-x}Ca_xCu_{24}O_{41}$. *Phys. Rev. Lett.*, 84:2714, 2000.

[6] C. Hess, C. Baumann, U. Ammerahl, B. Büchner, F. Heidrich-Meisner, W. Brenig, and A. Revcolevschi. Magnon heat transport in (Sr, Ca, La)$_{14}$Cu$_{24}$O$_{41}$. *Phys. Rev. B*, 64:184305, 2001.

[7] A. V. Sologubenko, K. Giannò, H. R. Ott, A. Vietkine, and A. Revcolevschi. Heat transport by lattice and spin excitations in the spin-chain compounds $SrCuO_2$ and Sr_2CuO_3. *Phys. Rev. B*, 64:054412, 2001.

[8] C. Hess. Heat conduction in low-dimensional quantum magnets. *Eur. Phys. J. Special Topics*, 151:73–83, 2007.

[9] C. Hess, C. Baumann, and B. Büchner. Scattering processes and magnon thermal conductivity in $La_5Ca_9Cu_{24}O_{41}$. *J. Mag. Mag. Mater.*, 290-291:322, 2005.

[10] U. Ammerahl, G. Dhalenne, A. Revcolevschi, J. Berthon, and H. Moudden. Crystal growth andcharacterization of the spin-ladder compound (Sr,Ca)$_{14}$Cu$_{24}$O$_{41}$. *J. Crystal Growth*, 193:55, 1998.

[11] U. Ammerahl and A. Revcolevschi. Crystal growth of the spin-ladder compound (Ca,La)$_{14}$Cu$_{24}$O$_{41}$ and observation of one-dimensional disorder. *J. Crystal Growth*, 197:825, 1999.

[12] U. Ammerahl, B. Büchner, L. Colonescu, R. Gross, and A. Revcolevschi. Interplay between magnetism, charge localization, and structure in $Sr_{14-x}Ca_xCu_{24}O_{41}$. *Phys. Rev. B*, 62:8630, 2000.

[13] U. Ammerahl, B. Büchner, C. Kerpen, R. Gross, and A. Revcolevschi. Ising-like antiferromagnetism in $Ca_9La_5Cu_{24}O_{41}$. *Phys. Rev. B*, 62:3592, 2000.

[14] G.I. Athanasopoulos, E. Svoukis, Z. Viskadourakis, and J. Giapintzakis. *Thermal conductivity measurements of anisotropic bulk samples using the 3ω method.* Daniela S. Gaal and Peter S. Gaal and ISBN: 978-1-60595-015-0, 2010.

[15] M. Azuma, Z. Hiroi, M. Takano, K. Ishida, and Y. Kitaoka. Observation of a spin gap in $SrCu_2O_3$ comprising spin-1/2 quasi two-leg ladders. *Phys. Rev. Lett.*, 73:3463, 1994.

[16] M. Azuma, M. Takano, and R. S. Eccleston. Disappearance of the spin gap in a zn-doped 2-leg ladder compound $Sr(Cu_{1-x}Zn_x)_2O_3$. *J. Phys. Soc. Jpn.*, 67:740, 1998.

[17] G. Blumberg, P. Littlewood, A. Gozar, B.S. Dennis, N. Motoyama, H. Eisaki, and S. Uchida. Sliding density wave in $Sr_{14}Cu_{24}O_{41}$. *Science*, 297:584, 2002.

[18] G. Blumberg, M. V. Klein, and S-W. Cheong. Charge and spin dynamics of an ordered stripe phase in $La_{5/3}Sr_{1/3}NiO_4$. *Phys. Rev. Lett.*, 80:564, 1998.

[19] S. A. Carter, B. Batlogg, R.J. Cava, J.J. Krajewski, W.F. Peck, Jr., and T.M. Rice. Hole doping of the CuO_2 chains in $(La,Sr,Ca)_{14}Cu_{24}O_{41}$. *Phys. Rev. Lett.*, 77:1378, 1996.

[20] H. Chen, Q. Wang, Y. Dai, C. Lin, Y. Ni, and Y. Zhang. Magnetic interaction between Cu ions in $La_xSr_{1-x}Cu_{24}O_{41}$ (x=0-6.0). *Physica C*, 337:317–321, 2000.

[21] S-W. Cheong, G. Aeppli, T. E. Mason, H. Mook, S. M. Hayden, P. C. Canfield, Z. Fisk, K. N. Clausen, and J. L. Martinez. Incommensurate magnetic fluctuations in $La_{2-x}Sr_xCuO_4$. *Phys. Rev. Lett.*, 67:1790, 1991.

[22] A.L. Chernyshev. Heat transport in real spin-chain materials. *JMMM*, 10:432, 2006.

[23] E. Dagotto and T. M. Rice. Surprises on the way from one- to two-dimensional quantum magnets: The ladder materials. *Science*, 271:618, 1996.

[24] R. S. Eccleston, M. Uehara, J. Akimitsu, H. Eisaki, N. Motoyama, and S. I. Uchida. Spin dynamics of the spin-ladder dimer-chain material $Sr_{14}Cu_{24}O_{41}$. *Phys. Rev. Lett.*, 81:1702, 1998.

[25] Y. Gotoh, I. Yamaguchi, Y. Takahashi, J. Akimoto, M. Goto, M. Onoda, H. Fujino, T. Nagata, and J. Akimitsu. Structural modulation, hole distribution, and hole-ordered structure of the incommensurate composite crystal $(Sr_2Cu_2O_3)_{0.70}CuO_2$. *Phys. Rev. B*, 68(22):224108, Dec 2003.

[26] A. Gozar, G. Blumberg, P. B. Littlewood, B. S. Dennis, N. Motoyama, H. Eisaki, and S. Uchida. Collective density-wave excitations in two-leg $Sr_{14-x}Ca_x$ $Cu_{24}O_{41}$ ladders. *Phys. Rev. Lett.*, 91:087401, 2003.

[27] M. Grüninger, M. Windt, T. Nunner, C. Knetter, K. P. Schmidt, G. S. Uhrig, T. Kopp, A. Freimuth, U. Ammerahl, B. Büchner, and A. Revcolevschi. Optical spectroscopy of $(La,Ca)_{14}Cu_{24}O_{41}$ spin ladders: comparison of experiment and theory. *Physica B*, 312-313:617–618, 2002.

[28] F. Heidrich-Meisner, A. Honecker, D. C. Cabra, and W. Brenig. Thermal conductivity of anisotropic and frustrated spin-1/2-chains. *Phys. Rev. B*, 66:R140406, 2002.

[29] F. Heidrich-Meisner, A. Honecker, D. C. Cabra, and W. Brenig. Zero-frequency transport properties of one-dimensional spin-(1/2) systems. *Phys. Rev. B*, 68:134436, 2003.

[30] F. Heidrich-Meisner, A. Honecker, and W. Brenig. Thermal transport of the XXZ chain in a magnetic field. *Phys. Rev. B*, 71:184415, 2005.

[31] C. Hess, U. Ammerahl, C. Baumann, B. Büchner, and A. Revcolevschi. Magnon hole scattering in $(Sr,Ca,La)_{14}Cu_{24}O_{41}$. *Physica B*, 312-313:612, 2002.

[32] C. Hess, H. ElHaes, B. Büchner, U. Ammerahl, M. Hücker, and A. Revcolevschi. Magnon-hole scattering and charge order in $Sr_{14-x}Ca_xCu_{24}O_{41}$. *Phys. Rev. Lett.*, 93:027005, 2004.

[33] C. Hess, P. Ribeiro, B. Büchner, H. ElHaes, G. Roth, U. Ammerahl, and A. Revcolevschi. Magnon heat conductivity and mean free paths in two-leg spin ladders: A model-independent determination. *Phys. Rev. B*, 73:104407, 2006.

[34] N. Hlubek, P. Ribeiro, R. Saint-Martin, A. Revcolevschi, G. Roth, G. Behr, B. Büchner, , and C. Hess. Ballistic heat transport of quantum spin excitations as seen in $SrCuO_2$. *Phys. Rev. B*, 81 020405(R), 2010.

[35] C. Jurecka and W. Brenig. Two-hole dynamics in spin ladders. *J. Low Temp. Phys.*, 126:1165, 2002.

[36] V. Kataev, K.-Y. Choi, M. Grüninger, U. Ammerahl, B. Büchner, A. Freimuth, and A. Revcolevschi. Interplay of spin and charge dynamics in $Sr_{14-x}Ca_xCu_{24}O_{41}$. *Phys. Rev. B*, 64:104422, 2001.

[37] A. Klümper and K. Sakai. The thermal conductivity of the spin 1/2 XXZ chain at arbitrary temperature. *J. Phys. A: Math. Gen.*, 35:2173, 2002.

[38] K. Kudo, S. Ishikawa, T. Noji, T. Adachi, Y. Koike, K. Maki, S. Tsuji, and K. Kumagai. Spin gap and hole pairing in the spin-ladder cuprate $Sr_{14-x}Cu_{24}O_{41}$ (a=Ca and La) studied by the thermal conductivity. *J. Phys. Soc. Jpn.*, 70:437, 2001.

[39] M. Matsuda, K. Katsumata, R. S. Eccleston, S. Brehmer, and H.-J. Mikeska. Magnetic excitations and exchange interactions in the spin-1/2 two-leg ladder compound $La_6Ca_8Cu_{24}O_{41}$. *Phys. Rev. B*, 62:8903, 2000.

[40] J. Akimitsu, M. Uehara, T. Nagata, S. Matsumoto, Y. Kitaoka, H. Takahashi, and N. Môri. Metal-insulator transition in the S = 1/2 spin ladder system $(Sr_{0.4}Ca_{0.6})_{14}Cu_{24-x}Co_xO_{41-\delta}$. *Physica C*, 263:475–481, 1996.

[41] T. Osafune, N. Motoyama, H. Eisaki, S. Uchida, and S. Tajima. Pseudogap and collective mode in the optical conductivity spectra of hole-doped ladders in $Sr_{14-x}Ca_xCu_{24}O_{41}$. *Phys. Rev. Lett.*, 82:1313, 1999.

[42] Z. V. Popovic, M. J. Konstantinovic, V. A. Ivanov, O. P. Khuong, R. Gajic, A. Vietkin, and V. V. Moshchalkov. Optical properties of the spin-ladder compound $Sr_{14}Cu_{24}O_{41}$. *Phys. Rev. B*, 62:4963, 2000.

[43] O. S. Barisic, P. Prelovsek, A. Metavitsiadis, and X. Zotos. Incoherent transport induced by a single static impurity in a heisenberg chain. *Physical Review B*, 80, 2009.

[44] T. M. Rice, S. Gopalan, and M. Sigrist. Superconductivity, spin gaps and luttinger liquids in a class of cuprates. *Europhys. Lett.*, 23:445, 1993.

[45] S. Langer, F. Heidrich-Meisner, J. Gemmer, I. P. McCulloch, and U. Schollwöck. Real-time study of diffusive and ballistic transport in spin 1/2 chains using the adaptive time-dependent density matrix renormalization group method. *Phys. Rev. B*, 79:214409, 2009.

[46] A. V. Sologubenko, T. Lorenz, H. R. Ott, and A. Freimuth. Thermal conductivity via magnetic excitations in spin-chain materials. *Journal of Low Temperature Physics*, 147:387, 2007.

[47] M. Windt, M. Grüninger, T. Nunner, C. Knetter, K. P. Schmidt, G. S. Uhrig, T. Kopp, A. Freimuth, U. Ammerahl, B. Büchner, and A. Revcolevschi. Observation of two-magnon bound states in the two-leg ladders of $(Ca, La)_{14}Cu_{24}O_{41}$. *Phys. Rev. Lett.*, 87:127002, 2001.

[48] X. Zotos. High temperature thermal conductivity of 2-leg spin-1/2 ladders. *Phys. Rev. Lett.*, 92:067202, 2004.

[49] X. Zotos. Finite temperature Drude weight of the one-dimensional spin- 1/2 Heisenberg model. *Phys. Rev. Lett.*, 82(8):1764–1767, Feb 1999.

[50] H. Hiraka, T. Machi, N. Watanabe, Y. Itoh, M. Matsuda, and K. Yamada. Ni impurity effect on antiferromagnetic order in hole-doped $La_{2-x}Sr_xCuO_4$. *Journal of the Physical Society of Japan*, 74:2197–2200, 2005.

[51] N. Hlubek. Magnetic heat transport in one-dimensional quantum antiferromagnets. *Dissertation, Chapter 6*, 2010.

[52] N. D. Mermin and H. Wagner. Absence of ferromagnetism or antiferromagnetism in one- or two-dimensional isotropic Heisenberg models. *Phys. Rev. Lett.*, 17(22):1133–1136, 1966.

[53] J. M. Luttinger. An exactly soluble model of a many-fermion system. 4(9):1154–1162, 1963.

[54] K.A. Müller. On the superconductivity in hole doped cuprates. *Journal of physics: condensed matter*, 19(25), 2007.

[55] V. O. Garlea, A. Zheludev, T. Masuda, H. Manaka, L.-P. Regnault, E. Ressouche, B. Grenier, J.-H. Chung, Y. Qiu, K. Habicht, K. Kiefer, and M. Boehm. Excitations from a Bose-Einstein condensate of magnons in coupled spin ladders. *Phys. Rev. Lett.*, 98(16):167202, Apr 2007.

[56] H. S. Carslaw and J. C. Jaeger. *Conduction of Heat in Solids*. At the Clarendon Press, Oxford, 1959.

[57] T. Vuletic, B. Korin-Hamzic, T. Ivek, S. Tomic, B. Gorshunov, M. Dressel, and J. Akimitsu. The spin-ladder and spin-chain system $(La,Y,Sr,Ca)_{14}Cu_{24}O_{41}$: Electronic phases, charge and spin dynamics. *Physics Reports*, 428(4):169 – 258, 2006.

[58] A. Zvyagin. *Finite size effects in correlated electron models: exact results*. Imperial College Press, London, 2005.

[59] D. Beariswyl and L. Degiorgi. *Strong interactions in low dimensions*. Kluwer Academic Publishers, 2004.

[60] L. Balents. Spin liquids in frustrated magnets. *Nature*, 464:199–208, 2010.

[61] H. Bethe. Zur theorie der metalle i. eigenwerte und eigenfunktionen der linearen atomkette. *Z. Phys.*, 71:205, 1931.

[62] S. Blundell. *Magnetism in Condensed Matter*. Oxford master series in condensed matter physics, 2001.

[63] L. D. Faddeev and L. A. Takhtajan. What is the spin of a spin wave? *Physics Letters A*, 85(6-7):375 – 377, 1981.

[64] N. Papanicolaou. Complete integrability for a discrete heisenberg chain. *Journal of Physics A: Mathematical and General*, 20(12), 1987.

[65] S. N. Evangelou. Soliton propagation in a classical heisenberg chain with impurities. *J. Phys.: Condens. Matter*, 8:1051–1058, 1996.

[66] M. Takano, M. Azuma, Z. Hiroi, Y. Bando, and Y. Takeda. Superconductivity in the Ba-Sr-Cu-O system. *Physica C: Superconductivity*, 176(4-6):441 – 444, 1991.

[67] L. Teske and Hk. Müller-Buschbaum. Ueber erdalkalimetall-oxocuprate. v. zur kenntnis von Ca_2CuO_3 und $SrCuO_2$. *Z. Anorg. Allg. Chem.*, 379(3):234–241, 1970.

[68] J. Kanamori. Superexchange interaction and symmetry properties of electron orbitals. *J. Phys. Chem. Solids*, 10:87–98, 1958.

[69] I. A. Zaliznyak, C. Broholm, M. Kibune, M. Nohara, and H. Takagi. Anisotropic spin freezing in the S=1/2 zigzag chain compound $SrCuO_2$. *Phys. Rev. Lett.*, 83(25):5370–, December 1999.

[70] Y. Mizuno, T. Tohyama, and S. Maekawa. Superexchange interaction in cuprates. *Phys. Rev. B*, 58:R14713–R14716, Dec 1998.

[71] H. Woo, I. Zaliznyaka, T.G. Perringb, C. Broholmc, C. Frostb, and H. Takagi. Spinons in a strongly correlated copper oxide chains. *Physica B*, 350:e249–e252, 2004.

[72] Jacques des Cloizeaux and J. J. Pearson. Spin-wave spectrum of the antiferromagnetic linear chain. *Phys. Rev.*, 128:2131–2135, Dec 1962.

[73] J. G. Bednorz and K. A. Müller. Possible high T_c superconductivity in the Ba-La-Cu-O system. *Z. Phys. B - Condensed Matter*, 64:189, 1986.

[74] Olav F. Syljuåsen, Sudip Chakravarty, and Martin Greven. Correlation lengths in quantum spin ladders. *Phys. Rev. Lett.*, 78:4115–4118, May 1997.

[75] T. Barnes, E. Dagotto, J. Riera, and E. S. Swanson. Excitation spectrum of heisenberg spin ladders. *Phys. Rev. B*, 47:3196, 1993.

[76] E. Dagotto, J. Riera, and D. Scalapino. Superconductivty in ladders and coupled planes. *Phys. Rev. B*, 45:5744, 1992.

[77] E. M. McCarron, M. A. Subramanian, J.C. Calabrese, and R. L. Harlow. The incommensurate structure of $(Sr_{14-x}Ca_x)Cu_{24}O_{41}$ ($0 < x \approx 8$) a superconductor byproduct. *Mat. Res. Bull.*, 23:1355, 1988.

[78] R. S. Eccleston, M. Azuma, and M. Takano. Neutron-scattering and susceptibility study of spin chains and spin ladders in $(Sr_{0.8}Ca_{0.2})_{14}Cu_{24}O_{41}$. *Phys. Rev. B*, 53(22):R14721–R14724, Jun 1996.

[79] S. Notbohm, P. Ribeiro, B. Lake, D. A. Tennant, K. P. Schmidt, G. S. Uhrig, C. Hess, R. Klingeler, G. Behr, B. Büchner, M. Reehuis, R. I. Bewley, C. D. Frost, P. Manuel, and R. S. Eccleston. One- and two-triplon spectra of a cuprate ladder. *Phys. Rev. Lett.*, 98(2):027403, Jan 2007.

[80] T. Siegrist, L. F. Schneemeyer, S. A. Sunshine, J. V. Wazczak, and R. S. Roth. A new layered cuprate structure-type, $(A_{1-x}A'_x)_{14}Cu_{24}O_{41}$. *Mat. Res. Bull.*, 23:1429, 1988.

[81] T. Osafune, N. Motoyama, H. Eisaki, and S. Uchida. Optical study of the $Sr_{14-x}Ca_xCu_{24}O_{41}$ system: Evidence for hole-doped Cu_2O_3 ladders. *Phys. Rev. Lett.*, 78(10):1980–1983, Mar 1997.

[82] N. Nücker, M. Merz, C. A. Kuntscher, S. Gerhold, S. Schuppler, R. Neudert, M. S. Golden, J. Fink, D. Schild, S. Stadler, V. Chakarian, J. Freeland, Y. U. Idzerda, K. Conder, M. Uehara, T. Nagata, J. Goto, J. Akimitsu, N. Motoyama, H. Eisaki, S. Uchida, U. Ammerahl, and A. Revcolevschi. Hole distribution in $(Sr,Ca,La)_{14}Cu_{24}O_{41}$ ladder compounds studied by x-ray absorption spectroscopy. *Phys. Rev. B*, 62:14384, 2000.

[83] K. Magishi, S. Matsumoto, Y. Kitaoka, K. Ishida, K. Asayama, M. Uehara, T. Nagata, and J. Akimitsu. Spin gap and dynamics in $Sr_{14-x}Ca_xCu_{24}O_{41}$ comprising hole-doped two-leg spin ladders: Cu NMR study on single crystals. *Phys. Rev. B*, 57:11533, 1998.

[84] T. Barnes and J. Riera. Susceptibility and excitation spectrum of $(VO)_2P_2O_7$ in ladder and dimer-chain models. *Phys. Rev. B*, 50:6817, 1994.

[85] S. Notbohm, P. Ribeiro, B. Lake, D. A. Tennant, K. P. Schmidt, G. S. Uhrig, C. Hess, R. Klingeler, G. Behr, B. Büchner, M. Reehuis, R. I. Bewley, C. D. Frost, P. Manuel, and R. S. Eccleston. One- and two-triplon spectra of a cuprate ladder. *Phys. Rev. Lett.*, 98(2):027403, Jan 2007.

[86] H. Fröhlich and W. Heitler. Time effects in the magnetic cooling method II – the conductivity of heat. *Proc. Roy. Soc. (London)*, A155:640, 1936.

[87] B. Lüthi. Thermal conductivity of yttrium iron garnet. *J. Phys. Chem. Solids*, 23:35, 1962.

[88] K. Kudo, S. Ishikawa, T. Noji, T. Adachi, Y. Koike, K. Maki, S. Tsuji, and K. Kumagai. Spin gap and hole pairing of $Sr_{14-x}A_xCu_{24}O_{41}$ (a = Ca and La) single crystals studied by the electrical resistivity and thermal conductivity. *Journal of Low Temperature Physics*, 117:1689–1693, 1999. 10.1023/A:1022588421579.

[89] W.J. Parker, R. J. Jenkins, C. P. Butler, and G. L. Abbott. Flash method of determining thermal diffusivity, heat capacity, and thermal conductivity. *J. Appl. Phys.*, 32:1679, 1961.

[90] D. J. Sanders and D. Walton. Effect of magnon-phon thermal relaxation on heat transport by magnons. *Phys. Rev. B*, 15:1489, 1977.

[91] R.Kubo. The fluctuation-dissipation theorem. *Rep. Prog. Phys.*, 29:255, 1966.

[92] P. Ribeiro. One-dimensional quantum magnets in cuprates: Single crystal growth and magnetic heat transport studies. *Dissertation*, 2007.

[93] P. Ribeiro, C. Hess, P. Reutler, G. Roth, and B. Büchner. Heat transport in doped $SrCuO_2$. *J. Mag. Mag. Mater.*, 290-291:334, 2005.

[94] T. Kawamata, N. Takahashi, T . Adachi, T. Noji, K. Kudo, N. Kobayashi, and Y. Koike. Evidence for ballistic thermal conduction in the one-dimensional s = 1/2 heisenberg antiferromagnetic spin system Sr_2CuO_3. *Journal of the Physical Society of Japan*, 77:034607, 2008.

[95] P. D. Thacher. Effect of boundaries and isotopes on the thermal conductivity of LiF. *Physical Review*, 156:975, 1967.

[96] S. Langer, F. Heidrich-Meisner, J. Gemmer, I. P. McCulloch, and U. Schollwöck. Real-time study of diffusive and ballistic transport in spin- $\frac{1}{2}$ chains using the adaptive time-dependent density matrix renormalization group method. *Phys. Rev. B*, 79(21):214409, Jun 2009.

[97] A. Revcolevschi, U. Ammerahl, and G. Dhalenne. Crystal growth of pure and substituted low-dimensionality cuprates $CuGeO_3$, La_2CuO_4, $SrCuO_2$, Sr_2CuO_3 and $Sr_{14}Cu_{24}O_{41}$ by the floating zone and travelling solvent zone methods. *Journal of Crystal Growth*, 198/199:593–599, 1999.

[98] O. V. Misochko, S. Tajima, C. Urano, H. Eisaki, and S. Uchida. Raman-scattering evidence for free spinons in the one-dimensional spin-1/2 chains of Sr_2CuO_3 and $SrCuO_2$. *Phys. Rev. B*, 53:R14733–R14736, Jun 1996.

[99] G. A. Zlateva, V. N. Popov, M. Gyulmezov, L. N. Bozukov, and M. N. Liev. Phonons in $Ca_{2-x}Sr_xCuO_3$ (x=0, 0.2 and 0.4): Raman and infrared spectroscopy, and lattice dynamics calculation. *Journal of Physics: Condensed matter*, 4:8543 – 8550, 1992.

[100] P. Kolodner and J. A. Tyson. Microscopic fluorescent imaging of surface temperature profiles with 0.01° c resolution. *J. Appl. Phys.*, 40:782, 1982.

[101] H. Winston, O. J. Marsh, C. K. Suzuki, and C. L. Telk. Fluorescence of europium thenoyltrifluoroacetonate. i. evaluation of laser treshold parameters. *J. Chem. Phys.*, 39:267, 1963.

[102] J. Georges and J. M. Mermet. Simultaneous time-resolved fluorescence and thermal lens measurements: application to energy transfer studies in europium chelates. *Spectrochimica Acta*, 49A:397, 1993.

[103] William R. Dawson, John L. Kropp, and Maurice W. Windsor. Internal-energy-transfer efficiencies in eu^{3+} and tb^{3+} chelates using excitation to selected ion levels. *The Journal of Chemical Physics*, 45(7):2410–2418, 1966.

[104] D. L. Barton and P. Tangyunyong. Fluorescent microthermal imaging - theory and methodology for achieving high thermal resolution images. *Microelectronic Engineering*, 31:271–279, 1996.

[105] P.R. Kolodner, K.G. Hampel, and P.L. Gammel. Fluorescent thermal imaging using rare-earth chelate films. *United States Patent 5971610*, 1999.

[106] Ø. Haugen and T.H. Johansen. Temperature dependent photoluminescence down to 4.2k in eutfc. *Journal of Luminescence*, 128:1479–1483, 2008.

[107] Guodong Qian and Z. Yang. Time-resolved spectra and energy migration of europium chelate with thenoyltrifluoroacetone in-situ synthesized in ormosil. *Journal Of Materials Science Letters*, 19:1315, 2000.

[108] Y. S. Touloukian. *Thermophysical Properties of Matter*. John Wiley & Sons Ltd, 1970.

[109] C. Hess and B. Büchner. Thermal conductivity of doped La_2CuO_4 as an example for heat transport by optical phonons in complex materials. *Eur. Phys. B*, 38:37, 2004.

[110] M. Montagnese, M. Otter, N. Hlubek, R. Saint-Martin, S. Singh, A. Revcolevschi, C. Hess, and P.H.M. van Loosdrecht. Optical time domain studies of magnetic heat transport in quantum spin chains and ladders: first evidence of magnon-phonon decoupling at the ms scale. in preparation, 2012.

[111] M. Otter, V. V. Krasnikov, D. A. Fishman, M. S. Pshenichnikov, R. Saint-Martin, A. Revcolevschi, and P. H. M. van Loosdrecht. Heat transport imaging in the spin-ladder compound $Ca_9La_5Cu24O_{41}$. *JMMM*, 321:796, 2008.

[112] F. Heidrich-Meisner, A. Honecker, D. C. Cabra, and W. Brenig. Comment on "anomalous thermal conductivity of frustrated heisenberg spin chains and ladders". *Phys. Rev. Lett.*, 92:069703, 2004.

[113] M. Braden, B. Hennion, W. Reichardt, G. Dhalenne, and A. Revcolevschi. Spin-phonon coupling in $CuGeO_3$. *Phys. Rev. Lett.*, 80:3634–3637, Apr 1998.

[114] R. Shaviv, E.R. Westrum, T.L. Yang, C.B. Alcock, and B. Li. Thermodynamics of the (lathanum+strontium+copper+oxygen) high T_c superconductors i. heat capacities of $SrCuO_2$, Sr_2CuO_3 and $Sr_{14}Cu_{24}O_{41}$. *J. Chem. Thermodynamics*, 22:1025–1034, 1990.

[115] Yoshitaka Matsushita, Yasunao Oyama, Masashi Hasegawa, and Humihiko Takei. Growth and structural refinement of orthorhombic $SrCuO_2$ crystals. *Journal of Solid State Chemistry*, 114(1):289 – 293, 1995.

[116] R. Nakayama, Y. Tanaka, H. Yui, H. Yamauchi, A.Q.R. Baron, and T. Sasagawa. Phonon properties in the simplest cuprate compound $SrCuO_2$. *Physica C: Superconductivity*, 470(Supplement 1):S151 – S152, 2010. Proceedings of the 9th International Conference on Materials and Mechanisms of Superconductivity.

[117] N. Gedik, J. Orenstein, Ruixing Liang, D. A. Bonn, and W. N. Hardy. Diffusion of nonequilibrium quasi-particles in a cuprate superconductor. *Science*, 300(5624):1410–1412, 2003.

[118] Z. V. Popovic, M. J. Konstantinovic, R. Gajic C. Thomsen, U. Kuhlmann, and A. Vietkin. Polarized far-infrared and raman spectra of $SrCuO_2$ single crystals. *Physica C*, 351:386–394, 2001.

[119] Fei Wu Jingkui Liang, Zhan Chen and Sishen Xie. Phase diagram of SrO-CaO-CuO ternary system. *Solid State Communications*, 75(3):247–252, 1990.

[120] J. Lorenzana and G. A. Sawatzky. Theory of phonon-assisted multimagnon optical absorption and bimagnon states in quantum antiferromagnets. *Phys. Rev. B*, 52:9576–9589, Oct 1995.

[121] I. A. Zaliznyak, H. Woo, T. G. Perring, C. L. Broholm, C. D. Frost, and H. Takagi. Spinons in the strongly correlated copper oxide chains in $SrCuO_2$. *Phys. Rev. Lett.*, 93(8):087202–, August 2004.

[122] M.V. Abrashev, A.P. Litvinchuk, C Thomsen, and V.N. Popov. Fröhlich-interaction-induced multiphonon raman scattering in $SrCuO_2$ and $Sr_{0.5}Ca_{0.5}CuO_2$. *Phys. Rev. B*, 55(14), April 1997.

[123] Optical probing of anisotropic heat transport in the quantum spin ladder $Ca_9La_5Cu_{24}O_{41}$. *International Journal of Heat and Mass Transfer*, 55(9-10):2531–2538, 2012.

[124] E. Dagotto. Experiments on ladders reveal a complex interplay between a spin-gapped normal state and superconductivity. *Rep. Prog. Phys.*, 62:1525, 1999.

[125] C. Hess, B. Büchner, U. Ammerahl, and A. Revcolevschi. Phonon thermal conductivity in doped La_2CuO_4: Relevant scattering mechanisms. *Phys. Rev. B*, 68:184517, 2003.

[126] Ascomp gmbh, 2010. transat: Equations & algorithms, transat handbook series 2.3.0. *www.ascomp.ch/transat*.

[127] Koshi Takenaka, Kenji Iida, Yuko Sawaki, Shunji Sugai, Yutaka Moritomo, and Arao Nakamura. Optical reflectivity spectra measured on cleaved surfaces of $La_{1-x}Sr_xMnO_3$: Evidence against extremely small drude weight. *Journal of the Physical Society of Japan*, 68(6):1828–1831, 1999.

[128] H. R. Shanks, P. D. Maycock, P. H. Sidles, and G. C. Danielson. Thermal conductivity of silicon from 300 to 1400°k. *Phys. Rev.*, 130(5):1743–1748, Jun 1963.

[129] T. R. Anthony, W. F. Banholzer, J. F. Fleischer, Lanhua Wei, P. K. Kuo, R. L. Thomas, and R. W. Pryor. Thermal diffusivity of isotopically enriched $c12$ diamond. *Phys. Rev. B*, 42(2):1104–1111, Jul 1990.

[130] Jae Hun Seol, Insun Jo, Arden L. Moore, Lucas Lindsay, Zachary H. Aitken, Michael T. Pettes, Xuesong Li, Zhen Yao, Rui Huang, David Broido, Natalio Mingo, Rodney S. Ruoff, and Li Shi. Two-dimensional phonon transport in supported graphene. *Science*, 328(5975):213–216, 2010.

[131] C. Thomsen, H. T. Grahn, H. J. Maris, and J. Tauc. Surface generation and detection of phonons by picosecond light pulses. *Phys. Rev. B*, 34:4129–4138, Sep 1986.

[132] H. B. Zhao, Y. Fan, G. Lüpke, A. T. Hanbicki, C. H. Li, and B. T. Jonker. Detection of coherent acoustic phonons by time-resolved second-harmonic generation. *Phys. Rev. B*, 83:212302, Jun 2011.

[133] S. Zherlitsyn, S. Schmidt, B. Wolf, H. Schwenk, B. Lüthi, H. Kageyama, K. Onizuka, Y. Ueda, and K. Ueda. Sound-wave anomalies in $SrCu_2(BO_3)_2$. *Phys. Rev. B*, 62:R6097–R6099, Sep 2000.

[134] Sheng-Fu Horng, Shi-Hsiang Lu, Jian-Shen Yu, Tsong-Ru Tsai, and Cheng-Chung Chi. Comparison of optical pump-probe characterization of low-temperature-grown gaas at well-above-bandgap and near-bandedge wavelengths. *Optical and Quantum Electronics*, 32:573–584, 2000. 10.1023/A:1007008003089.

[135] J. J. Baumberg, D. A. Williams, and K. Köhler. Ultrafast acoustic phonon ballistics in semiconductor heterostructures. *Phys. Rev. Lett.*, 78:3358–3361, Apr 1997.